COMPUTATIONAL MODELING OF THE TRANSITION FROM DAMAGE TO FRACTURE IN INTRINSICALLY ANISOTROPIC POROUS MEDIA

A Dissertation
Presented to
The Academic Faculty

By

Wencheng Jin

In Partial Fulfillment
of the Requirements for the Degree
Doctor of Philosophy in the
School of Civil and Environmental Engineering

Georgia Institute of Technology

December 2018

COMPUTATIONAL MODELING OF THE TRANSITION FROM DAMAGE TO FRACTURE IN INTRINSICALLY ANISOTROPIC POROUS MEDIA

Approved by:

Dr. Chloe Arson, Advisor
School of Civil and Environmental Engineering
Georgia Institute of Technology

Dr. Ronaldo I. Borja
Department of Civil and Environmental Engineering
Stanford University

Dr. J. David Frost
School of Civil and Environmental Engineering
Georgia Institute of Technology

Dr. Richard W. Neu
School of Mechanical Engineering
Georgia Institute of Technology

Dr. Glaucio H. Paulino
School of Civil and Environmental Engineering
Georgia Institute of Technology

Dr. Joshua White
Atmospheric, Earth and Energy Division
Lawrence Livermore National Laboratory

Date Approved: July 26, 2018

To my beloved wife,

Li Wang,

for giving me endless support and love.

ACKNOWLEDGEMENTS

I would like to express my sincere gratitude towards my advisor, Dr. Chloé Arson, for her patient guidance, warm encouragement, and continuous support through out my academic journey in Georgia Institute of Technology. Her insightful advice on my doctoral research and her constructive suggestion for my career development turned me into a passionate scholar, and will continuously inspire me for my future endeavors.

I would like to acknowledge my Ph.D. thesis committee members: Dr. Ronaldo Borja, Dr. David Frost, Dr. Glaucio Paulino, Dr. Richard Neu and Dr. Joshua White. Their invaluable comments and suggestions helped me to improve the quality of this thesis significantly. I want to thank Dr. Borja for attending my thesis defense at 6:00am in the morning. I am thankful to Dr. David Frost for being always supportive throughout my stay in Georgia Tech. I am grateful to Dr. Glaucio Paulino, not only for his great scientific mentoring, but also for his career advice. I wish to thank Dr. Neu for his great course of inelastic deformation. I also want to acknowledge Dr. White for flying to Atlanta for my defense and for giving me great advices on LBB conditions. I would like to take this opportunity to thank all the other geosystems faculty members, including Dr. Carlos Santamarina, Dr. Leonid Germanovich, Dr. Haiying Huang, Dr. Sheng Dai, Dr. Susan Burns, and Dr. Paul Mayne. Especially, I appreciate Dr. Sheng Dai for sharing experience and providing career suggestions.

The completion of this thesis is not possible without the help I received throughout the years. Special thanks to Dr. Giang D. Nguyen from University of Adelaide, Dr. Mohammad Vahab from University of New South Wales, Dr. Yongxiang Wang from Columbia University. Dr. Qizhi Zhu from Hohai University, and Dr. Seth Busetti from ConocoPhillips. I am grateful for their valuable suggestions.

I also wish to thank my former and current lab members: Dr. Hao Xu, Dr. Cheng Zhu, Pei Wang, Xianda Shen, Koochul Ji and Fernando Ramirez. The discussion related

or unrelated to research with them truly make my stay an enjoyable journey. I want to express my acknowledgement towards Geosociety members for sharing experience, jokes, and progress. In particular, I would like to thank the Geosociety leaders who helped me a lot when I was serving the vice president and the president.

Finally, my special appreciation is reserved for my wife, Li Wang, who sacrificed her job in China and came to US to accompany me. Her everlasting love and support motivate me to make progress. I am particularly indebted to my father, Diquan Jin, and mother, Guoxiu Gan, I cannot find the right words to express my gratitude and appreciation. All I am right now is because of their love and support. I wish them have a happy and enjoyable life in China. I would like to thank all my relatives and friends near and far for their support and encouragement at last.

TABLE OF CONTENTS

LIST OF TABLES

LIST OF FIGURES

SUMMARY

The initiation and propagation of discontinuities in brittle materials is of great interest to engineers, at several scales. Cracks can be detrimental for concrete structures but cracks are necessary to extract energy resources. A number of numerical tools are available to model fracture propagation, mostly in solids subjected to mechanical stresses or fluid pressures applied at a notch. However, the fundamental inception mechanisms are not fully understood. The goal of this doctoral research work is, therefore, to understand the processes that govern the initiation and propagation of micro-cracks in mixed mode in crystalline and porous media, and to predict the transition between a material that contains a high density of micro-cracks and a portion of discrete fracture. A particular attention is paid to materials with intrinsic anisotropy, such as sedimentary rocks. Advanced numerical methods including nonlocal continuum damage models, cohesive segments discretized with the Extended Finite Element Method (XFEM) are used to study complex phenomena induced by damage under mechanical and hydraulic loads, including softening, anisotropy, stiffness degradation.

In the first part of the thesis, two novel anisotropic damage models are formulated to explicitly account for the evolution of discrete sets of micro-cracks. Both models are based on the same free enthalpy expression, derived from a dilute homogenization scheme, using 42 sets of crack families of different orientations. These two models differ by their damage criteria and crack evolution laws: the first model is based on the theory of wing crack development, whereas the second model is based on a radial crack growth law, which depends on a phenomenological driving force. The phenomenological model is implemented into Abaqus User MATerial (UMAT) subroutines, and a return-mapping algorithm (closest point projection) is used to ensure that the state variables remain on the multiple activated yield surfaces. Results of material point and finite element simulations demonstrate that the models capture inelastic deformation, unilateral effects and distinct strength and stiffness

properties in tension and compression, for complex stress paths involving the propagation of both open and closed cracks in mixed mode.

Secondly, a computational tool is developed to simulate the propagation of a discrete fracture within a continuum damage process zone. Microcrack initiation and propagation prior to coalescence are represented by a nonlocal anisotropic Continuum Damage Mechanics (CDM) model in which the crack density is calculated explicitly. A damage threshold is defined to mark the beginning of crack coalescence. When that threshold is reached, a cohesive segment is inserted in the mesh to replace a portion of the damage process zone by a segment of discrete fracture. Discretization is done with the XFEM, which makes it possible to simulate fracture propagation without assigning the fracture path a priori. Rigorous calibration procedures are established for the cohesive strength (related to the damage threshold) and the cohesive energy release rate, to ensure the balance of energy dissipated at the micro and macro scales. The XFEM-based tool is implemented into an open source objective oriented numerical package (OOFEM) and an arc length control resolution algorithm is used to avoid convergence issues that can be encountered otherwise during softening.

Lastly, a numerical method is proposed to simulate multiscale fracture propagation driven by fluid injection in transversely isotropic porous media. Intrinsic anisotropy is accounted for at the continuum scale, by using a damage model in which four equivalent strains are defined to distinguish tension and compression, parallel and perpendicular to the layer. Nonlocal equivalent strains are calculated by integration, and are directly introduced in the damage evolution law. When the weighted damage exceeds a certain threshold, the transition from continuum damage to cohesive fracture is performed by dynamically inserting cohesive segments. Diffusion equations are used to model fluid flow inside the porous matrix and within the macro fracture, in which conductivity is obtained by Darcy's law and the cubic law, respectively. In the fractured elements, the displacement and pore pressure fields are discretized by using the XFEM technique. Interpolation on fracture ele-

ments is enriched with jump functions for displacements, and with level-set-based distance functions for fluid pressure, which ensures that displacements are discontinuous across the fracture, but that the pressure field remains continuous. After spatial and temporal discretization, the model is implemented in a Matlab code. A few simulations are carried out in plane strain. The results validate the formulation and implementation of the proposed model, and further demonstrate it can account for material and stress anisotropy.

Advanced numerical methods presented in this thesis shed light on the mechanical behavior of brittle materials at several scales, and provide tools to solve practical engineering problems. Future work can build on the findings presented in this thesis to understand multi-scale fracture propagation in other materials in addition to rock and concrete.

CHAPTER 1
INTRODUCTION

1.1 Motivations and Objectives

The study of the mechanical behavior of quasi-brittle solids such as rock and concrete is crucial for a wide range of engineering applications, including the disposal of nuclear waste [1, 2], the extraction of conventional energy (coal, oil and gas) [3, 4] and unconventional geothermal energy [5, 6], the cyclic storage of compressed air and natural gas [7], the geological sequestration of carbon dioxide [8, 9], failure analyses of concrete structures [10], and the prediction of fault reactivation [11, 12]. One the one hand, the development of micro-cracks and macro-fractures is detrimental. For example, the Excavation Damage Zone (EDZ) surrounding all free surfaces of an underground structure (borehole for nuclear waste disposal, cavity for storage, tunnel for transportation) has a profound influence on the performance and safety of this structure. One the other hand, the development of micro-cracks and macro-fractures is necessary. For example, hydraulic fracturing is widely used in the industry for fossil fuel recovery. The goal of hydraulic fracturing is to create conductive pathways and to enhance rock permeability, for natural hydrocarbons to flow more freely from rock pores to the fracture surfaces. In enhanced geothermal systems, hydraulic fracturing is used to create extensive micro-macro fracture surfaces, which allows heat exchange between the formation and the circulation of fluids.

Microstructure images obtained by computed tomography or scanning electron microscopy provide insights on the microscopic mechanisms that drive crack initiation, propagation and colaescence (Figure 1.1(a)). Stresses concentrate around pores and crack tips. Depending on the stress level, either pores collapse or cracks initiate from pores. Micro-cracks may propagate or develop secondary wing cracks. No analytical model exists to

predict all possible crack geometries and patterns, but several numerical tools can be used to predict crack propagation at the micro or at the macro scale (see the definition of scales in Figure 1.1). In micromechanics [13], cracks are often represented as spheres, ellipsoids or disks. Considering that the Representative Elementary Volume (REV) is a matrix-inclusion system, the classical Eshelby solution [14] can be used to predict the mechanical behavior at the meso-scale. Note that homogenization theories can only be used when the size of micro-defects is much smaller than the REV size (typically, 100 times smaller). Otherwise, numerical methods are required, and they are usually computationally expensive.

Typical laboratory tests performed in the laboratory to characterize the mechanical behavior of quasi-brittle materials include the uniaxial and triaxial compression test, the direct tension test, the Brazilian splitting test (Figure 1.1(b)). Force-displacement (or stress-strain) curves typically exhibit the following properties [15, 16, 17]:

- Non-linearity in the stress-strain relationship and anisotropic degradation of the stiffness (elasticity tensor);
- Hysteresis loops in the stress-strain curves due to frictional energy dissipation;
- Dilatancy and permanent volumetric strain after complete unloading;
- Crack closure effect (known as "unilateral effect") and resulting recovery of stiffness and strength in compression, but not in tension or shear;
- Up to one order of magnitude of strength difference between tension and compression;
- Confinement-dependent transition from brittle to ductile behavior.

In the theory of Continuum Damage Mechanics (CDM) used at the meso-scale, microstructure evolution is represented through internal state variables, which phenomenologically reflect the influence of micro-cracks and micro-pores on stress-strain curves. Elastoplastic and/or damage constitutive laws are expressed with *ad hoc* equations to capture all the

(a) Bakken shale (Conocophilips) (b) Cylindrical rock specimen (c) Hydraulic fracture

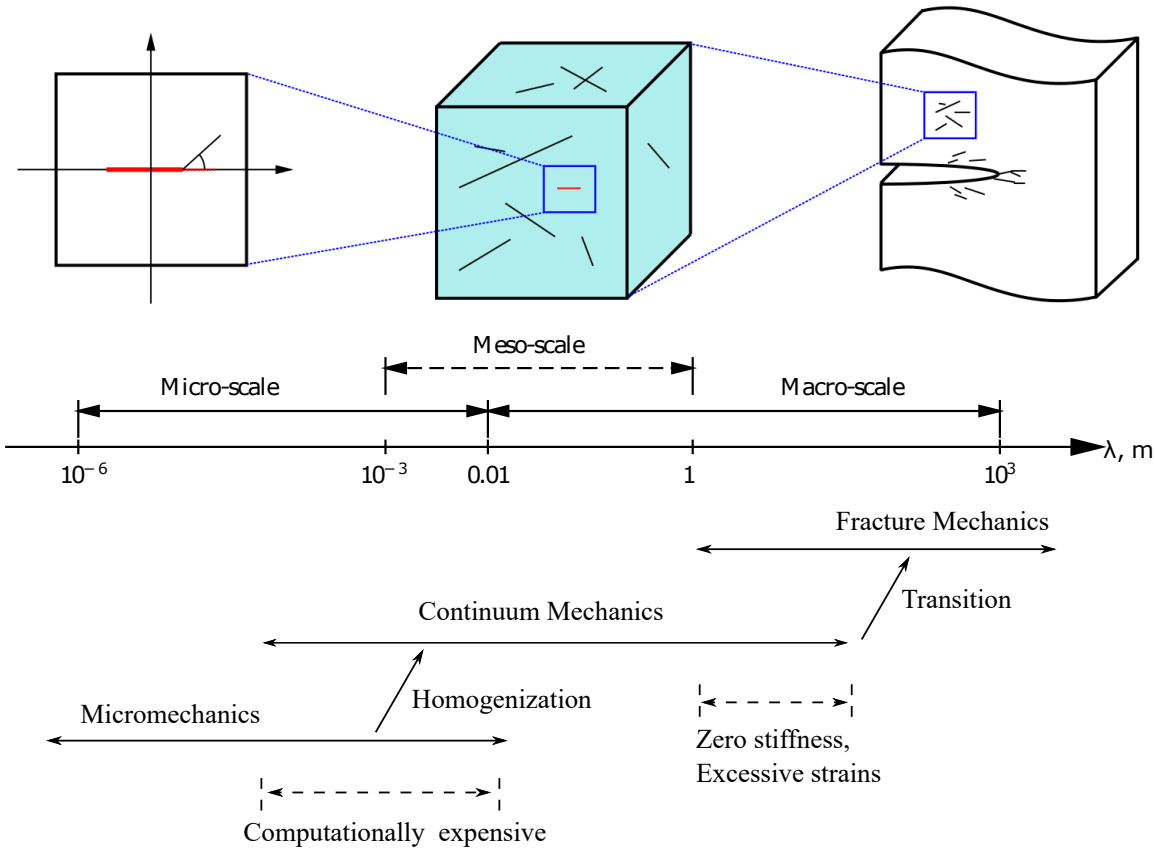

Figure 1.1: Definition of the scales under study: The micro-scale is the grain or mineral scale which can be measured by computed tomography or scanning electron microscopy. Micromechanics is the main theoretical framework at that scale. The meso-scale is in that of the Representative Elementary Volume (REV), i.e. the laboratory sample scale. Continuum mechanics is valid at that scale. The macro-scale defines the scale of the domain under study (e.g. thickness of formation, width of a concrete dam). Fracture mechanics is used for computation.

phenomena listed above. The more phenomena, the more material parameters, the more challenging the calibration of the model. In CDM, since microstructure evolution (e.g., micro-crack patterns) is not explicitly accounted for, it is impossible to quantify damage effects on physical properties such as permeability, unless additional assumptions are made.

When micro-cracks coalesce, the separation of scales rule does not hold and the continuum assumption is no longer valid. Reducing the stiffness to zero in CDM would lead to non-realistic excessive strains, with no explicit fracture surfaces, and mesh dependence would be expected. That is why the theory of fracture mechanics is usually employed to predict macro-fracture propagation as a result of micro-crack interaction and coalescence (Figure 1.1). A traction-separation law is used to model the softening mechanical behavior. Note that Linear Elastic Fracture Mechanics (LEFM) icannot be used for a damaged materials, unless the initial stage of diffused micro-crack initiation and propagation prior to macro-fracture formation is ignored.

Based on the short review above, the objectives of this dissertation are to answer the following scientific questions:

1. What are the micro-scale mechanisms that govern the complex stress/strain response of quasi-brittle materials? How to predict the mechanical behavior at both the micro- and the meso-scale with a limited number of physically meaningful parameters?

2. Why do macro-fractures form? How to capture the transition from diffused micro-crack propagation to localized macro-fracture growth at a reasonable computational cost?

3. Why do hydraulically fractured anisotropic materials break? Is it possible to develop efficient computational tools to predict the EDZ and to simulate hydraulic fracturing in transversely isotropic porous shale for practical engineering?

In the following, we use micro-scale refers to defects (pores, micro-cracks) that range from 10^{-6} m to 10^{-2} m in size, the meso-scale is used for the REV, between 10^{-3} m and 1 m

in size, and the macro-scale is used for fractures that are 10^{-2} m to 10^{3} m in size (e.g., geological faults, hydraulic fractures).

1.2 Thesis Structure

To address the scientific questions, this thesis is structured as follows:

Chapter 2 is a literature review on the topics of constitutive modeling, numerical regularization, multiscale fracture propagation and hydraulic fracturing.

Chapter 3 presents two micromechanical damage models. The first one is based on the theory of wing cracks and on the dilute homogenization scheme. The second one captures the same features at the REV scale, but is purely phenomenological; it is implemented in a Finite Element Methid (FEM) package, and the resolution algorithm is explained in detail. Simulations at both the material point and at the macro-scale are discussed.

Chapter 4 explains a computational framework for simulating multiscale fracture propagation. A nonlocal anisotropic damage model is coupled with a Cohesive Zone Model (CZM). The formulation of the nonlocal damage model, the transition from damage to fracture, the numerical implementation in the eXtended FEM (XFEM) are presented in detail.

Chapter 5 first describes the construction of a non-local damage model for materials with intrinsic transverse isotropy. Then, a FEM model of hydraulic fracturing in transversely isotropic porous media is explained in detail, from the strong formulation to the discretizatio nprocedures and the resolution algorithms. Hydraulic fracture propagation is controlled by a thereshold that marks the transition from continuum damage to discrete fracture.

Chapter 6 summarizes the major contributions of this doctoral thesis and proposes a few directions for future research.

CHAPTER 2

DAMAGE AND FRACTURE OF BRITTLE SOLIDS

2.1 Continuum Constitutive Laws

Brittle materials such as rock, concrete, and ceramic composites, exhibit a complex behavior, including stress-induced damage and stiffness anisotropy, non-linear stress/strain relationships and volumetric dilation, unilateral effects due to crack closure, and a transition from brittle to ductile behavior at increasing confining stress [18, 19]. All of these effects can be explained by the nucleation and propagation of micro-cracks at the grain boundaries and/or from pore spaces. To model these micro-structural effects on the behavior of a Representative Elementary Volume (REV), two possibiliites exist in Continuum Damage Mechanics (CDM): thermodynamically consistent formulations and micromechanics [20]. In this section, we review both types of damage models, and we summarize the regularization techniques used for simulating strain softening. We finish by a review of constitutive models for transversely isotropic materials.

2.1.1 Thermodynamically Consistent Damage Models

The first law of thermodynamics states that energy conservation is always satisfied for any engineering system [21, 22]. Specifically: *the rate of the internal energy $\dot{E}$ plus that of the kinetic energy $\dot{K}$ of a thermodynamic system Ω is equal to the rate of external mechanical work $\dot{W}$ plus the rate of heat supply $\dot{Q}$ to the system due to the heat flux and the heat source*

$$\dot{K} + \dot{E} = \dot{W} + \dot{Q} \tag{2.1}$$

where $\dot{X}$ is the material time derivative of X. The kinetic energy and the internal energy of the system Ω are defined as:

$$K = \int_\Omega \frac{1}{2}\rho \boldsymbol{v} \cdot \boldsymbol{v} d\Omega, \quad E = \int_\Omega \rho \boldsymbol{e} d\Omega \tag{2.2}$$

where ρ, $\boldsymbol{v}$ and $\boldsymbol{e}$ are the density, the velocity and and the internal energy per unit mass. We note $\boldsymbol{t}$ and $\boldsymbol{b}$ the traction per unit area and the body force per unit mass, respectively. Accordingly, the rate of external mechanical work can be expressed as:

$$\dot{W} = \int_\Omega \rho \boldsymbol{b} \cdot \boldsymbol{v} d\Omega + \int_{\partial\Omega} \boldsymbol{t} \cdot \boldsymbol{v} dS \tag{2.3}$$

We note r and $\boldsymbol{q}$ the rate of heat generation per unit mass of system Ω and the outward heat flux on $\partial\Omega$, respectively. The rate of heat supply is expressed as:

$$\dot{Q} = \int_\Omega r d\Omega - \int_{\partial\Omega} \boldsymbol{q} \cdot \boldsymbol{n} dS \tag{2.4}$$

where $\boldsymbol{n}$ is the outward unit normal vector of the boundary $\partial\Omega$. Substituting Equations 2.2-2.4 into Equation 2.1, we have

$$\frac{\mathrm{D}}{\mathrm{D}t}\int_\Omega \rho(\frac{1}{2}\boldsymbol{v}\cdot\boldsymbol{v} + \boldsymbol{e})\mathrm{d}\Omega = \int_\Omega (\rho\boldsymbol{b}\cdot\boldsymbol{v} + r)\mathrm{d}\Omega + \int_{\partial\Omega}(\boldsymbol{t}\cdot\boldsymbol{v} - \boldsymbol{q}\cdot\boldsymbol{n})\mathrm{d}S \tag{2.5}$$

The Reynolds transport theorem, Gauss divergence theorem, mass conservation equation and momentum balance equation are given as follows:

$$\begin{aligned}
&\frac{\mathrm{D}}{\mathrm{D}t}\int_\Omega \boldsymbol{A}\mathrm{d}\Omega = \int_\Omega [\frac{\partial \boldsymbol{A}}{\partial t} + \frac{\partial}{\partial x_i}(\boldsymbol{A}v_i)]\mathrm{d}\Omega = \int_\Omega (\frac{\mathrm{D}\boldsymbol{A}}{\mathrm{D}t} + \boldsymbol{A}\frac{\partial v_i}{\partial x_i})\mathrm{d}\Omega \\
&\int_\Omega \nabla * \boldsymbol{A}\mathrm{d}\Omega = \int_{\partial\Omega} \nabla * \boldsymbol{n}\mathrm{d}S \\
&\frac{\mathrm{D}\rho}{\mathrm{D}t} + \rho\nabla\cdot\boldsymbol{v} = 0 \\
&\rho\dot{\boldsymbol{v}} = \rho\boldsymbol{b} + \nabla\cdot\boldsymbol{\sigma},
\end{aligned} \tag{2.6}$$

From the four equations above, the first law of thermodynamics in Equation 2.5 can be expressed as:

$$\rho\dot{e} = \boldsymbol{\sigma} : \dot{\boldsymbol{\epsilon}} - \nabla \cdot \boldsymbol{q} + r, \tag{2.7}$$

known as the Euler form, where the small strain assumption $\dot{\epsilon} = \nabla \boldsymbol{v}$ is used.

The second law of thermodynamics expresses the direction of energy flow for reversible and irreversible processes as: *the rate of entropy increase of a system is never less than the rate of entropy increase due to the heat source r and the heat flux $\boldsymbol{q}$.*

$$\frac{\mathrm{D}S}{\mathrm{D}t} \geq \int_{\Omega} \frac{r}{T} \mathrm{d}\Omega - \int_{\partial\Omega} \frac{\boldsymbol{q} \cdot \boldsymbol{n}}{T} \mathrm{d}S \tag{2.8}$$

where S is the entropy, T is the absolute temperature. S can be written in terms of entropy per unit mass s as $S = \int_{\Omega} \rho s \mathrm{d}\Omega$. Using Reynolds transport and Gauss divergence theorem (Equations 2.6), in the above inequality, we have:

$$\int_{\Omega} \{\rho\dot{s} + [s(\dot{\rho} + \rho\nabla \cdot \boldsymbol{v})] + \nabla \cdot (\frac{\boldsymbol{q}}{T}) - \frac{r}{T}\} \mathrm{d}\Omega \geq 0. \tag{2.9}$$

Since the region Ω is arbitrary and the mass conservation holds, the local form of Equation 2.9 is

$$\rho\dot{s} + \nabla \cdot (\frac{\boldsymbol{q}}{T}) - \frac{r}{T} \geq 0. \tag{2.10}$$

Substituting the energy conservation law (Equation 2.7) into this relation, we have

$$\rho\dot{s} + \nabla \cdot (\frac{\boldsymbol{q}}{T}) - \frac{1}{T}(\rho\dot{e} - \boldsymbol{\sigma} : \dot{\boldsymbol{\epsilon}} + \nabla \cdot \boldsymbol{q}) \geq 0. \tag{2.11}$$

Substituting $\nabla \cdot (\frac{\boldsymbol{q}}{T}) = \frac{\nabla \cdot \boldsymbol{q}}{T} - \boldsymbol{q} \cdot \frac{\nabla T}{T^2}$ into the above equation, we obtain:

$$\boldsymbol{\sigma} : \dot{\boldsymbol{\epsilon}} + \rho(T\dot{s} - \dot{e}) - \boldsymbol{q} \cdot \frac{\nabla T}{T} \geq 0. \tag{2.12}$$

The Helmholtz free energy per unit mass is defined as

$$\psi = e - Ts, \tag{2.13}$$

Introducing the internal energy per unit mass e in Equation 2.12, we obtain the Clausius-Duhem inequality, as follows:

$$\boldsymbol{\sigma} : \dot{\boldsymbol{\epsilon}} - \rho(\dot{\psi} + \dot{T}s) - \boldsymbol{q} \cdot \frac{\nabla T}{T} \geq 0. \tag{2.14}$$

In the Clausius-Duhem inequality, Helmholtz free energy depends on independent state and internal variables that govern the system's behavior. For a non-isothermal elastic-inelastic-damage medium that undergoes an irreversible process, the Helmholtz free energy per unit mass can be expressed in terms of elastic strain $\boldsymbol{\epsilon}^E$, temperature T, and in terms of the internal damage variables $\boldsymbol{\chi}_k$:

$$\psi = \psi(\boldsymbol{\epsilon}^E, T, \boldsymbol{\chi}_k), \tag{2.15}$$

The derivative of Helmholtz free energy is:

$$\dot{\psi} = \frac{\partial \psi}{\partial \boldsymbol{\epsilon}^E} : \dot{\boldsymbol{\epsilon}}^E + \frac{\partial \psi}{\partial T}\dot{T} + \frac{\partial \psi}{\partial \boldsymbol{\chi}_k} : \dot{\boldsymbol{\chi}}_k \tag{2.16}$$

We have $\boldsymbol{\epsilon}^E + \boldsymbol{\epsilon}^{in} = \boldsymbol{\epsilon}$, in which the inelastic strain $\boldsymbol{\epsilon}^{in}$ is also called plastic strain $\boldsymbol{\epsilon}^p$. Substituting Equation 2.16 into the Clausius-Duhem inequality (2.14), we have

$$(\boldsymbol{\sigma} - \rho\frac{\partial \psi}{\partial \boldsymbol{\epsilon}^E}) : \dot{\boldsymbol{\epsilon}}^E + \boldsymbol{\sigma} : \dot{\boldsymbol{\epsilon}}^{in} - \rho(s + \frac{\partial \psi}{\partial T})\dot{T} - \rho\frac{\partial \psi}{\partial \boldsymbol{\chi}_k} : \dot{\boldsymbol{\chi}}_k - \boldsymbol{q} \cdot \frac{\nabla T}{T} \geq 0. \tag{2.17}$$

Because the variables are independent and because the inequality holds for any irre-

versible process, the Clausius-Duhem inequality yields:

$$\boldsymbol{\sigma} = \rho \frac{\partial \psi}{\partial \boldsymbol{\epsilon}^E}, \quad s = -\frac{\partial \psi}{\partial T}, \tag{2.18}$$

and

$$\boldsymbol{\sigma} : \dot{\boldsymbol{\epsilon}}^{in} - \rho \frac{\partial \psi}{\partial \boldsymbol{\chi}_k} : \dot{\boldsymbol{\chi}}_k - \boldsymbol{q} \cdot \frac{\nabla T}{T} \geq 0. \tag{2.19}$$

It is clear that once the expression of the free energy ψ is known, the constitutive behavior is determined by the thermodynamic conjugation relationships in Equation 2.18. However, to close the formulation, evolution functions need to be constructed in terms of generalized force $(\boldsymbol{\sigma}, -\rho\frac{\partial \psi}{\partial \boldsymbol{\chi}_k}, -\frac{\nabla T}{T})$ to determine the change of internal variables $(\dot{\boldsymbol{\epsilon}}^{in}, \dot{\boldsymbol{\chi}}_k, \boldsymbol{q})$. To ensure the positivity of dissipation in Equation 2.19, it is sufficient to choose non-negative convex functions. The rate of change of the internal variables can be obtained by the flow rule as

$$\dot{\boldsymbol{\epsilon}}^{in} = \dot{\lambda}_d \frac{\partial g_d}{\partial \boldsymbol{\sigma}}, \quad \dot{\boldsymbol{\chi}}_k = -\dot{\lambda}_d \frac{\partial g_d}{\partial \rho \frac{\partial \psi}{\partial \boldsymbol{\chi}_k}}, \quad \boldsymbol{q} = -\dot{\lambda}_d \frac{\partial g_d}{\partial \frac{\nabla T}{T}}. \tag{2.20}$$

where g_d is a plasticity (or damage) potential, and $\dot{\lambda}_d$ is the Lagrange Multiplier obtained by the consistence condition as

$$\dot{f}_d(\boldsymbol{\sigma}, -\rho \frac{\partial \psi}{\partial \boldsymbol{\chi}_k}, -\frac{\nabla T}{T}) = 0. \tag{2.21}$$

where f_d is a yield (or damage) criterion. The magnitude of the rate of internal variables is determined by the consistency condition, which ensures that the thermodynamic state of the material stays on the yield/damage surface. When the normality rule is adopted, Equation 2.20 is called an associate flow rule and g_d=f_d. The normality rule essentially states that the direction of the rate of internal variables is normal to the yield surface (or damage surface). If the normality rule is not adopted, a plasticity (or damage) potential g_d needs to be constructed to derive the evolution laws of the internal variables, independently from the construction of the criterion f_d. In summary, the thermodynamic states of a material is

completely determined by the Helmholtz free energy, the damage or yield criterion and the dissipation potential. It is worth noting that the mathematic formulae of these functions are usually constructed to reflect the phenomenological behavior observed in situ or in the lab, so energy-based constitutive models are also called phenomenological models.

Over the last few decades, numerous phenomenological damage models were formulated [32, 33, 34, 35, 36, 37, 25]. Table 2.1 summarizes the state-of-the-art CDM models that exist to describe the mechanical behavior of brittle solids. The list is not exhaustive, but it gives an overview of the categories of damage models proposed in the literature, by order of complexity. In the first category, a scalar damage variable is defined to account for isotropic stiffness reduction [23, 24]. Damage is expressed explicitly, as a function of equivalent strains. This type of model, widely used in failure analysis, fails to describe unilateral effects, damage-induced anisotropy, and cannot distinguish tension and compression strenghs. In the second category of damage models, multiple scalars are used to distinguish behaviors in tension and compression [38, 39, 25]. Two independent damage criteria are constructed to express the evolution laws of tensile and compressive damage. This type of damage model performs very well for predicting the failure of plain concrete under arbitrary stress paths. In the third and fourth categories, one or several tensors are defined to represent damage phenomena such as anisotropic stiffness degradation and direction dependent frictional sliding [26, 27, 28, 29, 30]. The damage driving forces conjugated to damage tensors awhich allows distinguishing tension and compression, and accounting for unilateral effects. Damage models in the last category have all the modeling features above, and are coupled to plasticity to account for the inelastic deformation [31, 32]. Additional yield criteria and plastic potentials are adde to the formulation to determine the magnitude and the direction of plastic variables, including the plastic strain increment. In summary, phenomenological damage models essentially predict the mechanical effects of damage (or damage phenomena) rather than the evolution of microstructure consequent to micro-crack propagation [40]. The expression of the free energy, the yield criterion and the poten-

Table 2.1: State-of-the-art continuum damage models for brittle solids that satisfy thermodynamic consistence

References	Damage scalar/tensor	Free Energy	Yield/Damage Criteria, Damage potential
Mazars [23, 24]	Combined scalar $D = \alpha_t D_t + \alpha_c D_c$	$\psi = \frac{1}{2}(1-D)\mathbf{C} : \boldsymbol{\epsilon}^E : \boldsymbol{\epsilon}^E$	$f_d = \bar{\boldsymbol{\epsilon}} - K(D), \quad \bar{\epsilon} = \sqrt{\sum_{j=1}^{3}(< \epsilon_j >^+)^2}$ $D_i = F_i(\bar{\epsilon}) = 1 - \frac{(1-A_i)K_0}{\bar{\epsilon}} - \frac{A_i}{\exp[B_i(\bar{\epsilon}-K_0)]}, (i = t, c)$
Comi & Perego [25]	Two scalars D_t, D_c	$\psi = \frac{1}{2}\{2\mu(1-D_t)(1-D_c)\boldsymbol{e} : \boldsymbol{e}$ $+K(1-D_t)(1-D_c)(\text{tr}^+\boldsymbol{\epsilon})^2 + K(1-D_c)(\text{tr}^-\boldsymbol{\epsilon})^2\}$	$f_t = J_2(\boldsymbol{\sigma}) - a_t I_1^2(\boldsymbol{\sigma}) + b_t h_t(D_t) I_1(\boldsymbol{\sigma}) - (1-\alpha D_c) k_t h_t^2(D_t)$ $f_c = J_2(\boldsymbol{\sigma}) + a_c I_1^2(\boldsymbol{\sigma}) + b_c h_c(D_c) I_1(\boldsymbol{\sigma}) - k_c h_c^2(D_c)$
Murikami et. al [26, 27]	Damage tensor $\boldsymbol{D}$	$\psi = \frac{1}{2}\lambda(\text{tr}\boldsymbol{\epsilon})^2 + \mu\text{tr}(\boldsymbol{\epsilon})^2 + \eta_1\text{tr}\boldsymbol{D}(\text{tr}\boldsymbol{\epsilon})^2 + \eta_2\text{tr}\boldsymbol{D}\text{tr}(\boldsymbol{\epsilon})^2$ $+\eta_3\text{tr}\boldsymbol{\epsilon}\text{tr}(\boldsymbol{\epsilon}\cdot\boldsymbol{D}) + \eta_4\text{tr}[(\bar{\boldsymbol{\epsilon}})^2\cdot\boldsymbol{D}] + \frac{1}{2}K_d\beta^2$	$\boldsymbol{Y} = -\partial\psi/\partial\boldsymbol{D}, \quad B = \partial\psi/\partial\beta$ $f_d = \sqrt{\frac{1}{2}\boldsymbol{Y}\cdot\mathbb{L} : \boldsymbol{Y}} - (B_0 + B)$
Halm & Dragon et. al [28, 29, 30]	$\boldsymbol{\Omega} = \sum_{k=1}^{3}\Omega_k \boldsymbol{v}^k \otimes \boldsymbol{v}^k$ $\gamma^i = \frac{s^i\xi^i}{V} sym(\boldsymbol{n}\otimes\boldsymbol{g})^i$	$\psi = \frac{1}{2}\lambda(\text{tr}\boldsymbol{\epsilon})^2 + \mu\text{tr}(\boldsymbol{\epsilon}\cdot\boldsymbol{\epsilon}) + g\text{tr}(\boldsymbol{\epsilon}\cdot\boldsymbol{\Omega}) + \alpha\text{tr}\boldsymbol{\epsilon}\text{tr}(\boldsymbol{\epsilon}\cdot\boldsymbol{\Omega}) +$ $2\beta\text{tr}(\boldsymbol{\epsilon}\cdot\boldsymbol{\epsilon}\cdot\boldsymbol{\Omega})$ $+\sum_{k=1}^{3} H(-\boldsymbol{v}^k\cdot\boldsymbol{\epsilon}\cdot\boldsymbol{v}^k)[-\alpha\boldsymbol{\epsilon} : (\Omega_k\boldsymbol{L}^k) : \boldsymbol{\epsilon} - 2\beta\text{tr}(\boldsymbol{\epsilon}\cdot\boldsymbol{\epsilon}\cdot$ $\boldsymbol{\Omega}^k) + 4\beta\text{tr}(\boldsymbol{\epsilon}\cdot\boldsymbol{\gamma}^k\cdot\boldsymbol{\Omega}^k) - 2\beta\text{tr}(\boldsymbol{\gamma}^k\cdot\boldsymbol{\gamma}^k\cdot\boldsymbol{\Omega}^k)]$	$f_d = \sqrt{\frac{1}{2}\text{tr}[(\boldsymbol{F}^D - \boldsymbol{F}^{D2} - \boldsymbol{F}^{D1-})\cdot(\boldsymbol{F}^D - \boldsymbol{F}^{D2} - \boldsymbol{F}^{D1-})]} +$ $B\text{tr}[(\boldsymbol{F}^D - \boldsymbol{F}^{D2} - \boldsymbol{F}^{D1-})\cdot\boldsymbol{D}] - (C_0 + C_1\text{tr}\boldsymbol{D}) \le 0$ $h^k = \sqrt{\frac{1}{2}\text{tr}(\boldsymbol{F}^k\cdot\boldsymbol{F}^k)} + \rho\boldsymbol{v}^k\cdot\boldsymbol{\epsilon}\cdot\boldsymbol{v}^k$
Voyiadjis et. al [31, 32]	Coupled effective damage tensor $\phi_{ij} = \delta_{ij} - (\delta_{ik} - s\phi_{ik}^+)(\delta_{jk} - \phi_{jk}^-)$ where $0 \le s \le 1$	$\psi = \psi^E(\boldsymbol{\epsilon}^E, \boldsymbol{\phi}^+, \boldsymbol{\phi}^-) + \psi^p(\epsilon_{eq}^+, \epsilon_{eq}^-) + \psi^d(\phi_{eq}^+, \phi_{eq}^-)$ $\psi^E = \frac{1}{2}\boldsymbol{\epsilon}^E : \mathbb{E} : \epsilon^E, \quad \mathbb{E} = \mathbb{M}^{-1} : \mathbb{C} : \mathbb{M}^{-T}$ $M_{ijkl} = 2[(\delta_{ij} - \phi_{ij})\delta_{kl} + \delta_{ij}(\delta_{kl} - \phi_{kl})]^{-1}$ $\psi^p = f_0^+\epsilon^{+ep} + \frac{1}{2}h(\epsilon_{eq}^+)^2 + f_0^-\epsilon_{eq}^-$ $+Q\Big(\epsilon_{eq}^- + \frac{1}{b}\exp(-b\epsilon_{eq}^-)\Big)$ $\psi^d = K_0^{\pm}[\phi_{eq}^{\pm} + \frac{1}{B^{\pm}}\{(1-\phi_{eq}^{\pm})\ln(1-\phi_{eq}^{\pm}) + \phi_{eq}^{\pm}\}]$	$f_p = \sqrt{3\bar{J}_2} + \alpha\bar{I}_1\beta(\kappa_i^p)H(\hat{\bar{\sigma}}_{\max})\hat{\bar{\sigma}}_{\max} - (1-\alpha)\dot{c}^-(\epsilon_{eq}^-) \le 0$ $F^p = \sqrt{3\bar{J}_2} + \alpha^p\bar{I}_1$ $\boldsymbol{Y}^{\pm} = -\partial\psi/\partial\boldsymbol{\phi}^{\pm}$ $f_d^{\pm} = \sqrt{\frac{1}{2}\boldsymbol{Y}^{\pm} : \mathbb{L} : \boldsymbol{Y}^{\pm}} - K^{\pm}(\phi_{eq}^{\pm}) \le 0$

D_t, D_c: Tensile/compressive damage
$\bar{\epsilon}$: Equivalent strain
K: Bulk Modulus
$h_{t,c}$: Isotropic hardening-softening
ψ^E, ψ^p, ψ^d: Elastic, plastic, and damage energy
$\boldsymbol{Y}$: Damage driven force
ψ: Helmholtz's free energy
F_i: Damage evolution law
$\boldsymbol{e}$: Deviatoric strain
$\boldsymbol{D}, \boldsymbol{\phi}, \boldsymbol{\Omega}$: Damage tensor
$f_{t/c}$: Damage criteria in tension/compression
$a_{t,c}, b_{t,c}, k_{t,c}$: Material parameters
$\boldsymbol{\epsilon}^E$: Elastic strain
A_i, B_i, K_0: Material parameters
I_1, J_2: 1st and 2ed stress invariants
λ, μ: Lamé constants
$\eta_i, i = 1, 4$: Material parameters
$\mathbb{C}$: Material stiffness matrix
$f_{t/c}, f_d$: Damage criteria
$K(D)$: Max($\bar{\epsilon}$) in history
h^k: Sliding criteria
f_p: Plastic yield criteria
F^p: Plastic potential
$\boldsymbol{F}^D, \boldsymbol{F}^k$: Damage, sliding driven force

tial functions are crafted so as to match the macroscopic behavior (usually represented by stress/strain curves). The more phenomoenological features, the more material parameters, hence the more calibration challenges.

2.1.2 Micromechanics Damage Models

Different from phenomenological models, in which the expression of the free energy is constructed to predict damage effects, the expression of Helmholtz energy (or Gibbs energy) in micromechanical models stems from the homogenization of micromechanical equations (often, fracture mechanics equations) used to represent micro-crack initiation, propagation, opening, closure and frictional sliding. Micromechanics models can be grouped into two categories based on whether the homogenization technique takes the crack interaction into account or not. In the dilute scheme, the calculation of the displacement jump across crack faces [41] is used as a basis to upscale the effective properties of the damaged REV [42, 43] and to express the corresponding energy potentials [44, 45, 46, 47]. The evolution law is based on fracture mechanics and can represent Mode I splitting [18, 48], Mode II friction sliding [48] or mixed mode wing crack development [45, 49]. In order to account for crack interactions, one can explicitly express the stress field as the sume of the stress that results from external loading and of hte stress that results from crack interaction [16]. Other homogenization techniques, such as the self-consistent method (e.g., [41, 50, 51]) and the Mori-Tanaka scheme (e.g., [52, 53, 54, 55, 56, 57]) resort to Eshelby homogenization procedure [14], in which the cracked solid is viewed as a matrix-inclusion system [13]. Once the upscaled energy potential is obtained, micro-crack evolution laws are derived from damage growth criteria (e.g.[58, 40, 46, 47]). Homogenization schemes were compared in several studies [59, 60]. Simulation results indicate that the dilute scheme is accurate prior to the peak strength, and all the other schemes that consider crack interaction can effectively capture softening behavior to some extent. Comparing to phenomenological models, micromechanics models require less material parameters, and can explicitly

represent micro-structure evolution. However, they are typically difficult to implement in Finite Element packages and they require a lot of computation power.

An important contribution to the micromechanics damage theory is the series of microplane models proposed by Bazant et al.[61, 62, 63, 64, 65], in which the macroscopic deformation is related to microscopic mechanisms that occur over a finite set of weak planes. The microplane theory was originated by G. I. Taylor (1938), who considered that either the stresses on the weak planes within the material are the components of the macroscopic stress tensor (static constraint), or that the strain on the weak planes are the components of the macroscopic strain tensor (kinematic constraint). The constitutive relations for each plane are formulated independently. The static constraint was extensively used in metal plasticity and applied with great success in the so-called "slip theory". The kinematic approach was applied by Bazant's research group to describe geomaterials with strain softening, especially concrete. Three categories of microplane models were developed since the inception of the Taylor's theory. In the first one, an additional assumption is made to state that the volumetric, deviatoric and shear responses on each microplane are mutually independent [61, 62]. In the second category, the microplane inelastic behavior is characterized by stress-strain boundaries [63, 64, 66], which can be treated as yield limits. Within the boundaries, the response is incrementally elastic, i.e. the elastic moduli are incrementally degraded due to damage. When the accumulated stress and strain get outside of the boundaries at some incremental step, they immediately drop back to the boundaries and and then follow the elastic boundary. It is possible to catch Bauschinger effect and realistic hysteresis loops during cyclic loading. In the third category, a kinematically constrained microplane system is coupled to a statically constrained microplane system to simulate cohesive tensile cracking [65]. Microplane models have been extensively used in engineering applications, however, one should bear in mind that the weak planes do nt corresond to any geometric feautre of the microstructure; there is no physical principle that dictates the evolution laws of the weak planes.

2.1.3 Regularization Techniques for Softening

The development of regularization techniques (localization limiters) was initiated by the pathologies encountered in Finite Element simulations of damage or strain softening, in which the results are mesh-dependent. In classical strain-softening CDM models, no convergent solution exist upon mesh refinement. As the energy dissipation per unit volume is finite, the vanishing damage zone volume causes the structure to fail with zero energy dissipation, which is, of course, physically unrealistic[67, 68] . From a mathematical standpoint, partial differential equations loose their hyperbolic (respectively elliptic) character in dynamic problems (respectively in quasi-statistic problems), thus making the initial-boundary problem ill-posed [69, 70]. To circumvent the deficiencies of classical local models, a number of approaches were proposed [71]: (1) spatial averaging of state variables (integral nonlocal formulation); (2) introduction of spatial gradients of state variables (differential nonlocal formulation); (3) microstructure enrichment; and (4) introduction of rate dependency. Because the constitutive models involved in this thesis are quasi-static, we only review non-local regularization techniques (1)-(3).

Integral nonlocal formulation

For an integral-type nonlocal material model, the constitutive law at a point of a continuum involves weighted averages of a state variable or thermodynamic force over a certain neighborhood of that point [72]. If $\eta(\boldsymbol{x})$ is some local field in a solid body occupying a domain V, the correspond nonlocal field $\bar{\eta}(\boldsymbol{x})$ is defined as:

$$\bar{\eta}(\boldsymbol{x}) = \int_V \alpha'(\boldsymbol{x}, \boldsymbol{\xi})\eta(\boldsymbol{\xi})\mathrm{d}\boldsymbol{\xi} \tag{2.22}$$

where $\alpha'(\boldsymbol{x}, \boldsymbol{\xi})$ is the chosen nonlocal weight function. The local and integral values of a uniform field at a point are equal. Thus, the weight function should satisfy the following

normalization condition:

$$\int_V \alpha'(\boldsymbol{x}, \boldsymbol{\xi})\eta(\boldsymbol{\xi})\mathrm{d}\boldsymbol{\xi} = 1 \tag{2.23}$$

The normalized weight function is defined as:

$$\alpha'(\boldsymbol{x}, \boldsymbol{\xi}) = \frac{\alpha(\mid \boldsymbol{x} - \boldsymbol{\xi} \mid)}{\int_V \alpha(\mid \boldsymbol{x} - \boldsymbol{\zeta} \mid)\mathrm{d}\boldsymbol{\zeta}} \tag{2.24}$$

In an infinite, isotropic and homogeneous medium, the weight function depends only on the distance $r = \mid \boldsymbol{x} - \boldsymbol{\xi} \mid$ between the source point $\boldsymbol{\xi}$ and the observation point $\boldsymbol{x}$. In the vicinity of the boundary of a finite body, it is assumed the nonlocal operator only applies on the part that lies within the solid.

The weighting function can take the form of Gaussian (normal) distribution function, as:

$$\alpha(\mid \boldsymbol{x} - \boldsymbol{\xi} \mid) = \alpha(r) = \exp[-(\frac{kr}{l_c})^2] \tag{2.25}$$

or the form of bell-shaped function, as:

$$\begin{aligned} &\alpha(r) = (1 - \frac{r^2}{R^2})^2 \qquad R \geq r \geq 0 \\ &\alpha(r) = 0 \qquad r \geq R \end{aligned} \tag{2.26}$$

where l_c, called the internal characteristic length, represents a material property and is of the same order of magnitude as the maximum size of material inhomogeneity. The length l_c can be determined experimentally by comparing the responses of specimens in which the damage remains distributed with the response of fractured specimens, in which damage localizes [73]. It can also be determined by comparing the simulation results for various values of l_c with the experimental response [74]. R is called the interaction radius related to the internal length. Its value corresponds to the largest distance of a point $\boldsymbol{\xi}$ to the observation point $\boldsymbol{x}$ [75].

A variety of state variables $\eta(\boldsymbol{x})$ were considered for nonlocal regularization, such as

the averaged energy released rate $\omega(\overline{Y_{max}(\boldsymbol{\epsilon})})$ [67], the damage variable $\overline{\omega(Y_{max}(\boldsymbol{\epsilon}))}$ [68], the equivalent strain $\omega(Y_{max}(\overline{\boldsymbol{\epsilon}}))$ [76], the specific fracture strain $\overline{\gamma} = \overline{\Omega/(1-\Omega)}$ [67], the inelastic stress $\overline{\omega(\boldsymbol{\epsilon})\boldsymbol{D}_e\boldsymbol{\epsilon}}$ [75], the inelastic stress rate $\overline{\dot{\omega}\boldsymbol{D}_e\boldsymbol{\epsilon}}$ [75] and the inelastic stress calculated from the nonlocal strain $\omega(\overline{\boldsymbol{\epsilon}})\boldsymbol{D}_e\overline{\boldsymbol{\epsilon}}$ [63]. Jirasek [75] demonstrated that only averaging the equivalent stain, the energy release rate or the specific fracturing strain can correctly reproduce large post-peak deformation or complete fracture. Other nonlocal models lead to spurious residual stresses and to a dilation of the softening zone.

Differential nonlocal formulation - strain/damage gradient model

In a differential or gradient type nonlocal model, the first or higher-rank gradient of some state variables or thermodynamic forces is taken into account to enrich the constitutive relations [72]. A Taylor expansion of $\eta(\boldsymbol{x}, \boldsymbol{\xi})$ is used, and we have [77, 78, 79, 69]:

$$\bar{\eta}(\boldsymbol{x}) = \eta(\boldsymbol{x}) + c_1\Delta^2\eta(\boldsymbol{x}) + c_2\Delta^4\eta(\boldsymbol{x}) + c_3\Delta^6\eta(\boldsymbol{x}) + ... \tag{2.27}$$

where the odd derivatives of η cancelled in the integration due to the symmetric character of the nonlocal weight function. Δ^2 denotes the Laplacian operator and the coefficients c_i depend on the weight function α and on the averaging volume V. As the nonlocal variable explicitly depends upon higher order derivatives, this formulation has the severe disadvantage that at least C^1-continuous interpolation functions of displacement must be employed for finite element simulation, even if we ignore the higher order terms $\Delta^n, n \geq 4$. Therefore, Peerlings et al. [80, 70] proposed to perform differentiation with respect to $\boldsymbol{x}$ twice for Equation 2.27 and to substitute the results back to Equation 2.27. The new form of the Taylor expansion is:

$$\bar{\eta}(\boldsymbol{x}) - c_1\Delta^2\bar{\eta}(\boldsymbol{x}) = \eta(\boldsymbol{x}) + (c_2 - c_1^2)\Delta^4\eta(\boldsymbol{x}) + (c_3 - c_1c_2)\Delta^6\eta(\boldsymbol{x}) + ... \tag{2.28}$$

Since $\bar{\eta}(\boldsymbol{x})$ is discretized independently, and we ignore the higher order terms $\Delta^n, n \geq 4$ in Equation 2.28. It is sufficient to employ C^0-continuous interpolation functions of displacement for general finite element implementation. The coefficients c_i can be expressed explcitly in terms of l_c if the weighting function is the Gaussian distribution. Because the nonlocal variable $\bar{\eta}(\boldsymbol{x})$ is explicitly related to the local variable $\eta(\boldsymbol{x})$, Equation 2.27 is referred to as the explicit differential-type nonlocal model, and can rewritten as:

$$\bar{\eta}(\boldsymbol{x}) = \eta(\boldsymbol{x}) + \frac{1}{2}l_c^2\Delta^2\eta(\boldsymbol{x}) + \frac{1}{8}l_c^4\Delta^4\eta(\boldsymbol{x}) + \frac{1}{48}l_c^6\Delta^6\eta(\boldsymbol{x}) + ... \tag{2.29}$$

Similarly, Equation 2.28 is referred to as the implicit differential-type nonlocal model because $\bar{\eta}(\boldsymbol{x})$ is implicitly related to the local variable $\eta(\boldsymbol{x})$. The complete development in series with the Gaussian weight function is expressed as:

$$\bar{\eta}(\boldsymbol{x}) - \frac{1}{2}l_c^2\Delta^2\bar{\eta}(\boldsymbol{x}) + \frac{1}{8}l_c^4\Delta^4\bar{\eta}(\boldsymbol{x}) - \frac{1}{48}l_c^6\Delta^6\bar{\eta}(\boldsymbol{x}) + ... = \eta(\boldsymbol{x}) \tag{2.30}$$

Note that both series are equivalent when no truncation of higher order is made. For the explicit series the shape functions have to be C^1 (respectively C^2) continuous if a truncation is done after the second-order term (respectively the fourth-order term). The shape function requirements for the implicit series are C^0 and C^1 continuity for truncation after the second-order term or fourth-order term, respectively [78]. With the additional boundary condition

$$\frac{\partial\bar{\eta}}{\partial\boldsymbol{n}} = n_i\frac{\partial\bar{\eta}}{\partial x_i} = 0, \tag{2.31}$$

the second order implicit series is the most widely used differential-type nonlocal model, in which the general types of shape function in FEM satisfy C^0 continuity requirement. For the same internal length, dispersion analysis [78] revealed that the difference between different orders of implicit nonlocal differential-type model is negligible, and that higher orders give a solution that approaches that obtained with integral-type nonlocal models. On

the contrary, the solutions obtained with explicit differential type non-local models totally differ from those obtained with implicit models, and the incorporation of higher orders in explicit differential type non-local models does not yield a stable solution. These shortcomings were overcome by Peerlings et al.[81, 70], who omitted higher order gradient terms in explicit models but indirectly preserved them in the implicit models. The resulting implicit formulation can be written in the form of an integral-type nonlocal model by using appropriate Green's functions as weight functions, considering that the spatial interaction span over the entire domain. The main drawback is that the spatial interactions for this explicit differential nonlocal model are limited to an infinitesimal neighborhood. It is essentially a local formulation because the nonlocal value at a point only depends upon the local value and its gradient at that point. Based on these analyses, the implicit nonlocal model of second order, expressed as:

$$\bar{\eta}(\boldsymbol{x}) - \zeta\Delta^2\bar{\eta}(\boldsymbol{x}) = \eta(\boldsymbol{x}), \tag{2.32}$$

is wildly invoked to simulate softening in problems of dynamics [78, 82], brittle damage [69, 77, 82] and plasticity [83, 82]. The parameter ζ with the dimension of a length squared is related to the internal length, it is a constant of the model. As indicated by Geers et al. [84], using a continuum damage approach with a constant ζ provides inconsistent predictions in mode I crack propagation, because the damage zone becomes wider and wider in a direction perpendicular to the crack, where the material should unload. It is possible to overcome this limitation by introducing a transient behaviour for the gradient parameter during damage evolution and crack propagation. If the averaging variable is the equivalent strain, the evolution law for this transient-differential damage can be specified as:

$$\begin{aligned} \zeta &= c(\frac{\boldsymbol{\epsilon}_{eq}}{\boldsymbol{\epsilon}_\zeta})^n_\zeta \qquad \boldsymbol{\epsilon}_{eq} \leq \boldsymbol{\epsilon}_\zeta \\ \zeta &= c \qquad \boldsymbol{\epsilon}_{eq} > \boldsymbol{\epsilon}_\zeta \end{aligned} \tag{2.33}$$

This equation reflects that the value of ζ is limited to a maximum value c, which is reached at the equivalent strain $\boldsymbol{\epsilon}_{\zeta}$.

Microstructure enrichment

The macroscopic properties of a material originate from the properties and interactions that take place at the scale of its microstructure. As a result, the overall behavior of materials strongly depends on the size, geometry, distribution and different properties of microstructure descriptors. Based on this observation, Toupin [85], Mindlin [86, 87] and Germain [88] developed the theory of microstructure enriched elasticity. Vernerey et. al [89] extended the formulation to microstructure enriched elastoplasticity for hierarchical materials. The basic assumptions of these theories are the following:

- The traditional assumption of conventional continuity is maintained with continuous displacement $u_i(x_i)$. At each material point of the continuum, the microstructure is represented by adding microscopic degrees of freedom. The micro-displacement $u'_i(x'_i)$ is defined as the displacement relative to the microscopic displacement $u_i(x_i)$, i.e. the axis of spatial position vector x'_i is parallel with x_i with origin fixed at the material point.

- The microscopic displacement u'_i can be expanded with respect to the relative position x'_i in a Taylor's series. An approximation can be made when terms with order higher than one are truncated - which implicitly indicates that the relative motion of various points of the material point is characterized by a homogeneous deformation.

$$u'_i = u_i + \chi_{ij} x'_j \tag{2.34}$$

With the assumption stated in theequation above, the microscopic displacement has a linear relationship with the relative position, and the material is called *the micromorphic continuum of degree one*. The macroscopic kinematic description of the continuum en-

riched with microstructure can be thoroughly defined with the macro-displacement field u_i and the gradient of micro-displacement $\partial u_i' = \chi_{ij}$. By definition, χ_{ij} is a second order tensor, the symmetric part of which, $\frac{1}{2}(\chi_{ij} + \chi_{ji})$, is called the micro-strain rate tensor, and the antisymmetric part of which, $\frac{1}{2}(\chi_{ij} - \chi_{ji})$, is named the micro-rotation rate tensor. Mindlin [86] defined the macro-strain (conventional strain)

$$\epsilon_{ij} = \frac{1}{2}(\partial_i u_j + \partial_j u_i), \tag{2.35}$$

the relative deformation

$$\eta_{ij} = \partial_i u_j - \chi_{ij}, \tag{2.36}$$

and the micro-deformation gradient

$$\kappa_{ijk} = \partial_i \chi_{jk} = \chi_{ij,k}, \tag{2.37}$$

Accordingly, the potential energy density ψ (Helmholtz free energy per unit of macro volume) can be expressed in terms of $\epsilon_{ij}, \eta_{ij}, \kappa_{ijk}$. These deformation tensors should satisfy thermodynamic principles; their conjugated part can be defined as

$$\sigma_{ij} = \frac{\partial \psi}{\partial \epsilon_{ij}}, \quad s_{ij} = \frac{\partial \psi}{\partial \eta_{ij}}, \quad \nu_{ijk} = \frac{\partial \psi}{\partial \kappa_{ijk}} \tag{2.38}$$

According to the theory of virtual work, the virtual work of the internal forces should be a linear combination of $u_{i,j}, \chi_{ij}, \chi_{ij,k}$ or equivalently of $u_{i,j}, \eta_{ij}, \kappa_{ijk}$ [88], and the virtual power of the "the internal force" in a system Ω can be written as

$$\begin{aligned} W^*_{\text{int}} &= -\int_\Omega \{(\sigma_{ij} + s_{ij})\partial_i u_j^* - s_{ij}\chi_{ij}^* + \nu_{ijk}\kappa_{ijk}^*\} d\Omega \\ &= \int_\Omega \{(\sigma_{ij,j} + s_{ij,j})u_i^* + (s_{ij} + \nu_{ijk,k})\chi_{ij}^*\} d\Omega - \int_{\partial\Omega} \{(\sigma_{ij} + s_{ij})n_j u_i^* + \nu_{ijk}\chi_{ij}^* n_k\} dS \end{aligned} \tag{2.39}$$

where $*$ denotes a virtual quantity. The virtual work provided by the external forces (volume forces and contact forces) can be generalized as

$$W^*_{\text{ext}} = \int_\Omega (f_i u^*_i + \Psi_{ij}\chi^*_{ij})d\Omega + \int_{\partial\Omega} (T_i u^*_i + M_{ij}\chi^*_{ij})dS \tag{2.40}$$

where Ψ_{ij} is a volumic double force, and M_{ij} is a double surface traction - both of the two tensors include a symmetric and an antisymmetric part. The principle of virtual power states that, for any virtual motion, the virtual power of all the "internal forces" and "external forces " acting on the system in equilibrium is null [88], i.e. $W^*_{\text{int}} + W^*_{\text{ext}} = 0$, consequently, we have the two following equilibrium equations:

$$\begin{aligned} \partial_j(\sigma_{ij} + s_{ij}) + f_i &= 0 \\ s_{ij} + \nu_{ijk,k} + \Psi_{ij} &= 0 \end{aligned} \tag{2.41}$$

and the two following boundary conditions:

$$\begin{aligned} T_i &= (\sigma_{ij} + s_{ij})n_j \\ M_{ij} &= \nu_{ijk}n_k \end{aligned} \tag{2.42}$$

In summary, the state of stress in a *micromorphic material of degree one* is thoroughly defined by the Cauchy symmetric stress σ_{ij}, the micro-structure relative stress tensor s_{ij}, and the third order double stress tensor ν_{ijk}. We note: f_i and Ψ_{ij} the volume force and volume double force, T_i and M_{ij} the surface traction and double surface traction. The equilibrium and boundary equations of the medium are given in Equations 2.41 and 2.42. From a physical point of view, the Cauchy stress represents the macroscopic average of forces per unit area, the micro-stress can be interpreted as a spatial average of forces arising from the nonlocal behavior of the microstructure, and the double stress (or couple stress) represents the spatial average of the microscopic moments per unit area. The micro-relative-stress is the stress necessary to balance the couple stress at micro-scale and can be thought of as an

additional stress that represents the nonlocal interactions within the microstructure.

Cosserat (micropolar) theory According to Mindlin [86], Germain [88], Chambon [90, 91] and Liu et al. [89], the linear equations of a *Cosserat continuum* can be seen as particular case of the previous general theory of the *micromorphic material of degree one*. Note the Cosserat theory was originated and named after the Cosserat brothers [92]. We note the macro rotation, micro strain and micro rotation as:

$$\begin{aligned} R_{ij} &= \frac{1}{2}(\partial_i u_j - \partial_j u_i) \\ d_{ij} &= \frac{1}{2}(\chi_{ij} + \chi_{ji}) \\ r_{ij} &= \frac{1}{2}(\chi_{ij} - \chi_{ji}) \end{aligned} \tag{2.43}$$

In Cosserat theory, the micro strain d_{ij} is assumed to be zero, which means that the gradient of micro-displacement $\chi_{ij} = r_{ij}$ is antisymmetric. The density of virtual work is now expressed as

$$\begin{aligned} w^*_{\text{int}} &= \sigma_{ij} u^*_{i,j} + s_{ij}(u^*_{i,j} - r^*_{ij}) + \nu_{ijk}\kappa^*_{ijk} \\ &= \alpha_{ij}\epsilon^*_{ij} + s_{ij}(R^*_{ij} - r^*_{ij}) + \nu_{ijk}\kappa^*_{ijk} \end{aligned} \tag{2.44}$$

where $\alpha_{ij} = \sigma_{ij} + s_{ij}$. It is clear that σ_{ij} and s_{ij} are the symmetric and antisymmetric parts of α_{ij}. ν_{ijk} is antisymmetric with respect to its first two indices. Similarly, without loss of generality, Ψ_{ij} and M_{ij} are antisymmetric with respect to i and j, and they are renamed as volume couple distribution and surface couple stress, respectively. The equilibrium equations and boundary conditions are the same as Equations 2.41 and Equations 2.42; the only difference is that micro-related tensors have zero symmetric parts. Media obeying Cosserat theory are called *micropolar media* [93]. The weak form of the governing equations and the finite-element discretization for Cosserat media in two dimensions were explained by Kadowaki and Liu [94], who successfully modeled the strain localization behavior using both coarse- and fine- scale meshes to decrease the number of degrees of freedom in the

domain and to achieve computational efficiency.

As explained by Chambon [91], laboratory experiments conducted for granular materials indicates that the macro rotation is the same as the average of the rotation of grains. If one interprets the average rotation of the grains as the microrotation, then,

$$r_{ij} = R_{ij} \tag{2.45}$$

This equation provides an additional constraint on the Cosserat media. The resulting approach was named *Cosserat second gradient theory* by Chambon [91]. The virtual work density takes the followin form:

$$w^*_{\text{int}} = (\sigma_{ij} + s_{ij})\epsilon^*_{ij} + \nu_{ijk}\kappa^*_{ijk} \tag{2.46}$$

After applying the principle of virtual work and some mathematical manipulations, we obtain the following simplified equilibrium equation:

$$\partial_j(\sigma_{ij} + s_{ij}) - \nu_{ijk,jk} + f_i = 0 \tag{2.47}$$

where the volume double force Ψ_{ij} is neglected.

Second gradient models Second gradient model are models of *micromorphic media of degree one* in which it is assumed that the micro deformation is equal to the macro deformation:

$$u_{i,j} = \chi_{ij}. \tag{2.48}$$

As a consequence of this constraint, the principle of virtual work yields, for every kinematic possible field u^*_i:

$$\int_\Omega (\sigma_{ij}u^*_{i,j} + \nu_{ijk}u^*_{i,jk})d\Omega = \int_\Omega (f_i u^*_i + \Psi_{ij}u^*_{i,j})d\Omega + \int_{\partial\Omega} (T_i u^*_i + M_{ij}u^*_{i,j})dS \tag{2.49}$$

Because u_i and χ_{ij} are not independent fields, f_i and Ψ_{ij} cannot be considered independently. We note D the normal derivative of any quantity q, ($Dq = (\partial q/\partial x_k)n_k$) and D_j the tangential derivatives ($D_j q = \partial q/\partial x_j - (\partial q/\partial x_k)n_k n_j$). With these definitions, the above equation can be converted conveniently by rewriting the external virtual work with p_i and P_i, as follows:

$$\begin{aligned} -\int_\Omega (\sigma_{ij,j} - \nu_{ijk,jk})u_i^* d\Omega + \int_{\partial\Omega} [(\sigma_{ij} + \nu_{ijk,k})n_j u_i^* + \nu_{ijk} u_{i,j} n_k] dS \\ = \int_\Omega (f_i - \Psi_{ij,j})u_i^* d\Omega + \int_{\partial\Omega} (\Psi_{ij} n_j u_i^* + p_i u_i^* + P_i D u_i^*) dS \end{aligned} \tag{2.50}$$

Note that the divergence theorem was applied. The volume integral in Equation 2.50 leads to the balance equation:

$$\sigma_{ij,j} - \nu_{ijk,jk} + f_i - \Psi_{ij,j} = 0 \tag{2.51}$$

and the surface integral in Equation 2.50 leads to the boundary conditions (after complex mathematical manipulations):

$$\begin{aligned} p_i &= \sigma_{ij} n_j - \Psi_{ij} n_j + (D_l n_l)\nu_{ijk} n_j n_k - D_j(\nu_{ijk} n_k) \\ P_i &= \nu_{ijk} n_j n_k \end{aligned} \tag{2.52}$$

The micropolar and second gradient theories were successfully applied to rocks [95, 96] and granular materials [91]. Chambon et al. [91, 96, 97] formulated the strain gradient theory relative to a reference configuration with assumptions that the deformation gradient follows multiplicative decomposition and the second gradient of the motion can be decomposed into an elastic and a plastic part. In their model, the free energy expression is used so as to formulate the evolution laws (yield functions, hardening laws) for both the plastic strain and the hyper strain tensor. As an alternative to plasticity theory for modeling the nonlinear irreversible behavior, continuum damage mechanics models coupled with

the strain gradient theory provide another way to circumvent scale effects encountered in conventional damage models and to simulate strain softening. For example, Zhao et al. [98, 99] proposed isotropic and anisotropic damage models with second strain gradient enhancement, in which the conventional strain and the strain gradient are split into an undamaged elastic part and a damaged irreversible part, and the increment of work conjugated Cauchy stress and higher order stress are updated thanks to the damage yield function and the damage potential. Bot hthe isotropic and anisotropic models were used to predict shear bands and to investigate size effects.

2.1.4 Continuum Model for Transversely Isotropic Materials

Many geomaterials exhibit strong orientation dependent mechanical behavior (anisotropy) due to bedding, layering or crack patterns, as evidenced in shale [100, 101, 102], clay stone [103], schists [104] and sand [105]. Laboratory tests, such as uniaxial and triaxial compression tests [100, 104, 106], Brazilian indirect tension tests [107, 108], direct shear tests [109], further demonstrate that material strength and failure modes significantly depend on the confining pressure and the loading orientation with respect to microstructure. Prior to crack propagation, most geomaterials can be considered transverse isotropic: the maximum uniaxial compressive strength is reached when weak planes are either parallel or perpendicular to the loading direction, and the minimum strength is reached when weak planes are oriented at $30^\circ - 60^\circ$ with respect to the loading direction [110, 100]. In indirect tensile tests, the tensile strength is maximum when tensile stress is applied within the weak plane, and gradually decreases as the orientation angle between the tensile stress direction and the bedding plane increases [107].

In geomaterials models, intrinsic and induced anisotropy are either accounted for in the failure criterion or in the expression of the free energy. Hill [111] extended the von Mises yield criterion to orthotropic ductile materials, by using 6 quadratic stress terms. To further account for the strength difference in tension and compression, Hoffman [112] added

3 linear terms of stress into Hill's failure criterion. Tsai and Wu [113] then expressed failure criteria that depend on all possible linear and quadratic stress terms. These yield criteria were used by de Borst [114, 115] to model perfectly plastic and hardening materials. Reinicke and Ralston [116] carried out limit analyses using parabolic yield functions (Hoffman's criteria).

Other approaches were proposed to introduce either the fourth order projection tensor or the second order microstructure tensor in the yield criteria or in the expression of the free energy [117]. Boehler and Sawczuk [118] used the microstructure tensor in the constitutive model for transverse isotropic materials. Cazacu et al. [119, 120] employed a fourth order projection tensor to transform the stress tensor into a characteristic tensor with embedded microstructure information. The extended the Mises-Schleicher yield criterion initially expressed for isotropic materials to transversely isotropic materials, by using the fourth order characteristic tensor. Another approach, based on different projection tensors, consists in projecting the strength in Drucker-Prager and Mohr-Coulomb yield criteria [121]. The microstructure tensor can also be constructed with eigenvectors representing the axes of material symmetry to capture the orientation dependence of strain hardening, softening, damage and plasticity in shale [122, 123, 124, 125]. For soils, fabric tensors were used to represent microstructure in yield criteria [126]. Thermodynamic models were also proposed, in which the free energy was expressed in terms of microstructure tensor and strain invariants [127, 128].

Alternatively, the REV can be viewed as a set of cracks or planes of discontinuities. Intrinsic anisotropy is accounted for by assigning different material properties to crack families of different orientations [129, 130]. In micromechanics models, a static constraint is applied to projections of stress on the crack planes, and the expression of the REV free energy is obtained by homogenization. In microplane models, a kinematic constraint is applied to projections of strains on the crack planes; the principle of virtual work is used to upscale the microscopic relationships and calculate the macroscopic stress. Anisotropy is

accounted for by considering complex microplane orientation distributions and by formulating different evolution criteria for different microplanes [131].

2.2 Multiscale Fracture Propagation

The ultimate mechanical response of brittle material is macro-fracture propagation, as a result of micro-crack inception, propagation and coalescent. Modeling fracture propagation at the macro-scale in interaction with micro-scale structure evolution is of great interest in many fields of engineering. Over the last few decades, numerous numerical methods were proposed to model multiscale fracture propagation. They can be generally grouped into three categories: (1) Direct numerical simulation (brute-force full scale simulation); (2) Homogenization-based multiscale approach; and (3) Damage-fracture transition techniques.

2.2.1 Direct Numerical Simulation

In direct numerical simulation approach, the morphology of each microstructure phase (grains, voids, micro-cracks) are all explicitly discretized and modeled with the corresponding constitutive laws of each phase. Examples of direct numerical simulation are the discrete element method (DEM) simulation of Brazilian tests of rock materials [132], and the finite element method (FEM) simulation of three-point bending tests of asphalt concrete [133]. The direct numerical simulation essentially only involves the micromechanical behavior, through constitutive laws in FEM and contact bonds in DEM, and the macroscopic behavior is represented by the superposition of microscopic behaviors. It is very efficient to simulate fracture initiation and propagation with samples at laboratory scale. However, the computational cost is not manageable for metric-scale problems, even with today's computational power.

2.2.2 Homogenization-based Multiscale Approach

The computational homogenized multiscale simulation method can be used in replacement of the standard stress-strain phenomenological constitutive models that depend on internal variables at macro-scale (Section 2.1). The pointwise overall stress-strain behavior (i.e. stress-strain behavior at each Gauss point), evaluated from the solution of an auxiliary Boundary Value Problem (BVP) over a REV, is endowed with a geometrical description of the material morphology [134]. Computation Homogenization (CH) is used to connect the two scales. Several CH techniques exist [135]. In the standard CH, the macroscopic kinematic quantities (strain or deformation gradient) are downscaled to the micro-scale as boundary conditions to solve the BVP. Once the micro-scale BVP with explicit inhomogeneities is solved by FEM, CH is performed over the RVE to obtain the stress tensor and the Jacobian at the macroscopic level. Typically, the CH is based on Hill-Mandel principles [136] to upscale the microscopic stress and stiffness to the macro-scale. Once the process is done for every gauss point, the global stiffness matrix and the residual force vector are obtained and used to solve the BVP at the macro-scale. Because finite element simulations are performed to solve two nested boundary value problems (micro and macro), the method is also known as FE^2 scheme [137]. The FE^2 scheme was successfully applied to various multiscale materials [138, 139]. Its implementation into the Abaqus and open source FE packages are detailed by [140] and [141]. As explained by Geers et al. [135], the standard CH essentially generates a continuous stress-strain relation for the bulk at the macro-scale, it is referred as first-order homogenization. The standard CH assumes that the microscopic length scale is much smaller than the characteristic length over which the macroscopic loading varies in space $l_{discrete} \ll l_{RVE} \ll l_{macro}$, which limits its application for localization problems. Kouznetsova and Geers [142, 143] extended the standard CH to the second order. In addition to the strain and stress tensors transferred through scales, they downscale the strain gradient to the micro-scale and upscale the higher-order stress to the macro-scale as well. The second order CH can simulate moderate localization, however,

it fails to treat intensive material softening. To overcome these shortcomings, Massart et al. [144] proposed a continuous-discontinuous homogenization for masonry cracking, in which a localization band is incorporated at the macro-scale, and the strain (stress) tensor located inside and outside the band are transferred through the two scales. Note that the *multiscale aggregating discontinuties* (MAD) method, developed by Belytschko et al. [145, 146], belongs to this category - a discrete crack is incorporated at the macro-scale. Aside from the continuous-discontinuous CH, efforts were made to homogenize the continuum softening behavior at the micro-scale into a cohesive zone model at the macro-scale [147, 148, 149]: the macro-scale interfacial displacement jump is downscaled as a boundary condition for a micro-scale interfacial REV with finite thickness, and the solution of interfacial REV traction is upscaled as the macro-scale cohesive traction by homogenization.

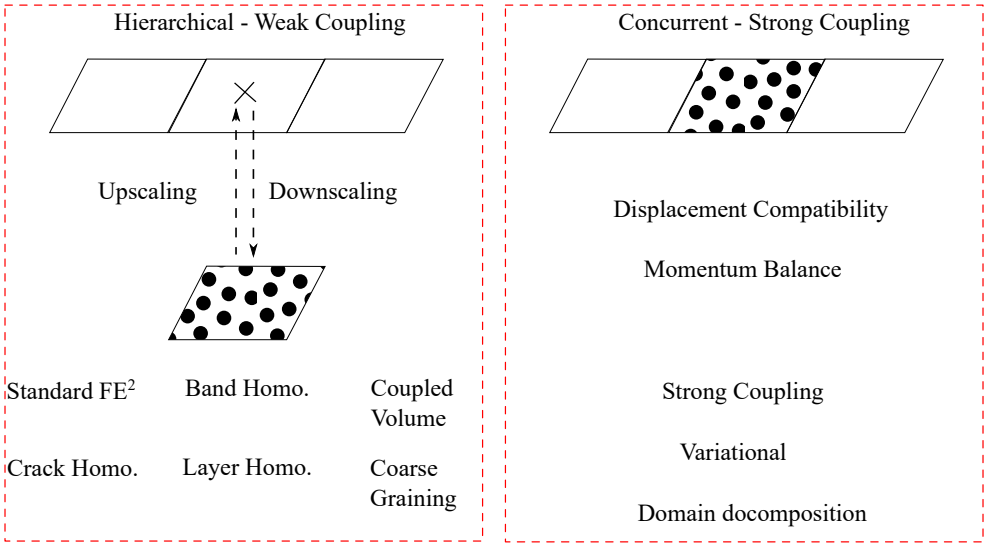

Figure 2.1: Multiscale strategies based on the structure of the computation method, adapted from Lloberas-Valls et al. [150].

In addition to the weak coupling between micro and macro models (hierarchical method) described in the above paragraph, one can distinguish another two scale simulation method, used by Belytschko and Song [146], Lloberas-Valls et al. [150]. In the strong coupling, also called concurrent method, the domain is decomposed into fine-scale and coarse-scale models. The global equilibrium and the displacement compatibility are enforced across the

interfaces between the fine-scale and coarse-scale models, and the governing equations at both scales are solved simultaneously (see Figure **??**). This method can predict multiscale fracture propagation by adaptively adding the fine-scale model with microstructure into the subdomain of the coarse-scale model. Examples of the concurrent method can be found in [151, 152, 153, 150]. Many atomistic/continuum multiscale methods are of this type. For example, in Xu et. al [154] and Budarapu et al. [155], the molecular dynamics and atomistic domains are embedded in a continuum domain. It is worth noting that the coupled DEM/FEM approach for granular materiasl belongs to the hierarchical method [156], in which the micro-scale REV with boundary conditions is modeled with the DEM.

2.2.3 Transition from Damage to Cohesive Fracture

In the direct numerical simulation approach, multiscale fracture propagation is the result of accumulation of micro-scale damage and cracking; only the micro-level constitutive laws are employed. The heirarchical and concurrent methods explicitly realize multiscale fracture propagation by two scale simulations, in which micro/macro constitutive laws are scaled by computational homogenization. For damage-fracture transition, however, only macro-scale constitutive models are used for simulation. Multiscale fracture propagation is captured phenomenologically by employing continuum damage models to simulate diffused micro cracking, and by employing cohesive zone models to simulate localized macro fracture propagation. Microstructure evolution is reflected through the internal variables, e.g., damage or crack density.

As argued in [157, 158, 159, 160, 161], the failure process of quasi-brittle materials involves two stages: diffused damage inception followed by extensive damage localization leading to macro-fracture propagation. Note that we call “process zone” the zone with diffused micro crack inception in the first stage. The most widely used numerical tools to model the failure process are classified either as continuum damage methods or as fracture mechanics methods. The continuum damage method employs constitutive law with full

stress softening (Section 2.1.1 and 2.1.2) and regularization techniques (Section 2.1.3) [79, 69, 162]. It can effectively model the diffused damage arising at the early phase of material failure by stiffness degradation. However, it cannot explicitly predict the formation of macro fracture surfaces, and it suffers from spurious damage development due to excessive strain in the later stage [84, 163]. Fracture mechanics models can avoid the issues encountered in nonlocal continuum damage models by creating discrete surfaces. However, linear elastic fracture mechanics model cannot account for the process zone development. In the widely used Cohesive Zone Model (CZM), the process zone is lumped into a single line (resectively, a single surface) in 2D (respectively, 3D). Besides, challenges exist for fracture mechanics models because the dynamic representation of discrete fracture surfaces requires sophisticated FE discretization. The embedded crack method [157], the eXtended Finite Element Method (XFEM) [161], and the method of interface-element-inserted-on-the fly [164] are among the most efficient ways to discretize the domain to conform with the geometry of the fracture.

Provided that neither continuum damage models nor fracture mechanics models alone can properly simulate the two stages of fracture propagation, a coherent computational framework that models the transition from diffused damage to localized cohesive fracture is desirable. The very first attempt of coupling CDM and fracture mechancis was made by Planas et al. [165], who proved that the cohesive fracture model is a particular case of nonlocal damage formulation. Later, Mazars and Pijaudier-Cabot published a seminal paper [166], in which they established an equivalence between the energy dissipated for opening a discrete fracture and the energy dissipated for producing a dilute distribution of micro-cracks (diffused damage). This energy equivalence was further used by Cazes et al.[167, 168] to construct a cohesive law from a nonlocal damage model in the framework of thermodynamics. Based on similar thermodynamic principles, Jirasek and Zimmermann [169, 157] used an integral type nonlocal damage model to predict micro-crack propagation and the transition to cohesive fracture debonding, in which the fracture is modeled by the

embedded crack method. The energy equivalence is enforced at the local element, and the transition triggers when when the local element strain across the embedded crack reaches a critical value. The same idea of energy equivalence at the tip element was adopted in Roth et al. [10], except that the transition at any level of damage, and the stress based nonlocal regularization with integral type was used. In [158], macro fracture is modeled with traction free surfaces (no cohesive model) using the XFEM, and the transition happens when the gradient enhanced damage variable reaches one. Comi et al. [170, 159] coupled an integral type nonlocal damage with a mode I cohesive zone using the XFEM. The transition triggers at a certain damage threshold, which is not a constant: it is related to the size of element at the fracture tip, and the energy equivalence is established by assigning to the cohesive zone model the same amount of energy as the energy not yet dissipated by the nonlocal model within the process zone. Wang and Waisman [171, 161] extended this idea to mixed mode fracture propagation with damage fracture transition. Recently, Cuvilliez et al. [160] designed a flexible modeling framework, in which the cohesive law is derived from the gradient damage model, and the transition from continuum damage to discrete cohesive fracture can happen at any level of damage. Leclerc et al. [172] further incorporated the effect of stress triaxiality into the macro cohesive zone model during the transition.

The schemes of transition from continuum damage to discrete fracture reviewed above have significant value, however, a few shortcomings still need to be addressed. First, in the diffused damage development phase, isotropic damage constitutive laws cannot account for anisotropic stiffness degradation due to the initiation of micro cracks in multiple directions. Second, phenomenological damage cannot explicitly represent crack density evolution. Micromechanical damage models should be used for modeling multiscale fracture propagation. Third, the transition is the result of micro crack interaction and coalescence, hence the threshold value should be rigorous defined and calibrated.

2.3 Hydraulic Fracturing

The study of damage and fracture in brittle solids has numerous engineering applications, one of which is hydraulic fracturing, used in the oil and gas industry to stimulate well production in regular and tight formations. Hydraulic fracturing is a complex process that involves host rock deformation, fracture propagation, fluid flow and fluid leak-off. Solving the problem of hydraulic fracturing either analytically or numerically is still very challenging because of the nonlinear, history dependent fluid flow with moving boundary conditions, and also because of the anisotropic nonlinear behavior of the host rock. We review the classical solutions of hydraulic fracturing obtained by relaxing the constraints (based on assumptions) in the following sections.

2.3.1 Analytical and Asymptotic Solutions

Pioneering work on hydraulic fracturing dates back from the 1950s [173, 174, 175]. Classical solutions are based on the so-called PKN and KDG models. In 1961, Perkins and Kern [176] used the theory of elasticity to solve for the fracture width w and the fluid pressure p along the fracture length l in plane strain conditions, in which the fracture height h was constant (Figure 2.2a). Later, Nordgren [177] improved the model by accounting for the fluid leak-off into the surrounding rock matrix (hence the name, PKN model). By further assuming that the width of the fracture w is constant in the direction perpendicular to the fracture plane (as shown in Figure 2.2b), Khristianvic and Zheltov [175], and Geertsma and De Klerk [178] independently developed another set of analytical solutions for hydraulic fracturing - the so-called KDG model. Spence and Sharp [179] extended the KGD model with self-similar relations (power law relation between the cavity volume and the injection time), and they accounted for rock toughness. In addition to the plane strain models, analytical solutions for the radial or penny-shaped fracture growth under constant fluid injection pressure was obtained by Sneddon [173], and later extended to elliptical fracture

growth [174]. The penny-shaped fracture growth model was further applied to hot, dry rock [180, 181]. Note that by invoking scaling laws, Detournay [182] found that there are three competing energy dissipation mechanisms that control the process of hydraulic fracturing, depending on the value of the fracture toughness, the fluid viscosity and the leak-off term. Based on Detournay's analyses, numerous semi-analytical solutions were developed for plane strain conditions [183, 184, 185, 186, 187, 188] and for penny-shaped fractures [189, 190, 191]. These solutions, based on a variety of governing laws for fluid rheology (viscosity), fluid flow in the matrix (leak-off), and rock toughness, are important tools to understand hydraulic fracture propagation regimes.

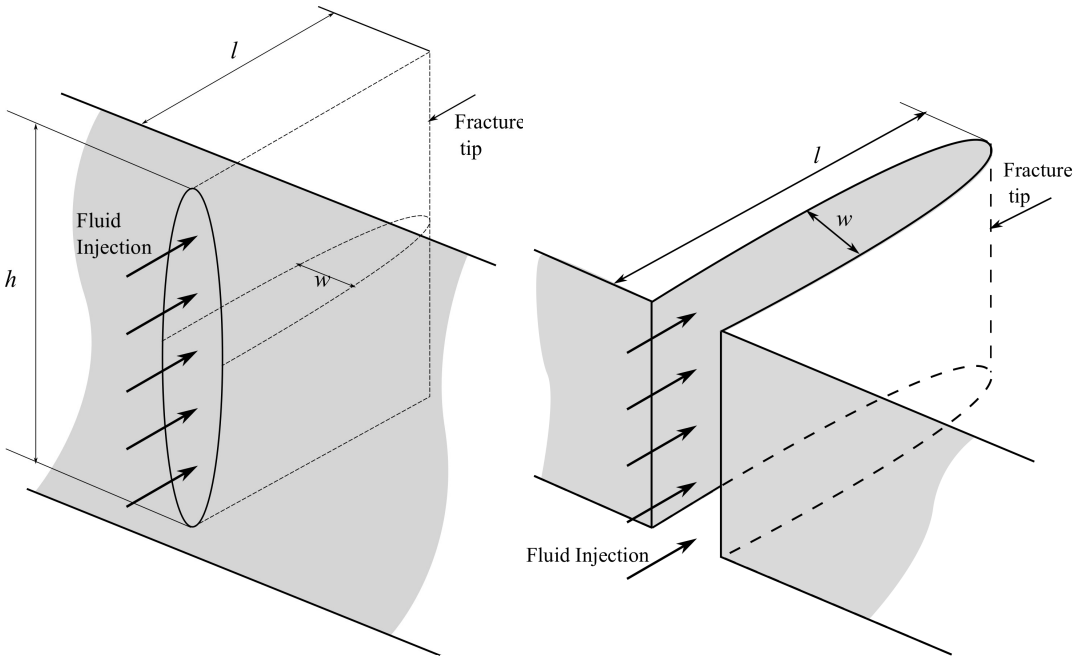

(a) PKN fracture geometry (b) KGD fracture geometry

Figure 2.2: Schematic representations of the PKN and KGD models with l, h and w representing fracture length, height, and width, respectively, adapted from [192].

As pointed out by Detournay and Peirce [193], the analytical solutions reviewed above were all obtained with *ad hoc* assumptions, and did not properly account for the boundary conditions at the tip and near the tip. To address these limitations, a number of studies were carried out to find analytical solutions for the singularity of tip and to predict the limiting

propagation regime. Fracture width solutions are:

$$
\begin{aligned}
w_k &= \frac{K'}{E'} s^{1/2} \\
w_{\tilde{m}} &= \beta_{\tilde{m}} \Big(\frac{4 {\mu'}^2 V {C'}^2}{{E'}^2} \Big)^{1/8} s^{5/8} \\
w_m &= \beta_m \Big(\frac{\mu' V}{E'} \Big)^{1/3} s^{2/3}
\end{aligned}
\tag{2.53}
$$

for the toughness dominated regime (index k), the leak-off dominated regime (index $\tilde{m}$), and the viscous dominated regime (index m). $\mu' = 12\mu$ is the scaled fluid viscosity, $E' = E/(1-\nu^2)$ is the plane strain modulus, $K' = 4\sqrt{2/\pi} K_{IC}$ and $C' = 2C_L$ is the scaled fracture toughness and the leak-off coefficient, respectively. $\beta_{\tilde{m}}$ and β_m are both constants, and s is the coordinate that originates at the fracture tip. Equations 2.53 are called vertex solutions. The $m-$vertex solution is explained in [194] for the zero-toughness and impermeable case, the $\tilde{m}-$vertex solution is presented in [195] for the zero-toughness and leak-off dominated case, and the $k-$vertex solution is obtained by LFEM asymptotes. In the general case, fracture propagation may travel within the parametric space of the three limiting cases, as shown in Figure 2.3; Garagash et al. [196], Dontsov and Peirce [197] obtained the universal tip asymptotic solution that can be used for any locations in the parametric space.

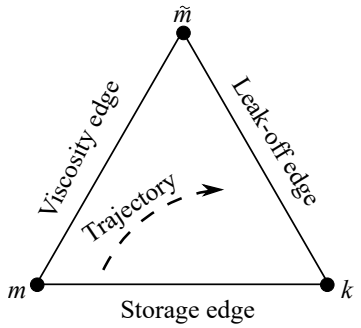

Figure 2.3: Parametric space of the three limiting propagation regimes and the vertex solution, adapted from [196].

2.3.2 Numerical Solutions

Analytical solutions were used for industry applications at the inception of hydraulic fracturing. however, the overly constraining assumptions limit their application. So-called pseudo-3D (P3D) models were the first numerical simulators developed to relax those constraints. Numerical P3D models are still based on the assumption that a vertical plane fracture propagates in a homogeneous rock formation, but fracture height growth is accounted for. In lumped P3D models, fractures are assumed to be ellispoidals [198]. In cell-based P3D models, fractures are regarded as connected rectangular elements [199, 200]. The latest P3D models include the stacked height [201] and the enhanced [202] models. The planar 3D numerical models (PL3D) were proposed to account for the variation of elasticity, toughness and confining pressure across formation layers [203, 204, 205, 206], which relaxes analytical constraints even further. Either the adaptive mesh method or the structured mesh enhanced with level set method is used to obtain the dynamic planar fracture footprint. The two dimensional fluid flow as well as the elastic equilibrium are considered. The PL3D model significantly increases the accuracy of the hydraulic fracturing model, but also increases dramatically its computational cost.

In the past years, research on hydraulic fracturing modeling focused on three major objectives. The first one is to reduce the computational cost while maintaining solution accuracy in P3D and PL3D models, by incorporating the tip asymptotic solutions [207, 208, 209] into the simulation code. The second is to relax the constraints of the P3D and PL3D models, by considering non-planar fracture geometries [210, 211], by simulating the simultaneous propagation of multiple hydraulic fractures [207, 212, 213], and by incorporating the interaction with natural fractures [214, 215, 216]. To meet both of these objectives, the force equilibrium in elastic formation, the mass balance equation for the fluid with leak-off, and the propagation of fracture tip are accounted for. However, the process of fluid flow within the porous matrix, as well as the nonlinear rock deformation and the cohesive fracture propagation are ignored. The third objective is thus to incorporate these

physical processes by employing advanced numerical methods, such as interface elements [217], the extended finite element method [218] and the phase field method [219]. Note that the successful implementation of the 2D/3D cohesive interface elements and of the 2D cohesive segments with XFEM in Abaqus have stimulated a significant amount of applied research [220, 213, 221, 222, 223, 217, 224]. However, novel numerical discretization schemes [225, 226] and novel coupling methods [227, 228, 229] are still needed to study unsaturated porous media, to predict the fluid pressure jump across the fracture, and to address convergence issues. In the United States, hydraulic fracturing is used extensively in shale, which is a transversely isotropic material. The application of models developed for isotropic material is questionable for shale. In addition, fracture propagation is a multiscale process, and cohesive laws cannot capture the whole initiation and propagation phases. In this thesis, we propose a numerical scheme to predict multi-scale hydraulic fracture propagation in intrisically anisotropic quasi-brittle porous media.

CHAPTER 3
MICRO-MECHANICAL ANISOTROPIC MODEL OF CRACK INITIATION AND PROPAGATION IN MIXED MODE

3.1 Introduction

This chapter presents the theoretical formulation and the numerical implementation of two anisotropic damage models, along with some engineering applications. Both formulations couple micro-mechanical crack propagation criteria with Continuum Damage Mechanics (CDM) energy principles in order to capture inelastic deformation due to damage, predict unilateral effects due to tensile cracks, distinguish strength and stiffness properties in tension and compression and simulate complex stress paths involving the propagation of both open and closed cracks in mode I, mode II, and mixed mode. In Section 3.2, we first express Gibbs energy at the scale of a Representative Elementary Volume (REV) by homogenizing the energy stored in sets of non-interacting micro-cracks of different orientations. We use a dilute homogenization scheme with Bazant's integration method based on 2×21 orientations on the unit sphere.

The formulation of the Discrete Equivalent Wing Crack based Damage (DEWCD) model presented in 3.3 is based on the expression of Gibbs free energy and on thermodynamic conjugation relationships. The damage variable is a second-order crack density tensor and the irreversible deformation is defined as the crack opening vector averaged over all possible crack orientations. In tension, cracks propagate in mode I in the direction normal to the tensile stress. In compression, wing cracks propagate in mode I in the direction of the minimum deviatoric stress. We calibrate and validate the DEWCD model against triaxial compression data obtained on North Dakota Bakken shale. Using the calibrated parameters, we simulate: (1) A loading path made of a uniaxial tension followed

by unloading and uniaxial compression; and (2) Two loading-unloading cycles of uniaxial compression of increasing amplitude.

In the DEWCD model, stress is employed to construct the wing crack propagation criterion. By contrast, in in Section 3.4, we formulate yield criteria with different damage driven forces for open and closed micro-cracks of various orientations. The elastic domain of the REV is defined by the intersection of activated damage surfaces. The overall damage yield surfaces are not smooth, which requires a special treatment to allow numerical implementation. We present a local Closest Point Projection algorithm, which we use to determine the set of activated cracks and the corresponding increments of crack density. We explain the detailed calculations required to calculate the Jacobian matrix at the material point. We also validate the implementation of the resolution algorithm by comparing the results of material-point simulations to those obtained with a one-element FEM model. In the final subsection, we calibrate the proposed discrete damage model against experimental results of triaxial compression and uniaxial tension tests reported in the literature. Using model parameters calibrated for concrete, we simulate triaxial compression tests and Hassanzadeh's direct tension test. We also model a composite made of a brittle matrix reinforced by stiff elastic fibers to study the influence of reinforcement orientations on the formation of crack patterns.

3.2 Micromechanics-based Free Enthalpy

Consider a REV of volume Ω_r and external boundary $\partial\Omega_r$, in which a large number of penny shaped microscopic cracks of various orientations are embedded in an isotropic linear elastic matrix of compliance tensor $\mathbb{S}^m$. Each microscopic crack is characterized by its normal direction $\overrightarrow{n}$ and its radius a, which is at least 100 times smaller than the REV size. Opposite crack faces are noted ω^+ and ω^-, with normal vectors $\overrightarrow{n}^+$ and $\overrightarrow{n}^-$ respectively. The displacement jump is noted:

$$[\overrightarrow{u}] = \overrightarrow{u}^+ - \overrightarrow{u}^- \tag{3.1}$$

where $\overrightarrow{u}^+$ (respectively $\overrightarrow{u}^-$) denotes the displacement vector at face ω^+ (respectively ω^-). We consider a uniform stress field $\boldsymbol{\sigma}$ applied at the boundary $\partial\Omega_r$. The displacement field at the REV scale is calculated by superposition, by adding up the displacement field in the elastic matrix in the absence of cracks and the displacement field induced by the opening and sliding of micro-crack faces (Figure 3.1).

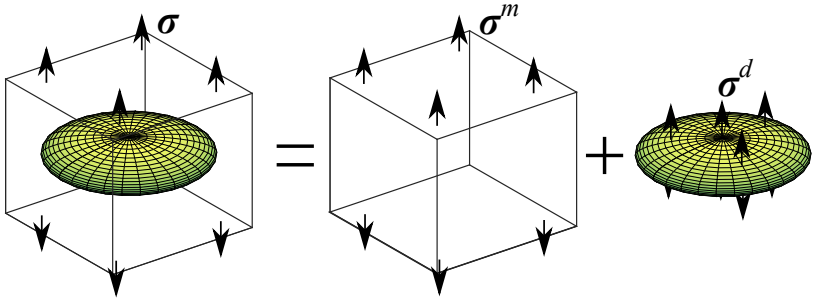

Figure 3.1: Homogenization based on the principle of superposition.

We consider that the mechanical interaction between cracks is negligible and we use a dilute homogenization scheme to calculate the crack displacement jumps. As a result, the average micro stress is equal to the stress applied to the REV, and we have:

$$\boldsymbol{\sigma} = \frac{1}{\Omega_r}\int_{\Omega_r}[\boldsymbol{\sigma}^m(\boldsymbol{x}) + \boldsymbol{\sigma}^d(\boldsymbol{x})]\mathrm{d}\boldsymbol{x} \tag{3.2}$$

in which $\boldsymbol{\sigma}^d(\boldsymbol{x})$ is the stress field that is applied at micro-crack faces and $\boldsymbol{\sigma}^m(\boldsymbol{x})$ is the stress field in the linear elastic matrix. Moreover, the static constraint imposed by the dilute homogenization scheme is applied to the elastic cracked REV when cracks do not propagate, which implies that the local stress $\boldsymbol{\sigma}^d(\boldsymbol{x})$ is the direct projection of the macro stress $\boldsymbol{\sigma}(\boldsymbol{x})$ on crack faces. Consequently, for each crack, the local stress that applies at the crack faces is self-equilibrating and the matrix stress is equal to the macro stress:

$$0 = \int_{\omega} \boldsymbol{\sigma}^d(\boldsymbol{x}) \mathrm{d}\boldsymbol{x}, \quad \boldsymbol{\sigma} = \boldsymbol{\sigma}^m \tag{3.3}$$

The elastic strain tensor of the matrix $\boldsymbol{\epsilon}^e$ depends on the undamaged compliance tensor $\mathbb{S}^m$, as follows:

$$\boldsymbol{\epsilon}^e = \mathbb{S}^m : \boldsymbol{\sigma}^m = \mathbb{S}^m : \boldsymbol{\sigma}. \tag{3.4}$$

In the dilute homogenization scheme adopted here, we treat each micro-crack as a single crack embedded in an infinite elastic homogeneous matrix, which allows calculating the displacement jumps from fracture mechanics principles [230, 231]. Considering a penny shaped crack of radius a subjected to a uniformly distributed normal stress p (respectively shear stress $\overrightarrow{\tau}$) at its faces and embedded in an infinite elastic medium with Young's modulus E_0 and Poisson's ratio ν_0, the average normal (respectively shear) displacement jump, also known as Crack Opening Displacement (COD), is expressed as:

$$\begin{aligned} \langle [u_n] \rangle &= \frac{16}{3} \frac{1-\nu_0^2}{\pi E_0} pa \\ \langle [\overrightarrow{u_t}] \rangle &= \frac{32}{3} \frac{1-\nu_0^2}{(2-\nu_0)\pi E_0} \overrightarrow{\tau} a \end{aligned} \tag{3.5}$$

We first consider that the REV contains families of penny shaped cracks that have same orientation $\overrightarrow{n_i}$ and same radius a_i. Such a family of micro-cracks is shown in Figure 3.2a. If the family contains N cracks, the volume fraction of the normal and shear displacement

jumps can be calculated as follows:

$$\beta_i = \frac{N}{\Omega_r}\langle[u_n]\rangle\pi a_i^2 = \rho_i c_0 \boldsymbol{\sigma}^d : (\overrightarrow{n_i} \otimes \overrightarrow{n_i}) = \rho_i c_0 \boldsymbol{\sigma} : (\overrightarrow{n_i} \otimes \overrightarrow{n_i})$$
$$\overrightarrow{\gamma_i} = \frac{N}{\Omega_r}\langle[\overrightarrow{u_t}]\rangle\pi a_i^2 = \rho_i c_1[\boldsymbol{\sigma}^d \cdot \overrightarrow{n_i} - (\overrightarrow{n_i} \cdot \boldsymbol{\sigma}^d \cdot \overrightarrow{n_i})\overrightarrow{n_i}] = \rho_i c_1[\boldsymbol{\sigma} \cdot \overrightarrow{n_i} - (\overrightarrow{n_i} \cdot \boldsymbol{\sigma} \cdot \overrightarrow{n_i})\overrightarrow{n_i}] \tag{3.6}$$

where $\overrightarrow{\tau} = \boldsymbol{\sigma} \cdot \overrightarrow{n_i} - (\overrightarrow{n_i} \cdot \boldsymbol{\sigma} \cdot \overrightarrow{n_i})\overrightarrow{n_i}$. Note that according to the dilute scheme assumption, the direct projection of the macro stress $\boldsymbol{\sigma}$ on crack faces is equal to the direct projection of the local stress $\boldsymbol{\sigma}^d$ on crack faces. $\rho_i = Na_i^3/\Omega_r$ is the crack density parameter along the direction $\overrightarrow{n_i}$ introduced in [41] . Note that the value of ρ_i can exceed one. The coefficient c_0 (respectively c_1) is defined as the normal (respectively shear) elastic compliance of the crack [41, 42]:

$$c_0 = \frac{16}{3}\frac{1-\nu_0^2}{E_0}, \quad c_1 = \frac{32}{3}\frac{1-\nu_0^2}{(2-\nu_0)E_0} \tag{3.7}$$

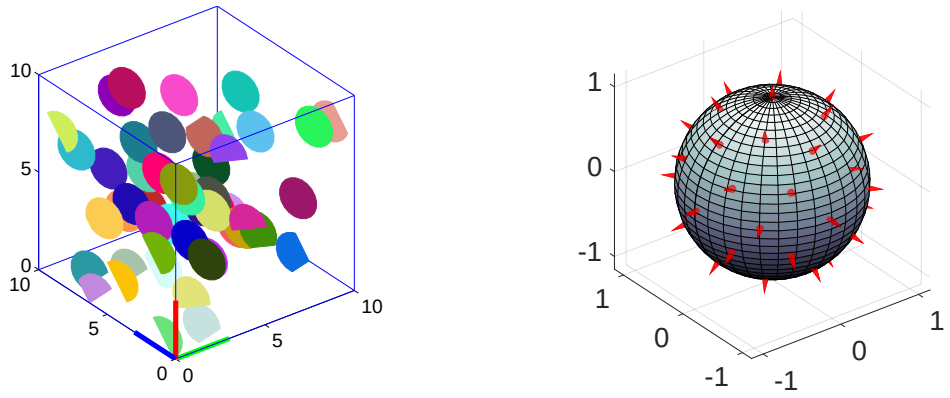

(a) Single crack family (b) Discrete crack family orientations

Figure 3.2: (a) Sketch of a REV with one family of parallel equally sized penny shaped micro-cracks; (b) Repartition of the integration points on the unit sphere, following the microplane approach based on 2×21 points presented in [232].

A normal displacement jump can only be induced by a tensile force, i.e. for $\overrightarrow{n_i} \cdot \boldsymbol{\sigma} \cdot \overrightarrow{n_i} \leq 0$ (in which compression is counted positive, according to the soil mechanics convention).

The unilateral contact condition at crack faces can be expressed as

$$[u_n] \geq 0, \quad \sigma_{nn} = \overrightarrow{n} \cdot \boldsymbol{\sigma} \cdot \overrightarrow{n} \leq 0, \quad [u_n]\sigma_{nn} = 0 \tag{3.8}$$

The average strain due to the displacement jumps of the all the micro-cracks of the family with normal $\overrightarrow{n_i}$ is calculated as:

$$\begin{aligned} \boldsymbol{\epsilon}^d &= \frac{N}{\Omega_r} \int_{\partial\omega^+} [u_n](\overrightarrow{n_i} \otimes \overrightarrow{n_i}) \mathrm{d}S + \frac{N}{2\Omega_r} \int_{\partial\omega^+} ([\overrightarrow{u_t}] \otimes \overrightarrow{n_i} + \overrightarrow{n_i} \otimes [\overrightarrow{u_t}]) \mathrm{d}S \\ &= \beta_i \overrightarrow{n_i} \otimes \overrightarrow{n_i} + \frac{1}{2}(\overrightarrow{\gamma_i} \otimes \overrightarrow{n_i} + \overrightarrow{n_i} \otimes \overrightarrow{\gamma_i}) \end{aligned} \tag{3.9}$$

According to the principle of superposition, the Helmholtz free energy W^* of the REV containing the N cracks of orientation $\overrightarrow{n_i}$ is the sum of the elastic deformation energy of the matrix and the energy stored in the micro cracks displacement jumps, as follows:

$$W^* = \frac{1}{2}\boldsymbol{\epsilon}^e : \mathbb{C}^m : \boldsymbol{\epsilon}^e + \frac{1}{2}\boldsymbol{\sigma} : [\beta_i \overrightarrow{n_i} \otimes \overrightarrow{n_i} + \frac{1}{2}(\overrightarrow{\gamma_i} \otimes \overrightarrow{n_i} + \overrightarrow{n_i} \otimes \overrightarrow{\gamma_i})] \tag{3.10}$$

in which it is recalled that $\sigma : \overrightarrow{n_i} \otimes \overrightarrow{n_i} = \sigma^d : \overrightarrow{n_i} \otimes \overrightarrow{n_i}, \sigma : \overrightarrow{n_i} \otimes \overrightarrow{\gamma_i} = \sigma^d : \overrightarrow{n_i} \otimes \overrightarrow{\gamma_i}$. The Gibbs energy (free enthalpy) is obtained by Legendre transformation, as follows:

$$G^* = \boldsymbol{\sigma} : \boldsymbol{\epsilon}^E - W^* \tag{3.11}$$

in which $\boldsymbol{\epsilon}^E = \boldsymbol{\epsilon}^e + \boldsymbol{\epsilon}^d$ is the REV elastic strain. As a result, G^* is expressed as:

$$\begin{aligned} G^* &= \frac{1}{2}\boldsymbol{\sigma} : \mathbb{S}^m : \boldsymbol{\sigma} + \frac{1}{2}\boldsymbol{\sigma} : \boldsymbol{\epsilon}^d \\ &= \frac{1}{2}\boldsymbol{\sigma} : \mathbb{S}^m : \boldsymbol{\sigma} + \frac{1}{2}\boldsymbol{\sigma} : [\beta_i \overrightarrow{n_i} \otimes \overrightarrow{n_i} + \frac{1}{2}(\overrightarrow{\gamma_i} \otimes \overrightarrow{n_i} + \overrightarrow{n_i} \otimes \overrightarrow{\gamma_i})] \end{aligned} \tag{3.12}$$

By substituting Equation 3.6 into the expression of the free enthalpy above, and introducing

the unilateral contact condition in Equation 3.8, we get:

$$G^* = \frac{1}{2}\boldsymbol{\sigma} : \mathbb{S}^m : \boldsymbol{\sigma} + \frac{1}{2}c_0\rho_i H(\overrightarrow{n_i} \cdot \boldsymbol{\sigma} \cdot \overrightarrow{n_i})\boldsymbol{\sigma} : \mathbb{N}_i : \boldsymbol{\sigma} + \frac{1}{2}c_1\rho_i\boldsymbol{\sigma} : \mathbb{T}_i : \boldsymbol{\sigma} \tag{3.13}$$

where $H(\cdot)$ is the Heaviside jump function and $\overrightarrow{n_i} \cdot \boldsymbol{\sigma} \cdot \overrightarrow{n_i} = \sigma^i_{nn}$ is the normal stress at the crack face. The fourth order normal (respectively, tangent) operator $\mathbb{N}_\alpha$ (respectively, $\mathbb{T}_\alpha$) is defined by:

$$\begin{aligned} \mathbb{N}_\alpha &= N^\alpha_{ijkl} = n^\alpha_i n^\alpha_j n^\alpha_k n^\alpha_l \\ \mathbb{T}_\alpha &= T^\alpha_{ijkl} = \frac{1}{4}(n^\alpha_i n^\alpha_k \delta_{jl} + n^\alpha_i n^\alpha_l \delta_{jk} + \delta_{ik} n^\alpha_j n^\alpha_l + \delta_{il} n^\alpha_j n^\alpha_k) - n^\alpha_i n^\alpha_j n^\alpha_k n^\alpha_l \end{aligned} \tag{3.14}$$

in which n^α_j is the unit normal vector of each direction α.

For more than on crack orientation, we can calculate the total Gibbs energy of the REV by integrating G^* for a distribution of crack orientations $\rho(n)$, over the unit sphere $S^2 = \{\overrightarrow{n}, |\overrightarrow{n}| = 1\}$, as follows:

$$G = \frac{1}{2}\boldsymbol{\sigma} : \mathbb{S}^m : \boldsymbol{\sigma} + \frac{1}{8\pi}\int_{S^2} \rho(\overrightarrow{n})\{c_0\, H(\sigma^i_{nn})\boldsymbol{\sigma} : \mathbb{N}_i : \boldsymbol{\sigma} + c_1\, \boldsymbol{\sigma} : \mathbb{T}_i : \boldsymbol{\sigma}\}\mathrm{d}S \tag{3.15}$$

Since the calculation of the integral above is impractical for a continuous distribution $\rho(\overrightarrow{n})$, we use a numerical integration scheme, with M integration points:

$$G = \frac{1}{2}\boldsymbol{\sigma} : \mathbb{S}^m : \boldsymbol{\sigma} + \frac{1}{2}\sum_{i=1}^{M} w_i\rho_i\Big[\boldsymbol{\sigma} : (c_0\, H(\sigma^i_{nn})\mathbb{N}_i + c_1\, \mathbb{T}_i) : \boldsymbol{\sigma}\Big] \tag{3.16}$$

where w_i is the weight in direction n_i. Note that the calculation of G requires M calculations at each time step. Increasing M can increase exponentially the computational cost of the numerical integration. We adopt Bazant's discrete scheme with 2×21 microplanes [232] as shown in Figure 3.2b. This scheme provides satisfactory accuracy at reasonable computation cost. For a detailed discussion about the performance of the numerical inte-

gration scheme, the reader is referred to [233, 234].

The expression of Gibbs energy given in Equation 3.16 accounts for the displacement field induced by crack opening and crack sliding, but not for crack growth (i.e., the model does not account for the increase of crack radius). In order to account for inelastic crack dedonding (i.e. crack radius growth), we introduce the inelastic strain $\boldsymbol{\epsilon}^{in}$ in the formulation. We adopt a hyper-elastic framework [37], in which the REV strain tensor $\boldsymbol{\epsilon}$ is split into a pure elastic part $\boldsymbol{\epsilon}^{e}$ which corresponds to the deformation of elastic matrix, an additional elastic part $\boldsymbol{\epsilon}^{d}$ which represents the micro-crack elastic strain, and the inelastic deformation $\boldsymbol{\epsilon}^{in}$, as follows:

$$\boldsymbol{\epsilon} = \boldsymbol{\epsilon}^{e} + \boldsymbol{\epsilon}^{d} + \boldsymbol{\epsilon}^{in} = \boldsymbol{\epsilon}^{E} + \boldsymbol{\epsilon}^{in} \tag{3.17}$$

in which:

$$\begin{aligned} \boldsymbol{\epsilon}^{E} &= \boldsymbol{\epsilon}^{e} + \boldsymbol{\epsilon}^{d} = \frac{\partial G}{\partial \boldsymbol{\sigma}} \\ \boldsymbol{\epsilon}^{e} &= \frac{1+\nu_0}{E_0}\boldsymbol{\sigma} - \frac{\nu_0}{E_0}\mathrm{Tr}(\boldsymbol{\sigma})\boldsymbol{\delta} \\ \boldsymbol{\epsilon}^{d} &= \sum_{i=1}^{M} \rho_i w_i (c_0 \mathbb{N}_i H(\sigma^i_{nn}) + c_1 \mathbb{T}_i) : \boldsymbol{\sigma} \end{aligned} \tag{3.18}$$

For each micro-plane orientation i, conjugation relationships are established to calculate the damage driving force Y_i:

$$Y_i = \frac{\partial G}{\partial \rho_i} = \frac{1}{2} w_i \boldsymbol{\sigma} : (c_0 \mathbb{N}_i H(\sigma^i_{nn}) + c_1 \mathbb{T}_i) : \boldsymbol{\sigma} \tag{3.19}$$

3.3 Discrete Equivalent Wing Crack based Damage Model

3.3.1 Damage Criteria with Wing Crack Theory

Uniaxial compression tests performed on two-dimensional photoelastic materials highlighted the occurrence of two wing cracks at the tips of pre-existing cracks. Wing cracks propagate along a curved path, of average direction parallel to the direction of maximum

compression [235, 236, 237]. The sliding wing crack model was initially presented in the pioneering work of Bombolakis and Brace [238]. Since then, numerous studies were devoted to the mechanisms of crack propagation in brittle solids under compression, for instance: [235, 236, 237, 239, 49, 240]. 3D lab experiments [241, 242], numerical simulations [243] and theoretical derivations [239] were also proposed to model the propagation of tensile wing cracks at the tip of sliding cracks ('slips'). Friction forces at the faces of slips are thus the forces driving the propagation of wing cracks. 3D wing cracks propagate due to mixed failure modes (I, II or III) at different locations along the edge of the pre-exiting slip cracks. The shape of 3D wing cracks is therefore extremely complex, and depends on a high number of parameters.

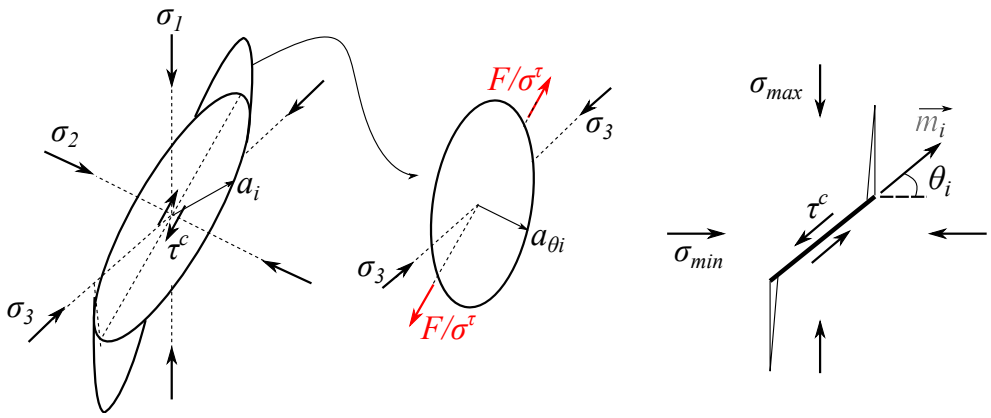

Figure 3.3: Wing crack propagation model under compression.

For practicality, we ignore friction at crack faces, i.e. we assume that wing cracks propagate in pure mode I and we represent the propagation of shear cracks in the form of tensile wing cracks. We ignore the interaction between these tensile micro-cracks and we apply the dilute hogenization scheme. If the unilateral contact condition is satisfied, cracks propagate due to normal tensile stresses, according to the following mode I propagation criterion:

$$f_d(\boldsymbol{\sigma}, a_i) = \sigma^i_{nn} - \frac{K_c}{\sqrt{a_i}} \tag{3.20}$$

where K_c is a constitutive parameter which represents the material toughness. We define

the second-order crack density tensor $\boldsymbol{\Omega}$ (also called second-order damage tensor) as follows:

$$\boldsymbol{\Omega} = \sum_{i=1}^{M} \rho_i \overrightarrow{n_i} \otimes \overrightarrow{n_i}. \tag{3.21}$$

If the unilateral contact condition is not satisfied, shear stresses at the faces of slip cracks induce the propagation of wing cracks. Following [237, 240], we represent two half wing cracks as a single fictitious circular crack, as shown in Figure 3.3.

The direction of maximum shear stress at the faces of the cracks perpendicular to direction $\overrightarrow{n_i}$ can be calculated as follows:

$$\overrightarrow{m_i} = \frac{\tau^c}{||\tau^c||} = \frac{\boldsymbol{\sigma} \cdot \overrightarrow{n_i} - (\overrightarrow{n_i} \cdot \boldsymbol{\sigma} \cdot \overrightarrow{n_i})\overrightarrow{n_i}}{||\boldsymbol{\sigma} \cdot \overrightarrow{n_i} - (\overrightarrow{n_i} \cdot \boldsymbol{\sigma} \cdot \overrightarrow{n_i})\overrightarrow{n_i}||} \tag{3.22}$$

We solve the wing crack propagation problem in two dimensions, by assuming that the normal of the equivalent fictitious circular crack that represents the wing cracks is contained in the plane (m_i, n_i). Therefore, we have:

$$\begin{aligned} \sigma^i_{nn} &= \overrightarrow{n_i} \cdot \boldsymbol{\sigma} \cdot \overrightarrow{n_i} \\ \tau^i_{nm} &= ||\boldsymbol{\sigma} \cdot \overrightarrow{n_i} - (\overrightarrow{n_i} \cdot \boldsymbol{\sigma} \cdot \overrightarrow{n_i})\overrightarrow{n_i}|| \\ \sigma^i_{mm} &= \overrightarrow{m_i} \cdot \boldsymbol{\sigma} \cdot \overrightarrow{m_i} \end{aligned} \tag{3.23}$$

The tensile force F applied at the faces of the fictitious wing crack is equal to the shear forces undergone by the pre-existing 'slip' of radius a_i, and can be calculated as:

$$F = \pi a_i^2 \tau^c = \pi a_i^2 \tau^i_{nm} \tag{3.24}$$

Experimental [242] and numerical [243] studies indicate that wing cracks propagate along the direction of maximum compression stress. When the pre-existing 'slip' crack is in compression and subjected to shear stresses, the normal to the fictitious planar crack representing the wing cracks is therefore oriented in the direction of minimum compression

(Equation 3.23). Using Mohr's circles, the intensity σ_{min} and direction θ_i of the mimimum compression are calculated as follows:

$$\begin{aligned} tan(2\theta_i) &= \frac{2\tau^i_{nm}}{\sigma^i_{mm} - \sigma^i_{nn}} \\ \sigma_{min} &= \frac{\sigma^i_{mm} + \sigma^i_{nn}}{2} - \sqrt{(\frac{\sigma^i_{mm} - \sigma^i_{nn}}{2})^2 + (\tau^i_{nm})^2} \end{aligned} \tag{3.25}$$

Based on the theory of linear fracture mechanics, we consider that the wing crack propagates only if the stress intensity factor reaches the material toughness. Assuming that the tensile driving force F is uniformly distributed along the faces of the fictitious planar crack (Figure 3.3), we define the wing micro crack propagation criterion as follows:

$$f_{d0}(\boldsymbol{\sigma}, a_{\theta i}) = \sqrt{\pi\, a_{\theta i}} \left(\frac{F cos(\theta_i)}{\pi a^2_{\theta i}} - \sigma_{min} \right) - K_c \sqrt{\pi} \tag{3.26}$$

Satisfying the criterion f_{d0} is equivalent to satisfying the following criterion, which will be adopted in the following for wing crack propagation:

$$f_d(\boldsymbol{\sigma}, a_{\theta i}) = \left(cos(\theta_i) \tau^i_{nm} (\frac{a_i}{a_{\theta i}})^2 - \sigma_{min} \right) - \frac{K_c}{\sqrt{a_{\theta i}}} \tag{3.27}$$

where $a_{\theta i}$ is the radius of the fictitious wing crack, which can be determined by projecting the damage tensor defined in Equation 3.21 as follows:

$$a_{\theta i} = (\frac{|\Omega_r|}{N} \overrightarrow{n_\theta} \cdot \boldsymbol{\Omega} \cdot \overrightarrow{n_\theta})^{1/3} \tag{3.28}$$

$\overrightarrow{n_\theta}$ is the unit vector normal to the family of wing cracks of orientation θ, and is expressed as:

$$\overrightarrow{n_\theta} = \overrightarrow{m_i} cos(\theta_i) + \overrightarrow{n_i} sin(\theta_i) \tag{3.29}$$

The progressive stiffness degradation observed before the peak of stress in experimental rock mechanics compression tests indicates that wing micro-cracks propagate in a stable

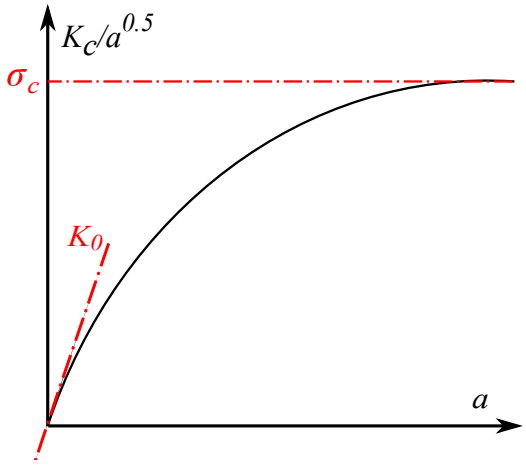

Figure 3.4: Hyperbolic damage hardening function used in the DEWCD model.

way [20]. Theoretically, in the subcritical regime, cracks can propagate even when the stress intensity factor is lower than the material toughness. Moreover, the stress intensity required for crack propagation increases as the crack propagates [244]. In order to account for this hardening effect, we propose to express the material toughness as a hyperbolic function of the crack radius, as follows:

$$K_c = \frac{a^{3/2}}{\frac{1}{K_0} + \frac{a}{\sigma_c}} \tag{3.30}$$

where $a = a_{\theta i}$ for a crack in compression (leading to the propagation of wing cracks), and $a = a_i$ for a crack in tension. As shown in Figure 3.4, the yield point depends on K_0, the slope of the plot that represents the variations the toughness with the square root of the fracture length. The parameter σ_c controls the peak driving force that the REV can sustain.

3.3.2 Damage Potential and Flow Rule

Inelastic strains observed after unloading are due to residual geometric incompatibilities at the crack faces, which depend on the damage-driving forces Y_i. The micro-crack propagation criteria formulated in Equation 3.20 and 3.27 depend on stress and cannot properly represent the occurrence of residual displacement fields after unloading. We thus derive

the evolution laws of inelastic strains from non associate flow rules. We introduce discrete damage potentials (expressed in terms of Y_i) in a homogeneous function of degree one, as follows:

$$g_d(n_i) = Y_i - C_0 \tag{3.31}$$

Following a non-associate flow rule, the inelastic strain increment can be computed from the damage potential as

$$\begin{aligned} \dot{\boldsymbol{\epsilon}}^{in} &= \sum_{i=1}^{M} \dot{\lambda}_i \frac{\partial g_d(n_i)}{\partial \boldsymbol{\sigma}} = \sum_{i=1}^{M} \dot{\lambda}_i \frac{\partial Y_i}{\partial \boldsymbol{\sigma}} \\ &= \sum_{i=1}^{M} w_i \dot{\lambda}_i (c_0 \mathbb{N}_i H(\sigma^i_{nn}) + c_1 \mathbb{T}_i) : \boldsymbol{\sigma} \end{aligned} \tag{3.32}$$

where λ_i is Lagrange multiplier for each family of crack with normal $\overrightarrow{n_i}$. Similarly, the increment of damage density is calculated as:

$$\dot{\rho}_i = \dot{\lambda}_i \frac{\partial g_d}{\partial Y_i} = \dot{\lambda}_i \tag{3.33}$$

The incremental damage density is calculated from the increments of crack radius, as follows:

$$\Delta\rho_i = \frac{N}{|\Omega_r|} \Delta(a_i^3) \tag{3.34}$$

in which $\Delta(a_i^3)$ represents the variation of the value of a_i^3 between two iterations. We have: $\Delta(a_i^3) = 3(a_i)^2 \Delta(a_i)$ in which $\Delta(a_i)$ is obtained by using the consistency rule:

$$\Delta(a_i) = -\frac{\frac{\partial f_d}{\partial \boldsymbol{\sigma}}}{\frac{\partial f_d}{\partial a_i}} \; : \; \Delta\boldsymbol{\sigma} \tag{3.35}$$

The equation above requires calculating the derivatives of τ^i_{nm} and σ_{min} with respect to the stress tensor $\boldsymbol{\sigma}$, which is computationally intensive. We employ the Newton iteration

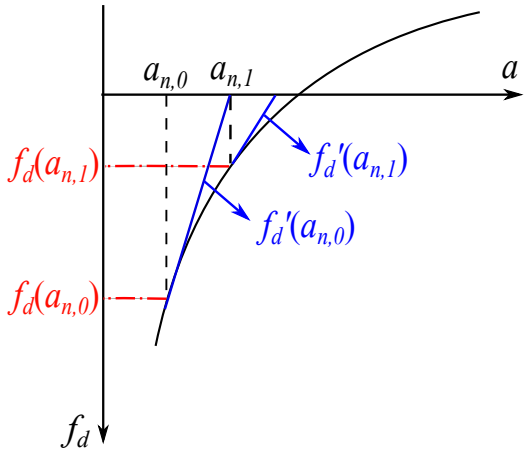

Figure 3.5: Newton iteration scheme used to calculate the Lagrange multiplier with the hyperbolic hardening law used in the DEWCD model.

scheme to update the radius of the micro cracks at each load step. As shown in Figure 3.5, the tangent of the yield criterion is calculated at each iteration i to approach the exact crack size at load step n+1, as follows:

$$a_{n,i+1} = a_{n,i} - \frac{f_d(\boldsymbol{\sigma}_{n,i}, a_{n,i})}{f_d'(\boldsymbol{\sigma}_{n,i}, a_{n,i})} \tag{3.36}$$

The convergence criterion ($r_{n,i}$) is expressed as

$$||r_{n,i}|| = ||a_{n,i+1} - a_{n,i}|| \leq \epsilon_{TOL} \tag{3.37}$$

where ϵ_{TOL} is a tolerance value. Once the increment of crack radius is obtained for each crack orientation ($\Delta(a_i)$, $\Delta(a_{\theta i})$), the increment of damage tensor $\Delta\boldsymbol{\Omega}$ can be updated as

$$\Delta\boldsymbol{\Omega} = \sum_{i=1}^{M} \frac{N}{|\Omega_r|} \Delta({a_i}^3) \overrightarrow{n_i} \otimes \overrightarrow{n_i} + \sum_{i=1}^{M} \frac{N}{|\Omega_r|} \Delta({a_{\theta i}}^3) \overrightarrow{n_{\theta_i}} \otimes \overrightarrow{n_{\theta_i}} \tag{3.38}$$

In the equation above, the variation of crack density in direction $\overrightarrow{n_i}$ accounts for the growth of cracks perpendicular to direction $\overrightarrow{n_i}$ in mode I, and for the growth of wing cracks that develop at the tips of cracks that are not perpendicular to $\overrightarrow{n_i}$. We used the

quadrature rules explained above [232] to project the vectors $\overrightarrow{n_{\theta_i}}$ on the 2×21 directions $\overrightarrow{n_i}$. Ultimately, the increment of crack density is obtained by projecting the increment of damage tensor in each of the 2×21 directions considered in the quadrature:

$$\Delta\rho_i = \overrightarrow{n_i} \cdot \Delta\boldsymbol{\Omega} \cdot \overrightarrow{n_i} \tag{3.39}$$

3.3.3 Model Calibration and Validation

The Discrete Equivalent Wing Crack based Damage (DEWCD) model depends on six constitutive parameters: the reference (initial) Young's modulus E_0, the reference (initial) Poission's ratio ν_0, the reference (initial) microcrack radius a_0, the microcrack density (Number of crack per unit volume) $\mathbb{N} = \frac{N}{|\Omega_r|}$, the initial toughness slope K_0 and the critical stress σ_c. For an intrinsically anisotropic material (i.e. with anisotropy not induced by micro-crack propagation), the model can easily be adapted by choosing different values of reference radius (a_0) for different crack orientations. The six parameters above have a sound physical meaning and can be determined by performing standard mechanical tests (e.g., uniaxial and triaxial compression tests; uniaxial tension test; Brazilian test), and microstructure characterizations (e.g. Scanning Electron Microscopy; acoustic emissions). In the following, we calibrate and validate the DEWCD model against a series of triaxial compression tests performed on North Dakota Bakken shale plugs in ConocoPhillips rock mechanics laboratory. All the samples were dry [245]. Plugs were cored from the same depth and lithology and were selected to avoid major bedding discontinuities, and were considered homogeneous. We used the stress/strain curves obtained with a confinement of 2000 psi (13.8 MPa) for calibration, and we validated the model with confinements of 1000 psi (6.9 MPa) and 3000 psi (20.7 MPa). Note that the soil mechanics sign convention was adopted (with compression counted positive).

We used the Interior Point Algorithm programmed in MATLAB to determine the unknown vector $\boldsymbol{B} = (E_0, \nu_0, a_0, \mathbb{N}, K_0, \sigma_c)$ that minimizes the squared residual of the dis-

Table 3.1: DEWCD parameters calibrated for Bakken Shale.

Elasticity		Initial State		Damage function	
E_0	ν_0	a_0	$\mathbb{N}$	K_0	σ_c
GPa	$-$	m	$1/m^3$	MPa/m	MPa
40.8	0.32	0.022	960	3.6	1×10^4

tance between experimental results y_i and numerical predictions $f_i(\boldsymbol{X}, \boldsymbol{B})$. The residual that is minimized iteratively is defined as:

$$R(\boldsymbol{B}) = \sum_{i=1}^{n} [y_i - f_i(\boldsymbol{X}, \boldsymbol{B})]^2 \tag{3.40}$$

where $\boldsymbol{X}$ stands for the vector of known input variables (e.g., strain or stress, depending whether the load is controlled in force or displacement). The algorithm was initialized with an initial guess, as well as the lower bound and the upper bound of the coefficients of the unknown parameter vector $\boldsymbol{B}$. Then, triaxial compression tests were simulated with the DEWCD model at the material point, and the value of the residual $R(\boldsymbol{B})$ was calculated based on the set of parameters obtained at the previous iteration. The gradient of the residual $R(\boldsymbol{B})$ with respect to each parameter in the vector $\boldsymbol{B}$ was calculated and used to minimize the difference between numerical and experimental stress-strain curves, as follows:

$$\boldsymbol{B}_{n+1} = \boldsymbol{B}_n - \gamma_n \Delta R(\boldsymbol{B}) \tag{3.41}$$

Where γ_n is the barrier parameter, which is updated at each iteration step in the Interior Point Algorithm. The procedure is described in detail in [246, 247].

Figure 3.6a shows the experimental stress-strain curve (green star marker) and the numerical stress-strain curve obtained after model calibration (green solid line) for a confinement of $\sigma_3 = 13.8$ MPa. Note that the calibration of the DEWCD model was based on experimental data obtained before the failure stress, because the DEWCD model does not capture the interaction and coalescence of cracks during post peak softening regime.

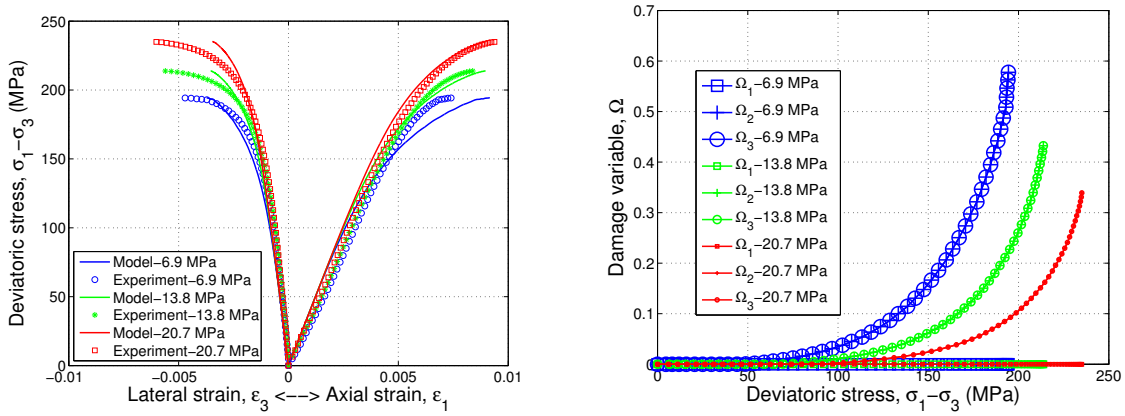

(a) Calibration and validation of DEWCD model stress/strain curves

(b) Prediction of damage with the DEWCD model

Figure 3.6: Calibration and validation of the DEWCD model parameters against experimental stress-strain curves obtained during triaxial compression tests under various confining pressures. (a) Triaxial data with a confining pressure $\sigma_3 = 13.8$MPa is used to calibrate the model. Triaxial datasets for confining pressures of $\sigma_3 = 6.9$MPa and $\sigma_3 = 20.7$MPa are employed to validate the calibration. (b) Evolution of the three principal values of the damage tensor with the calibrated parameters, for the three confining pressures.

Curves match closely except for the lateral deformation, which is underestimated by the DEWCD model for damage values higher than 10%. We interpret this discrepancy by the fact that shale is not a purely brittle material. Ductile deformation at high damage induces large lateral strains, which cannot be captured by the DEWCD model, especially for shales that contain significant amounts of clay/organic matter [102, 248]. We simulated the triaxial compression tests performed under confinements of $\sigma_3 = 6.9$ MPa (solid blue line) and $\sigma_3 = 20.7$ MPa (solid red line) using the calibrated parameters, and compared the DEWCD predictions with experimental data (blue circle markers and red square makers, respectively). Similar to the the theory of plasticity, we define the yield stress as the value of stress at which micro cracks start to propagate (damage initiation), and we define the material strength as the peak value of stress in the stress/strain curve. Figure 3.6a shows that the DEWCD model captures the increase of the yield stress σ_y with increasing confining pressure σ_3. Over 800 sampling points were used on the experimental stress/strain curves before the failure peak to assess the accuracy of the model predictions after calibra-

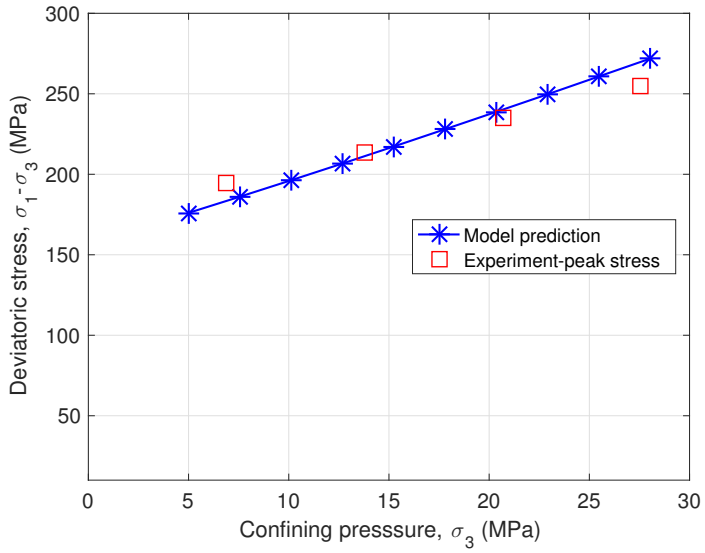

Figure 3.7: Shale compression strength under triaxial loading. Comparison of DEWCD model predictions with experimental data. Note: the peak stress is chosen as the stress value when the tangent modulus is reduced to $1/4$ of the initial value E_0.

tion. The error, defined as the distance between the numerical and experimental curves, is less than 5%, which is considered very satisfactory provided the unavoidable microstructural differences between the initial rock samples. Figure 3.6b shows the evolution of the principal values of the damage tensor for the three confining pressures considered. Micro-cracks normal to the axial direction of the compression load (x_1) are fully closed, therefore $\Omega_1 = 0$ in all tests. The lateral damage components Ω_2 and Ω_3 are induced by the opening of wing cracks at the tips of non horizontal cracks, which are subjected to local shear stresses. Lateral damage increases exponentially with deviatoric stress. As the deviatoric stress approaches the value of the peak stress noted in the stress/strain curves, the tangent to the damage evolution curve approaches infinity. Physically, this phenomenon corresponds to strong micro-crack interactions leading to crack coalescence and macroscopic discontinuities. Overall, the performance of the DEWCD model with the calibrated parameters is very satisfactory. The DEWCD model parameters calibrated for North Dakota Bakken Shale are reported in Table 3.1. Using these calibrated model parameters, we simulated triaxial compression tests under confining pressures ranging from 5 MPa to 28 MPa. We calculated the deviatoric stress at which the Young's modulus was decreased to 25% of

its initial value. As shown in Figure 3.7, the value of that threshold stress increases linearly with the confining pressure. Moreover, the variations of the threshold stress with the confining pressure match those of the compressive strength obtained experimentally. This indicates that the DEWCD allows predicting the failure (peak) stress.

3.3.4 Gauss Point Simulation

Simulation of uniaxial tension followed by compression

One of the major characteristics of brittle solids such as rocks, concrete and ceramics, is that they yield at a very low tensile stress and fail soon after yielding. Before complete failure, stiffness damaged in tension can be partially recovered in compression, due to the unilateral effects of crack closure [249]. In order to assess the performance of the DEWCD model to capture tensile failure and unilateral effects, we simulated a uniaxial tension test followed by unloading and uniaxial compression. All simulations were done in MATLAB at the material point, with the model parameters calibrated above (Table 3.1).

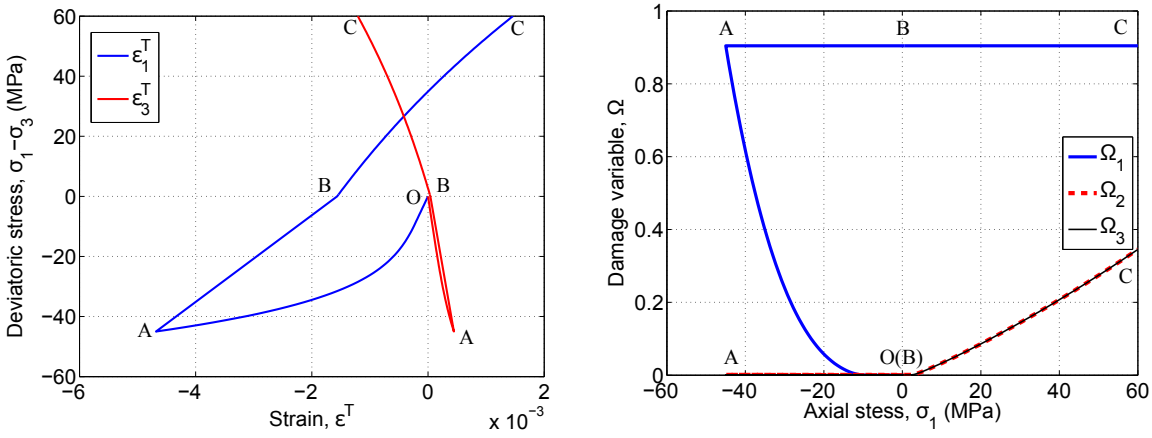

(a) Predicted stress/strain curve

(b) Simulated damage evolution

Figure 3.8: Stress-strain behavior and damage evolution predicted by the DEWCD model, for a stress path that comprises a uniaxial tension (OA), an elastic compressive unloading (AB), followed by an inelastic compressive loading (BC).

Figure 3.8 presents the stress-strain paths and damage evolution predicted with the DEWCD model. Results show that Bakken shale yields at $\sigma_y = 12$ MPa in uniaxial tension.

After yielding, the damage propagation rate is high. Large inelastic strains accumulate in the axial direction (Figure3.8a), which is unrealistic, because brittle solids subject to tensile loads tend to fail catastrophically without large deformation. That being said, crack interactions other than the occurrence of wing cracks are ignored in the DEWCD model, which is aimed to capture the damaged behavior before the peak of stress (Equation 3.16). After a certain level of damage, micro-crack interaction and coalescence cannot be neglected. In order to capture the transition between smeared and localized damage propagation, it would be more suitable to couple the DEWCD model to a model of fracture mechanics (this will be done in the next chapter of this thesis). We note that the introduction of a damage potential together with non-associate flow rules in the DEWCD model allows capturing the occurrence of residual inelastic strains after unloading. Simulation results also highlight unilateral effects induced by crack closure in compression.

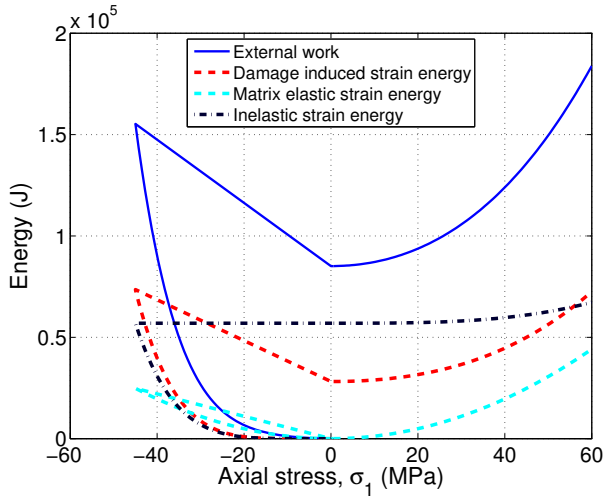

Figure 3.9: Evolution of the energy potentials during the simulation of uniaxial tension followed by unloading and compressive reloading.

Figure 3.9 shows the evolution of the energy potentials during the simulation of a uniaxial tension simulation followed by unloading and uniaxial compression. Note that at any point, the external work input equals the sum of the elastic deformation energy stored in the REV and the dissipation potentials. In the DEWCD model, elastic strain energy is stored in the matrix ("matrix elastic strain energy" in Figure 3.9) and between crack faces (displace-

ment jumps - “damage induced strain energy” in Figure 3.9), and energy is dissipated in the form of inelastic strain energy. Note that the damage-induced strain energy predicted by the DEWCD model accounts for a significant percentage of the total input work, because of the significant damage growth rate after the peak stress. In addition, the DEWCD model predicts that the compressive yield stress of the initial material is higher than that of the material that has been damaged during the uniaxial tension loading stage: the yield stress is about 50 MPa in the virgin material (Figure 3.10b), while is it only 5 MPa in the presence of tensile damage (Figure 3.8b).

Simulation of uniaxial compression cycles of increasing amplitude

The compression strength of rock-like brittle solids is usually an order of magnitude larger than the tensile strength. Requirements of thermodynamic consistency (i.e. positive dissipation potentials) and yield function differentiability make it challenging to combine two different criteria in tension and compression. Some formulations split the stress into compressive and tensile components [25, 15]; other models are based on the decomposition of strains into positive and negative parts [30]. In the DEWCD model, crack propagation in modes I and II is modeled with two mode I propagation criteria applied to two different categories of cracks (tensile crack propagation and tensile wing crack propagation). In order to assess the performance of this modeling strategy in distinguishing the yield and failure in tension and compression, we simulate a cyclic compressive loading path with the DEWCD models. Results obtained with the parameters calibrated above for Bakken shale are shown in Figure 3.10.

According to Kachanov’s calculations [42], a damage of 0.3 corresponds to the initiation of crack interactions, above which the framework of CDM is no longer valid and the REV has reached failure. Accordingly, the present simulations indicate that the uniaxial tensile strength is 30 MPa (Figure 3.8b), and the uniaxial compression strength is 180 MPa (Figure 3.10b). In addition, the yield stress predicted by the DEWCD model in uniaxial

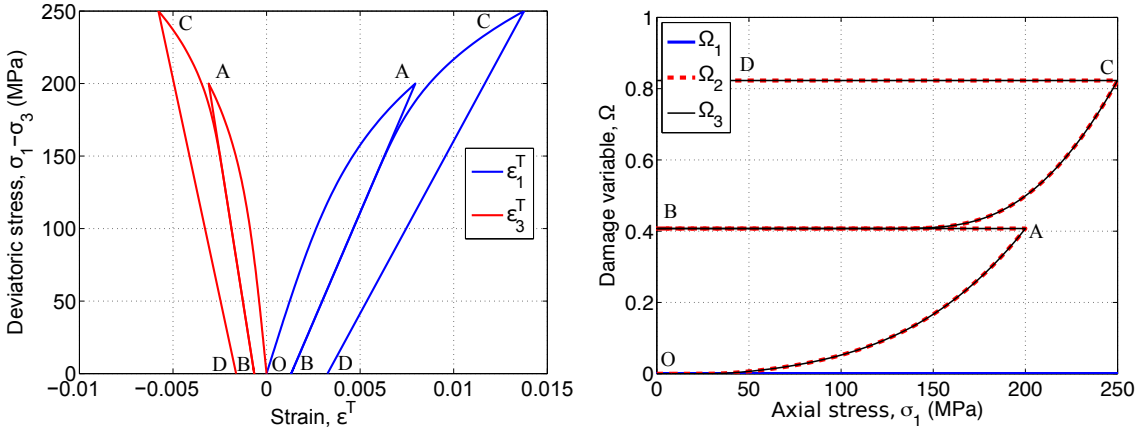

(a) Simulated stress-strain behavior (b) The evolution history of damage components

Figure 3.10: Stress-strain behavior and damage evolution predicted with the DEWCD models, for a stress path that comprises two cycles of uniaxial compression loading - elastic unloading.

compression is 50 MPa. We conclude that the DEWCD model predicts values of yield stress and strength that are in the range of values expected for a rock material like shale. It is also worth noting that the DEWCD model predicts realistic damage evolution for uniaxial compression, as the axial damage (crack planes perpendicular to the loading axis) does not propagate, and the lateral damage components grow exponentially after the yield stress is reached. In the simulations done with the DEWCD model, damage during the second loading cycle initiates at a lower stress value than the maximum stress value reached during the first cycle, which indicates that the DEWCD model can capture the hysteric effect.

3.4 Crack growth model with multiple damage surfaces

3.4.1 Thermodynamically Consistent Yield Function and Evolution Law

The wing crack growth damage model proposed in Section 3.3 provides excellent predictions at the Gauss Point, with 5 material parameters that have physical meaning. However, the projection of the crack density due to wing crack growth to the damage tensor, and the subsequent projection of the damage tensor onto the 2×21 discrete orientations, necessary to calculate the damaged stiffness tensor, makes its implementation in finite element code

challenging. In this section, we propose alternative damage criteria, and we implement them in Abaqus UMAT to carry out engineering simulations.

In the framework of thermodynamics, the damage driving force in direction i is defined as the energy release rate necessary to propagate a unit crack density in that direction. Additionally, in fracture mechanics, the energy release rate must exceed the crack resistance $R(\rho_i)$ to allow the crack boundary to grow. Thus, the most general expression for the yield surface is:

$$f_i(\rho_i, Y_i) = Y_i - R(\rho_i) \tag{3.42}$$

where $R(\rho_i)$ is the equation of the crack resistance curve, which accounts for the heterogeneities inside the material matrix and depends on the crack radius (crack density). According to Equation 3.19, the expression of the energy release rate is quadratic in deviatoric stress when the unilateral contact condition is not satisfied. However, rock samples subjected to compression tests exhibit a brittle behavior at low confining pressure and a ductile behavior at higher confining pressure. In order to capture this brittle-ductile transition, a term depending on the mean stress is added to Equation 3.42. The yield criterion adopted in the proposed model is inspired from Drucker-Prager model, and is expressed as follows:

$$f_i(\rho_i, Y_i) = Y_i - \alpha_t \mathrm{Tr}\boldsymbol{\sigma} - R(\rho_i) \tag{3.43}$$

From a mechanical point of view, the expression of the resistance curve $R(\rho_i)$ controls the hardening or softening behavior after the initial yield surface is reached. In this study, we consider that $R(\rho_i)$ is a linear function of the crack density ρ_i [47] and we emphasize that our model is only applicable for dilute distributions of micro-cracks, i.e. before crack coalescence and before the peak of strength. In addition, we distinguish the increase of open crack density in Modes I & II (when the unilateral condition is satisfied for the i^{th} microplane direction) and the increase of closed crack density in Mode II (when the unilateral

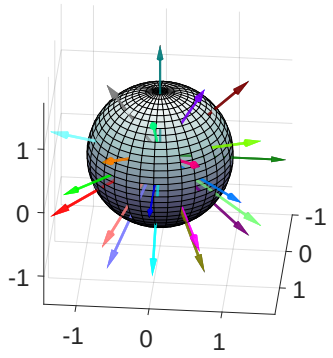

(a) Color code used for microplane orientations

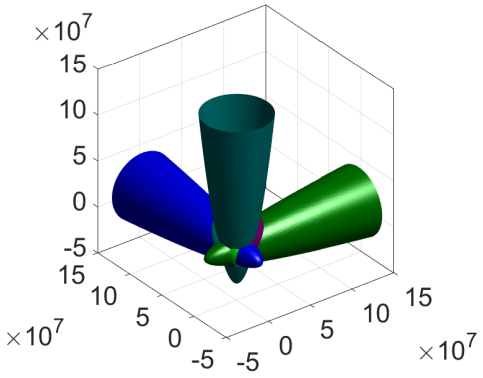

(b) Yield surfaces in stress space for closed cracks

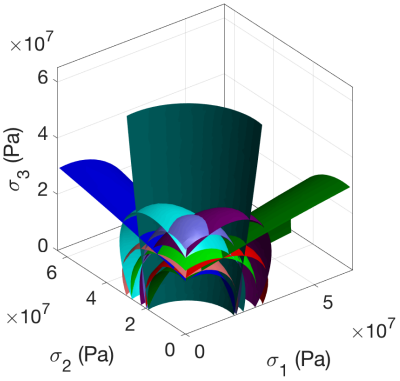

(c) Yield surfaces in compressive stress space for closed cracks

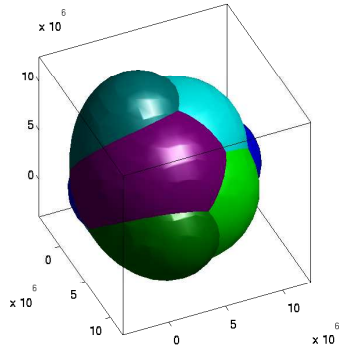

(d) Yield surfaces in stress space for open cracks

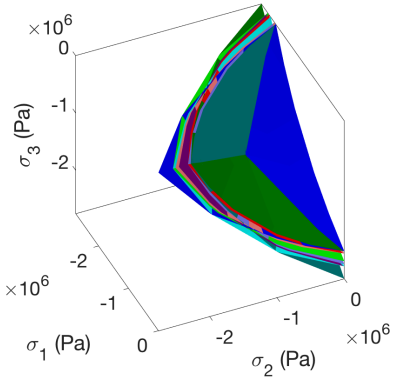

(e) Yield surfaces in tensile stress space for open cracks

Figure 3.11: Representation of crack yield surfaces in the 3D stress space, for a uniformly distributed damage density $\rho_i = 0.001$ in all microplane directions. Material parameters are $k_c = 278.9$, $\eta_c = 116.6, \alpha_t = 10^{-5}$ for closed crack families and $k_o = 35.9, \eta_o = 20.6, \alpha_t = 10^{-5}$ for open crack families. For a given state of stress, the elastic domain is the space at the intersection of all the non-smooth activated crack yield surfaces. Note the shape difference between the open crack yield surfaces and the closed crack yield surfaces, due to the expression of energy release rate Y_i.

condition is not satisfied for the i^{th} microplane direction), as follows:

$$f_i(\rho_i, Y_i) = Y_i - \alpha_t \text{Tr}\boldsymbol{\sigma} - k(1 + \eta\rho_i) \tag{3.44}$$

Where $k = k_c, \eta = \eta_c$ if cracks of the i^{th} family are closed , and $k = k_o, \eta = \eta_o$ if cracks of the i^{th} family are open. Each crack yield criterion f_i is associated with one particular crack family. The macroscopic yield surface is the boundary of the elastic domain intersected by all the activated crack yield surfaces, as shown in Figure 3.11. For each active microplane direction, the closed crack criterion is activated if the macroscopic stress projected on the crack plane is a compression, and the open crack criterion is activated if the macroscopic stress projected on the crack plane is a tension. Note that in Equation 3.44, the crack yield criterion f_i can be rewritten in the form of a function of stress and crack density only, because the energy release rate is a function of stress. As a result, the increment of crack density of an activated crack family ($f_i > 0$) can be readily calculated by means of the consistency condition under controlled stress conditions:

$$\dot{f}_i(\rho_i, Y_i) = \frac{\partial f_i}{\partial \boldsymbol{\sigma}} : \dot{\boldsymbol{\sigma}} + \frac{\partial f_i}{\partial \rho_i}\dot{\rho}_i = 0 \tag{3.45}$$

The present discrete damage model requires solving all the equations that express consistency conditions for all activated crack families simultaneously. By contrast, only one consistency condition is used in Continuum Damage Mechanics models, which limits the number of crack propagation modes considered. Figure 3.12 shows the evolution of activated crack yield surfaces during an oedometric test (with no lateral expansion). Crack yield surfaces expand independently from each other because of the crack non interaction assumption.

Inelastic strains observed after unloading are due to residual geometric incompatibilities at the crack faces, which purely depend on the damage driving forces Y_i. Microscopic crack yield criteria depend on the mean stress and not only on the damage driving forces,

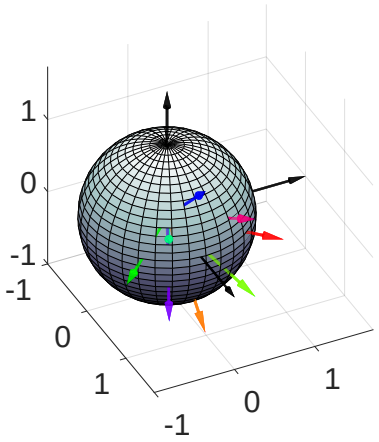

(a) Color code used for activated crack directions

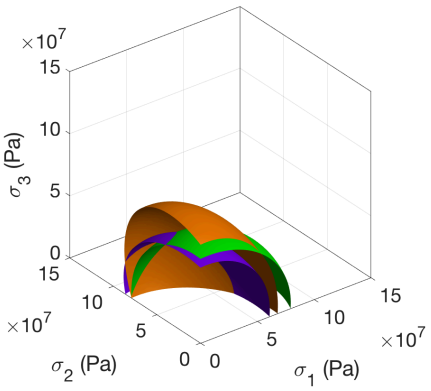

(b) Initial crack yield surfaces

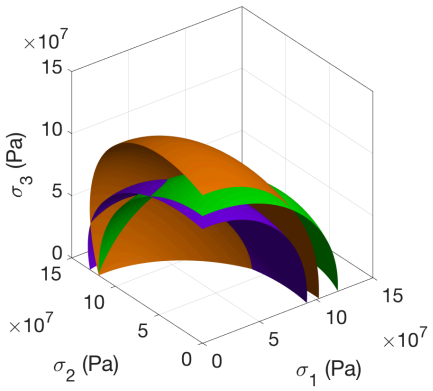

(c) Crack yield surfaces after the test

Figure 3.12: Evolution of activated yield surfaces ($i = 4-7, 18-20$) during an oedometer test (no lateral expansion). (b) Initial yield surfaces with a uniformly distributed crack density $\rho_i = 0.012$. (c) Activated yield surfaces at the end of the test: $\rho_{4-7} = 0.253$, $\rho_{18-21} = 0.300$. Note that some yield surfaces are superimposed due to symmetries.

which makes it challenging to represent the residual geometric incompatibilities that arise at crack faces after unloading. In order to overcome this limitation, we predict the evolution of inelastic strains due to these geometric incompatibilities by resorting to non-associate flow rules. We use the same discrete damage potentials as in the DEWCD model (3.31), expressed as homogeneous functions of degree one in Y_i, as follows:

$$g_i(Y_i) = Y_i - C_0 \tag{3.46}$$

Following a non-associate flow rule, the macroscopic inelastic strain increment can be computed from the damage potential, as follows:

$$\dot{\boldsymbol{\epsilon}}^{in} = \sum_{i=1}^{M} \dot{\lambda}_i \frac{\partial g_i(Y_i)}{\partial \boldsymbol{\sigma}} = \sum_{i=1}^{M} w_i \dot{\lambda}_i (c_0 \mathbb{N}_i H(\sigma^i_{nn}) + c_1 \mathbb{T}_i) : \boldsymbol{\sigma} \tag{3.47}$$

where λ_i is the Lagrange multiplier for the i^{th} crack family of normal $\overrightarrow{n_i}$. Note that the non associate flow rule for the crack density is expressed as:

$$\dot{\rho}_i = \dot{\lambda}_i \frac{\partial g_i}{\partial Y_i} = \dot{\lambda}_i. \tag{3.48}$$

Therefore, the Lagrange multiplier is equal to the increment of crack density, because plastic deformation is coupled to damage evolution.

Rate form of the proposed constitutive law: In summary, the damage criteria, the inelastic strain rate and the stress-strain relationship close the constitutive formulation. The

rate forms are expressed as:

Damage criteria:

$$f^{\alpha} = \frac{1}{2}\boldsymbol{\sigma} : \mathbb{P}_{\alpha} : \boldsymbol{\sigma} - \alpha_t \text{Tr}\boldsymbol{\sigma} - k(1 + \eta\rho^{\alpha}), \quad \alpha = 1, ..., M$$

Inelastic strain rate:

$$g_{\alpha} = \frac{1}{2}\boldsymbol{\sigma} : \mathbb{P}_{\alpha} : \boldsymbol{\sigma} - C_0$$

$$\dot{\boldsymbol{\epsilon}}^{in} = \sum_{\alpha=1}^{M} \dot{\lambda}_{\alpha} \frac{\partial g_{\alpha}}{\partial \boldsymbol{\sigma}} = \sum_{i=1}^{M} \dot{\rho}^{\alpha} \mathbb{P}_{\alpha} : \boldsymbol{\sigma}$$

Stress-strain relationship in rate form:

$$\dot{\boldsymbol{\sigma}} = \Big[\mathbb{S}^m + \sum_{\alpha=1}^{M} \rho^{\alpha} \mathbb{P}_{\alpha}\Big]^{-1} : \Big(\dot{\boldsymbol{\epsilon}} - \dot{\boldsymbol{\epsilon}}^{in}\Big) + \Big[\sum_{\alpha=1}^{M} \dot{\rho}^{\alpha} \mathbb{P}_{\alpha}\Big]^{-1} : \boldsymbol{\epsilon}^{E}$$

where we note $\mathbb{P}_{\alpha} = w_{\alpha}(c_0 \mathbb{N}_{\alpha} H(\sigma_{nn}^{\alpha}) + c_1 \mathbb{T}_{\alpha})$ for simplification. Please note that the additive strain splitting is used: $\boldsymbol{\epsilon} = \boldsymbol{\epsilon}^{E} + \boldsymbol{\epsilon}^{in}$.

3.4.2 Local Return Mapping Algorithm

Closest Point Projection

As shown in Figure 3.11, the elastic domain in the proposed discrete damage model is defined by the intersection of multiple non-smooth yield surfaces. At singular points, the normal to this macroscopic yield surface is not unique. In order to achieve the numerical implementation of the model into a UMAT subroutine in Abaqus Finite Element program, we adopt the closest point projection algorithm presented in [250]. In the following, we note Δ a variation within a load increment and δ a variation within an iteration performed during a load increment. We use the subscript n to refer to load increment, and the superscript (k) to refer to the iteration number. From the constitutive relations stated in Equation

3.4 and 3.18, we have:

$$\begin{aligned}\boldsymbol{\epsilon}^E &= \left[\mathbb{S}^m + \sum_{\alpha=1}^{M} \rho^\alpha w_\alpha (c_0 \mathbb{N}_\alpha^+ + c_1 \mathbb{T}_\alpha)\right] : \boldsymbol{\sigma} \\ \dot{\boldsymbol{\epsilon}}^{in} &= \sum_{\alpha=1}^{M} \dot{\lambda}^\alpha \partial_{\boldsymbol{\sigma}} g_\alpha(\boldsymbol{\sigma}) = \sum_{\alpha=1}^{M} \dot{\rho}^\alpha w_\alpha (c_0 \mathbb{N}_\alpha^+ + c_1 \mathbb{T}_\alpha) : \boldsymbol{\sigma}\end{aligned} \tag{3.49}$$

where $\mathbb{N}_\alpha^+ = \mathbb{N}_\alpha H(\sigma_{nn}^\alpha)$. From the discrete Kuhn Tucker conditions, we have:

$$\text{if} \quad f_{\beta,n+1}^{trial} > 0, \quad \text{for some} \quad \alpha \in (1, 2, ..., M), \tag{3.50}$$

then, it is an inelastic loading step. We define the inelasitc strain residual $\boldsymbol{R}_{n+1}$ as follows:

$$-\boldsymbol{R}_{n+1} = -\Delta\boldsymbol{\epsilon}_{n+1}^{in} + \sum_{\alpha \in \mathcal{J}_{act}} \Delta\rho_{n+1}^\alpha \partial_{\boldsymbol{\sigma}} g_{\alpha,n+1} \tag{3.51}$$

where $\mathcal{J}_{act}$ is the set of crack families that are activated. From Equation 3.51, the iterative correction is obtained as follows:

$$\delta\boldsymbol{\epsilon}_{n+1}^{in(k)} = \boldsymbol{R}_{n+1}^{(k)} + \sum_{\alpha \in \mathcal{J}_{act}} \Delta\rho_{n+1}^{\alpha(k)} \partial_{\boldsymbol{\sigma}\boldsymbol{\sigma}} g_{\alpha,n+1} \delta\boldsymbol{\sigma}_{n+1}^{(k)} + \sum_{\alpha \in \mathcal{J}_{act}} \delta\rho_{n+1}^{\alpha(k)} \partial_{\boldsymbol{\sigma}} g_{\alpha,n+1} \tag{3.52}$$

The first trial stress is given as:

$$\boldsymbol{\sigma}_{n+1}^{trial} = (\mathbb{S}^m)^{-1} : \left[\boldsymbol{\epsilon}_n + \Delta\boldsymbol{\epsilon}_{n+1} - \boldsymbol{\epsilon}_n^d - \boldsymbol{\epsilon}_n^{in}\right] \tag{3.53}$$

Thereafter, iterations are performed to satisfy the yield criteria, flow rules and stress-strain relationships. Throughout the iteration process, the given total strain increment $\Delta\boldsymbol{\epsilon}_{n+1}$ is fixed. Correspondingly, the iterative change in stress is obtained as:

$$\delta\boldsymbol{\sigma}_{n+1}^{(k)} = -(\mathbb{S}^m)^{-1} : \left[\delta\boldsymbol{\epsilon}_{n+1}^{d,(k)} + \delta\boldsymbol{\epsilon}_{n+1}^{in,(k)}\right] \tag{3.54}$$

where the iterative change of damage-induced elastic strain is given by

$$\delta\boldsymbol{\epsilon}_{n+1}^{d(k)} = \sum_{\alpha=1}^{M} \rho_{n+1}^{\alpha(0)} \mathbb{P}_\alpha : \delta\boldsymbol{\sigma}_{n+1}^{(k)} + \boldsymbol{\sigma}_{n+1}^{(k)} : \sum_{\alpha\in\mathcal{J}_{act}} \mathbb{P}_\alpha \delta\rho_{n+1}^{\alpha(k)} \tag{3.55}$$

Making use of Equation 3.52 and 3.55, Equation 3.54 is rearranged as

$$\delta\boldsymbol{\sigma}_{n+1}^{(k)} = -\mathbb{C}_c : \left[\boldsymbol{R}_{n+1}^{(k)} + \boldsymbol{\sigma}_{n+1}^{(k)} : \sum_{\alpha\in\mathcal{J}_{act}} 2\mathbb{P}_\alpha \delta\rho_{n+1}^{\alpha(k)}\right] \tag{3.56}$$

in which the consistent stiffness matrix is defined as follows:

$$\begin{aligned} \mathbb{C}_c &= \left[\mathbb{S}^m + \sum_{\alpha=1}^{M} \rho_{n+1}^{\alpha(0)} \mathbb{P}_\alpha + \sum_{\alpha\in\mathcal{J}_{act}} \Delta\rho_{n+1}^{\alpha(k)} \mathbb{P}_\alpha\right]^{-1} \\ \partial_{\boldsymbol{\sigma}} g_{\alpha,n+1} &= \mathbb{P}_\alpha : \boldsymbol{\sigma}_{n+1}^{(k)} \end{aligned} \tag{3.57}$$

By using a first order Taylor expansion to linearize the yield criteria that apply for the sets of activated crack families, we get:

$$f_{\alpha,n+1}^{(k)} + \partial_{\boldsymbol{\sigma}} f_\alpha : \delta\boldsymbol{\sigma}_{n+1}^{(k)} + \partial_{\rho^\alpha} f_\alpha \cdot \delta\rho_{n+1}^{\alpha(k)}, \quad \alpha \in \mathcal{J}_{act} \tag{3.58}$$

After substituting Equation 3.56 into the above formulae, we obtain a system of coupled equations in which the $\delta\rho_{n+1}^{\alpha}$ are the unknowns (in blue in the following equation):

$$\begin{aligned} &f_{\alpha,n+1}^{(k)} - \partial_{\boldsymbol{\sigma}} f_\alpha : \mathbb{C}_c : \boldsymbol{R}_{n+1}^{(k)} \\ &\quad = \partial_{\boldsymbol{\sigma}} f_\alpha : \mathbb{C}_c : \sum_{\beta\in\mathcal{J}_{act}} 2\partial_{\boldsymbol{\sigma}} g_{\beta,n+1} \delta\rho_{n+1}^{\beta(k)} - \partial_{\rho^\alpha} f_\alpha \cdot \delta\rho_{n+1}^{\alpha(k)} = 0, \quad \alpha \in \mathcal{J}_{act} \end{aligned} \tag{3.59}$$

For the given trial stress $\boldsymbol{\sigma}_{n+1}^{trial}$, we obtain the crack density at the current increment and at the current iteration $\delta\rho_{n+1}^{\alpha(k)}$ by solving the coupled equations for all activated orientations $\alpha \in \mathcal{J}_{act}$. Then it is possible to update the correction of stress and the inelastic strain using

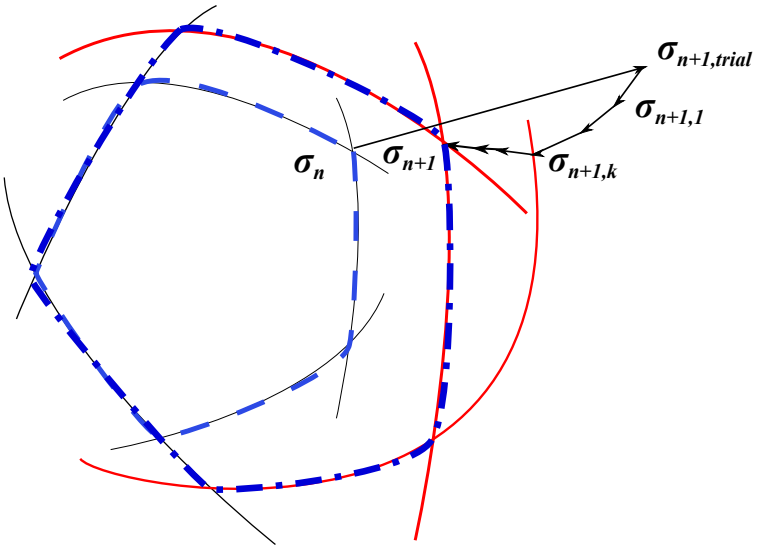

Figure 3.13: Geometrical representation of the return mapping algorithm used in this study: the Closest Point Projection Method is applied for multiple non-smooth yield surfaces.

Equation 3.56 and 3.52. The updated stress is then used to check the yield criteria as well as the inelastic strain residual. If $f_{\alpha,n+1}^{(k+1)}$ or $R_{n+1}^{(k+1)}$ exceeds the tolerance, the iterative process is continued until both the yield criteria and the residual fall below some given tolerances:

$$\begin{aligned} & f_{\alpha,n+1}^{(k+1)} < \text{TOL}_1, \quad \alpha \in \mathcal{J}_{act} \\ & ||\boldsymbol{R}_{n+1}^{(k+1)}|| < \text{TOL}_2 \end{aligned} \tag{3.60}$$

As shown in Figure 3.13, the set of activated crack families estimated from the trial stress may contain crack families that are actually non active. For a given increment of total strain, the true stress state must be at the intersection of the active yield surfaces only. In order to ensure the convergence from the trial stress to the true stress, the non-active crack families need to be eliminated from the set J_{act}. To do so, the sign of the iterative increment of crack density is checked after each iteration (in addition to checking the yield criteria): if the value of the crack density increment is negative, the corresponding crack family is removed from the activated crack set and the iteration is restarted by using the trial stress.

Algorithm to calculate tangent moduli

We use the direct solver of Abaqus UMAT, in which the iterative resolution algorithm is based on Newton-Raphson method. Consequently, we need not only to update the stress and the state internal variables, but also to calculate the Jacobian matrix at the integration point level. In this section, we derive the explicit expression of the Jacobian matrix. The differentiation operator is noted as d. Note that differentiations are done at the end of iterations for each loading increment, as explained in Table 3.2. First, we differentiate the stress strain relationship and the discrete flow rules, as follows:

$$\begin{aligned}
\mathrm{d}\boldsymbol{\epsilon}^{E}_{n+1} =& \Big[\mathbb{S}^{m}_{n+1} + \sum_{\alpha=1}^{M} \rho^{\alpha}_{n+1}\mathbb{P}_{\alpha}\Big] : \mathrm{d}\boldsymbol{\sigma}_{n+1} + \boldsymbol{\sigma}_{n+1} : \sum_{\alpha\in\mathcal{J}_{act}} \mathbb{P}_{\alpha}\mathrm{d}\rho^{\alpha}_{n+1} \\
\mathrm{d}\boldsymbol{\epsilon}^{in}_{n+1} =& \sum_{\alpha\in\mathcal{J}_{act}} \Delta\rho^{\alpha}_{n+1}\partial^{2}_{\boldsymbol{\sigma}\boldsymbol{\sigma}} g_{\alpha}(\boldsymbol{\sigma}_{n+1}) : \mathrm{d}\boldsymbol{\sigma}_{n+1} + \sum_{\alpha\in\mathcal{J}_{act}} \mathrm{d}\rho^{\alpha}_{n+1}\partial_{\boldsymbol{\sigma}} g_{\alpha}(\boldsymbol{\sigma}_{n+1}) \\
=& \sum_{\alpha\in\mathcal{J}_{act}} \Delta\rho^{\alpha}_{n+1}\mathbb{P}_{\alpha} : \mathrm{d}\boldsymbol{\sigma}_{n+1} + \sum_{\alpha\in\mathcal{J}_{act}} \mathrm{d}\rho^{\alpha}_{n+1}\mathbb{P}_{\alpha} : \boldsymbol{\sigma}_{n+1}
\end{aligned} \tag{3.61}$$

By substituting the above two equations into $\mathrm{d}\boldsymbol{\epsilon}_{n+1} = \mathrm{d}\boldsymbol{\epsilon}^{E}_{n+1} + \mathrm{d}\boldsymbol{\epsilon}^{in}_{n+1}$, we obtain the following relationship:

$$\begin{aligned}
&\mathrm{d}\boldsymbol{\epsilon}_{n+1} - \sum_{\alpha\in\mathcal{J}_{act}} \Delta\rho^{\alpha}_{n+1}\mathbb{P}_{\alpha} : \mathrm{d}\boldsymbol{\sigma}_{n+1} - \sum_{\alpha\in\mathcal{J}_{act}} \mathrm{d}\rho^{\alpha}_{n+1}\mathbb{P}_{\alpha} : \boldsymbol{\sigma}_{n+1} \\
=& \Big[\mathbb{S}^{m}_{n+1} + \sum_{\alpha=1}^{M} \rho^{\alpha}_{n+1}\mathbb{P}_{\alpha}\Big] : \mathrm{d}\boldsymbol{\sigma}_{n+1} + \boldsymbol{\sigma}_{n+1} : \sum_{\alpha\in\mathcal{J}_{act}} \mathbb{P}_{\alpha}\mathrm{d}\rho^{\alpha}_{n+1}
\end{aligned} \tag{3.62}$$

Equivalently,

$$\mathrm{d}\boldsymbol{\sigma}_{n+1} = \mathbb{C}_{hom} : \Big[\mathrm{d}\boldsymbol{\epsilon}_{n+1} - 2\sum_{\alpha\in\mathcal{J}_{act}} \mathrm{d}\rho^{\alpha}_{n+1}\mathbb{P}_{\alpha} : \boldsymbol{\sigma}_{n+1}\Big] \tag{3.63}$$

Where $\mathbb{C}_{hom}$ is the consistent modulus, expressed as

$$\mathbb{C}_{hom} = \Big[\mathbb{S}^m_{n+1} + \sum_{\alpha=1}^{M} \rho^\alpha_{n+1}\mathbb{P}_\alpha + \sum_{\alpha\in\mathcal{J}_{act}} \Delta\rho^\alpha_{n+1}\mathbb{P}_\alpha\Big]^{-1} \tag{3.64}$$

The crack density increment $\mathrm{d}\rho^\alpha_{n+1}$ is obtained from the discrete consistency condition by differentiating $f_\alpha(\boldsymbol{\sigma}_{n+1}) = 0$ for all activated orientations:

$$\partial_{\boldsymbol{\sigma}} f_\alpha : \mathrm{d}\boldsymbol{\sigma}_{n+1} + \partial_{\rho^\alpha} f_\alpha \cdot \mathrm{d}\rho^\alpha_{n+1} = 0, \quad \alpha \in \mathcal{J}_{act} \tag{3.65}$$

By substituting Equation 3.63 into Equation 3.65, we have

$$\begin{aligned}\partial_{\boldsymbol{\sigma}} f_\alpha(\boldsymbol{\sigma}_{n+1}) : \mathbb{C}_{hom} : \mathrm{d}\boldsymbol{\epsilon}_{n+1} =& \partial_{\boldsymbol{\sigma}} f_\alpha(\boldsymbol{\sigma}_{n+1}) : \mathbb{C}_{hom} : \Big[2\sum_{\beta\in\mathcal{J}_{act}} \mathrm{d}\rho^\beta_{n+1}\mathbb{P}_\beta : \boldsymbol{\sigma}_{n+1}\Big] \\ &- \partial_{\rho^\alpha} f_\alpha(\boldsymbol{\sigma}_{n+1}) \cdot \mathrm{d}\rho^\alpha_{n+1}, \quad \alpha \in \mathcal{J}_{act}\end{aligned} \tag{3.66}$$

Equivalently,

$$\mathrm{d}\rho^\alpha_{n+1} = \frac{\partial_{\boldsymbol{\sigma}} f_\alpha(\boldsymbol{\sigma}_{n+1}) : \mathbb{C}_{hom} : \mathrm{d}\boldsymbol{\epsilon}_{n+1}}{2\sum_{\beta\in\mathcal{J}_{act}} \partial_{\boldsymbol{\sigma}} f_\alpha(\boldsymbol{\sigma}_{n+1}) : \mathbb{C}_{hom} : \partial_{\boldsymbol{\sigma}} g_\beta - \partial_{\rho^\alpha} f_\alpha(\boldsymbol{\sigma}_{n+1})}, \quad \alpha \in \mathcal{J}_{act} \tag{3.67}$$

Note that the number of equations required to express the relationship between $\mathrm{d}\rho^\alpha_{n+1}$ and $\mathrm{d}\boldsymbol{\epsilon}_{n+1}$ is equal to the number of activated yield surfaces. Substituting $\mathrm{d}\rho^\alpha_{n+1}$ back into Equation 3.63 results in a stress/strain relationship that exhibits the desired tangent moduli used in the Newton-Raphson method:

$$\frac{\mathrm{d}\boldsymbol{\sigma}_{n+1}}{\mathrm{d}\boldsymbol{\epsilon}_{n+1}} = \mathbb{C}_{hom} : \Big[\boldsymbol{I} - 2\sum_{\alpha\in\mathcal{J}_{act}} \frac{\partial_{\boldsymbol{\sigma}} g_\alpha \otimes \partial_{\boldsymbol{\sigma}} f_\alpha : \mathbb{C}_{hom}}{2\sum_{\beta\in\mathcal{J}_{act}} \partial_{\boldsymbol{\sigma}} f_\alpha : \mathbb{C}_{hom} : \partial_{\boldsymbol{\sigma}} g_\beta - \partial_{\rho^\alpha} f_\alpha}\Big] \tag{3.68}$$

The steps of the return mapping algorithm including the local Closest Point Projection that we implemented in ABAQUS for multiple non-smooth yield surfaces are summarized in Table 3.2.

Table 3.2: Closest point projection algorithm for multiple non-smooth yield surfaces implemented in UMAT subroutines for the Abaqus direct solver.

Step	Description
1	Get the stored state variables $\rho_n^{\alpha}(\alpha = 1, ..., 42); \boldsymbol{\epsilon}_n^{in}; \boldsymbol{\sigma}_n$ from the previous increment n; Abaqus calculates the total strain increment $\Delta\boldsymbol{\epsilon}_{n+1}$
2	Initialize $\boldsymbol{\epsilon}_{n+1}^{in(0)} = \boldsymbol{\epsilon}_n^{in}; \quad \rho_{n+1}^{i(0)} = \rho_n^i$ $\boldsymbol{\sigma}_{n+1}^{trial} = \boldsymbol{\sigma}_n + \left[\mathbb{S}^m + \sum_{i=1}^{M} \rho_{n+1}^{i(0)} \mathbb{P}_i\right]^{-1} : \Delta\boldsymbol{\epsilon}_{n+1}$ Compute $f_{i,n+1}^{trial}(\boldsymbol{\sigma}_{n+1}^{trial}, \rho_{n+1}^{i(0)})$ for $i \in \{1, 2, ..., M\}, \quad \Delta\rho_{n+1}^{\alpha} = 0$
3	Check the yield criteria IF: $f_{i,n+1}^{trial} \leq 0$ for all $i \in \{1, 2, ..., M\}$ THEN: $(\cdot)_{n+1} = (\cdot)_{n+1}^{tr}$, EXIT ELSE: $\mathcal{J}_{act}^{(0)} = \{\alpha \in \{1, 2, ..., M\} \mid f_{i,n+1}^{trial} > 0\}, \quad \Delta\rho_{n+1}^{\alpha(0)} = 0$
4	Evaluate the inelastic residual $\boldsymbol{R}_{n+1}^{(k)}$ from Equation 3.51
5	Check the convergence of $f_{\alpha,n+1}^{(k)}(\boldsymbol{\sigma}_{n+1}^{(k)}, \rho_{n+1}^{\alpha(k-1)})$ for $\alpha \in \mathcal{J}_{act}^{(k)}$ IF: $f_{\alpha,n+1}^{(k)} <$ TOL$_1$ for all $\alpha \in \mathcal{J}_{act}^{(k)}$ and $\|\boldsymbol{R}_{n+1}^{(k)}\| <$ TOL$_2$ THEN: Provide the Jacobian matrix by using Equation 3.68 to ABAQUS, and EXIT
6	Compute the consistent stiffness matrix by using Equation 3.57. Introduce $\mathbb{C}_c$ and $\boldsymbol{R}_{n+1}^{(k)}$ in Equation 3.59.
7	Solve Equation 3.59 for $\delta\rho_{n+1}^{\alpha}, \quad \alpha \in \mathcal{J}_{act}$ Update $\Delta\rho_{n+1}^{\alpha(k+1)} = \Delta\rho_{n+1}^{\alpha(k)} + \delta\rho_{n+1}^{\alpha}$ IF: $\Delta\rho_{n+1}^{\alpha(k+1)} < 0, \quad \alpha \in \mathcal{J}_{act}^{k}$, THEN: Reset $\mathcal{J}_{act}^{(k+1)} = \{\alpha \in \mathcal{J}_{act}^{(k)} \mid \Delta\rho_{n+1}^{\alpha(k+1)} > 0\}$, Goto 4. ELSE: Calculate the inelastic strain increment correction by using Equation 3.52
8	Update state variables and compute the new trial stress $\boldsymbol{\epsilon}_{n+1}^{in(k+1)} = \boldsymbol{\epsilon}_n^{in} + \delta\boldsymbol{\epsilon}_{n+1}^{in(k+1)}$ $\rho_{n+1}^{\alpha(k+1)} = \rho_n^{\alpha} + \Delta\rho_{n+1}^{\alpha(k+1)}, \quad \alpha \in \mathcal{J}_{act}^{k}$ $\boldsymbol{\sigma}_{n+1}^{(k+1)} = \left[\mathbb{S}^m + \sum_{\alpha=1}^{M} \rho_{n+1}^{\alpha(k+1)} \mathbb{P}_{\alpha}\right]^{-1} : (\boldsymbol{\epsilon}_n + \mathrm{d}\boldsymbol{\epsilon}_{n+1} - \boldsymbol{\epsilon}_{n+1}^{in(k+1)})$ Goto 5.

Table 3.3: Material parameters used for the verification of the implementation of the algorithm.

Elasticity		Initial State		Damage function				
E_0	ν_0	a_0	$\mathcal{N}$	α	k_c	η_c	k_o	η_o
GPa	$-$	m	$1/m^3$	$-$	Pa	Pa	Pa	Pa
53.5	0.35	0.05	960	10^{-5}	278.9	116.6	35.9	20.6

3.4.3 Gauss Point Simulation - Implementation Verification

The implementation of the resolution algorithm is checked by comparing the model predictions obtained at the integration point (with a Matlab code) to those obtained with the Finite Element Method (one-element Abaqus model). For the tests performed at the integration point, we simulated pure shear in plane strain condition and confined compression (oedometer test) by applying strain loads of $\gamma_{12} = 2\%$ and $\epsilon_{11} = 2\%$ respectively. All the other strain components were set to zero. Pure shear tests were simulated with the FEM by applying a ± 0.0005m displacement along the edges of a square with sides of 1m in length. The oedometer test was simulated with the FEM by applying a -0.002m displacement in direction 1 and by using fixed boundaries on all the other faces of a cube. The cube edge length was 1m. 200 loading increments were used for all of the simulations. Table 3.3 summarizes the material parameters used for the simulations. Note that these parameters do not correspond to any specific material, although parameter values fall within the range that would be expected for a granite rock. In particular, the Young's modulus, the yield and hardening parameters represent the behavior of a rock material in tension or compression.

Figure 3.14 shows the results. For all the cases simulated, both the linear elastic response and the non-linear damaged response are well captured by the discrete damage model. The difference between the stress/strain curves obtained at the material point (Matlab) and in the one-element FEM model (Abaqus) is negligible. Note that the reason why the stress/strain curve is almost linear in the oedometer test is because the lateral pressure increases the hardening effects. Figure 3.14b shows the crack density distribution for the

oedometer test. Results show that only mode II crack propagation driven by deviatoric stress is possible. As a result, the direction normal to the activated crack planes is closer to the loading direction than the direction normal to the inactivated crack planes . Figure 3.14d shows the crack density distribution for the pure shear test. During a pure shear path, principal tension and compression components rotate by 45 degree with respect to the shear axes 1 and 2. In brittle materials, the resistance to tension is much less than the shear resistance, which explains the predominance of crack propagation in planes of normal oriented by an angle of 45 degrees to the horizontal or vertical. Note that because the Matlab simulations are done in plane strain and the Abaqus simulations are done in 3D, there is a small discrepancy between the two stress/strain curves at the later stage of the pure shear test (Figure 3.14c). We conclude that the proposed discrete damage model is suitable to track anisotropic crack density evolution and that the Closest Point Projection algorithm implemented in UMAT is accurate.

3.4.4 Engineering Applications

The proposed discrete damage model depends on 9 constitutive parameters, which can be grouped into 3 categories: elasticity, initial state, and damage (Table 3.3). The model can account for intrinsic anisotropy (i.e. with anisotropy not induced by micro-crack propagation), if different values are chosen for the reference (initial) microcrack radius (a_0) and the initial number of microcracks $\mathcal{N} = \frac{N}{\Omega_r}$ for different crack orientations. By construction of the yield criteria, two independent loading paths are needed in tension and in compression to calibrate the material parameters (depending on whether the unilateral condition is satisfied or not). If the simulation only involves compressive stress (respectively tensile stress), the two damage function parameters k_o, η_o (respectively k_c, η_c) can be omitted. We use the same procedures described in Section 3.3.3 to calibrate the model against triaxial compression and uniaxial tension tests, and employ the calibrated material parameters to carry out engineering simulations in the following.

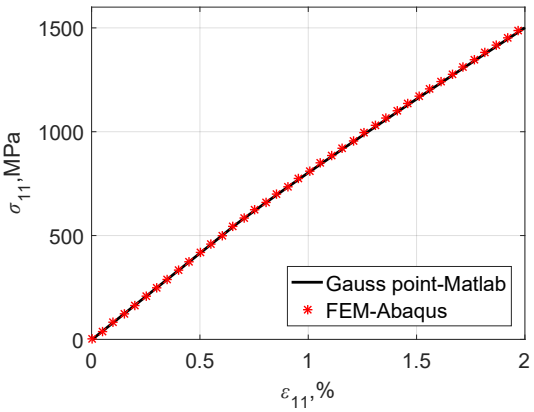

(a) Stress/strain curves - Oedometer Test

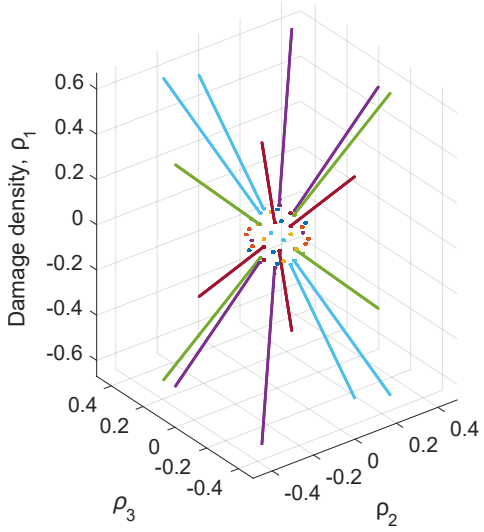

(b) Crack density Distribution - Oedometer Test

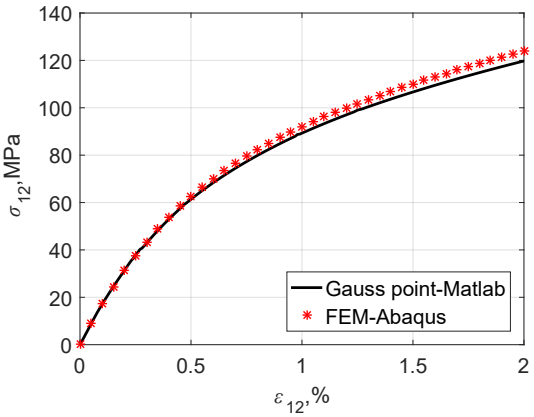

(c) Stress/strain curves - Pure Shear Test

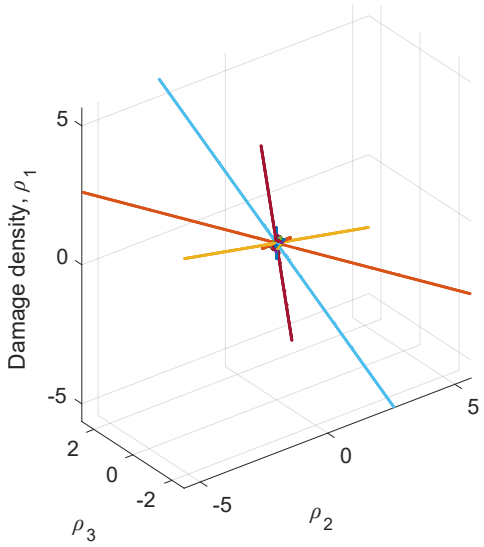

(d) Crack density Distribution - Pure Shear Test

Figure 3.14: Verification and accuracy tests. Comparison of the stress/strain curves obtained at the material point and with the FEM for an oedometer test (a) and for a pure shear test (c). The corresponding distributions of damage density are shown in Figures (b) and (d) respectively.

Table 3.4: Model parameters calibrated against triaxial compression tests reported in [251] for high strength concrete.

Elasticity		Initial State		Damage function		
E_0	ν_0	a_0	$\mathcal{N}$	α	k_c	η_c
GPa	$-$	m	$1/m^3$	$-$	Pa	Pa
53.6	0.22	2×10^{-4}	8178	3.3×10^{-5}	34.3	615.7

Triaxial compression test for concrete

We first calibrate and validate the discrete damage model against a series of triaxial compression tests performed on high strength concrete by Papanikolaou and collaborators [251]. The experimental stress/strain curves obtained with confinements of 4 and12 MPa were used for calibration. Experimental data obtained with a confining pressure of 8 MPa was used for validation. The soil mechanics sign convention was adopted (with compression counted positive). Note that only the portion of the experimental data obtained before the peak of the stress/strain curve was used, because the proposed discrete damage model is only valid for non-interacting cracks. Table 3.4 summarizes the values of the calibrated material parameters.

Figure3.15a shows the results obtained after model calibration for confining pressures of σ_3 =4, 8 and 12 MPa. The excellent match between numerical and experimental curves, especially for the test performed at 8 MPa (used for model validation) shows that the discrete damage model allows representing the non-linear behavior of concrete subject to compressive damage. Because the yield criteria depend on the mean stress via the term $\alpha \mathrm{Tr}\boldsymbol{\sigma}$, the model can capture the increase of the yield stress σ_y with increasing confining pressure σ_3, as can be seen from the evolution of the crack densities in the different directions of space in Figure 3.15b. The discrete damage model highlights the difference of crack density magnitude among the activated crack families. Overall, the performance of the discrete damage model for the calibrated parameters is very satisfactory for closed micro-crack propagation.

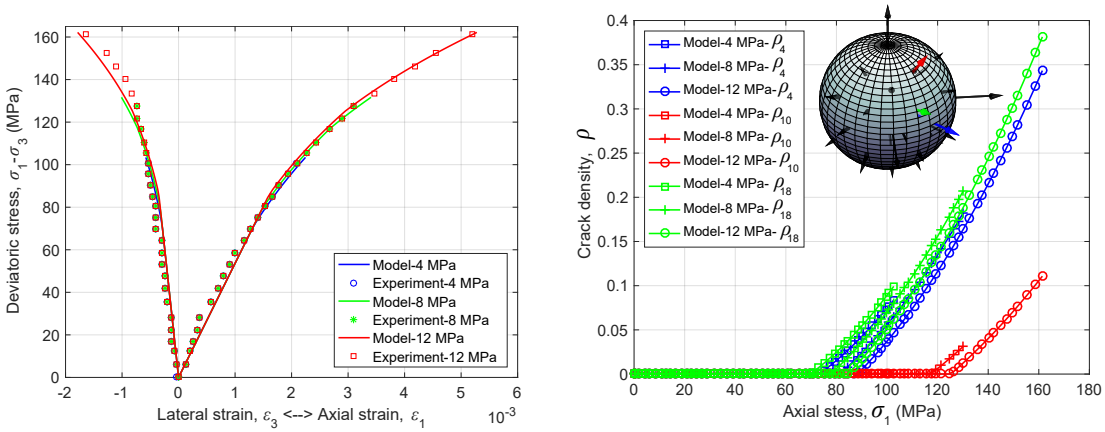

(a) Triaxial test stress-strain curves

(b) Evolution of crack densities during triaxial tests

Figure 3.15: Calibration and validation of the discrete damage model parameters against experimental stress-strain curves obtained during triaxial compression tests performed on concrete under various confining pressures. (a) Results of tests performed with a confining pressure of $\sigma_3 = 4$ and 12 MPa were used to calibrate the model. Experimental results obtained for a confining pressure of $\sigma_3 = 8$ MPa were employed to validate the calibration. (b) Evolution of the typical damage densities in different directions with the calibrated parameters, for the three confining pressures.

With the parameters calibrated above for concrete, we simulated a triaxial compression test performed under a confinement 4 MPa with the Finite Element Method (FEM). Following the standards of the American Society for Testing and Materials (ASTM), we modeled a cylindrical concrete sample of diameter 0.1 m and length 0.2 m. Due to symmetries, only $1/8$ of sample is meshed in Abaqus, as shown in Figure 3.16. In total, 4,000 hexahedral elements were used. Besides the symmetry boundary conditions, a zero horizontal displacement (in directions x_1 and x_2) was imposed at the top surface (perpendicular to x_3 axis), in order to mimic the friction effect between the steel plate and the concrete sample. After applying a 4 MPa hydrostatic confinement on all the external boundaries, the top surface was subjected to a vertical displacement of 0.0003 m. Figure 3.16 shows the crack density distribution for all activated crack families at the end of the test. By contrast with the oedometer test, the confining pressure is maintained to a constant value, therefore, more crack families are activated during the triaxial compression test. As expected, the space variations of crack density differs from one crack plane orientation to the other. Note

however that for all activated crack families, the highest crack density is reached at the edge of the sample that is in contact with the steel plate. This phenomenon is a frictional boundary effect, which explains macro fracture initiation in isotropic and homogeneous samples. It can also be noted that for all damage directions, activated cracks concentrate in the center of the sample. This result is in agreement with experimental measures of damage based on acoustic emission velocity and lateral deformation. Given that cracks of different directions are superposed, it is clear that the inner part of the sample is the most damaged during the test. The proposed discrete damage model provides a detailed description of the fabric of materials damaged in compression with only 3 damage parameters (α, k_c, η_c), 2 initial crack parameters (a_0 and $\mathcal{N}$) and 2 elasticity parameters (E_0 and ν_0). This is a significant gain of information compared to former damage models implemented in FEM, which are formulated with second-order damage tensor at most [252, 253].

Hassanzadeh's direct tension test for concrete

In most brittle materials, uniaxial tension results in a highly localized macroscopic crack propagation followed by tensile failure. The stress-strain curve recorded during uniaxial tension tests cannot truly reflect the material behavior because the strain is not uniform throughout the sample. That is the reason why Bazant and Pijaudier-Cabot [73] designed a specific testing apparatus, in which the concrete sample is glued to parallel thin-steel rods. The testing procedure allows obtaining the stress strain curve even when micro-cracks are diffused throughout the sample. We used the hardening portion of the stress/strain curves reported in [73] in order to calibrate the discrete damage model for open crack propagation modes (i.e., when the unilateral condition is satisfied). Calibration results are given in Table 3.5 and shown in Figure 3.17a, in which the soil mechanics sign convention was adopted (compression counted positive). Concrete behaves as a perfectly plastic material prior to yielding. The hardening behavior is captured, but as explained before, the post-peak behavior cannot be represented with the dilute homogenization scheme adopted here.

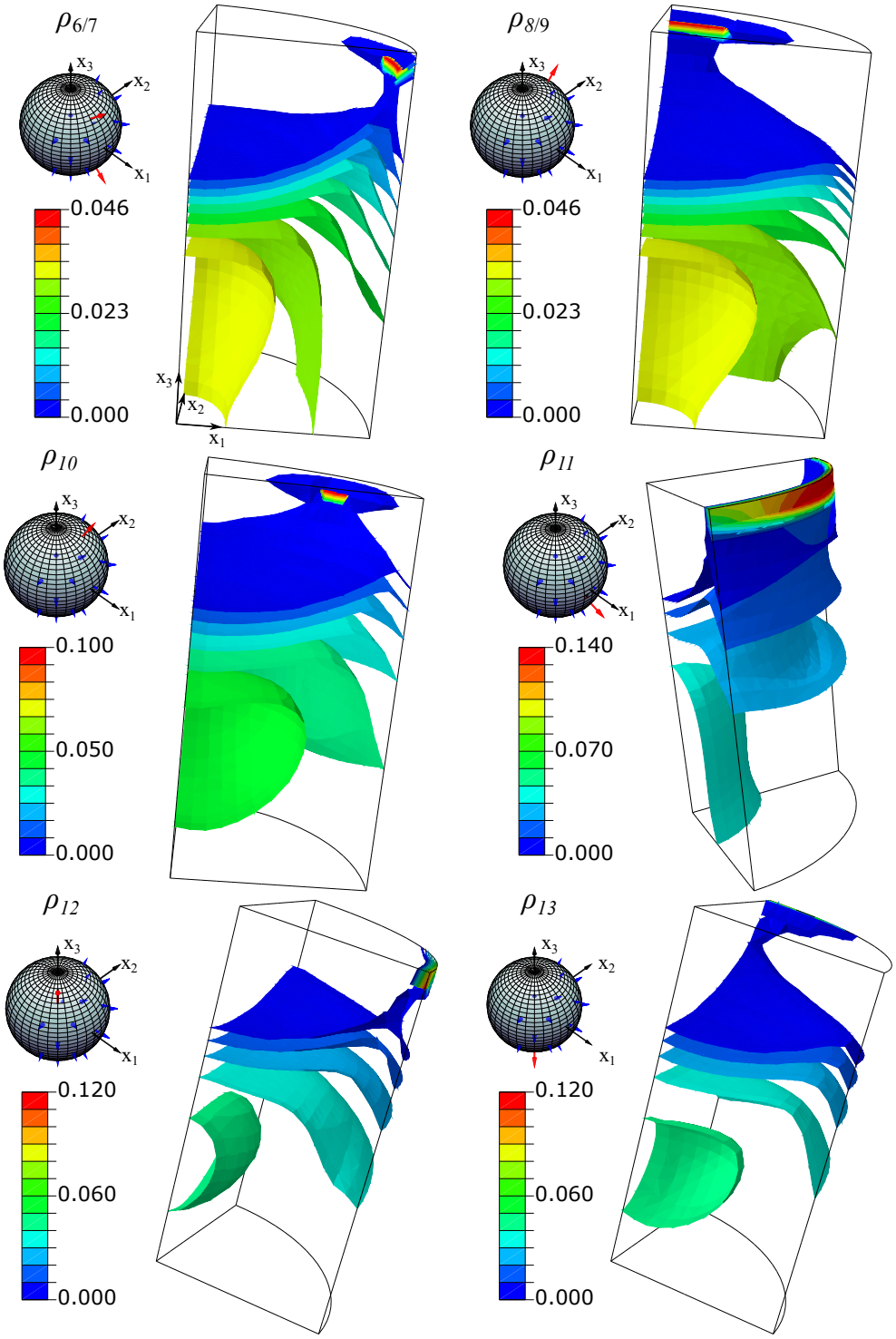

Figure 3.16: FEM simulation of a triaxial compression test performed on an ASTM concrete sample subjected to a 4 MPa confining pressure. Isosurfaces of the crack densities for the activated crack families.

Table 3.5: Model parameters calibrated against uniaxial tension tests reported in [73] for concrete.

Elasticity		Initial State		Damage function		
E_0	ν_0	a_0	$\mathcal{N}$	α	k_o	η_o
GPa	$-$	m	$1/m^3$	$-$	Pa	Pa
27.0	0.23	4.8×10^{-3}	485	0.5×10^{-5}	95.0	0.095

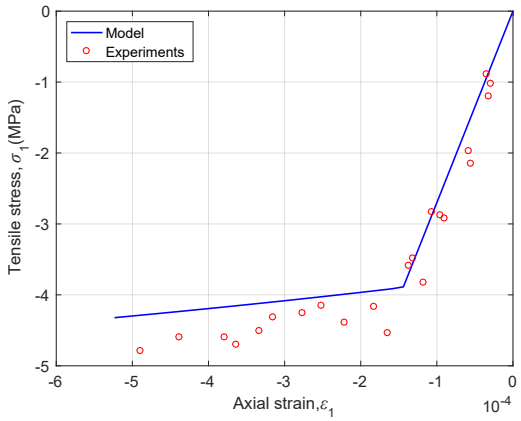

(a) Stress - strain curves - Uniaxial Tension

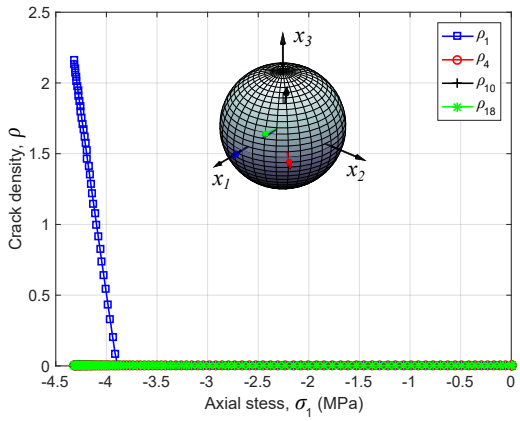

(b) Crack density evolution - Uniaxial Tension

Figure 3.17: Calibration of the discrete damage model against uniaxial tension experimental data [73] for open crack propagation.

Note that because all the cracks are initially closed, the cracks that propagate during the test are those in the planes perpendicular to the loading direction, as can be seen from the evolution of ρ_1 in Figure 3.17b.

In order to demonstrate the capability of the proposed model to predict the behavior of brittle solids in tension, we simulated Hassanzadeh's direct tension test [254]. A four-edge notched specimen was assigned the calibrated parameters listed in Table 3.5. The specimen geometry and the applied boundary conditions are shown in Figure 3.18. Due to symmetries, only $1/8$ of sample was modeled. A vertical displacement field was imposed at the bottom face of the domain ($u = 0.01$ mm). We used a coarse mesh with 9,943 3D hexahedral elements and a fine mesh with 35,550 elements.

The isosurfaces of horizontal crack density (i.e. density of crack planes perpendicular to the tensile loading axis) are shown in Figure 3.19 for both the coarse and fine meshes.

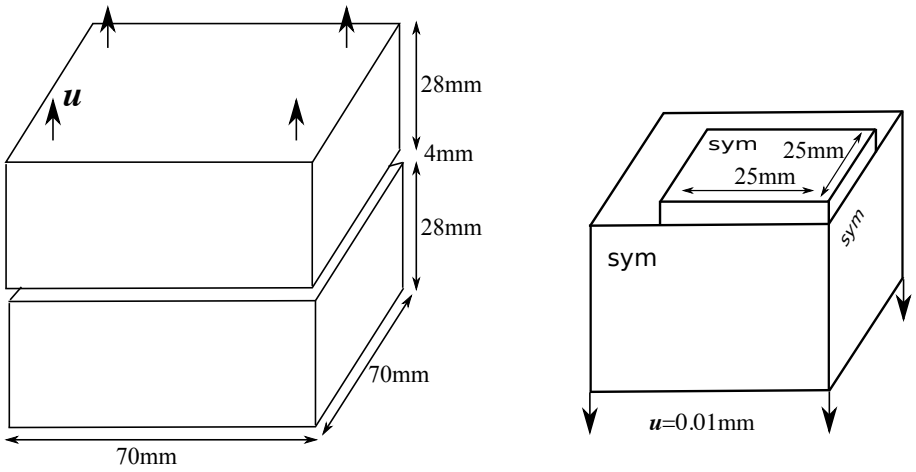

Figure 3.18: Hassanzadeh's direct tension test: problem definition, simulation domain and boundary conditions.

Of course, in this purely hypothetical simulation test the high magnitude reached by ρ_3 is not realistic: physically, a macroscopic horizontal fracture would propagate during the test, which cannot be captured by using a dilute homogenization scheme. Interestingly, results show that micro-cracks propagate from the edges to the center of the central part of the sample, which is in agreement with experimental observations. Note that the maximum crack density calculated with the coarse mesh is less than with the fine mesh, and the extent of the damaged zone is larger with the coarse mesh than with the fine mesh. To avoid this problem of mesh-dependency, a non-local discrete damage model formulation is required. Such a regularization work will be presented in the next chapter of this thesis. For both mesh densities, the extent of the damaged zone exceeded the size of a single Finite Element. In addition to the crack families perpendicular to the loading direction (x_3-axis), four crack sets were activated during the test, as shown in Figure 3.20. As expected, these four directions are the closest to the loading direction. Overall, the discrete damage model can predict micro crack propagation in tension at a very low yield stress.

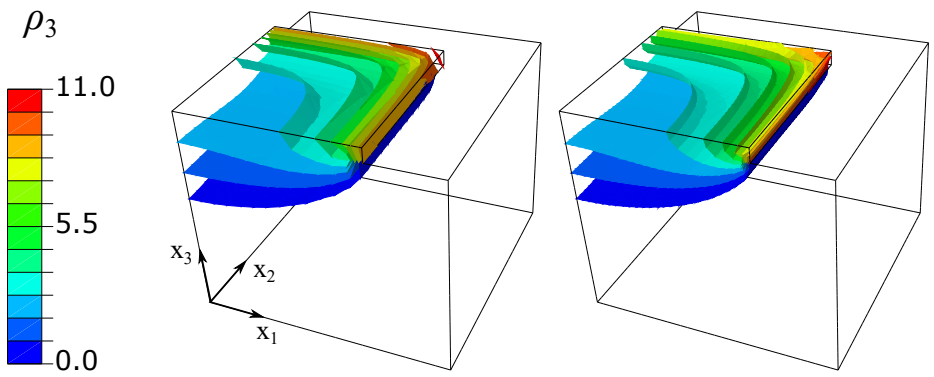

Figure 3.19: Hassanzadeh's direct tension test: Final horizontal crack density isosurfaces for the coarse (left) and fine (fine) meshes.

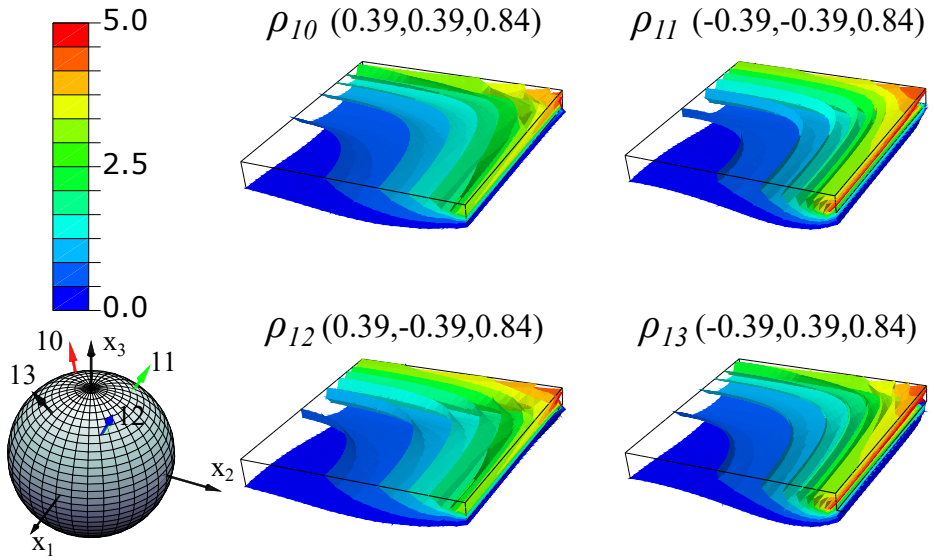

Figure 3.20: Hassanzadeh's direct tension test: Isosurfaces of damage density for non-horizontal activated crack families obtained from fine mesh results. Only the top of the sample is shown.

Table 3.6: Model parameters used in the simulation of tension tests on a fiber-reinforced composite.

Elasticity (fibers)		Elasticity (matrix)		Initial State		Damage function		
E_0	ν_0	E	ν	a_0	$\mathcal{N}$	α	k_o	η_o
GPa	$-$	GPa	$-$	m	$1/m^3$	$-$	Pa	Pa
50	0.3	35	0.25	0.001	120	2×10^{-5}	20	24

Plane stress tension test for a fiber-reinforced composite

In the following, we study the activation and propagation of crack sets in a fiber-reinforced composite subjected to a plane stress tensile test. The fibers are assumed to have a much higher tensile strength than the matrix, and are modeled as linear elastic materials. The matrix material is assigned the discrete damage model, in which only open crack propagation modes are considered. The material parameters adopted in the simulations are listed in Table 3.6. Note that the Young's modulus of the matrix material is less than that of the fibers. We compare the results obtained when fibers are either aligned or perpendicular to the direction of the applied tension to those obtained when the fibers are all oriented by an angle of 45^o to the tensile direction, as shown in Figure 3.21. Simulations were done in 3D. The elements' thickness was 0.1 m. The same boundary conditions were adopted in both cases. Hexahedral elements with an average edge size of 0.025 m were used in both cases. The mesh was structured for the simulation of tension in the axis of the fibers, and random for the simulation of tension at 45^o from the axis of the fibers (due to the complexity of the geometry). At the interface between the fibers and the matrix, nodes were tied, i.e. the two materials were perfectly bonded so that the interface friction was not considered. The composite plates were assumed to be symmetric about the horizontal and vertical axes, therefore fixed displacements were applied at the bottom and left boundaries of the domain. A displacement of 0.01 mm was applied normal to the top boundary. On the right boundary, a zero horizontal displacement and a zero vertical stress were imposed.

Figure 3.22 shows the distributions of horizontal and vertical stress for both composites.

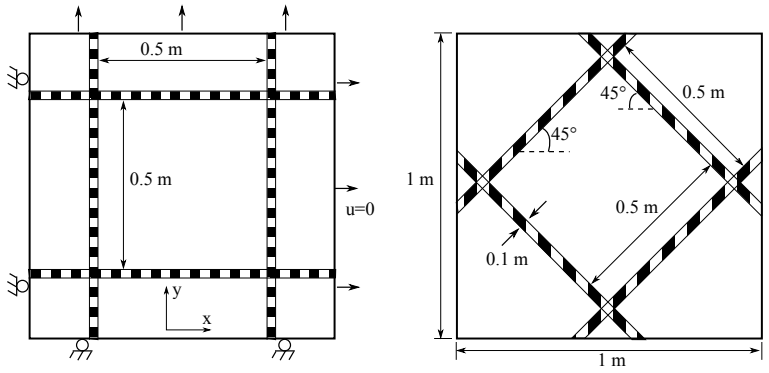

Figure 3.21: Problem definition and boundary conditions for the simulation of tension tests on a fiber-reinforced composite.

Note that results are displayed in a plane located at at mid-thickness of the plates in the x_3 direction (thickness direction). As expected, fibers bear most of the load applied due to their higher stiffness. Note that when fibers are aligned with a principal stress direction, all the stress in that direction concentrates in the fibers. For example, the vertical stress (in x_2 direction) is concentrated along the vertical fibers, and the horizontal stress (in x_1 direction) is concentrated along the horizontal fibers. When tension is applied at an angle of 45^o to the fibers, the maximum vertical stress reached in the fibers is less than in vertical fibers, and the maximum horizontal stress reached in the fibers is more than in horizontal fibers.

The effect of fiber orientation on the distribution of cracks in the matrix material is illustrated in Figure 3.23. Note the color code used to represent the families of activated crack planes: ρ_1, ρ_2 in green, ρ_4 in blue and ρ_{14} in red. The variations of ρ_4 (respectively ρ_{14}) inside the domain are similar to those of $\rho_{5,25,26}$ (respectivley $\rho_{15-17,36-39}$), due to the symmetry in crack orientations. Note that all the crack families that are activated during the test are inside the plane of x_1, x_2, or have a very small component in the direction of axis x_3. The smallest and largest of all possible values reached by the crack densities are obtained at the intersection of the inclined fiber reinforcements. Cracks also concentrate at the boundary, close to the inclined fibers. Crack densities are more uniformly distributed in the composites with non-inclined fibers. This example illustrates the benefits of accounting

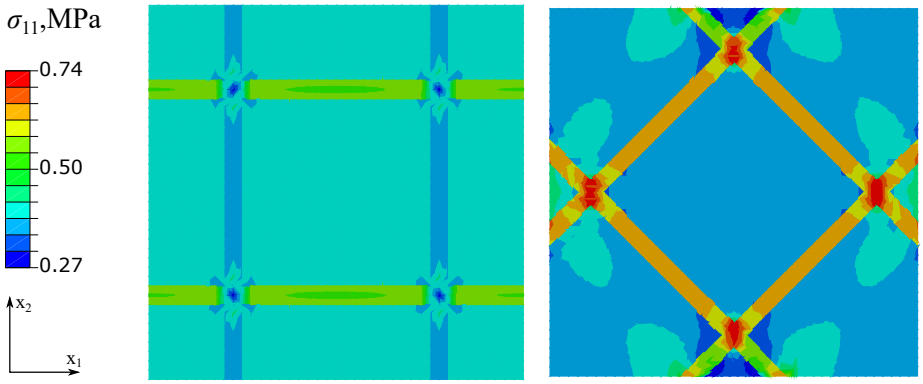

(a) Horizontal stress distribution

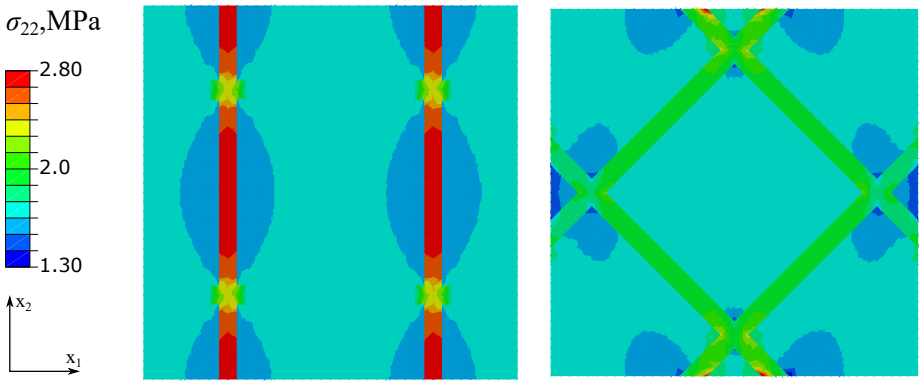

(b) Vertical stress distribution

Figure 3.22: Distribution of horizontal and vertical stress in composites with various orientations of fiber reinforcements.

for fiber orientation in the design of thin structures subjected to tension, such as the walls of pressurized vessels. In this particular case, putting fibers in the axis of the tensile load will allow reducing the load borne by the matrix material, and therefore, to reduce the density of tensile cracks. Fiber intersections are the parts of the composite plate that are the most exposed to tensile damage, and need to be checked in priority for monitoring purposes. The proposed discrete damage model thus provides useful predictions of crack patterns in brittle materials subject to mixed mode crack propagation, with a small number of material parameters which all have a sound physical meaning.

3.5 Conclusions

This chapter explains two anisotropic damage models that couple micro-mechanics and Continuum Damage Mechanics principles to study brittle materials like rocks, ceramics and concrete. We focus on the following complex features: (1) A non-linear stress/strain relationship; (2) Damage-induced anisotropy of stiffness; (3) The occurrence of irreversible strains due to volume dilation; (4) A reduction of strength after the peak stress has been reached (softening) ; (5) An apparent increase of strength and ductility in compression when the confinement increases; (6) Increasing hysteresis on unloading-reloading paths as damage increases; (7) Unilateral effects and partial recovery of stiffness in compression; (8) Different mechanical responses in tension and compression.

The DEWCD model is based on a dilute homogenization scheme, which allows summing up the energy potentials stored in the displacement jumps of crack families of 2×21 orientations to represent the energy stored at the scale of the REV. Damage at the REV scale is obtained by integrating the crack densities over all the discrete orientations. The damage yield criterion is expressed at the microscopic scale: if a crack is in tension, crack growth is controlled by a mode I fracture mechanics criterion; if a crack is in compression, the shear stress that applies at its faces is projected on the 2×21 directions considered in the numerical integration scheme, and cracks perpendicular to these projected force com-

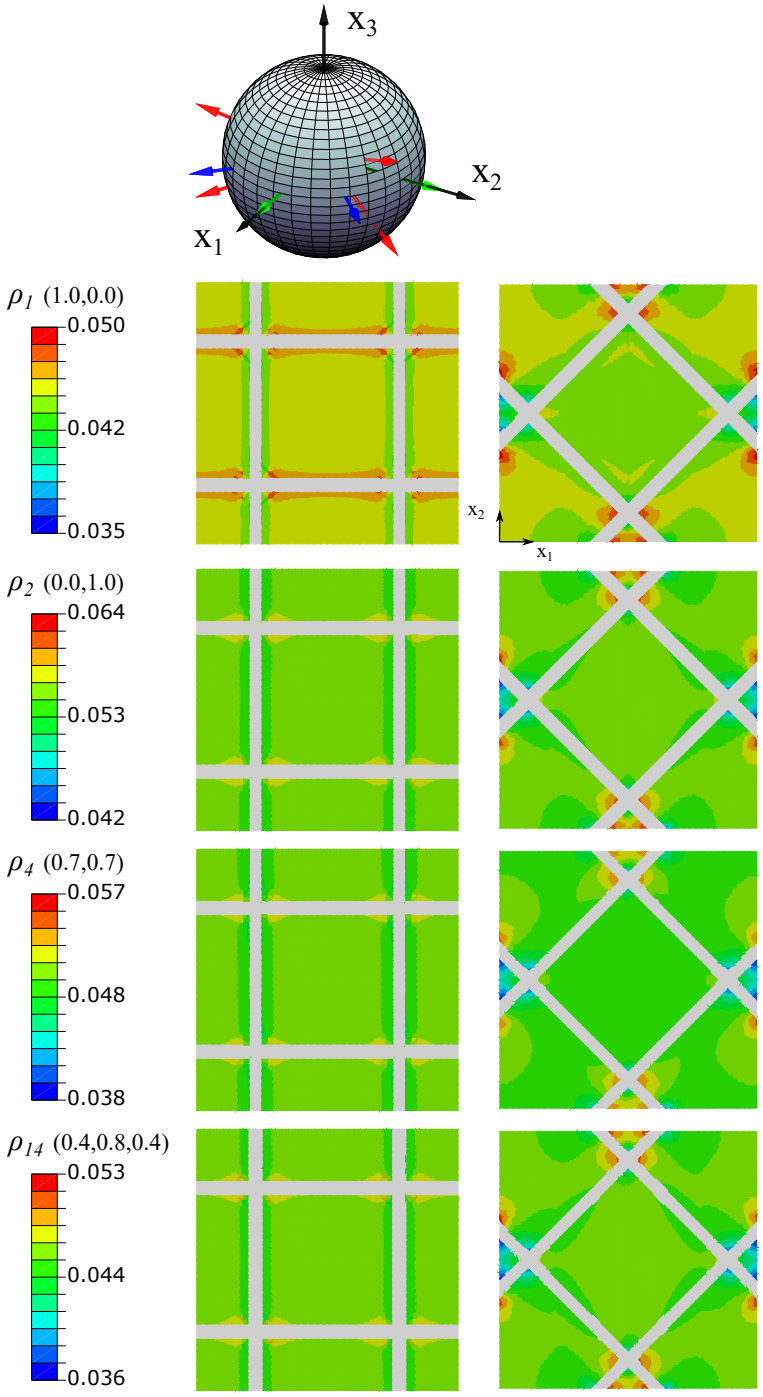

Figure 3.23: Crack density distribution for typical directions inside the base material.

ponents grow according to a mode I fracture mechanics criterion. The projection of shear stresses into a set of tensile forces allows predicting the occurrence of wing cracks at the tips of pre-existing defects subject to mode II failure. We assume that all the resulting mode I cracks do not interact. A hardening law is introduced to account for subcritical crack propagation, and non-associate flow rules are adopted for damage and irreversible strains induced by residual crack displacements after unloading.

The DEWCD model is calibrated and validated against triaxial compression tests performed on Bakken Shale in ConocoPhillips rock mechanics laboratory. With the calibrated material parameters, we simulated: (a) A uniaxial tension followed by unloading and reloading in compression; and (b) Uniaxial compression loading cycles of increasing amplitude. Results show that the DEWCD model can capture all phenomena (1)-(8) except the softening behavior (4), which characterizes the mechanical response in case of crack interaction (beyond the scope of the present study). This is a significant advancement in the theoretical modeling of rock brittle behavior, because unified models of tension and compression failure proposed so far could not distinguish properly the difference of behavior of materials in tension and compression.

In the second model, the same Gibbs energy expression as in the DEWCD model is adopted. However, damage criteria for each set of crack families are formulated in terms of thermodynamically consistent damage driving forces. Closed cracks propagate in pure mode II, whereas open cracks propagate in mixed mode (I/II), and all cracks are assumed to grow in a similar way, without wing crack development. A linear hardening law is introduced to maintain the stress on the yield surface. The latter is formed by the intersection of the yield surfaces of all the activated crack families, and it is not smooth. In order to solve for the 2×21 crack densities, a Closest Point Projection algorithm is adopted locally. The irreversible strains at the REV scale are obtained by using a Newton-Raphson algorithm.

The discrete damage model was rigorously calibrated for both compressive and tensile stress paths. Using these calibrated material parameters, we simulated triaxial compression

tests and Hassanzadeh's direct tension test for concrete, as well as a plane stress tension test for complex fiber reinforced composite. FEM results show that the model capture all phenomena (1)-(8) except the softening behavior (4) and the hysteresis behavior (6). In addition, the cracks' density, orientation and location predicted in the simulations are in agreement with experimental observations, which demonstrates that the model can be used to interpret crack patterns, design composite structures and recommend reparation techniques for structural elements subjected to multiple damage mechanisms.

CHAPTER 4
MECHANICAL MODELING OF THE TRANSITION FROM CONTINUUM DAMAGE TO DISCRETE FRACTURE

4.1 Introduction

Simulating fracture propagation in brittle materials is necessary to analyze concrete failure in civil engineering, to assess hydraulic fracturing in petroleum engineering and to model fault reactivation in geophysics. Most numerical models proposed to date do not explicitly consider the fundamental mechanism of micro crack inception and its evolution to macro fracture initiation and propagation. Continuum Damage Mechanics (CDM) models are used to predict stiffness reduction due to crack propagation: micro-cracks and macro-fractures are not explicitly represented. By contrast, in fracture mechanics models, the topology of macro-fracture paths is calculated explicitly. However, the initiation and growth of micro-cracks inside the process zone is either ignored (Linear Elastic Fracture Mechanics, LEFM) or indirectly constrained to a single surface (Cohesive Zone Model, CZM).

In this chapter, a computational framework is proposed to capture the transition of scale from micro-crack inception to macro-fracture propagation. We couple a nonlocal micromechanics based damage model with a CZM by using the eXtended Finite Element Method (XFEM). In Section 4.2, we present a CDM model in which the free enthalpy is obtained by integrating open and closed crack surface displacement jumps for a discrete set of crack orientations. We construct equivalent strains induced by open and closed cracks. Following a phenomenological approach, we formulate two criteria to predict the evolution of the damage tensor in terms of equivalent strains. An integration based nonlocal regularization is employed to alleviate mesh dependence when cracks are open. In Section 4.3, we briefly

introduce the Park-Paulino-Roesler (PPR) CZM [255] employed in this chapter to characterize the macro cohesive fracture behavior. We rigorously calibrate the critical damage value that marks the transition from diffused micro-cracks to macro-fracture, as well as the strength and energy release rate of the PPR cohesive law. Constitutive laws at both micro- and macro- scales are coupled by employing the XFEM. In Section 4.4, we derive the strong and weak forms of the governing equations, we describe the algorithm used for computing the Jacobian and the macro-fracture tip advancement and we explain the state variables mapping technique. Wedge splitting and three-point bending tests are simulated to assess the performance of the proposed framework; results are presented in Section 4.5.

4.2 Micro-scale Damage Model

4.2.1 Derivation of Energy Expression

We adopt the expression of the free enthalpy established by Shao and collaborators [256], for a REV of volume Ω_r and external boundary $\partial\Omega_r$ subjected to a uniform stress $\boldsymbol{\sigma}$. It is assumed that penny shaped microscopic cracks of various orientations are embedded in an isotropic linear elastic matrix of compliance tensor $\mathbb{S}_0$. Each microscopic crack is characterized by its normal direction $\overrightarrow{n}$ and its radius a. The macro strain of a REV that contains a single set of N microcracks oriented in planes normal to $\overrightarrow{n}$ is the sum of the elastic strain of the matrix and of the strains due to the normal and shear crack displacement jumps, as sketched in Figure 4.1. Following the same derivation procedure as in Section 3.2, the expression of the free enthalpy for a REV with a single set of N cracks is obtained as:

$$\begin{aligned} G^* =& \frac{1}{2}\boldsymbol{\sigma} : \mathbb{S}_0 : \boldsymbol{\sigma} + \frac{1}{2}c_0\rho(\overrightarrow{n}\cdot\boldsymbol{\sigma}\cdot\overrightarrow{n})\langle\overrightarrow{n}\cdot\boldsymbol{\sigma}\cdot\overrightarrow{n}\rangle^+ \\ &+ \frac{1}{2}c_1\rho[(\boldsymbol{\sigma}\cdot\boldsymbol{\sigma}) : (\overrightarrow{n}\otimes\overrightarrow{n}) - \boldsymbol{\sigma} : (\overrightarrow{n}\otimes\overrightarrow{n}\otimes\overrightarrow{n}\otimes\overrightarrow{n}) : \boldsymbol{\sigma}] \end{aligned} \tag{4.1}$$

in which we note $\langle x \rangle^+ = x, x \geq 0$, and $\langle x \rangle^+ = 0, x < 0$. Note: Equation 4.1 is the same as Equation 3.13, but we use the form of Equation 4.1 in the following derivations. The coefficient c_0 (respectively c_1) is defined as the normal (respectively shear) elastic compliance of the crack. $\rho(\overrightarrow{n})$ is the crack density, for the set of N cracks oriented in planes perpendicular to $\overrightarrow{n}$. We define:

$$c_0 = \frac{16}{3}\frac{1-\nu_0^2}{E_0}, \quad c_1 = \frac{32}{3}\frac{1-\nu_0^2}{(2-\nu_0)E_0}, \quad \rho = \frac{Na^3}{|\Omega_r|} \tag{4.2}$$

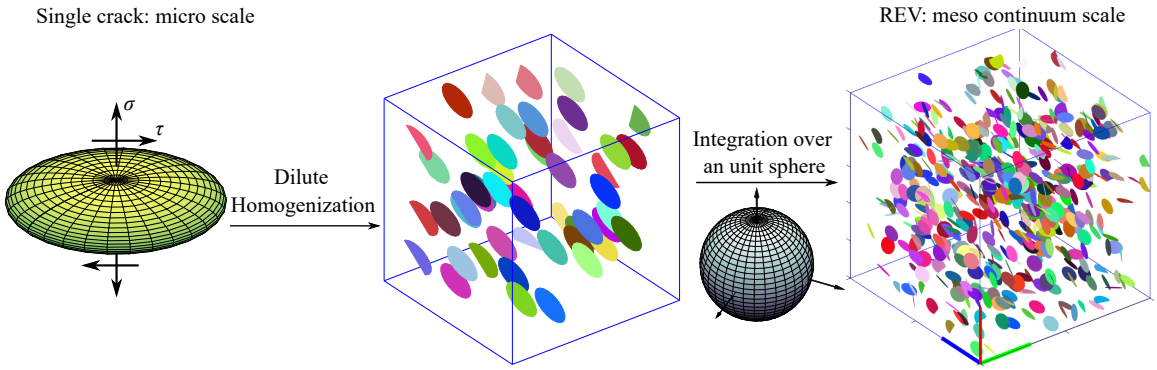

Figure 4.1: Dilute homogenization technique: from a crack to the REV.

For several crack sets of different orientations, the Gibbs free energy of the REV is obtained by integrating G^* for a distribution of crack densities $\rho(\overrightarrow{n})$, over the unit sphere $S^2 = \{\overrightarrow{n}, |\overrightarrow{n}| = 1\}$ shown in Figure 4.1, as follows:

$$\begin{aligned} G = &\frac{1}{2}\boldsymbol{\sigma} : \mathbb{S}_0 : \boldsymbol{\sigma} + \frac{1}{8\pi}\int_{S^2} \{c_0\,\rho(\overrightarrow{n})(\overrightarrow{n}\cdot\boldsymbol{\sigma}\cdot\overrightarrow{n})\langle\overrightarrow{n}\cdot\boldsymbol{\sigma}\cdot\overrightarrow{n}\rangle^+ \\ &+ c_1\,\rho(\overrightarrow{n})[(\boldsymbol{\sigma}\cdot\boldsymbol{\sigma}) : (\overrightarrow{n}\otimes\overrightarrow{n}) - \boldsymbol{\sigma} : (\overrightarrow{n}\otimes\overrightarrow{n}\otimes\overrightarrow{n}\otimes\overrightarrow{n}) : \boldsymbol{\sigma}]\}\mathrm{d}S \end{aligned} \tag{4.3}$$

At the scale of the REV, the second order crack density tensor $\boldsymbol{\rho}$ is defined in such a way that: $\rho(\overrightarrow{n}) = \overrightarrow{n}\cdot\boldsymbol{\rho}\cdot\overrightarrow{n}$. The second order damage tensor is defined as follows:

$$\boldsymbol{\Omega} = \frac{1}{4\pi}\int_{S^2}\rho(\overrightarrow{n})(\overrightarrow{n}\otimes\overrightarrow{n})\mathrm{d}S = \frac{1}{4\pi}\int_0^{2\pi}\int_0^{\pi}\rho(\overrightarrow{n})(\overrightarrow{n}\otimes\overrightarrow{n})sin\theta\mathrm{d}\phi\mathrm{d}\theta \tag{4.4}$$

It can be shown mathematically (see [257, 258] for details) that the crack density func-

tion $\rho(\overrightarrow{n})$ is related to the damage tensor as follows:

$$\rho(\overrightarrow{n}) = \frac{3}{2}(5\,\overrightarrow{n}\cdot\boldsymbol{\Omega}\cdot\overrightarrow{n} - \mathrm{Tr}\boldsymbol{\Omega}) \tag{4.5}$$

The free energy is the sum of the elastic deformation energy stored in the matrix and of the elastic energy stored in the displacement jumps across crack surfaces. Let us consider two particular cases: either all cracks are open ($\overrightarrow{n}\cdot\boldsymbol{\sigma}\cdot\overrightarrow{n} > 0$), or all cracks are closed. After introducing the relation 4.5 in the expression of Gibbs energy and integrating over the unit sphere (Equation 4.4), we obtain the macroscopic free enthalpy as a function of the second order damage tensor $\boldsymbol{\Omega}$, as follows:

$$\begin{aligned} G(\boldsymbol{\sigma},\boldsymbol{\Omega}) =& \frac{1}{2}\boldsymbol{\sigma} : \mathbb{S}_0 : \boldsymbol{\sigma} + a_1\,\mathrm{Tr}\boldsymbol{\Omega}(\mathrm{Tr}\boldsymbol{\sigma})^2 + a_2\,\mathrm{Tr}(\boldsymbol{\sigma}\cdot\boldsymbol{\sigma}\cdot\boldsymbol{\Omega}) \\ &+ a_3\,\mathrm{Tr}\boldsymbol{\sigma}\,\mathrm{Tr}(\boldsymbol{\Omega}\cdot\boldsymbol{\sigma}) + a_4\,\mathrm{Tr}\boldsymbol{\Omega}\,\mathrm{Tr}(\boldsymbol{\sigma}\cdot\boldsymbol{\sigma}) \end{aligned} \tag{4.6}$$

The four coefficients a_1, a_2, a_3 and a_4 are given as

$$a_1 = \frac{-\mu}{140}c_1, \quad a_2 = \frac{7+2\mu}{14}c_1, \quad a_3 = \frac{\mu}{14}c_1, \quad a_4 = \frac{-\mu}{70}c_1 \tag{4.7}$$

with $\mu = -\nu_0$ for open cracks and $\mu = -2$ for closed cracks. Note that the expression of the free enthalpy obtained from micro-mechanical principles in Equation 4.6 is similar to that assumed in a number of purely phenomenological models, e.g. [259, 27]. The damage driving force (energy release rate), conjugated to the damage tensor, is defined as:

$$\boldsymbol{Y} = \frac{\partial G(\boldsymbol{\sigma},\boldsymbol{\Omega})}{\partial\boldsymbol{\Omega}} = a_1\,(\mathrm{Tr}\boldsymbol{\sigma})^2\,\boldsymbol{\delta} + a_2\,\boldsymbol{\sigma}\cdot\boldsymbol{\sigma} + a_3\,\mathrm{Tr}(\boldsymbol{\sigma})\boldsymbol{\sigma} + a_4\,\mathrm{Tr}(\boldsymbol{\sigma}\cdot\boldsymbol{\sigma})\boldsymbol{\delta} \tag{4.8}$$

The isosurfaces of the principal damage driving forces defined in Equation 4.8 are plotted in the principal stress space shown in Figure 4.2. For closed cracks, the iso-contour of the principal energy release rate $Y_i, (i = 1, 2, 3)$ is symmetric with respect to the plane of

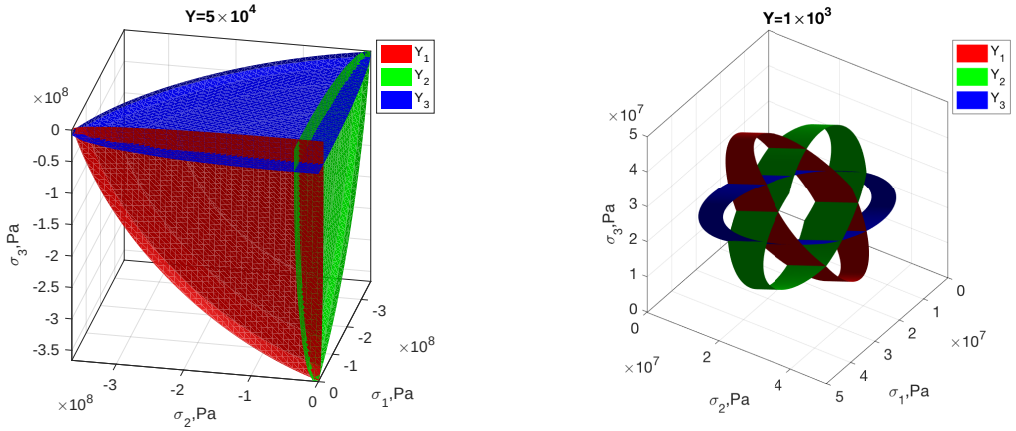

(a) Closed cracks (b) Open cracks

Figure 4.2: Damage driving force isosurfaces in the space of principal stresses.

equation $\sigma_i = 0, (i = 1, 2, 3)$. For open cracks, the iso-contours of the principal damage driving forces $Y_i, (i = 1, 2, 3)$ are cylinders with an elliptical base, in which the short axis is parallel to the principal stress axis $\sigma_i = 0, (i = 1, 2, 3)$.

The stress/strain relation is obtained by thermodynamic conjugation:

$$\begin{aligned}\boldsymbol{\epsilon} = \frac{\partial G(\boldsymbol{\sigma}, \boldsymbol{\Omega})}{\partial \boldsymbol{\sigma}} =& \frac{1+\nu_0}{E_0}\boldsymbol{\sigma} - \frac{\nu_0}{E_0}(\mathrm{Tr}\boldsymbol{\sigma})\,\boldsymbol{\delta} + 2a_1(\mathrm{Tr}\boldsymbol{\Omega}\,\mathrm{Tr}\boldsymbol{\sigma})\,\boldsymbol{\delta} + a_2(\boldsymbol{\sigma}\cdot\boldsymbol{\Omega} + \boldsymbol{\Omega}\cdot\boldsymbol{\sigma}) \\ &+ a_3[\,\mathrm{Tr}(\boldsymbol{\sigma}\cdot\boldsymbol{\Omega})\,\boldsymbol{\delta} + (\mathrm{Tr}\boldsymbol{\sigma})\,\boldsymbol{\Omega}\,] + 2a_4(\mathrm{Tr}\boldsymbol{\Omega})\,\boldsymbol{\sigma}\end{aligned} \tag{4.9}$$

4.2.2 Phenomenological Damage Criteria and Evolution Law

Because brittle solids present different behaviors in tension (open cracks) and compression (closed cracks), we formulate two damage evolution laws and utilize the volumetric strain to distinguish tensile and compressive loading. Equivalent strains for tension ($\hat{\epsilon}_t$) and compression ($\hat{\epsilon}_c$) are defined as:

$$\begin{aligned}\hat{\epsilon}_t &= \sqrt{\sum_{I=1}^{3}\langle\epsilon_I\rangle^2}, \quad \text{if } \mathrm{Tr}\boldsymbol{\epsilon} > 0 \\ \hat{\epsilon}_c &= \sqrt{\sum_{I=1}^{3}\langle e_I\rangle^2}, \quad \text{if } \mathrm{Tr}\boldsymbol{\epsilon} \le 0\end{aligned} \tag{4.10}$$

in which ϵ_I are the principal strain components and e_I are the principal deviatoric strain components calculated as $e_I = \epsilon_I - \text{Tr}\boldsymbol{\epsilon}/3$. We consider linear hardening/softening in the damage criteria:

$$\begin{aligned} f_t &= \hat{\epsilon}_t - (\kappa_t + \alpha_t \text{Tr}\boldsymbol{\Omega}) \\ f_c &= \hat{\epsilon}_c + \eta \text{Tr}\boldsymbol{\epsilon} - (\kappa_c + \alpha_c \text{Tr}\boldsymbol{\Omega}) \end{aligned} \tag{4.11}$$

The volumetric strain in the expression of the compression damage criterion allows capturing the brittle-ductile transition that occurs upon increasing confining pressure. Figure 4.3 shows the damage surfaces in plane strain conditions, with two different values of damage, for the material parameters listed in Table 4.1.

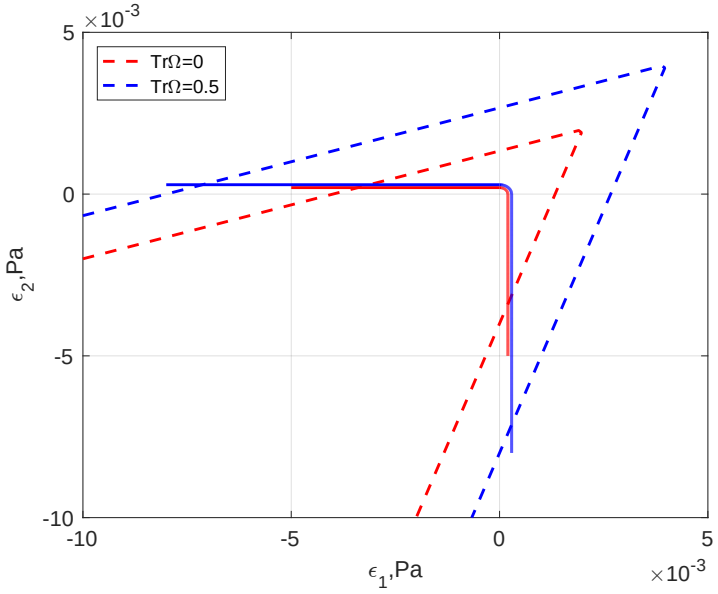

Figure 4.3: Damage surfaces at different damage levels in plane strain conditions. Dashed lines represent compressive yield surfaces; solid lines represent tensile yield surfaces.

Damage evolution laws in tension and compression are postulated so as to obtain damage patterns that conform to the observations made by Dragon and collaborators [30], as

follows:

$$\dot{\boldsymbol{\Omega}} = \dot{\lambda}_t \boldsymbol{D}_t = \dot{\lambda}_t \begin{bmatrix} \langle \epsilon_1 \rangle^2 / \hat{\epsilon}_t^2 & 0 & 0 \\ 0 & \langle \epsilon_2 \rangle^2 / \hat{\epsilon}_t^2 & 0 \\ 0 & 0 & \langle \epsilon_3 \rangle^2 / \hat{\epsilon}_t^2 \end{bmatrix}, \tag{4.12}$$

$$\dot{\boldsymbol{\Omega}} = \dot{\lambda}_c \boldsymbol{D}_c = \dot{\lambda}_c \begin{bmatrix} \langle e_1 \rangle^2 / \hat{\epsilon}_c^2 & 0 & 0 \\ 0 & \langle e_2 \rangle^2 / \hat{\epsilon}_c^2 & 0 \\ 0 & 0 & \langle e_3 \rangle^2 / \hat{\epsilon}_c^2 \end{bmatrix}. \tag{4.13}$$

in which the Lagrange multipliers $\dot{\lambda}_t$ and $\dot{\lambda}_c$ are determined from consistency conditions applied to the damage criteria (Equation 4.11). We can easily verify that a uniaxial tensile loading in direction 1 will result in cracks perpendicular to direction 1 because $\hat{\epsilon}_t = \epsilon_1 > 0$. A triaxial compression test with loading axis in direction 1 results in lateral damage (i.e. cracks perpendicular to directions 2 and 3) because $\hat{\epsilon}_c = \sqrt{2} e_2 = \sqrt{2} e_3 > 0$, even when all the strain components are negative.

For compressive loadings, we have:

$$\begin{aligned} 0 =& \frac{\partial f_c}{\partial \hat{\epsilon}_c} \mathrm{d}\hat{\epsilon}_c + \frac{\partial f_c}{\partial \mathrm{Tr}\boldsymbol{\epsilon}} \mathrm{d}(\mathrm{Tr}\boldsymbol{\epsilon}) + \frac{\partial f_c}{\partial \boldsymbol{\Omega}} : \mathrm{d}\boldsymbol{\Omega} \\ =& \dot{\hat{\epsilon}}_c + \eta \boldsymbol{\delta} : \mathrm{d}\boldsymbol{\epsilon} - \alpha_c \boldsymbol{\delta} : \dot{\boldsymbol{\Omega}} \end{aligned} \tag{4.14}$$

By substituting the compressive flow rule (Equation 4.13) into Equation 4.14, we obtain the expression of the Lagrange multiplier as:

$$\dot{\lambda}_c = \frac{\dot{\hat{\epsilon}}_c + \eta \boldsymbol{\delta} : \mathrm{d}\boldsymbol{\epsilon}}{\alpha_c} \tag{4.15}$$

Note that by construction of the flow rule (Equation 4.13), we have $\alpha_c \boldsymbol{\delta} : \dot{\boldsymbol{\Omega}} = \alpha_c \dot{\lambda}_c$. In the same way, for tensile loading, we have

$$\dot{\lambda}_t = \dot{\hat{\epsilon}}_t / \alpha_t \tag{4.16}$$

Table 4.1: Material parameters used for ploting the yield surfaces in Figure 4.3 and for performing the Gauss point simulations in Section 4.2.3.

Elasticity		Tension		Compression		
E_0/GPa	ν_0	κ_t	α_t	κ_c	α_c	η
38	0.18	2.0×10^{-4}	1.8×10^{-4}	1.0×10^{-3}	2.0×10^{-3}	0.5

According to the two consistency equations for open and closed cracks, the damage rate $\dot{\Omega}$ is always non-negative. Since the damage driving force $\boldsymbol{Y}$ is positive definite (Equation 4.8), the positivity of energy dissipation is ensured, i.e., the second law of thermodynamics is satisfied:

$$\boldsymbol{Y} : \dot{\boldsymbol{\Omega}} \geq 0 \tag{4.17}$$

4.2.3 Simulations at the Material Point

We implemented the proposed anisotropic model into ABAQUS Finite Element package, in a UMAT subroutine. We consider a cubic element, with 8 nodes and 8 Gauss points. Table 4.1 summarizes the material parameters employed. We first simulate a sequence of tensile loading, unloading, compressive loading (under zero confinement), and tensile reloading. The vertical displacement of the bottom 4 nodes is set to zero. Two orthogonal horizontal displacements are also set to zero to prevent free body movements. Positive and negative displacements are applied to the top 4 nodes to simulate tensile and compressive loading stages. Since damage evolution laws are strain based, no iterative process is needed for strain controlled tests. Note that for stress-controlled tests, governing equations have to be solved iteratively, to ensure that boundary conditions are satisfied (e.g., confining pressure). Stress, strain and damage values are averaged over the 8 Gauss points.

Figure 4.4 shows the stress-strain curve and the evolution of damage during the uniaxial tension/compression test. Initially, the material is elastic (A-B). The damage component perpendicular to the tensile loading axis grows linearly after the yield point has been reached (B), and the stress/strain curve then exhibits softening (B-C). During unload-

ing, the material responds elastically. But due to damage accumulation, the slope of the stress/strain curve is lower than initially, i.e. the material has a lower stiffness (C-D). Upon further compression (D-E), the material recovers its initial stiffness due to unilateral effects (i.e. crack closure), and responds elastically (i.e. no damage development). Then, upon reloading in tension, the stress/strain curve is first identical to that obtained during tension unloading (E-F-G). When the stress reaches the value it had at the end of the first tensile loading phase (G), a new yielding point is reached: the stress/strain curve then exhibits softening, and damage grows again (G-H). Note that here, crack density was defined from micro-mechanical principles, and can thus exceed unity.

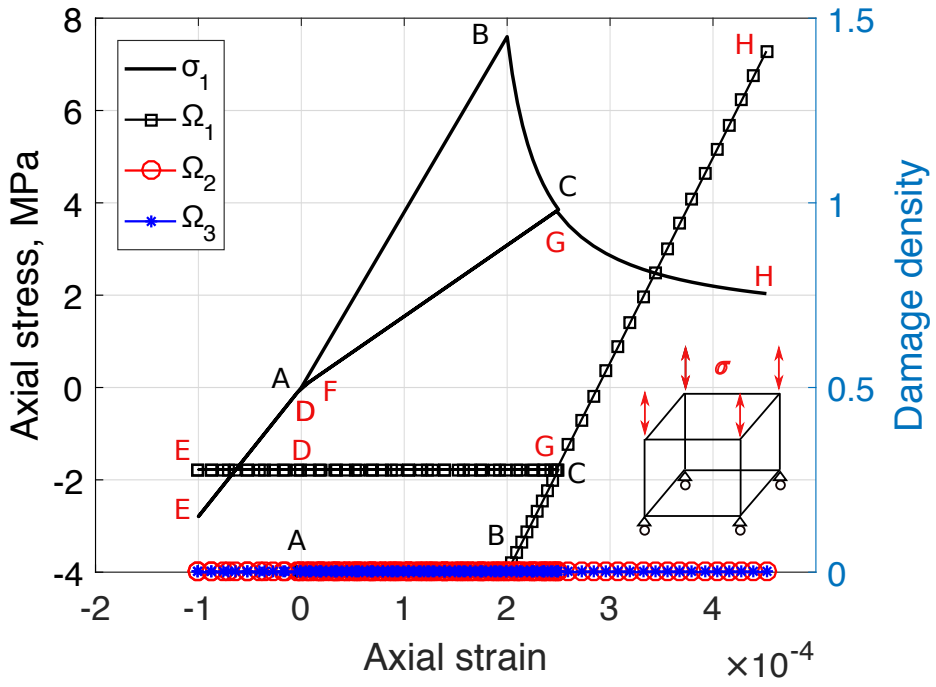

Figure 4.4: Simulation of a uniaxial tension-unloading-compression-tension loading sequence for a single element.

Next, we simulate a triaxial compression test under various confining pressures. Figure 4.5 shows the stress-strain curve and the evolution of damage components obtained for a single cubic element with 8 Gauss points. The element geometry, material parameters and boundary conditions are the same as in the previous case, except that a confining pressure

is applied on the lateral faces. A monotonic displacement-controlled compressive load is applied until damage components grow to some extent. For all confining pressures considered, triaxial compression resulted in lateral damage (i.e. crack planes containing the loading axis). The dependence of damage development on the confining pressure is captured by the model: in the simulations presented here, the yield stress is higher under 5 MPa confinement than under 0 MPa confinement. By examining the results of the uniaxial compression test in Figure 4.5 and of those of the uniaxial tension test in Figure 4.4, we note that tensile softening and compressive hardening are captured. In addition, a difference of up to one order magnitude exists between tensile and compressive yield stresses, which is conform to experimental observations made on quasi-brittle materials.

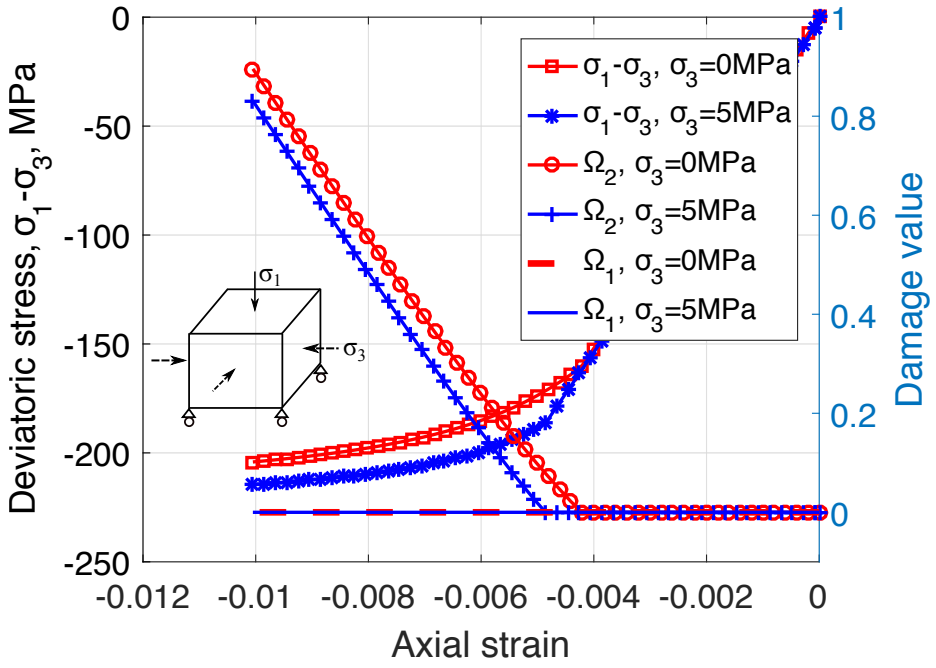

Figure 4.5: Simulation of triaxial compression tests under various confining pressures for a single element.

4.2.4 Nonlocal Regularization

As illustrated in Figure 4.4, the initiation and propagation of mode I cracks leads to strain softening, which makes the associated boundary value problem ill-posed. Numerically, the

tensile failure path development is mesh dependent. The energy that needs to be released to create a unit surface of tensile fracture does not converge upon mesh refinement. This is inconsistent with experimental observations, since the energy release rate is found to be material-specific [75]. To regularize the damage model formulated in section 4.2.1 and 4.2.2, we use an integration-based non-local technique [67]: the evolution of the damage variables at a material point does not only depend on the stress and strain at that point, but also on the field variables within an influence domain surrounding that point. The size of the nonlocal influence domain is controlled by a characteristic internal length, which is a material parameter usually equal to 2 to 3 times the maximum size of grains encountered in a polycrystal [73]. In order to account for the non-local nature of damage, we replaced the equivalent strains that control damage evolution (Equation 4.10) by their weighted average defined on an influence domain V, as follows:

$$\hat{\epsilon}_i^{nl}(\boldsymbol{x}) = \int_V \alpha(\boldsymbol{x}, \boldsymbol{\xi}) \hat{\epsilon}_i(\boldsymbol{\xi}) \mathbf{d}V(\boldsymbol{\xi}), \quad (i = t,\, c) \tag{4.18}$$

where $\boldsymbol{x}$ is the position vector of the material point considered, and $\boldsymbol{\xi}$ is the position vector of points in the influence domain of $\boldsymbol{x}$. $\alpha(\boldsymbol{x}, \boldsymbol{\xi})$ is the nonlocal weight function, which decreases monotonically as the distance $r = \|\boldsymbol{x} - \boldsymbol{\xi}\|$ increases. Note that if field variables are uniform, the value of damage should be uniform. Hence the non-local value of the equivalent strains should be equal to the local value of equivalent strains in the uniform strain field. This implies that weight functions should satisfy the partition of unity:

$$\int_V \alpha(\boldsymbol{x}, \boldsymbol{\xi}) \mathbf{d}V(\boldsymbol{\xi}) = 1 \tag{4.19}$$

In order to satisfy the property of partition of unity, the weight functions usually take the following general form:

$$\alpha(\boldsymbol{x}, \boldsymbol{\xi}) = \frac{\alpha_0(\boldsymbol{x}, \boldsymbol{\xi})}{\int_V \alpha_0(\boldsymbol{x}, \boldsymbol{\xi}) \mathbf{d}V(\boldsymbol{\xi})} = \frac{\alpha_0(\boldsymbol{x}, \boldsymbol{\xi})}{V_r(\boldsymbol{x})} \tag{4.20}$$

where $V_r(\boldsymbol{x})$ is the so-called characteristic volume. The exact form of the weight function $\alpha_0(\boldsymbol{x}, \boldsymbol{\xi})$ depends on the material considered. The Gauss function (normal distribution) and the bell-shaped function are the most widely used weight functions for isotropic media. Here, we adopt the bell-shaped function, expressed as:

$$\alpha_0(\boldsymbol{x}, \boldsymbol{\xi}) = \left\langle 1 - \frac{\|\boldsymbol{x} - \boldsymbol{\xi}\|^2}{l_c^2} \right\rangle^2. \tag{4.21}$$

in which l_c is the characteristic length. The advantage of the bell-shaped function is that the nonlocal influence zone only depends on l_c: no cut-off is needed to ensure that the weight function is zero outside of the influence zone, as shown in Figure 4.6.

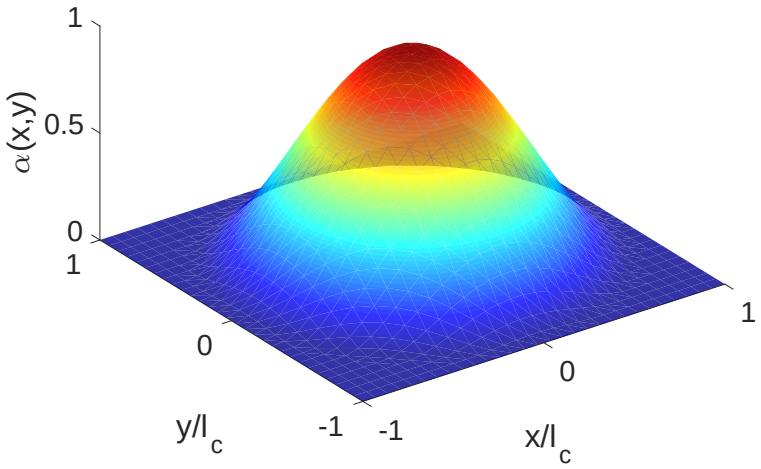

Figure 4.6: Bell-shaped nonlocal weight function with $l_c = 0.02$.

In the Finite Element Method (FEM), nonlocal variables are calculated as the weighted average of local variables obtained iteratively at the Gauss points located in the influence zone [69, 260]. For instance, the nonlocal equivalent strain for $i = t, c$ is expressed as:

$$\hat{\epsilon}_i^{nl}(\boldsymbol{x}) = \frac{\sum_{j=1}^{N_{GP}} \alpha_0(\|\boldsymbol{x} - \boldsymbol{\xi}_j\|)\hat{\epsilon}_i(\boldsymbol{\xi}_j)\Delta V_j}{\sum_{j=1}^{N_{GP}} \alpha_0(\|\boldsymbol{x} - \boldsymbol{\xi}_j\|)\Delta V_j} \tag{4.22}$$

where N_{GP} the total number of Gauss points inside the influence zone of material point $\boldsymbol{x}$.

ΔV_j is the integration volume associated with the $j-th$ Gauss point.

4.3 Coupling Cohesive Fracture Propagation with Continuum Damage Zone Evolution

4.3.1 Critical Damage Threshold Calibration

The constitutive model proposed in Section 4.2, based on dilute homogenization, can predict accurate macro-scale stress-strain behavior with micro-scale crack density, as long as crack interactions can be neglected. Crack interaction is followed by crack coalescence and macro-fracture formation. Macro-scale fracture propagation is governed by Fracture Mechanics; models based on the concept of stress-intensity factor, energy release rate, Crack Tip Opening Displacement (CTOD) or Crack Mouth Opening Displacement (CMOD). In this chapter, a CZM is adopted to capture the softening induced by the separation of macro-fracture surfaces. We start by calibrating the critical damage (i.e., crack density) which marks the transition betweem continuum damage propagation and macro-fracture formation. To this aim, we calculate the damaged Young's modulus of a 2D REV that contains one set of parallel equally sized cracks, by using two methods: first, the proposed continuum damage model, which does not account for micro-crack interaction; second, Kachanov's micro-mechanical model [261], which accounts for micro-crack interaction. The critical damage value is defined as the level of damage above which the predictions of damaged elatic stiffness differ in the two models. Details are provided below.

In the 2D micro-mechanical damage model proposed by Kachanov, the stress and strain fields in a linear elastic plate containing N cracks subjected to the stress $\boldsymbol{\sigma}^{\infty}$ at infinity are calculated as those in a plate subjected to zero far field stress and containing N loaded micro-cracks. The faces of each micro-crack $(i = 1, ..., N)$ are subjected to the traction $\boldsymbol{t}_i^0 = \boldsymbol{n}_i \cdot \boldsymbol{\sigma}^{\infty}$, in which $\boldsymbol{n}_i$ is the unit vector normal to the faces of the $i-th$ crack. According to the superposition theory for elastic media, this problem can be solved by considering N plates containing only one crack subjected to the traction $\boldsymbol{t}_i$ $(i = 1, ..., N)$, defined as the

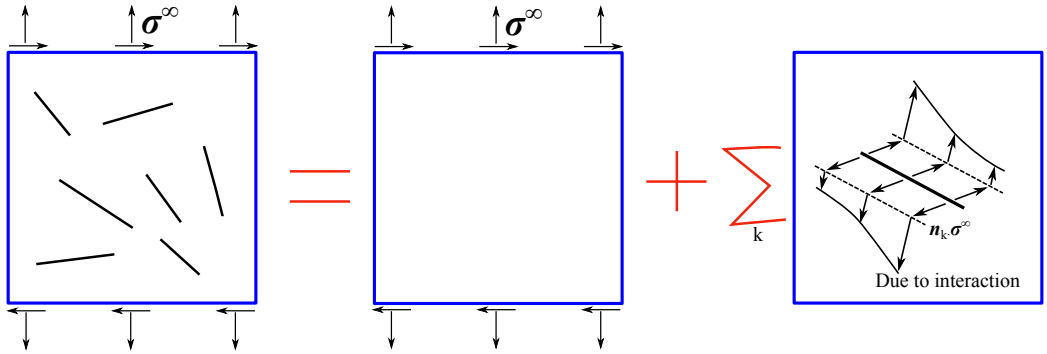

Figure 4.7: Crack interaction model in Kachanov's theory.

sum of $\boldsymbol{t}_i^0$ and the additional tractions due to stress interactions with the other micro-cracks. The superposition method is illustrated in Figure 4.7. The tractions can be determined by solving a system of integral equations, as follows [261]:

$$\boldsymbol{t}_i(\zeta_i) = \boldsymbol{t}_i^0 + \boldsymbol{n}_i \cdot \sum_{j \neq i} \int_{-l_j}^{l_j} \boldsymbol{\sigma}_j^n(\zeta_i, \zeta_j)[\boldsymbol{n}_j \cdot \boldsymbol{t}_j(\zeta_j)] + \boldsymbol{\sigma}_j^\tau(\zeta_i, \zeta_j)[\boldsymbol{\tau}_j \cdot \boldsymbol{t}_j(\zeta_j)] d\zeta_j \qquad (4.23)$$

in which l_j is the half length of the $j-th$ crack and $\boldsymbol{\tau}_j$ is the unit vector that is tangential to the faces of the $j-th$ crack. $\boldsymbol{\sigma}_j^n(\zeta_i, \zeta_j)$ (respectively $\boldsymbol{\sigma}_j^\tau(\zeta_i, \zeta_j)$) is the stress tensor at the current point ζ_i on the $i-th$ crack, generated by a pair of equal and opposite unit forces located at point ζ_j along the normal (respectively tangential) direction of the $j-th$ crack. Following the approximation proposed and validated by Kachanov [261], we consider that the stress applied at the $i-th$ crack is that due to the traction applied at infinity and the average tractions along the faces of the $j-th$ cracks. In other words, we assume that the stress at ζ_j is not sensitive to the deviations of $\boldsymbol{t}_j(\zeta_j)$ from the average $\langle \boldsymbol{t}_j \rangle$. This allows transforming equation 4.23 into:

$$\boldsymbol{t}_i(\zeta_i) = \boldsymbol{t}_i^0 + \langle \boldsymbol{n}_j \cdot \boldsymbol{t}_j(\zeta_j) \rangle \, \boldsymbol{n}_i \cdot \sum_{j \neq i} \overline{\boldsymbol{\sigma}}_{\boldsymbol{j}}^{\boldsymbol{n}}(\zeta_i) + \langle \boldsymbol{\tau}_j \cdot \boldsymbol{t}_j(\zeta_j) \rangle \, \boldsymbol{n}_i \cdot \sum_{j \neq i} \overline{\boldsymbol{\sigma}}_{\boldsymbol{j}}^{\boldsymbol{\tau}}(\zeta_i) \qquad (4.24)$$

in which:

$$\begin{aligned}
\langle \boldsymbol{n}_j \cdot \boldsymbol{t}_j(\zeta_j) \rangle &= \int_{-l_j}^{l_j} \boldsymbol{n}_j \cdot \boldsymbol{t}_j(\zeta_j) d\zeta_j \\
\langle \boldsymbol{\tau}_j \cdot \boldsymbol{t}_j(\zeta_j) \rangle &= \int_{-l_j}^{l_j} \boldsymbol{\tau}_j \cdot \boldsymbol{t}_j(\zeta_j) d\zeta_j \\
\overline{\boldsymbol{\sigma}}_{\boldsymbol{j}}^{\boldsymbol{n}}(\zeta_i) &= \int_{-l_j}^{l_j} \boldsymbol{\sigma}_j^n(\zeta_i, \zeta_j) d\zeta_j \\
\overline{\boldsymbol{\sigma}}_{\boldsymbol{j}}^{\boldsymbol{\tau}}(\zeta_i) &= \int_{-l_j}^{l_j} \boldsymbol{\sigma}_j^\tau(\zeta_i, \zeta_j) d\zeta_j
\end{aligned} \tag{4.25}$$

$\overline{\boldsymbol{\sigma}}_{\boldsymbol{j}}^{\boldsymbol{n}}(\zeta_i)$ is the stress generated at point ζ_i due to a uniform tensile load of unit intensity applied in the direction normal to the faces of the $j-th$ crack. Noting $x = \tau_j$ and $y = n_j$, we have [261]:

$$\begin{aligned}
\sigma_{xx}^n &= I_2 - 8y^2 I_4 + 8y^4 I_6 \\
\sigma_{xy}^n &= 2(-yI_3 + xyI_4 + 4y^3 I_5 - 4xy^3 I_6) \\
\sigma_{yy}^n &= I_2 + 4y^2 I_4 - 8y^4 I_6
\end{aligned} \tag{4.26}$$

Note that in the last of the above equations, we corrected a typo in the equations presented in [261]. $\overline{\boldsymbol{\sigma}}_{\boldsymbol{j}}^{\boldsymbol{\tau}}(\zeta_i)$ is the stress generated at point ζ_i due to a uniform tensile load of unit intensity applied in the direction tangential to the faces of the $j-th$ crack. Noting $x = \tau_j$ and $y = n_j$, we have [261]:

$$\begin{aligned}
\sigma_{xx} &= 2(3yI_3 - 3xyI_4 - 4y^3 I_5 + 4xy^3 I_6) \\
\sigma_{xy} &= I_2 - 8y^2 I_4 + 8y^4 I_6 \\
\sigma_{yy} &= 2(-3yI_3 + xyI_4 + 4y^3 I_5 - 4xy^3 I_6)
\end{aligned} \tag{4.27}$$

in which:

$$I_1 = 4l^3 \frac{\sqrt{\gamma}-\sqrt{\alpha}}{\sqrt{\delta}(\sqrt{\alpha}+\sqrt{\gamma}+\sqrt{\delta})^2}$$

$$I_2 = 4l^2 \frac{1}{\sqrt{\delta}(\sqrt{\alpha}+\sqrt{\gamma}+\sqrt{\delta})}$$

$$I_3 = 2l^3 \frac{\sqrt{\gamma}-\sqrt{\alpha}}{(\alpha\gamma)^{1/2}\delta^{3/2}}$$

$$I_4 = 2l^2 \frac{\sqrt{\gamma}+\sqrt{\alpha}}{(\alpha\gamma)^{1/2}\delta^{3/2}}$$

$$I_5 = \frac{l^3}{2} \frac{3\sqrt{\alpha\gamma}(\sqrt{\gamma}+\sqrt{\alpha})^2(\sqrt{\gamma}-\sqrt{\alpha})+\delta(\gamma^{3/2}-\alpha^{3/2})}{(\alpha\gamma)^{3/2}\delta^{5/2}}$$

$$I_6 = \frac{l^2}{2} \frac{3\sqrt{\alpha\gamma}(\sqrt{\gamma}+\sqrt{\alpha})^3+\delta(\gamma^{3/2}+\alpha^{3/2})}{(\alpha\gamma)^{3/2}\delta^{5/2}}$$

$$\alpha = (x-l)^2 + y^2$$

$$\beta = 2(x^2 + y^2 - l^2)$$

$$\gamma = (x+l)^2 + y^2$$

$$\delta = \beta + 2\sqrt{\alpha\gamma}$$

Equations 4.23 allow solving for the tractions $\boldsymbol{t}_i(\zeta_i)$. The average relative displacement vector $< \boldsymbol{b}_i >$ across the faces of the $i-th$ crack is found by superposing the displacements due to punctual tractions at each point of the $i-th$ crack faces [261]:

$$< \boldsymbol{b}_i >= \frac{4l_i}{E_0} \int_{-l_i}^{l_i} \boldsymbol{t}_i(\zeta_i)[1-(\zeta_i/l_i)^2]^{1/2} d\zeta_i \tag{4.28}$$

in which E_0 is the Young's modulus of the matrix (bounding material) between the cracks. The fourth order effective compliance tensor $\mathbb{S}^{eff}$ is used to relate the average strain $< \boldsymbol{\epsilon} >$ to the applied far field stress $\boldsymbol{\sigma}^\infty$ over a representative area A:

$$< \boldsymbol{\epsilon} >= \mathbb{S}^{eff} : \boldsymbol{\sigma}^\infty = \mathbb{S}^0 : \boldsymbol{\sigma}^\infty + \frac{1}{2A} \sum_{i=1}^{N} \int_{-l_i}^{l_i} [\boldsymbol{n}_i(\zeta_i)\boldsymbol{b}_i(\zeta_i) + \boldsymbol{b}_i(\zeta_i)\boldsymbol{n}_i(\zeta_i)] d\zeta_i \tag{4.29}$$

where $\mathbb{S}^0$ is elastic compliance tensor without cracks, and $\boldsymbol{n}_i(\zeta_i)$ is the unit vector normal to the $i-th$ crack face at point ζ_i. We consider flat cracks, for which $\boldsymbol{n}_i(\zeta_i)$ is a constant. Equation 4.29 thus becomes:

$$< \boldsymbol{\epsilon} >= \mathbb{S}^0 : \boldsymbol{\sigma}^\infty + \frac{l_i}{A} \sum_{i=1}^{N} [\boldsymbol{n}_i < \boldsymbol{b}_i > + < \boldsymbol{b}_i > \boldsymbol{n}_i] \tag{4.30}$$

The expressions of the stress distributions that are involved in the integral terms of Equations 4.23 and 4.28 are very complex, which makes it challenging to obtain the exact solution of the traction and displacement distributions along each crack face. To overcome this problem, several approximation methods were proposed [261, 42, 262, 263]. In the following, we adopt Kachanov's approximation method [261], in which Equation 4.28 is written as follows:

$$< \boldsymbol{b}_i >= \frac{\pi\, l_i}{E_0} < \boldsymbol{t}_i > \tag{4.31}$$

where $< \boldsymbol{t}_i >$ is the mean traction field that applies to the $i-th$ crack.

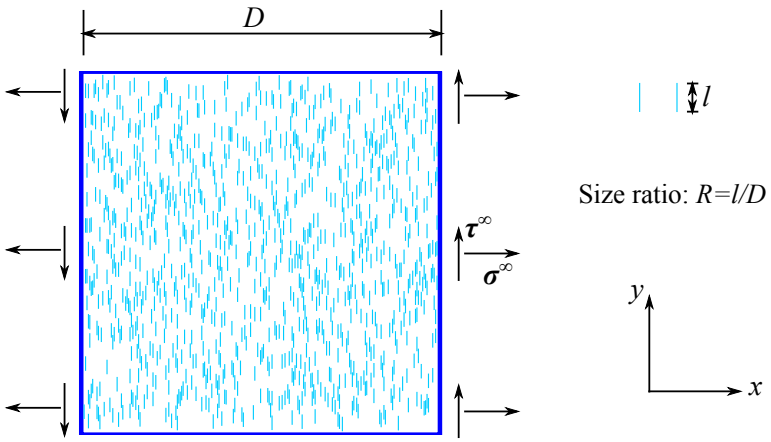

Figure 4.8: Random crack pattern adopted to calculate the reduction of stiffness due to damage in the proposed CDM model and in Kachanov's theory.

In the following, we consider a 2D REV that contains cracks perpendicular to the x-axis, and we calculate the Young's modulus in the x-direction. We randomly populate the crack centers inside the REV as shown Figure 4.8. The crack density in Kachanov's model ρ is defined by Equation 4.2, like in the continuum model. But since the problem solved here is in 2D, the crack surface area and the REV volume are replaced by the crack length and the REV area, respectively. As a result:

$$\rho = \frac{1}{A}\sum_{i=1}^{N} l_i^2 \tag{4.32}$$

In the present case, because all the cracks are perpendicular to the x-axis, the elastic

moduli are affected by the crack density (ρ) in Kachanov's model, and by the $xx-$ component of the damage tensor (Ω_{xx}) in the continuum damage model. We simulated a simple tensile test at the material point with the continuum model. The effective Young's modulus along the x-direction (solid black line in Figure 4.9) was obtained from the compliance tensor, as follows:

$$\mathbb{S} = \frac{\partial^2 G(\boldsymbol{\sigma}, \boldsymbol{\Omega})}{\partial \boldsymbol{\sigma}^2} \tag{4.33}$$

where G is Gibbs free energy expressed in Equation 4.6. We calculated the damaged elastic tensor with Kachanov's model for several values of crack density, by either increasing the number of cracks in the REV with a fixed crack length (crack initiation), or by increasing the length of a fixed number of cracks in the REV (crack propagation). Note that in all simulations, the centers of the cracks were randomly distributed inside the REV, with non-overlap and non-intersection constraints. To ensure that the domain of size D remained a REV, we used a ratio $R = l/D$ of $1/25$.

Figure 4.9 shows the evolution of effective modulus E_{xx}^{eff} as the crack density (damage) in the x-axis increases, for two different initial moduli. It is worth noting that the value of the damaged Young's modulus only depends on crack density - and not on the type of damage growth (crack initiation vs. crack propagation). Since the free energy expression (Equation 4.6) is calculated from a dilute homogenization scheme, the effective modulus predicted by the continuum model (solid black line) coincides with that predicted by Kachanov's model (markers & red dashed line) until crack density exceeds $\Omega_{xx}^{eff} = \rho_x = 0.2$. When crack density exceeds 0.2, the modulus degradation rate predicted by Kachanov's theory is lower than in the CDM model, because of stress shadow effects (due to crack interactions). Moreover, the point that marks the divergence between the two models does not depend on the initial modulus used for calculation (case 1 vs. case 2). In summary, $\Omega_{crit} = 0.2$ is the limit value above which the interaction between micro cracks

cannot be ignored: it marks the transition from diffused micro-scale cracks to concentrated macro-fracture.

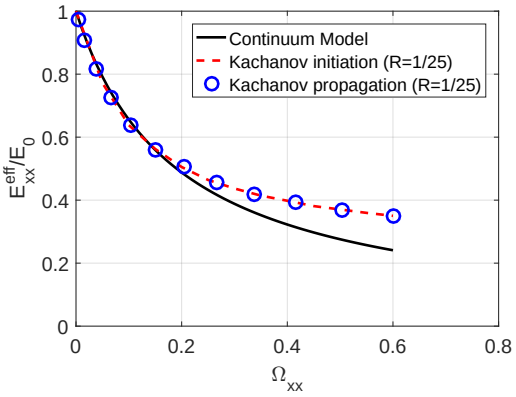

(a) Case 1: $E_0 = 25.2GPa, \nu_0 = 0.2$

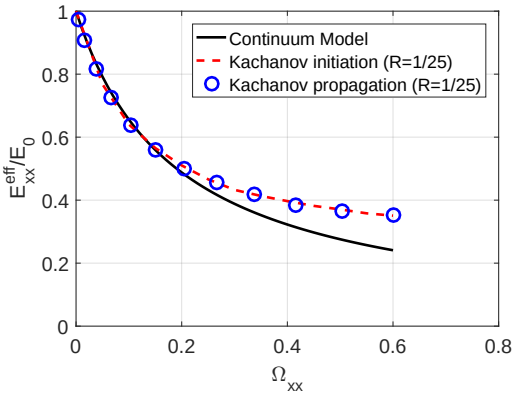

(b) Case 2: $E_0 = 50GPa, \nu_0 = 0.2$

Figure 4.9: Damaged Youngs' modulus calculated with the continuum model and with Kachanov's micro-mechanical model for a set of cracks perpendicular to the x-axis.

4.3.2 Macro-scale Cohesive Zone Model: PPR

Above the critical damage threshold $\Omega_{crit} = 0.2$,a macro-fracture segment needs to be inserted in the FEM model. We use a CZM governed by a traction-separation law to represent the macro fracture. In this chapter, we list the main equations of the potential based Park-Paulino-Roesler (PPR) [255] cohesive model, adopted here.

In [255], Park and collaborators constructed a unified potential so as to meet the following requirements: (i) Complete normal and shear failure are reached when normal or tangential separation reaches a maximum value; (ii) The traction rate is equal to zero when the traction is equal to the cohesive strength; (iii) The energy release rate is equal to the area enclosed by the traction-separation curve. The expression of the potential is

$$\begin{aligned}\Psi(\Delta_n, \Delta_t) = &\min(\phi_n, \phi_t) + \left[\Gamma_n\left(1 - \frac{\Delta_n}{\delta_n}\right)^{\alpha}\left(\frac{m}{\alpha} + \frac{\Delta_n}{\delta_n}\right)^{m} + \langle\phi_n - \phi_t\rangle\right] \\ &\times \left[\Gamma_t\left(1 - \frac{|\Delta_t|}{\delta_t}\right)^{\beta}\left(\frac{n}{\beta} + \frac{|\Delta_t|}{\delta_t}\right)^{n} + \langle\phi_t - \phi_n\rangle\right].\end{aligned} \tag{4.34}$$

where Δ_n and Δ_t (respectively δ_n and δ_t) stand for the separations in the normal and shear

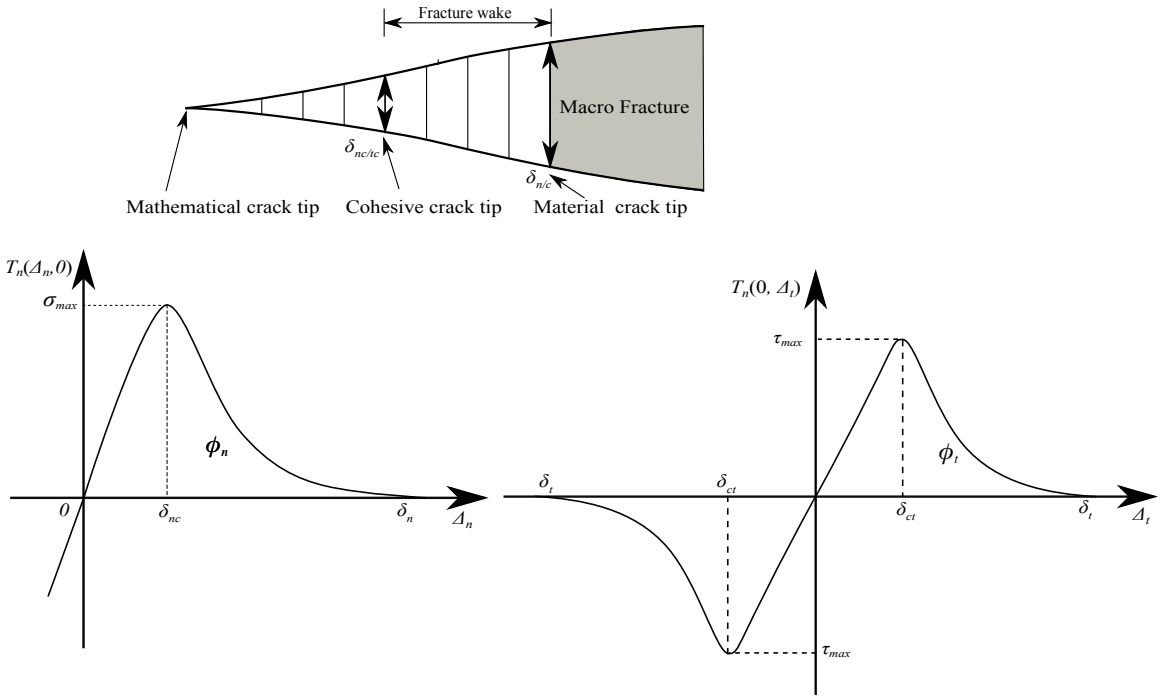

Figure 4.10: PPR cohesive model of macro-fracture propagation.

directions at the current time (respectively, at failure) as shown in Figure 4.10. ϕ_n (respectively ϕ_t) is the mode I (respectively, mode II) cohesive energy release rate. α and β are the shape factors that control the concave or convex nature of the softening curve. The mechanical response of brittle materials is best represented by power law softening equations or bilinear softening laws [264]. Accordingly, we use $\alpha = \beta = 4$, which allows representing concave shaped softening curves with a power law. The traction vector (T_n, T_t) is obtained directly from the derivative of the potential in Equation 4.34:

$$
\begin{aligned}
T_n(\Delta_n, \Delta_t) =& \frac{\Gamma_n}{\delta_n}\Big[m\Big(1-\frac{\Delta_n}{\delta_n}\Big)^{\alpha}\Big(\frac{m}{\alpha}+\frac{\Delta_n}{\delta_n}\Big)^{m-1} - \alpha\Big(1-\frac{\Delta_n}{\delta_n}\Big)^{\alpha-1}\Big(\frac{m}{\alpha}+\frac{\Delta_n}{\delta_n}\Big)^{m}\Big] \\
& \times \Big[\Gamma_t\Big(1-\frac{|\Delta_t|}{\delta_t}\Big)^{\beta}\Big(\frac{n}{\beta}+\frac{|\Delta_t|}{\delta_t}\Big)^{n} + \langle\phi_t-\phi_n\rangle\Big] \\
T_t(\Delta_n, \Delta_t) =& \frac{\Gamma_t}{\delta_t}\Big[n\Big(1-\frac{|\Delta_t|}{\delta_t}\Big)^{\beta}\Big(\frac{n}{\beta}+\frac{|\Delta_t|}{\delta_t}\Big)^{n-1} - \beta\Big(1-\frac{|\Delta_t|}{\delta_t}\Big)^{\beta-1}\Big(\frac{n}{\beta}+\frac{|\Delta_t|}{\delta_t}\Big)^{n}\Big] \\
& \times \Big[\Gamma_n\Big(1-\frac{\Delta_n}{\delta_n}\Big)^{\alpha}\Big(\frac{m}{\alpha}+\frac{\Delta_n}{\delta_n}\Big)^{m} + \langle\phi_n-\phi_t\rangle\Big]\frac{\Delta_t}{|\Delta_t|}
\end{aligned}
\tag{4.35}
$$

where Γ_n and Γ_t are energy constants, related to ϕ_n and ϕ_t as follows:

$$\Gamma_n = (-\phi_n)^{\langle \phi_n - \phi_t \rangle / (\phi_n - \phi_t)} \left(\frac{\alpha}{m}\right)^m, \quad \Gamma_t = (-\phi_t)^{\langle \phi_t - \phi_n \rangle / (\phi_t - \phi_n)} \left(\frac{\beta}{n}\right)^n. \tag{4.36}$$

where m, n, called the non-dimensional exponents, are expressed in terms of the shape factors α, β (constants in this thesis) and of the initial slope indicator (λ_n, λ_t), as follows:

$$m = \frac{\alpha(\alpha-1)\lambda_n^2}{(1-\alpha\lambda_n^2)}, \quad n = \frac{\beta(\beta-1)\lambda_t^2}{(1-\beta\lambda_t^2)} \tag{4.37}$$

The initial slope indicators are defined as the ratios of critical crack opening width to the final crack opening width (Figure 4.10), i.e. $\lambda_n = \delta_{nc}/\delta_n, \lambda_t = \delta_{tc}/\delta_t$. Usually, the extrinsic CZM, in which the elastic behavior (or initial ascending slope) is excluded, is used to model fracture propagation when a cohesive segment or a cohesive interface element is adaptively inserted. Only the softening branch is used, because the elastic deformation of the material is already accounted for by the continuum model. However, numerical simulations indicate that the absence of one-to-one relationship at the point $\Delta_n = \Delta_t = 0$ causes stability issues. In the following, we use the intrinsic cohesive zone model with $\lambda_n = \lambda_t = 0.001$ to improve the convergence rate, and to avoid unwanted elastic separation.

To close the formulation of the PPR cohesive model, relationships between the cohesive strengths $(\sigma_{\max}, \tau_{\max})$ and the final normal and shear crack opening widths (δ_n, δ_t) are needed. The traction rate is equal to zero when traction is equal to the cohesive strength, so we have:

$$\begin{aligned} \delta_n &= \frac{\phi_n}{\sigma_{\max}} \alpha\lambda_n \Big(1-\lambda_n\Big)^{\alpha-1} \Big(\frac{\alpha}{m}+1\Big)\Big(\frac{\alpha}{m}\lambda_n+1\Big)^{m-1} \\ \delta_t &= \frac{\phi_t}{\tau_{\max}} \beta\lambda_t \Big(1-\lambda_t\Big)^{\beta-1} \Big(\frac{\beta}{n}+1\Big)\Big(\frac{\beta}{n}\lambda_t+1\Big)^{n-1} \end{aligned} \tag{4.38}$$

As explained in [265], the tangent Jacobian matrix can be calculated analytically in the potential based CZM, which is critical to achieve quadratic convergence in FEM simula-

tions. The reader is referred to [255, 266] for the expression of the Jacobian matrix for loading, unloading and reloading phases.

4.3.3 Cohesive Strength and Energy Release Rate of the PPR CZM

The cohesive zone model presented in Section 4.3.2 for pure mode I macro fracture propagation requires 4 material parameters. Here, we consider that the shape factor $\alpha = 4$ and that the initial slope indicator $\lambda_n = 0.001$ - these values are typical for brittle materials. As a result, only the cohesive strength $\sigma_{\max}$ and the cohesive energy release rate ϕ_n need to be calibrated. The transition from an element with diffuse damage at $\Omega_{crit} = 0.2$ to an element with a cohesive fracture is handled by writing the equilibrium of forces before and after the separation of the damaged element. The cohesive strength at a Gauss Point along the cohesive segment should equal the projected stress interpolated from the stress state of the element, as shown in Figure 4.11. Numerically, we first obtain the stress tensor $\boldsymbol{\sigma}_n$ at all the nodes of the element from the stress state $\boldsymbol{\sigma}_g$ of the Gauss Points, according to the procedure described in Section 4.4.4. Then, we use the shape functions to interpolate the stress state at the location of the Gauss points of the cohesive zone. Finally, we multiply the interpolated stress tensor by the normal unit vector of the fracture segment $\overrightarrow{n}$ to obtain the cohesive strength $\sigma_{\max}$.

For the cohesive energy release rate, we adopt the method described in [161], which ensures that the energy dissipated for propagating a unit area of fracture is the same if the cohesive zone model is used alone or if it is coupled to a nonlocal damage model. Mathematically, this energy equivalence is expressed as

$$\int_0^t \sum_{i=1}^{N_{cz}} G_f l_i^{\Gamma} \mathrm{d}\tau = \int_0^t \sum_{i=1}^{N_{cz}} \phi_i l_i^{\Gamma} \mathrm{d}\tau + E_{\Omega} \tag{4.39}$$

where G_f is the fracture energy release rate measured from laboratory experiments, in which the creation of macro-scale fracture surfaces is assumed to be the only source of

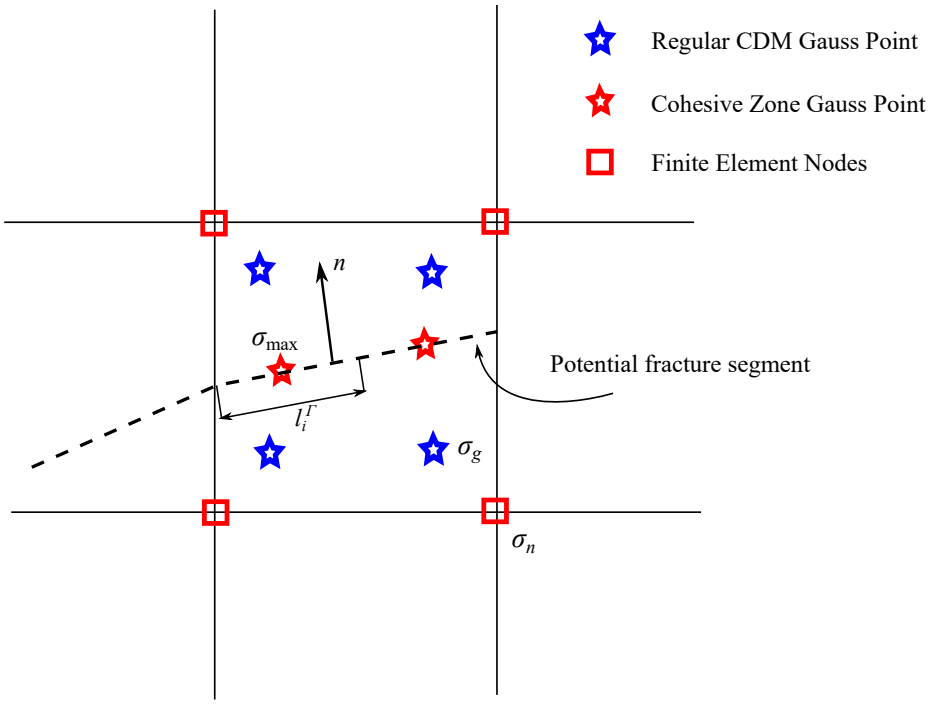

Figure 4.11: Numerical method employed to determine the CZM PPR cohesive strength.

energy dissipation. l_i^Γ is the fracture length in 2D (or fracture surface area in 3D) associated with the Gauss Point i as shown in Figure 4.11. N_{cz} is the total number of cohesive Gauss Points in the system. E_Ω represents the amount of energy dissipated by diffused damage $\mathbf{\Omega}$ development within the process zone, expressed as:

$$E_\Omega = \int_0^t \int_{\Omega_p} \boldsymbol{\sigma} : \dot{\boldsymbol{\epsilon}} d\Omega \mathrm{d}\tau - \int_{\Omega_p} \boldsymbol{\sigma} : \boldsymbol{\epsilon} d\Omega. \tag{4.40}$$

Numerically, we first use Equation 4.40 to calculate the total energy released by continuum damage development within the process zone Ω_p (shaded in blue in Figure 4.12). The size of the process zone in the direction perpendicular to the macro fracture is related to the nonlocal internal length parameter l_c. Here, the width of the process zone size is equal to l_c because the nonlocal weight function is bell-shaped (i.e., the weight is zero beyond a distance l_c). Through Equation 4.40, it is also assumed that the previously developed process zone (shaded in gray) is frozen after the transition from continuum damage to cohesive fracture. In other words, the elements in the shaded gray area are governed by a linear elas-

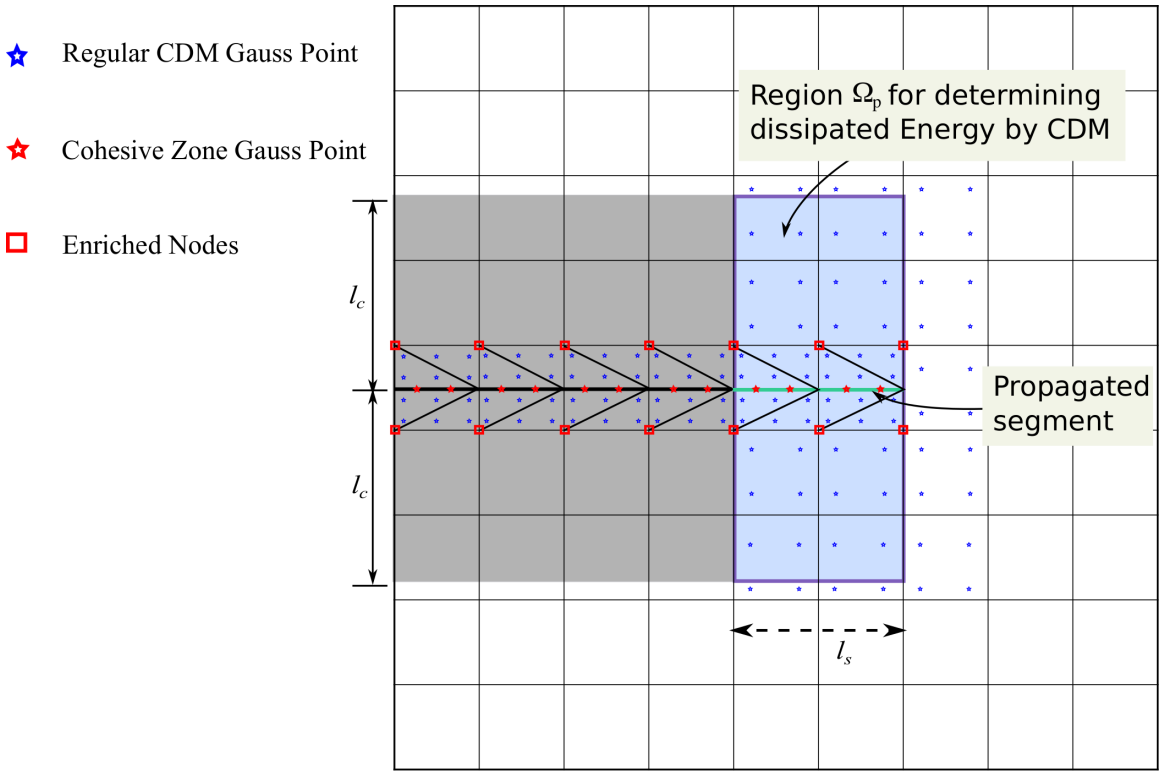

Figure 4.12: Numerical method employed to determine cohesive energy release rate.

tic constitutive function with reduced stiffness $\mathbb{C}(\Omega_{crit})$; no more energy dissipation comes from those bulk elements. Furthermore, we note that the length (area in 3D) of the newly formed cohesive segments is l_s, which indicates that the energy that should be dissipated to create the correct amount of fracture surfaces is $G_f l_s$. We use Equation 4.39 to obtain the energy release rate for each cohesive Gauss point, as

$$\phi_n = G_f - E_\Omega / l_s. \tag{4.41}$$

4.4 Numerical Implementation

4.4.1 Governing Equation

Consider a domain Ω, as shown in Figure 4.13, containing a fracture Γ_d. A prescribed traction $\bar{\boldsymbol{t}}$ is imposed on the boundary Γ_t and a prescribed displacement $\bar{\boldsymbol{u}}$ is imposed on the boundary Γ_u. Along the boundary of the macro-fracture, positive and negative cohesive

tractions ($\boldsymbol{t}^+, \boldsymbol{t}^-$) are imposed on the positive and negative surfaces (Γ_d^+, Γ_d^-). The equilibrium governing equation and the associated natural boundary conditions are expressed as:

$$\begin{aligned} &\nabla \cdot \boldsymbol{\sigma} + \boldsymbol{b} = 0 \quad \text{in} \quad \Omega \\ &\boldsymbol{\sigma} \cdot \boldsymbol{n} = \bar{\boldsymbol{t}} \quad \text{on} \quad \Gamma_t \\ &\boldsymbol{\sigma} \cdot \boldsymbol{n}_{\Gamma_d}^+ = -\boldsymbol{\sigma} \cdot \boldsymbol{n}_{\Gamma_d}^- = \boldsymbol{t}^+ = -\boldsymbol{t}^- = \boldsymbol{t}(T_n, T_t) \quad \text{on} \quad \Gamma_d \end{aligned} \tag{4.42}$$

where $\boldsymbol{\sigma}$ is the Cauchy stress tensor and $\boldsymbol{b}$ is the body force per unit volume. $\boldsymbol{n}$ is the outward normal unit vector on the outer boundary, $\boldsymbol{n}_{\Gamma_d}^+$ and $\boldsymbol{n}_{\Gamma_d}^-$ are the inward unit normals on the fracture boundary, as shown in Figure 4.13.

The kinematic equations include the strain-displacement relationship, the definition of cohesive separation and the essential boundary conditions, as follows:

$$\begin{aligned} &\boldsymbol{\epsilon} = \nabla^s \boldsymbol{u} \quad \text{in} \quad \Omega \\ &[\![\boldsymbol{u}]\!](\Delta_n, \Delta_t) = \boldsymbol{u}^- - \boldsymbol{u}^+ \quad \text{on} \quad \Gamma_d \\ &\boldsymbol{u} = \bar{\boldsymbol{u}} \quad \text{on} \quad \Gamma_u \end{aligned} \tag{4.43}$$

Finally, we relate the stress $\boldsymbol{\sigma}$ with the strain $\boldsymbol{\epsilon}$ and the cohesive traction $\boldsymbol{t}$ with the separation $[\![\boldsymbol{u}]\!]$ through the constitutive laws developed in Sections 4.2 and 4.3.2, and formally written as:

$$\begin{aligned} &\boldsymbol{\sigma} = \mathbb{C}(\boldsymbol{\Omega}) : \boldsymbol{\epsilon} = \mathbb{S}^{-1}(\boldsymbol{\Omega}) : \boldsymbol{\epsilon} \quad \text{in} \quad \Omega \\ &\boldsymbol{t}(T_n, T_t) = \boldsymbol{K}_{coh}[\![\boldsymbol{u}]\!](\Delta_n, \Delta_t) \quad \text{on} \quad \Gamma_d \end{aligned} \tag{4.44}$$

where $\mathbb{C} = \mathbb{S}^{-1}$ is the stiffness fourth order tensor. $\boldsymbol{K}_{coh}$ is the stiffness of the cohesive zone (i.e. the stiffness in the separation law).

In order to implement the governing equation into a finite element code, the strong form of the governing equations above needs to be transformed into a weak form. We multiply

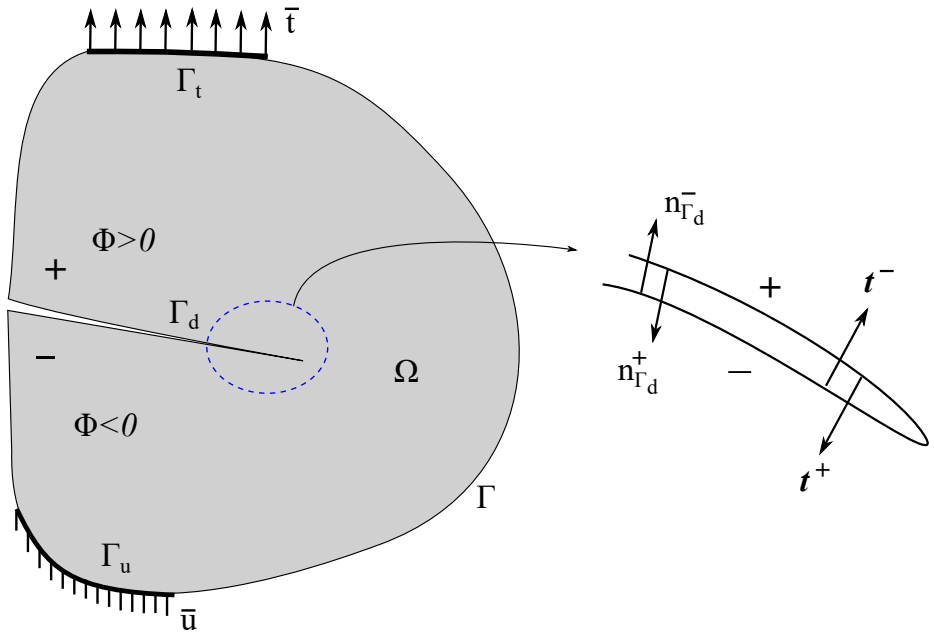

Figure 4.13: Boundary conditions imposed on the domain of the bulk, Ω, and on the macro-fracture Γ_d.

the equilibrium equations by a virtual displacement function $\delta \boldsymbol{u}$ and integrate it over the whole domain Ω. After utilizing the divergence theorem and the boundary conditions, we have the weak form as:

$$\int_{\Omega} \nabla^s \delta \boldsymbol{u} : \boldsymbol{\sigma} \mathrm{d}\Omega + \int_{\Gamma_d} \delta [\![\boldsymbol{u}]\!] \cdot \boldsymbol{t} \mathrm{d}\Gamma = \int_{\Gamma_t} \delta \boldsymbol{u} \cdot \bar{\boldsymbol{t}} \mathrm{d}\Gamma + \int_{\Omega} \delta \boldsymbol{u} \cdot \boldsymbol{b} \mathrm{d}\Omega, \quad \forall \delta \boldsymbol{u} \in V \tag{4.45}$$

where V represents the space of all possible displacement fields that satisfy $\delta \boldsymbol{u} = 0$ on Γ_u.

4.4.2 XFEM Discretization

Simulating fracture propagation without imposing a predefined fracture path is a long-standing issue. Techniques employed in engineering include: inserting interface elements to the boundaries of all regular finite elements prior to the loading simulation [267, 268], dynamically inserting interface elements to the fracture path during the simulation [269, 164], and using the eXtended Finite Element Method (XFEM) in which extra degrees of freedom are added to the nodes of elements where the fracture passes through [270], based

on the concept of partition of unity [271]. In this thesis, we adopt the XFEM to discretize the primary variable, the displacement field. Note that the classical branch functions which are used to approximate the near tip stress singularity are not used here, because the stress field does not present ingularities in the coupled CDM-CZM problem. Only the Heaviside jump function is used. Consequently, the approximation of the displacement field reads:

$$\begin{aligned}\boldsymbol{u}^h(\boldsymbol{x}) &= \sum_{i\in S} N_i(\boldsymbol{x})\boldsymbol{u}_i + \sum_{i\in S_H} N_i(\boldsymbol{x})\frac{1}{2}[H(\boldsymbol{x}) - H(\boldsymbol{x}_i)]\boldsymbol{a}_i, \quad \forall \boldsymbol{x}\in\Omega \\ &= \boldsymbol{N}_u(\boldsymbol{x})\boldsymbol{U} + \boldsymbol{N}_a(\boldsymbol{x})\boldsymbol{A}\end{aligned} \tag{4.46}$$

in which S is the set of all nodal points and S_H is the set of enriched nodes located in a support bisected by the fracture. $\boldsymbol{u}_i$ and $\boldsymbol{a}_i$ denote the nodal values of the displacement field associated with the standard and enriched degrees of freedom (DOF), respectively. $N_i(\boldsymbol{x})$ is the standard shape function associated with node i, and the Heaviside jump function $H(\boldsymbol{x})$ is defined as

$$H_{\Gamma_d}(\boldsymbol{x}) = \begin{cases} +1, & \Phi(\boldsymbol{x}) > 0 \\ -1, & \Phi(\boldsymbol{x}) < 0 \end{cases} \tag{4.47}$$

where $\Phi(\boldsymbol{x})$ is the level set function, the definition of which is illustrated in Figure 4.13. It is worth noting that we shift the jump function in Equation 4.46, to avoid the problem of post processing and blending element [272]. By substituting the values of the Heaviside definition in Equation 4.46, we obtain the following form of displacement jump:

$$[\![\boldsymbol{u}(\boldsymbol{x},t)]\!] = \sum_{i\in S_H} N_i(\boldsymbol{x})\boldsymbol{a}_i = \boldsymbol{N}_u(\boldsymbol{x})\boldsymbol{A} \tag{4.48}$$

By substituting the approximation functions 4.46-4.48 into the weak form of the gov-

erning equation 4.45, the following residual equations can be obtained:

$$\begin{aligned} \boldsymbol{R^u} &= \boldsymbol{K}_{uu}\boldsymbol{U} + \boldsymbol{K}_{ua}\boldsymbol{A} - \boldsymbol{F}_u^{\text{ext}} = 0 \\ \boldsymbol{R^a} &= \boldsymbol{K}_{ua}^T\boldsymbol{U} + \boldsymbol{K}_{aa}\boldsymbol{A} + \boldsymbol{F}^{\text{coh}} - \boldsymbol{F}_a^{\text{ext}} = 0 \end{aligned} \tag{4.49}$$

in which we used Voigt notations. $\boldsymbol{K}_{\alpha\beta}$ is the tangent stiffness matrix, expressed as

$$\boldsymbol{K}_{\alpha\beta} = \int_\Omega \Big(\boldsymbol{B}_\alpha^T \mathbb{S}^{-1}(\Omega) \boldsymbol{B}_\beta + \boldsymbol{B}_\alpha^T \frac{\partial \mathbb{S}^{-1}}{\partial \boldsymbol{u}} \boldsymbol{B}_\beta \boldsymbol{u} \Big) \mathrm{d}\Omega \tag{4.50}$$

where $\boldsymbol{B}_\alpha$ represents the derivatives of the shape functions, as follows:

$$\boldsymbol{B}_\alpha = \begin{bmatrix} N_{\alpha,x} & 0 \\ 0 & N_{\alpha,y} \\ N_{\alpha,y} & N_{\alpha,x} \end{bmatrix} \tag{4.51}$$

$\boldsymbol{F}_\alpha^{\text{ext}}$ and $\boldsymbol{F}^{\text{coh}}$ are the external force vector and the cohesive force vector respectively, defined as:

$$\begin{aligned} \boldsymbol{F}_\alpha^{\text{ext}} &= \int_{\Gamma_\text{t}} \boldsymbol{N}_\alpha \bar{\boldsymbol{t}} \mathrm{d}\Gamma + \int_\Omega \boldsymbol{N}_\alpha \boldsymbol{b} \mathrm{d}\Omega \\ \boldsymbol{F}^{\text{coh}} &= \int_{\Gamma_d} \boldsymbol{N}_u \boldsymbol{\Lambda}^T \boldsymbol{t}(T_n, T_t) \mathrm{d}\Gamma \end{aligned} \tag{4.52}$$

in which $\boldsymbol{\Lambda}$ is the rotation matrix defined as

$$\boldsymbol{\Lambda} = \begin{bmatrix} \cos\theta & \sin\theta \\ -\sin\theta & \cos\theta \end{bmatrix} \tag{4.53}$$

where θ is the angle between the fracture path and the horizontal axis. $\boldsymbol{\Lambda}$ is used here to transform the cohesive traction $\boldsymbol{t}$, formulated in the local coordinate system, to the global coordinate system.

The nonlinear system of Equations 4.49 needs to be solved iteratively. We adopt the

Newton-Raphson solution strategy, in which Equation 4.49 is linearized with respect to displacements at the equilibrium iteration k of the incremental step $n+1$, as follows:

$$\begin{bmatrix} \boldsymbol{R^u} \\ \boldsymbol{R^a} \end{bmatrix}_{n+1}^{k+1} = \begin{bmatrix} \boldsymbol{R^u} \\ \boldsymbol{R^a} \end{bmatrix}_{n+1}^{k} + \boldsymbol{J}_{n+1}^{k} \begin{bmatrix} \mathrm{d}\boldsymbol{u} \\ \mathrm{d}\boldsymbol{a} \end{bmatrix}_{n+1}^{k} = \boldsymbol{0} \tag{4.54}$$

where $\boldsymbol{J}$ is the Jabobian matrix (or the consistent tangent stiffness matrix), expressed as:

$$\boldsymbol{J} = \begin{bmatrix} \boldsymbol{R^u_{,u}} & \boldsymbol{R^u_{,a}} \\ \boldsymbol{R^a_{,u}} & \boldsymbol{R^a_{,a}} \end{bmatrix} = \begin{bmatrix} \boldsymbol{K}_{uu} & \boldsymbol{K}_{ua} \\ \boldsymbol{K}_{ua}^T & \boldsymbol{K}_{aa} + \frac{\partial \boldsymbol{F}^{\text{coh}}}{\partial \boldsymbol{a}} \end{bmatrix} \tag{4.55}$$

In the FEM, the analytical expression of $\boldsymbol{J}$ is typically sought so as to achieve a quadratic convergence rate. Unfortuntaly, due to the particular formulation of the continuum damage model, we cannot obtain analytical expression of the second term of Equation 4.50 because the stiffness tensor $\mathbb{C} = \mathbb{S}^{-1}$ cannot be expressed explicitly. So we use the secant stiffness matrix method, in which only the first term of Equation 4.50 is considered. Convergence can still be achieved at the cost of more iterations (linear convergence rate). Note that $\partial \boldsymbol{F}^{\text{coh}}/\partial \boldsymbol{a}$ can be obtained explicitly through $\partial(T_n, T_t)/\partial(\Delta_n, \Delta_t)$.

4.4.3 Fracture Tip Advancement Algorithm

In order to couple the CZM with the continuum damage model with the XFEM, an explicit algorithm is needed: (1) To determine when to split bulk elements and to insert cohesive segment; (2) To calculate the propagation direction of the macro-fracture; and (3) To determine the fracture propagation length. In Section 4.3, we calibrated the transition from continuum damage to macro-fracture and we found that the critical damage value was $\Omega_{crit} = 0.2$ for the continuum damage model presented in Section 4.2. A simple implementation scheme consists in checking systematically the state variables at the Gauss points of elements ahead of fracture tip (Figure 4.14). If the value of damage at one Gauss point

exceeds Ω_{crit}, the fracture tip advances towards that Gauss point, with known propagation direction and length. However, this simple algorithm becomes ineffective when multiple Gauss points at different locations exceed the threshold at the same load increment. Let us recall that the continuum damage model is enhanced with nonlocal regularization for tensile softening, thus, the area of damage development ahead of the fracture tip (i.e. the size of process zone) is correlated with the internal length parameter l_c, as shown in Figure 4.14. In line with the methods presented in [273, 161], we assume that the fracture propagates when the component of the weighted damage tensor over the half circle patch ahead of the fracture tip (shaded in blue) exceeds the threshold Ω_{crit}. We first obtain the weighted damage tensor $\bar{\boldsymbol{\Omega}}$ using the bell-shaped weight function $\alpha_0(\|\boldsymbol{x}-\boldsymbol{\xi}\|)$ through

$$\bar{\boldsymbol{\Omega}}(\boldsymbol{x}_{tip}) = \int_{\Omega_T} \alpha(\boldsymbol{x}_{tip},\boldsymbol{\xi})\boldsymbol{\Omega}(\boldsymbol{\xi})\mathbf{d}\Omega_T(\boldsymbol{\xi}) = \frac{\sum_{j=1}^{N_{GP}} \alpha_0(\|\boldsymbol{x}_{tip}-\boldsymbol{\xi}_j\|)\boldsymbol{\Omega}(\boldsymbol{\xi}_j)\Delta V_j}{\sum_{j=1}^{N_{GP}} \alpha_0(\|\boldsymbol{x}_{tip}-\boldsymbol{\xi}_j\|)\Delta V_j} \tag{4.56}$$

where $\boldsymbol{x}_{tip}$ and $\boldsymbol{\xi}$ are the global coordinates of fracture tip and Gauss points in Ω_T, respectively. N_{GP} is the total number of Gauss points in Ω_T, and ΔV_J is the geometrical volume associated with Gauss point j. Please note that the size of Ω_T is controlled by the internal length l_c since we chose a bell-shaped weight function (4.21) for nonlocal enhancement.

We discretize the half circle shown in Figure 4.14 into a series of directions $\boldsymbol{m}$, and we project the weighted damage tensor on the direction $\boldsymbol{n}$ normal to the direction $\boldsymbol{m}$ used for discretization: $\Omega_n = \boldsymbol{n}^T \cdot \boldsymbol{\Omega} \cdot \boldsymbol{n}$. Then we compare the maximum projected damage components $\max(\Omega_n)$ with the threshold Ω_{crit}. If $\max(\Omega_n) \geq \Omega_{crit}$, we propagate the fracture along the direction of $\boldsymbol{m}$ normal to the unit vector $\boldsymbol{n}$. For all simulation in this chapter, we choose a user-defined growth length $\Delta a = l_c$, since the size of the process zone is controlled by the internal length and equal to $2 \times l_c$. It is worth noting that since only the Heaviside function is used for XFEM discretization, cohesive segments are never inserted into and element that contains a fracture tip.

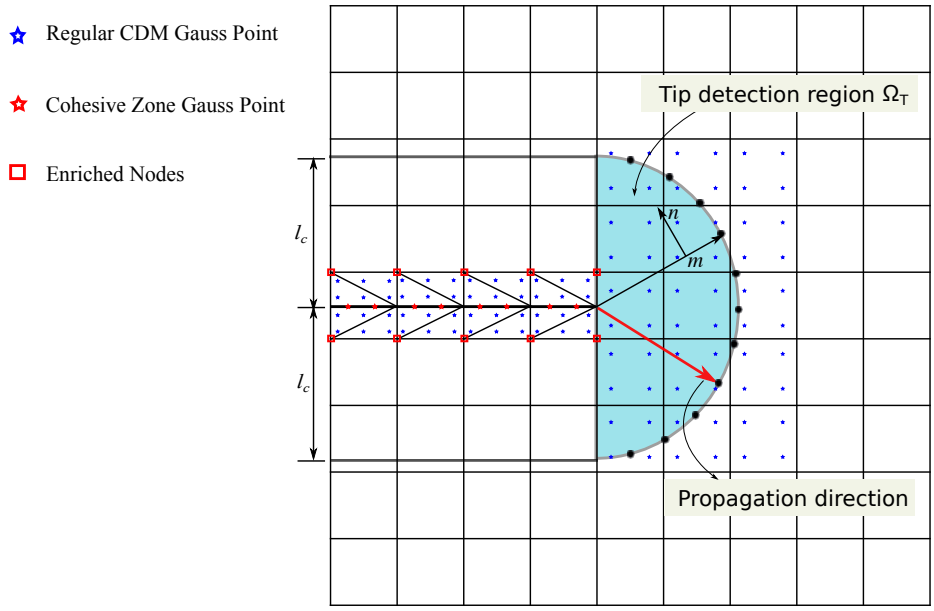

Figure 4.14: Macro cohesive fracture initiation algorithm based on the projection of the weighted damage tensor.

4.4.4 SPR State Variable Mapping

An element being cut by a fracture should be divided into subdomains inside which the displacements are continuous functions. In this study, we employ the classical sub-region quadrature technique [274] to divide a quadrilateral element into multiple triangles, and we use three Gauss points within each triangle to calculate the Jacobian matrix and the residual. Consequently, the number and the location of Gauss points with in an element that is cut during fracture propagation is changed. It is thus necessary to remap the internal and state variables, such as damage and stress, from the initial to the new set of Gauss points. Variable mapping accuracy has a significant influence on the equilibrium recovery rate after the fracture tip advancement. In this thesis, the super-convergent patch recovery (SPR) proposed by Zienkiewicz and Zhu [275] is adopted. In the SPR, two steps need to be performed numerically: (1) A construction step, in which the state variables at nodes of an element are interpolated by least square fitting from the neighboring Gauss points; (2) A recovery step, in which the state variables at the new Gauss points are interpolated from the nodes by using the shape functions of the element.

In the construction step, we assume that a nodal state s_{node} can be interpolated by a polynomial function $S_p(x, y)$, in which p denotes the polynomial order. We have

$$S_p(x, y) = \boldsymbol{P} \cdot \boldsymbol{a} \tag{4.57}$$

where $\boldsymbol{P}$ is the polynomial of order p and $\boldsymbol{a}$ is a set of coefficients, which can be expressed as follows in the case of a 2D simulation:

$$\begin{aligned} \boldsymbol{P} &= [1, x, y, x^2, y^2, xy, ...] \\ \boldsymbol{a} &= [a_0, a_1, a_2, a_{11}, a_{22}, a_{12}, ...] \end{aligned} \tag{4.58}$$

The coefficient vector $\boldsymbol{a}$ is obtained by using the least square fitting thechnique applied to the neighboring sampling points s_{old} (old Gauss points):

$$\sum_{k=1}^{n} \boldsymbol{P}(x_k, y_k)^T \boldsymbol{P}(x_k, y_k)\boldsymbol{a} = \sum_{k=1}^{n} \boldsymbol{P}(x_k, y_k)^T s_{old}(x_k, y_k) \tag{4.59}$$

where n is the total number of sampling Gauss points. The nodal state s_{node} is then interpolated, as follows:

$$s_{node} = \boldsymbol{P}(x_{node}, y_{node})^T \boldsymbol{a}. \tag{4.60}$$

Once all variables have been interpolated at the nodes of an element, we move to the recovery step, in which the variable at the new Gauss point s_{new} is obtained by

$$s_{new} = \sum_i N_i(x_{new}, y_{new}) s^i_{node} \tag{4.61}$$

in which N_i is the shape function associated with node i.

4.5 Engineering Examples of Micro-macro Fracture Propagation

4.5.1 Wedge Splitting

We implemented the coupled CDM-CZM framework based on the XFEM into an open source finite element package in C++, called 'Object Oriented Finite Element Method' (OOFEM) [276, 277]. To check that the framework can be used to model micro-macro fracture propagation, a wedge splitting benchmark example is first simulated. The geometry and boundary conditions are shown in Figure 4.15. The thickness of the specimen is 97 mm, like in the laboratory experiment described in [278]. The material parameters listed in Table 4.2 are used, in which the elastic constants (E, ν) and the total energy release rate G_f are adopted from [278]. Note that l_c is typically 2-3 times of maximum aggregate size in brittle solids [73]. We calibrate the damage evolution parameters (α_t, κ_t) for an internal length of $l_c = 16$ mm, by matching the numerical load-displacement curve to the experimental one. The domain is discretized with linear quadrilateral elements with two different mesh densities to investigate mesh dependency. It is expected that a straight fracture will initiate from the notch and will gradually propagate into a horizontal fracture in pure mode I.

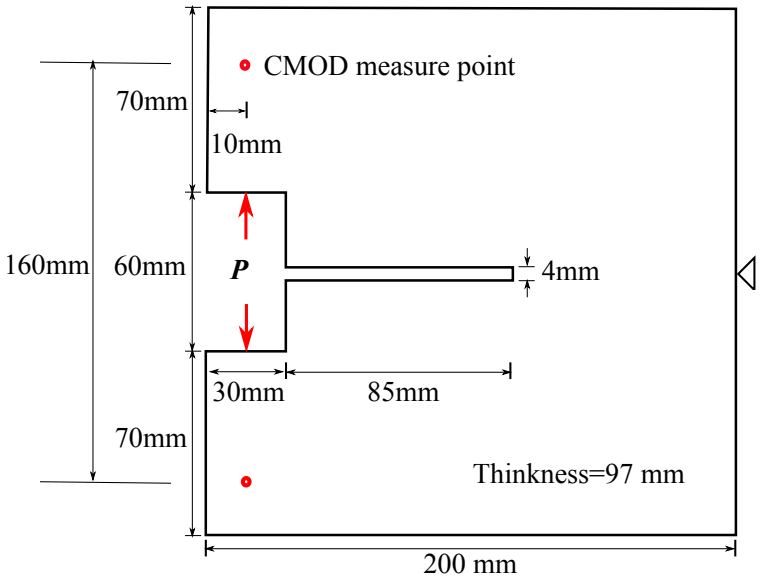

Figure 4.15: Geometry and boundary conditions of the wedge splitting test.

Table 4.2: Material parameters used for the wedge splitting test.

Young's modulus	E (GPa)	25.2
Poission's ratio	ν	0.2
Damage evolution parameters	α_t	1.325×10^{-4}
	κ_t	2.5×10^{-4}
Internal length	l_c (mm)	16
Total energy release rate	G_f (N/mm)	0.101

As shown in Figure 4.16, we simulate wedge-splitting test with different values of (α_t, κ_t) until the simulated force-CMOD (crack mouth opening displacement) curves (dashed lines) match well the experimental measurements [278] (solid dark line). In addition, we simulate a case in which the matrix is elastic (no damage) and in which the energy is solely dissipated by macro fracture surface formation (CZM). For this particular case, we used a cohesive strength of 6.6 MPa from [278], and the cohesive segments along the pre-assigned fracture path were inserted at the start of simulation. The global force-CMOD response of the CZM is represented by a solid blue line in Figure 4.16. The curves predicted by the proposed CDM-CZM framework match the experimental data until the maximum force is reached. After the peak, the CDM-CZM simulation results are similar to those obtaied with the CZM, but depart from the experimental response by up to 25%. These discrepancies can be explained by: (i) The pre-assigned cohesive segment with zero thickness, which has artificial compliance, which results in additional CMOD in the CZM simulation before the peak; (ii) The shape of the cohesive traction-separation law, which influences the global softening curve: the shape factors $\alpha = \beta = 4$ used in the PPR cohesive law are not exact. Overall, the global response reflected in the load-CMOD curve is predicted accurately before the peak; an error of up to 25% is made between the peak and a residual load of 1 kN, and the error is around 65% when the residual load is close to zero.

Figure 4.17 shows several stages of the macro fracture propagation accompanied by the damage process zone evolution. The tip of the macro cohesive fracture is behind of the front of process zone at all stages, which indicates a smooth transition from damage to

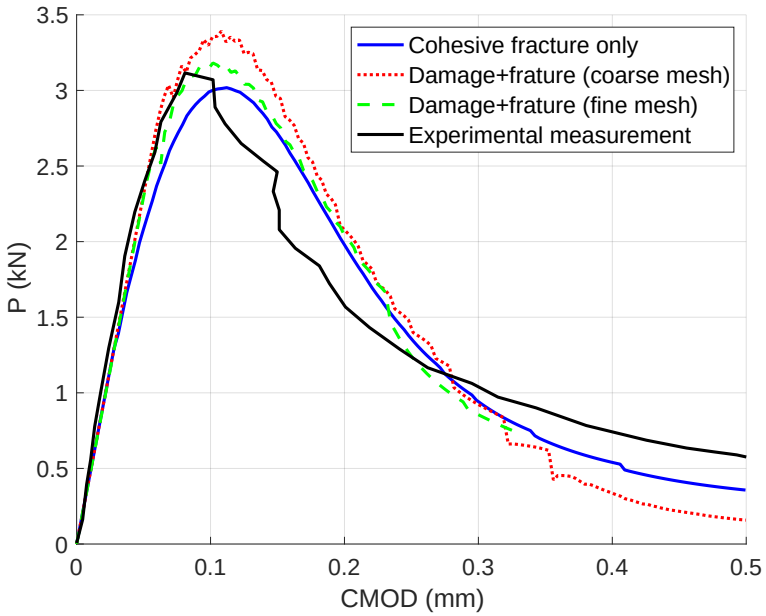

Figure 4.16: Load vs CMOD response: comparison of numerical and experimental results.

fracture. The size of the process zone is constant throughout the simulation, and it is not mesh dependent thanks to nonlocal enhancement. Note that the maximum damage within the process zone is $\max(\Omega_y) = 0.4$ - greater than the damage threshold $\Omega_{crit} = 0.2$. This is due to the fact that the threshold Ω_{crit} is applied on a weighted damage tensor and not on the components of damage itself.

Figure 4.18 illustrates the transformation the energy input into elastic deformation energy and dissipated energy over time, as a function of the CMOD. E_T denotes the total energy input, computed by multiplying the applied force P with the displacement at the nodes where the force is applied. E_E is the elastic energy stored within the system. E_C represents the dissipated cohesive energy due macro fracture propagation, and it is calculated by multiplying the cohesive energy release rate ϕ_n by the length of propagated macro fracture, and the thickness of the specimen. The last term E_Ω is the dissipated energy due to micro fracture development; it can be computed by Equation 4.40. We present the evlution of energy for the three cases simulated in Figure 4.16 (CZM only, CDM-CZM with a coarse mesh, CDM-CZM with a fine mesh). Like for the load-displacement curve, the

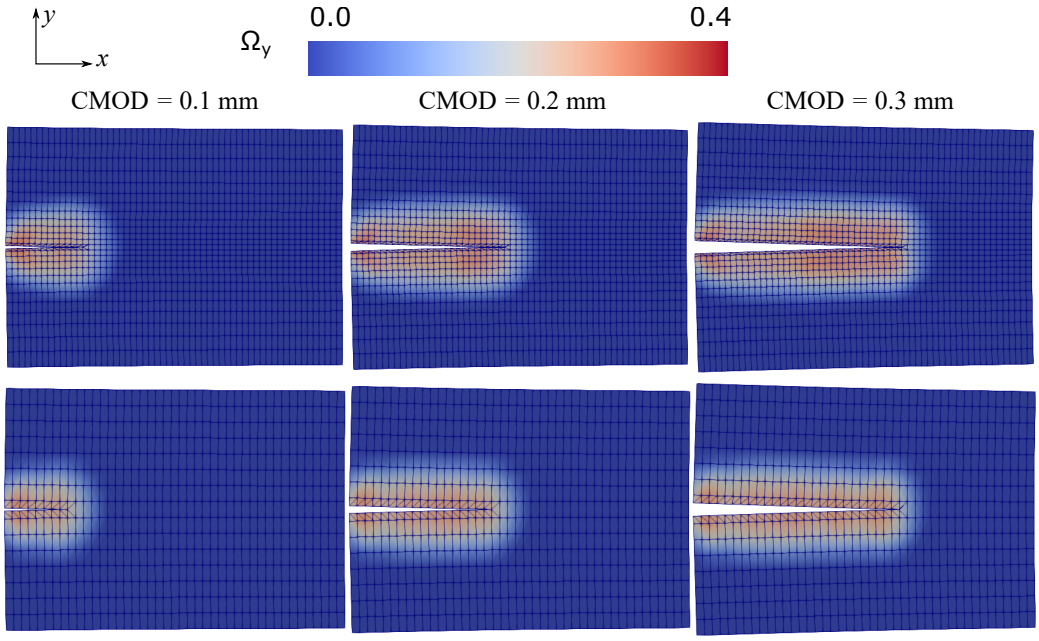

Figure 4.17: Contour of the damage component Ω_y (horizontal micro cracks) and macro cohesive fracture path shown on the deformed mesh (displacements magnified $\times 5$). Top row: fine mesh; lower row: coarse mesh.

differences between the three cases are due to the artificial compliance of the CZM and to the shape factors of the PPR cohesive model. Despite these discrepancies, all the simulated cases show that the evolution of energy follows three phases. In the initial phase, all the input work is transformed and stored as elastic energy within the system. In the second phase, energy is dissipated by micro-crack and macro-fracture propagation while the elastic energy of the system keeps increasing. In the final phase, most of the input work is dissipated immediately, and some of the stored elastic energy gets dissipated as well, to propagate micro-cracks and the macro-fracture. The elastic energy of the system tends to zero. We can also note that the percentage of energy dissipated by micro-crack propagation (damage development) is significantly smaller than the amount of energy dissipated by macro-fracture surface formation. To conclude, the proposed framework can successfully simulate mode I macro-fracture propagation with a damage process zone, the size of which depends on microstructure. Most of the input work is dissipated to create macro-fracture surfaces.

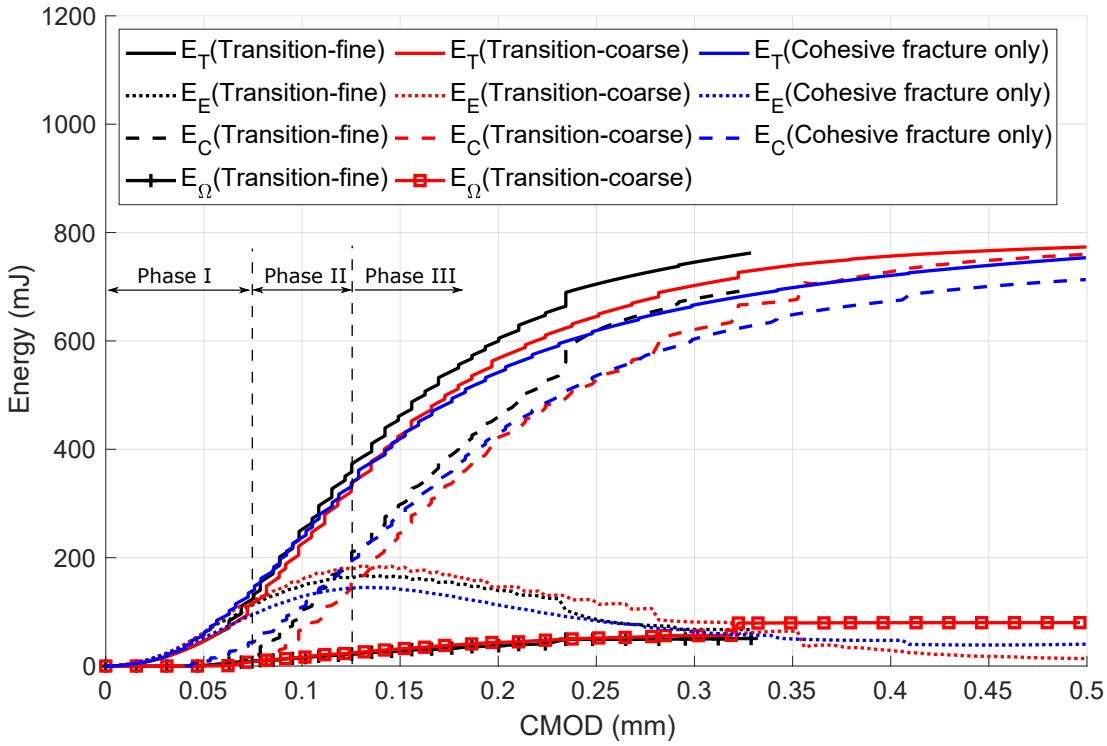

Figure 4.18: Evolution of the components of energy during the wedge splitting test: work input E_T, elastic energy E_E, dissipated energy by cohesive fracture propagation E_C and by continuum damage E_Ω. CZM only ("Cohesive fracture only"), CDM-CZM with coarse mesh ("Transition-coarse"), CDM-CZM with fine mesh ("Transition-fine").

4.5.2 Three-point Bending

A three-point bending test is now simulated. The geometry and boundary conditions of the laboratory experiment described in [279] are adopted here - see Figure 4.19. An initial notch of 20 mm in depth and 4 mm in width is considered. The thickness of the specimen is 100 mm. Like in the previous case, the elastic constants and the total energy release rate measured from [279] are directly used for the simulation. The internal length is fixed as $l_c = 6$ mm, and the material parameters controlling continuum damage evolution are calibrated by fitting the force-deflection curve against experimental results. By trial and error, the best match was found to be the one shown in Figure 4.20, in which the experimental data is marked in black solid curve, and the numerical prediction is marked in red dashed line. We also simulated the three-point bending test with CZM only by inserting cohesive

segments alined with the notch before the loading simulation. The CZM global response curve $(F - u)$ marked in blue solid line matches the the results obtained with the CDM-CZM framework. Note that for the case with CZM only, we chose the cohesive strength $\sigma_{\max} = 6.12$ MPa and the cohesive energy release rate $\phi_n = G_f = 0.1963 N/mm$, from [279]. The 6 CDM-CZM parameters used for the simulations are listed in Table 4.3. Note only one mesh is employed here since it was already shown that nonlocal regularization can alleviate mesh dependency.

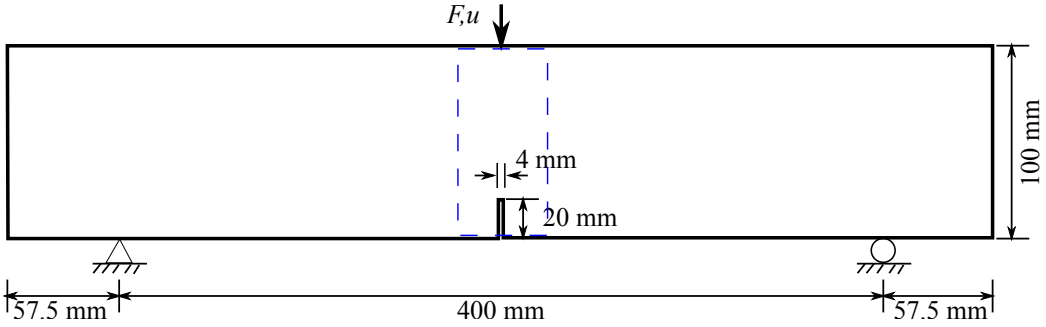

Figure 4.19: Geometry and boundary conditions of the three-point bending test.

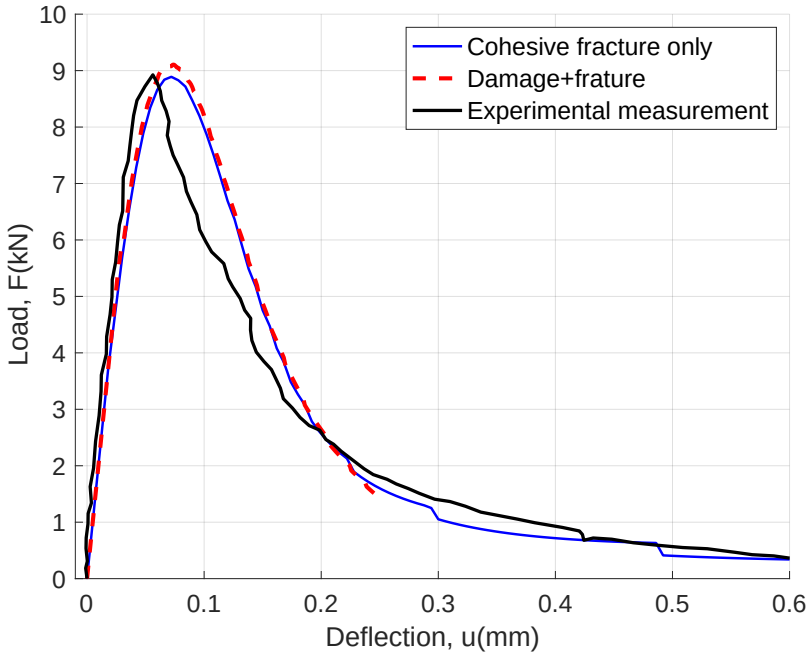

Figure 4.20: Load-deflection curve for the three-point bending test: comparison of experimental and numerical results.

Table 4.3: Material parameters used for the three-point bending test.

Young's modulus	E (GPa)	50.0
Poission's ratio	ν	0.2
Damage evolution parameters	α_t	1.25×10^{-4}
	κ_t	2.5×10^{-4}
Internal length	l_c (mm)	6
Total energy release rate	G_f (N/mm)	0.1963

Figure 4.21 represents the distribution of horizontal stress σ_x, nonlocal equivalent strain $\hat{\epsilon}_t^{nl}$ and damage component Ω_x in the central zone of the beam, marked by a blue dashed in Figure 4.19. The traction-separation law predicts traction (reflected from σ_x) even after the initiation of the macro-fracture. The material fracture tip (no traction, defined in Figure 4.10) is behind of the mathematical fracture tip (cohesive segment inserted). The nonlocal equivalent strain is non-zero only in the vicinity of the macro fracture tip area, indicating that the fracture surface behind the material fracture tip is unloaded: the elastic energy stored during previous load increments flows into the tip area and is dissipated. Vertical micro-cracks develop within the process zone, which surrounds the macro-fracture.

Figure 4.21 shows the evolution of the total input work E_T, the stored elastic energy E_E, and the dissipated energy by macro cohesive fracture propagation E_C and by micro-cracks development E_Ω. Similar to the wedge splitting case, the evolution of energy presents three main phases, and the percentage of dissipated energy by micro-crack initiation and propagation E_Ω is insignificant compared to the energy dissipated by macro-fracture formation. It is also worth noting that a discrepancy exists between the predictions made by the proposed CDM-CZM framework and those made by the CZM alone, even if the global responses ($F - u$ curve in Figure 4.20) are similar.

4.6 Conclusions

In this chapter, we present a novel numerical framework that couples a nonlocal micromechanics based anisotropic damage model with a cohesive zone model. This multi-scale framework captures the failure process in brittle solids, from the nucleation of micro-cracks to the formation of macro-fracture.

A non-local micromechanics-based continuum damage model is proposed to predict the material response from the microscopic scale to the REV scale. A dilute homogenization scheme is adopted for calculating the deformation energy of the REV, which is attributed to the elastic deformation of the matrix and to the displacement jumps at open and closed micro-crack faces. The Gibbs free energy is obtained by integrating the energy potentials of the different sets of micro-cracks on the unit sphere. An explicit expression of the free energy of the REV is provided when all micro-cracks are open and when all micro-cracks are closed. Tensile (respectively compressive) damage criteria depend on equivalent strains defined in terms of positive principal strains (respectively deviatoric) strains. Damage evolution laws are obtained from consistency conditions and from postulates on damage potentials. The model is enriched by non-local equivalent strains, calculated as the weighted average of equivalent strains on an influence zone of material-specific characteristic size.

From the REV scale to the macroscopic scale, the potential based PPR cohesive zone model is adopted to characterize the macro-fracture behavior. The critical damage level that marks the transition from continuum damage to discrete cohesive fracture is defined as the damage above which the damaged stiffness tensor calculated with proposed non-local damage model (which does not account fro crack interactions) stops matching the stiffness tensor calculated from Kachanov's micromechancis-based damage model (which accounts for crack interactions). We find a critical damage threshold of 0.2. Furthermore, an energy equivalence criterion is established to determine the cohesive strength and the cohesive energy release rate, so that the total dissipated energy by propagating macro-fracture and

micro-cracks for a unit area equals to the energy release rate measured at the laboratory.

We couple the non-local continuum damage model with the discrete cohesive zone model by using a XFEM discretization technique. After deriving the secant Jacobian matrix, we implement the proposed framework into an open source finite element package (OOFEM). A weighted damage tensor around the tip area is empolyed to determine the direction and length of the macro-fracture that propagates. The SPR method is used to map state variables after remeshing. Utilizing the proposed computational tool, a wedge splitting test and a three-point bending test are simulated. Results demonstrate that the framework can successfully capture the propagation of a mode I macro-fracture within a damage process zone. The size of the process zone is mesh independent owing to the nonlocal regularization, and the predicted global responses match well with experimental measurements. In addition, simulation results reveal that most of the energy is dissipated to create macro-fracture surfaces and that very little energy is dissipated due to damage development.

The proposed CDM-CZM framework still have limitations. For instance, it is imposible to properly simulate micro-macro fracture propagation in mixed ode, due to the choice of the constitutive CDM model. First, it is impossible to obtain the tangent Jacobian matrix without the explicit expression of the damaged stiffness matrix $\mathbf{C}$, which results in convergence issues for complex stress paths. Second, the dilute homogenization scheme limits the degradation of modulus, so that the softening stress-strain curve cannot reach zero stress, which can weaken the performance of nonlocal regularization.

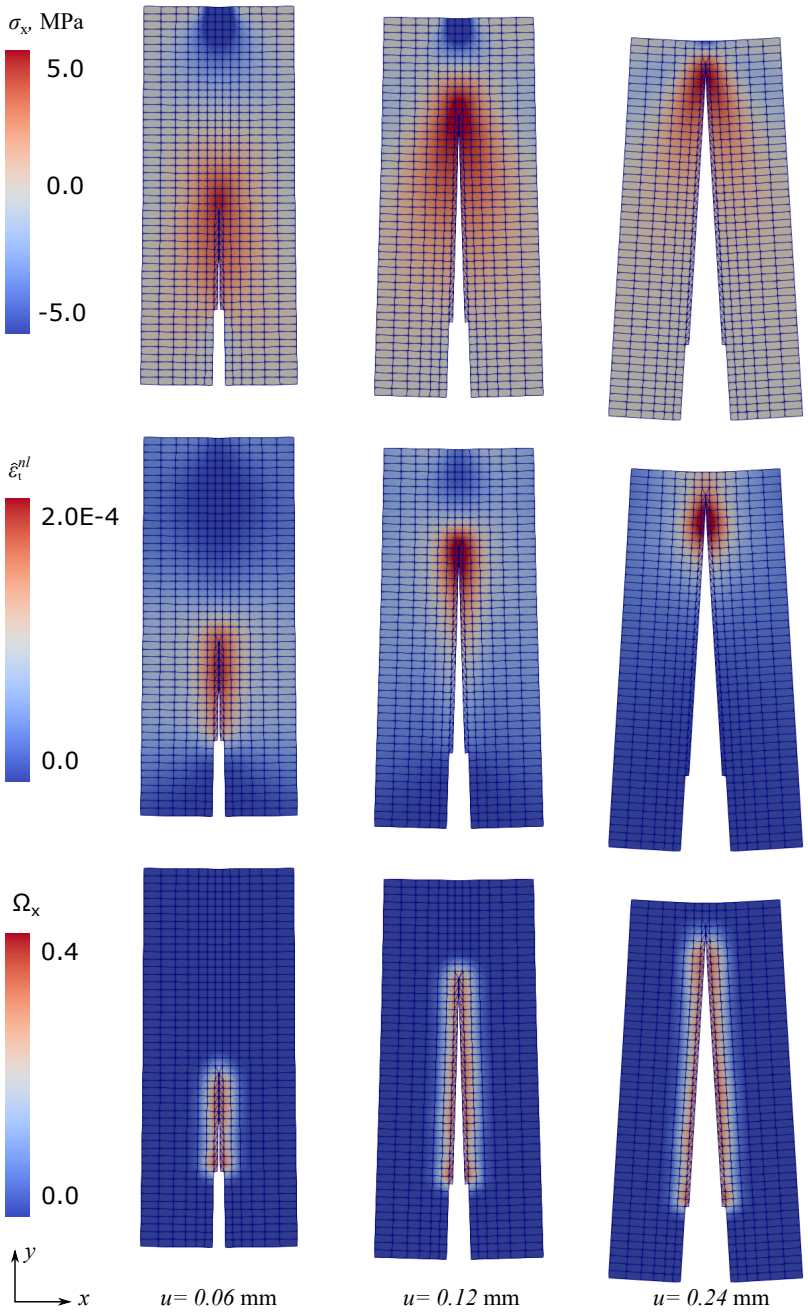

Figure 4.21: Contour of horizontal stress σ_x, nonlocal equivalent strain $\hat{\epsilon}_t^{nl}$ and damage component Ω_x (vertical micro cracks) in the central part of the beam subjected to three -point bending (see blue area in Figure 4.19). Deformed mesh ($\times 5$) at different stages of macro fracture propagation.

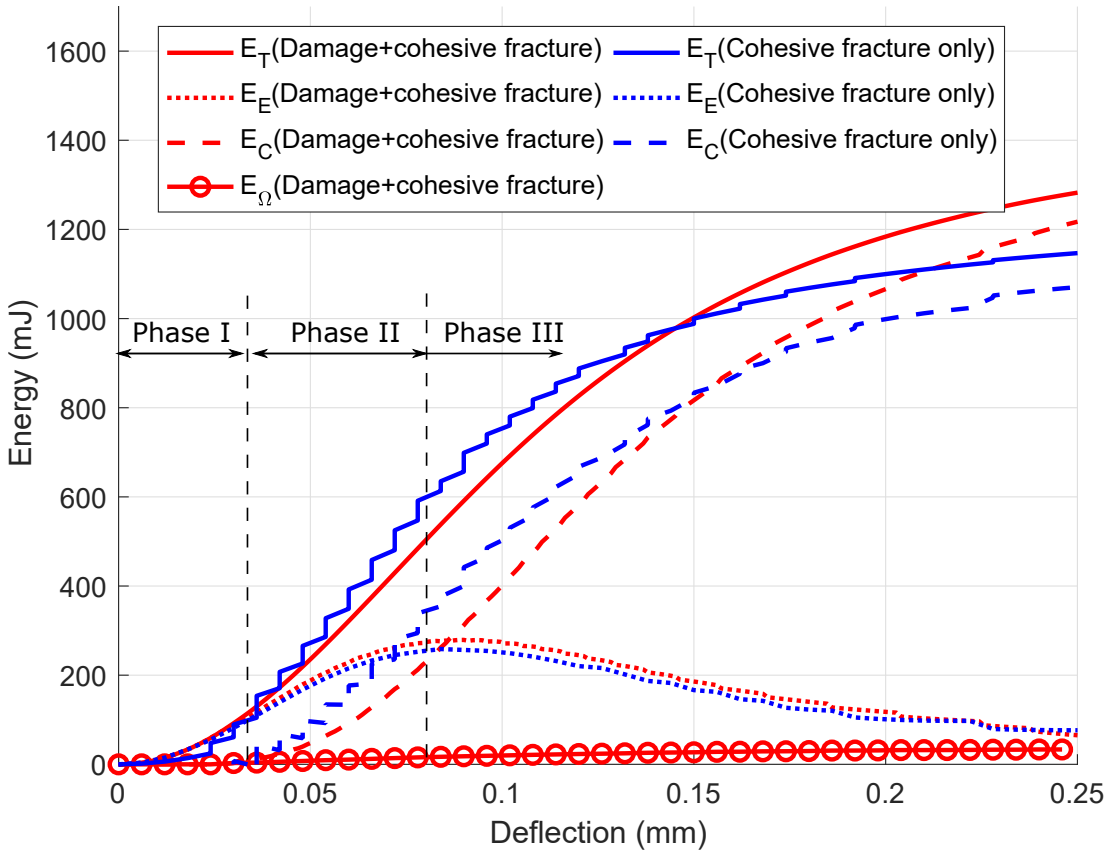

Figure 4.22: Evolution of the components of energy during the three-point bending test: work input E_T, elastic energy E_E, dissipated energy by cohesive fracture propagation E_C and by continuum damage E_Ω. CZM only ("Cohesive fracture only"), CDM-CZM ("Damage+cohesive fracture").

CHAPTER 5
HYDRAULIC FRACTURING IN TRANSVERSELY ISOTROPIC MATERIALS

5.1 Introduction

Modeling fluid driven fracture propagation in porous formations is still a challenging issue, because of the couplings between the deformation and fracturing of the solid skeleton (matrix), the flow of fluid in both the porous matrix and the macroscopic fractures, and the fluid exchange at the fracture faces. Numerical tools developed to date were successfully applied in engineering for isotropic elastic materials. Modeling hydraulic fracturing in anisotropic material is still an open issue, especially under anisotropic in-situ stress conditions.

In this chapter, we present a computational tool to simulate hydraulic fracturing in transversely isotropic porous materials based on the eXtended Finite Element Method (XFEM). In Section 5.2, we first formulate a constitutive law for predicting stress-induced anisotropy in an initially transverse isotropic material. The evolution laws of the damage components are expressed in terms of equivalent strains, which are direction dependent. In Section 5.3, we explain how to avoid mesh dependency while accounting for intrinsic anisotropy, by using an anisotropic nonlocal regularization technique. After deriving the analytical expression of the Jacobian matrix, a three-point bending test is simulated by means of a dissipation based arc length control algorithm. The strong and weak forms of the governing equations of the problem of hydraulic fracturing in saturated porous media are presented in Section 5.4. We detail the momentum balance equations for the solid and fluid phases and well as the mass balance equations for the fluid phase inside the solid skeleton and inside the fracture. Constitutive equations are the proposed anisotropic damage model (for the deformation and damage of the porous matrix), the PPR cohesive model (for fracture propagation), Darcy's law (for fluid flow in the solid matrix) and the cubic law (for fluid flow

within the fractures). In Section 5.5, we present the XFEM used for space discretization and the finite difference method used for time discretization. A Newton-Raphson iterative scheme is employed to solve the global nonlinear system of equations. In Section 5.6, we first validate the formulation and implementation of the computational model by simulating the Khristianovic-Geertsma-de Klerk (KGD) problem; we conduct parametric studies in plain strain conditions to understand the mechanisms that control fracture path formation in the presence of both material and stress anisotropy.

5.2 Anisotropic Damage Model for Transversely Isotropic Materials

5.2.1 Damage Operator and Damaged Stiffness Tensor

In brittle materials, the inception, propagation and coalescence of micro-cracks result in hardening or softening of stress/strain relations and stiffness reduction at the scale of the REV. The nominal stress, $\boldsymbol{\sigma}$, is related to the damaged effective stress, $\hat{\boldsymbol{\sigma}}$, through

$$\hat{\boldsymbol{\sigma}} = \mathrm{M} \,:\, \boldsymbol{\sigma} \tag{5.1}$$

where M is a fourth-order damage operator (second-order with Voigt notation). Assuming that damage components in each direction evolve independently, the damage operator M has a diagonal form, as follows:

$$M_{ii} = \frac{1}{1-\omega_i} \quad i = 1, 2, ..., 6 \tag{5.2}$$

Note that Voigt notations are adopted here, so that $\hat{\sigma}_4 = \hat{\tau}_{23} = \frac{\tau_{23}}{1-\omega_4}$, in which:

$$\begin{aligned} \omega_4 &= 1 - (1-\omega_2)(1-\omega_3) \\ \omega_5 &= 1 - (1-\omega_1)(1-\omega_3) \\ \omega_6 &= 1 - (1-\omega_1)(1-\omega_2) \end{aligned} \tag{5.3}$$

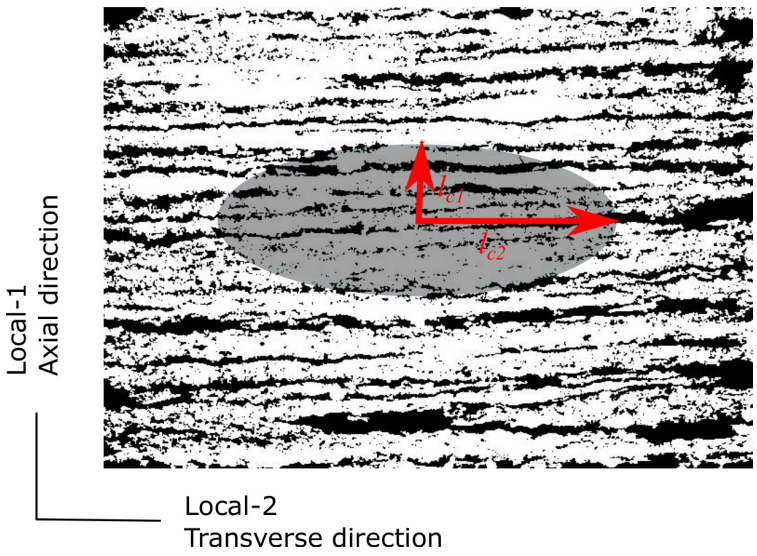

Figure 5.1: Definition of the intrinsic damage directions in transverse isotropic shale, modified from [282].

The diagonal form of $\mathbf{M}$ ensures that the damaged compliance matrix resulting from Equation 5.1 is symmetric. We consider a geomaterial with transverse isotropy with respect to the normal direction of bedding planes. Figure 5.1 shows the example of shale, which is a sedimentary rock [280, 101, 281]. We set the local coordinate system so that direction 1, called the axial direction, is perpendicular to the bedding plane. Directions 2 and 3, along the bedding plane, are called transverse directions. Correspondingly, in Equation 5.2, ω_1 is called axial damage and ω_2, ω_3 are the transverse damage variables.

We focus on transverse isotropic quasi-brittle materials. With negligible inelastic deformation, the non-linear stress/strain relation results from damage evolution only (microcrack development). Adopting the principle of strain equivalence, the constitutive relation is expressed as

$$\boldsymbol{\epsilon} = \mathbf{S}^0 \,:\, \mathbf{M} \,:\, \boldsymbol{\sigma}. \tag{5.4}$$

For a transverse isotropic material, the elastic compliance matrix $\mathbf{S}^0$ depends on 5 pa-

rameters. In the local coordinate system, $\mathbf{S}^0$ is expressed as:

$$\mathbf{S} = \begin{pmatrix} \frac{1}{E_1} & -\frac{\nu_{12}}{E_2} & -\frac{\nu_{12}}{E_2} & 0 & 0 & 0 \\ -\frac{\nu_{21}}{E_1} & \frac{1}{E_2} & -\frac{\nu_{23}}{E_2} & 0 & 0 & 0 \\ -\frac{\nu_{21}}{E_1} & -\frac{\nu_{32}}{E_2} & \frac{1}{E_2} & 0 & 0 & 0 \\ 0 & 0 & 0 & \frac{2(1+\nu_{23})}{E_2} & 0 & 0 \\ 0 & 0 & 0 & 0 & \frac{1}{G_{13}} & 0 \\ 0 & 0 & 0 & 0 & 0 & \frac{1}{G_{12}} \end{pmatrix} \tag{5.5}$$

where $\frac{\nu_{12}}{E_2} = \frac{\nu_{21}}{E_1}, \nu_{23} = \nu_{32}$ and $G_{13} = G_{12}$.

We construct damage evolution laws that directly relate damage components to equivalent strain measures, defined below. We focus on plane strain loading conditions, in which the out-of-plane components of equivalent strains are zero, and consequently, the out-of-plane component of damage, ω_3, is zero. With $\omega_3 = 0$, the damaged stiffness matrix $\mathbf{C}$ can be explicitly expressed as

$$\mathbf{C} = \begin{pmatrix} C_{11} & C_{12} & C_{13} & 0 \\ C_{21} & C_{22} & C_{23} & 0 \\ C_{31} & C_{32} & C_{33} & 0 \\ 0 & 0 & 0 & C_{44} \end{pmatrix} \tag{5.6}$$

in which

$$
\begin{aligned}
C_{11} &= E_1(1-\omega_1)((1-\omega_2)\nu_{23}^2 - 1)/D \\
C_{22} &= E_2(1-\omega_2)((1-\omega_1)\nu_{12}\nu_{21} - 1)/D \\
C_{33} &= E_2(1-\omega_1)(1-\omega_2)(\nu_{21}\nu_{12} - 1)/D \\
C_{44} &= G_{12}(1-\omega_1)(1-\omega_2) \\
C_{12} &= -E_1\nu_{21}(1-\omega_1)(1-\omega_2)(1+\nu_{23})/D \\
C_{21} &= -E_2\nu_{12}(1-\omega_1)(1-\omega_2)(1+\nu_{23})/D \\
C_{13} &= -E_1\nu_{21}(1-\omega_1)(1+(1-\omega_2)\nu_{23})/D \\
C_{31} &= -E_2\nu_{12}(1-\omega_1)(1+(1-\omega_2)\nu_{23})/D \\
C_{32} &= C_{23} = -E_2(1-\omega_2)(\nu_{23}+(1-\omega_1)\nu_{12}\nu_{21})/D
\end{aligned}
\tag{5.7}
$$

where $\boldsymbol{\sigma} = \mathbf{C} : \boldsymbol{\epsilon} = (\mathbf{S}^0 \ : \ \mathbf{M})^{-1} : \boldsymbol{\epsilon}$, $E_2\nu_{12} = E_1\nu_{21}$, and

$$
D = (1-\omega_2)\nu_{23}^2 + 2(1-\omega_1)(1-\omega_2)\nu_{12}\nu_{21}\nu_{23} + (1-\omega_1)(2-\omega_2)\nu_{12}\nu_{21} - 1 \tag{5.8}
$$

5.2.2 Concept of Equivalent Strain

Equivalent strains can take various forms [283, 23, 69, 284, 285, 286]. For isotropic materials, the most widely used equivalent strains are: the energy release rate thermodynamically conjugated to damage [283], the square root of the positive principal strains [23], and a modified von Mises strain [69]. Equivalent strain measures were introduced in damage evolution laws to capture unilateral effects, differences of behavior in tension and compression, and macroscopic hardening and softening due to mixed mode micro crack initiation and propagation. For direction dependent transverse isotropic materials, a complete set of new equivalent strains needs to be defined. Inspired from the stress invariants used in Hill's yield criterion [111] and in Hashin's failure criterion [287] (for unidirectional fiber composites), we introduce the following strain measures, which are strain invariants if axis 1 is

normal to the bedding planes:

$$
\begin{aligned}
I_1 &= \epsilon_{11} \\
I_2 &= \epsilon_{22} + \epsilon_{33} \\
I_3 &= \frac{1}{4}(\epsilon_{22} - \epsilon_{33})^2 + \epsilon_{23}^2 \\
I_4 &= \epsilon_{12}^2 + \epsilon_{13}^2 \\
I_5 &= 2\epsilon_{12}\epsilon_{13}\epsilon_{23} - \epsilon_{22}\epsilon_{13}^2 - \epsilon_{33}\epsilon_{12}^2
\end{aligned}
\tag{5.9}
$$

where I_3 is the square of the maximum transverse shear strain while I_4 is the square of the maximum axial shear strain. Following the form of Hill's and Hashin's models, we choose a quadratic damage criterion. Based on the invariants defined above, the most general form of a transversely isotropic *quadratic* failure criterion is

$$
A_1 I_1^2 + A_2 I_2^2 + A_3 I_3 + A_4 I_4 + B_{12} I_1 I_2 = 1 \tag{5.10}
$$

in which A_1, A_2, A_3, A_4 and B_{12} are material parameters. Field investigation and laboratory experiments [288, 289] indicate that there are two primary failure modes in transversely isotropic rock (Figure 5.2): the sliding mode, in which failure is controlled by the tensile and shear strength of the bedding planes, and the non-sliding mode, in which failure is controlled by the strength of the matrix material. In sliding mode, failure is the result of normal and shear stresses, and occurs along the bedding plane $(x_2 - x_3)$. In terms of continuum mechanics variables, it implies that failure in sliding mode is controlled by strain components $\epsilon_{11}, \epsilon_{12}$ and ϵ_{13}. In non-sliding mode, the normal direction of the failure surface is contained in the bedding plane. Due to material isotropy in the bedding plane $(x_2 - x_3)$, failure in non-sliding mode is controlled by all strain components except ϵ_{11}.

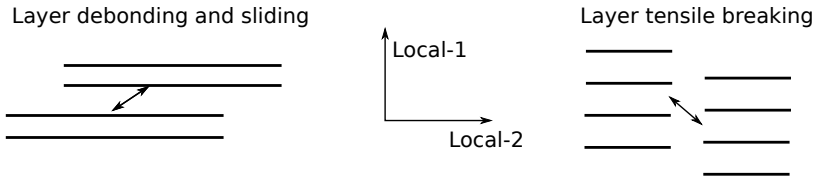

Figure 5.2: The two primary failure modes in transversely isotropic materials.

Consequently, we are seeking two failure criteria expressed in the following form:

$$\begin{aligned} A_1 I_1^2 + A_4 I_4 &= 1 \\ A_2 I_2^2 + A_3 I_3 + A_4 I_4 &= 1 \end{aligned} \tag{5.11}$$

for the sliding mode and the non-sliding mode, respectively.

We define the equivalent strain measures as $\epsilon_1^{eq}/\kappa_1^0 = \sqrt{A_1 I_1^2 + A_4 I_4}$ and $\epsilon_2^{eq}/\kappa_2^0 = \sqrt{A_2 I_2^2 + A_3 I_3 + A_4 I_4}$. Noting ϵ_{11}^{t0} (respectively ϵ_{22}^{t0}) and ϵ_{11}^{c0} (respectively ϵ_{22}^{c0}) the initial tensile and compressive strain thresholds for the sliding mode (respectively for the non-sliding mode), we have κ_1^0=ϵ_{11}^{t0} (respectively κ_2^0=ϵ_{22}^{t0}) in tension, κ_1^0=ϵ_{11}^{c0} (respectively κ_2^0=ϵ_{22}^{c0}) in compression. Hence the equivalent strain in the axial direction is constructed as:

$$\epsilon_{1j}^{eq} = \sqrt{I_1^2 + I_4 \left(\epsilon_{11}^{j0}/\epsilon_{12}^{s0}\right)^2} = \sqrt{(\epsilon_{11})^2 + ((\epsilon_{12})^2 + (\epsilon_{13})^2)\left(\frac{\epsilon_{11}^{j0}}{\epsilon_{12}^{s0}}\right)^2}, \quad j = t,\, c \tag{5.12}$$

we took $A_1^j = 1/(\epsilon_{11}^{j0})^2$ and $A_4 = 1/(\epsilon_{12}^{s0})^2$ where ϵ_{12}^{s0} is the initial out-of-bedding-plane shear strain threshold. Similarly, the equivalent strain in the transverse directions is defined as:

$$\begin{aligned} \epsilon_{2j}^{eq} &= \sqrt{I_2^2 + I_3\left(\frac{\epsilon_{22}^{j0}}{\epsilon_{23}^{s0}}\right)^2 + I_4\left(\frac{\epsilon_{22}^{j0}}{\epsilon_{12}^{s0}}\right)^2}, \quad j = t,\, c \\ \epsilon_{2j}^{eq} &= \sqrt{(\epsilon_{22}+\epsilon_{33})^2 + \frac{1}{4}\left(\frac{\epsilon_{22}^{j0}}{\epsilon_{23}^{s0}}\right)^2 [(\epsilon_{22}-\epsilon_{33})^2 + \epsilon_{23}^2] + \left(\frac{\epsilon_{22}^{j0}}{\epsilon_{12}^{s0}}\right)^2 (\epsilon_{12}^2 + \epsilon_{13}^2)} \end{aligned} \tag{5.13}$$

we took $A_2^j = 1/(\epsilon_{22}^{j0})^2$ and $A_3 = 1/(\epsilon_{23}^{s0})^2$, where ϵ_{23}^{s0} is the initial shear strain threshold within the bedding plane.

5.2.3 Damage Criteria and Evolution Laws in Tension

Since crack orientations and propagation modes are different in tension and compression [290, 291], we distinguish tensile and compressive damage components, noted $\omega_{it}, \omega_{ic}, i = 1, 2, 3$ respectively. Unlike Mazars' approach [24], in which total damage is calculated as the weighted average of tensile and compressive damage components, we consider that tensile damage components ω_{it} and compressive damage components ω_{ic} are two sets of independent internal state variables. When the volumetric strain $\epsilon_v = \epsilon_1 + \epsilon_2 + \epsilon_3$ is positive (respectively, negative), compressive damage components ω_{ic} (respectively, tensile damage components ω_{it}) are substituted into Equation 5.2 to construct the damage operator. As a result, unilateral effects due to crack closure can be captured. Damage components take values between 0 (no micro-crack in the direction considered) and 1 (no more stiffness in the direction considered).

Two loading surfaces are used to distinguish micro-crack propagation in the axial and transverse directions. For tensile damage, we consider the two following damage criteria:

$$g_{1t}(\boldsymbol{\epsilon}, \kappa_1) = \epsilon_{1t}^{eq} - \kappa_1, \quad g_{2t}(\boldsymbol{\epsilon}, \kappa_2) = \epsilon_{2c}^{eq} - \kappa_2 \tag{5.14}$$

Where the equivalent strains ϵ_i^{eq} are scalar measures of strain defined in the axial and transverse directions. κ_1 and κ_2 are the internal state variables that control the evolution of damage: they represent the equivalent strain thresholds before the initiation of damage in directions 1 and 2, respectively. After damage initiation, κ_1 and κ_2 are the largest equivalent strains ever reached during the past loading history of the material. Damage can only grow if the current stress state reaches the boundary of the elastic domain, $g_i = 0$. Karush-Kuhn-Tucker complementary conditions are used to account for loading-unloading stress

paths:

$$\begin{aligned} g_1 \leq 0, \quad \dot{\kappa}_1 \geq 0, \quad \dot{\kappa}_1 g_1 = 0 \\ g_2 \leq 0, \quad \dot{\kappa}_2 \geq 0, \quad \dot{\kappa}_2 g_2 = 0 \end{aligned} \tag{5.15}$$

Now, we establish a relationship between the internal state variables κ_1, κ_2, defined as the maximum equivalent strains ever encountered in the material, and the damage variable $\boldsymbol{\omega}$. Since both the internal variables and the damage components grow monotonically, it is admissible to postulate the evolution law of damage in the form $\omega_i = f(\kappa_i)$, $i = 1, 2$. The exact form of the function f should be identified from actual stress paths monitored in experiments, such as uniaxial stress-strain curve in axial and transverse directions. In the absence of such data, we assume that in tension, the axial damage component follows an exponential law, which reflects rapid micro crack propagation in mixed I-II mode:

$$\omega_{1t} = \begin{cases} 0, & \text{if } \kappa_1 \leq \epsilon_{11}^{t0} \\ 1 - \exp\left(-\frac{\kappa_1 - \epsilon_{11}^{t0}}{\alpha_{11}^t}\right), & \text{if } \kappa_1 > \epsilon_{11}^{t0} \end{cases} \tag{5.16}$$

where α_{11}^t is a material parameter that controls the damage growth rate. We use a similar evolution law for tensile damage growth in the transverse directions:

$$\lambda_{2t} = \frac{1}{2}\left(\chi_{2t} + \chi_{3t}\right) = \begin{cases} 0, & \text{if } \kappa_2 \leq \epsilon_{22}^{t0} \\ 1 - \exp\left(-\frac{\kappa_2 - \epsilon_{22}^{t0}}{\alpha_{22}^t}\right), & \text{if } \kappa_2 > \epsilon_{22}^{t0} \end{cases} \tag{5.17}$$

where α_{22}^t controls the ductility of the response in the transverse directions. Based on the definition of the equivalent strain ϵ_{2t}^{eq}, we split the transverse damage components as

follows:

$$\chi_{2t} = 2\lambda_{2t}\frac{\epsilon_{22}^2 + \epsilon_{22}\epsilon_{33} + (\frac{1}{4}\langle\epsilon_{22}-\epsilon_{33}\rangle^2 + \frac{1}{2}(\epsilon_{23})^2)\left(\frac{\epsilon_{22}^{t0}}{\epsilon_{23}^{s0}}\right)^2 + \epsilon_{12}^2\left(\frac{\epsilon_{22}^{t0}}{\epsilon_{12}^{s0}}\right)^2}{(\kappa_2)^2}$$
$$\chi_{3t} = 2\lambda_{2t}\frac{\epsilon_{33}^2 + \epsilon_{22}\epsilon_{33} + (\frac{1}{4}\langle\epsilon_{33}-\epsilon_{22}\rangle^2 + \frac{1}{2}(\epsilon_{23})^2)\left(\frac{\epsilon_{22}^{t0}}{\epsilon_{23}^{s0}}\right)^2 + \epsilon_{13}^2\left(\frac{\epsilon_{22}^{t0}}{\epsilon_{12}^{s0}}\right)^2}{(\kappa_2)^2} \tag{5.18}$$
$$\omega_{2t} = \begin{cases} \bar{\omega}_{2t}, & \text{if } \chi_{2t} \le \bar{\omega}_{2t} \\ \chi_{2t}, & \text{if } \chi_{2t} > \bar{\omega}_{2t} \end{cases}, \quad \omega_{3t} = \begin{cases} \bar{\omega}_{3t}, & \text{if } \chi_{3t} \le \bar{\omega}_{3t} \\ \chi_{3t}, & \text{if } \chi_{3t} > \bar{\omega}_{3t} \end{cases}$$

where we introduced the McAuley brackets: $\langle x\rangle = 0$ if $x < 0$, $\langle x\rangle = x$ if $x \ge 0$. $\bar{\omega}_{2t}$ and $\bar{\omega}_{3t}$ are the tensile damage values in the two transverse directions at the previous increment. Figure 5.3a below shows the evolution of tensile damage with the tensile equivalent strain: once the threshold is reached, damage evolves rapidly, and the growth rate slows down close to final failure.

5.2.4 Damage Criteria and Evolution Laws in Compression

Different from mixed mode crack propagation, pure mode II sliding in compression is confining (normal) stress dependent. We reconstruct the two compressive loading surfaces in axial and transverse directions as:

$$\begin{aligned} g_{1c}(\boldsymbol{\epsilon}, \kappa_1) &= \epsilon_{1c}^{eq} + \eta\langle(\sigma_2+\sigma_3)/2\rangle - \kappa_1 \\ g_{2c}(\boldsymbol{\epsilon}, \kappa_2) &= \epsilon_{2c}^{eq} + \eta\langle\sigma_1\rangle - \kappa_2 \end{aligned} \tag{5.19}$$

Where η controls the influence of the confining stress on compressive damage. Note that the McAuley brackets are introduced to account for compressive confining stress only. Similar to tensile loading functions in Equation 5.14, the internal state variables κ_1, κ_2 in Equation 5.19 represent the largest value taken by the terms $\epsilon_{1c}^{eq} + \eta\langle(\sigma_2+\sigma_3)/2\rangle$, $\epsilon_{2c}^{eq} + \eta\langle\sigma_1\rangle$ in the entire loading history of the material. Since geomaterials exhibit a pre-peak hardening and post-peak softening behavior for mode II sliding in compression [245], we choose an

evolution function $f(\kappa_1)$ with a low growth rate at the beginning and a high growth rate after the peak, as follows:

$$\omega_{1c} = \begin{cases} 0, & \text{if } \kappa_1 \leq \epsilon_{11}^{c0} \\ \frac{\exp\left[(\kappa_1 - \beta_{11}^c)/\alpha_{11}^c\right]}{1+\exp\left[(\kappa_1 - \beta_{11}^c)/\alpha_{11}^c\right]}, & \text{if } \kappa_1 > \epsilon_{11}^{c0} \end{cases} \tag{5.20}$$

where β_{11}^c and α_{11}^c are parameters that represent the initiation of softening in the absence of confinement and the damage growth rate in the axial direction, respectively. Figure 5.3b shows the evolution of compressive damage with the compressive equivalent strain. We define the evolution function $f(\kappa_2)$ in the transverse directions in a similar way as in the axial direction, as follows:

$$\lambda_{2c} = \frac{1}{2}\left(\chi_{2c} + \chi_{3c}\right) = \begin{cases} 0, & \text{if } \kappa_2 \leq \epsilon_{22}^{c0} \\ \frac{\exp\left[(\kappa_2 - \beta_{22}^c)/\alpha_{22}^c\right]}{1+\exp\left[(\kappa_2 - \beta_{22}^c)/\alpha_{22}^c\right]}, & \text{if } \kappa_2 > \epsilon_{22}^{c0} \end{cases} \tag{5.21}$$

in which we split the transverse damage components based on the definition of equivalent strain ϵ_{2c}^{eq} in Equation 5.13 and loading surface in Equation 5.19, as follows:

$$\begin{aligned} \chi_{2c} &= 2\lambda_{2c}\frac{\epsilon_{22}^2 + \epsilon_{22}\epsilon_{33} + \left(\frac{1}{4}\langle\epsilon_{22} - \epsilon_{33}\rangle^2 + \frac{1}{2}(\epsilon_{23})^2\right)\left(\frac{\epsilon_{22}^{c0}}{\epsilon_{23}^{s0}}\right)^2 + \epsilon_{12}^2\left(\frac{\epsilon_{22}^{c0}}{\epsilon_{12}^{s0}}\right)^2 + \frac{\eta\langle\sigma_1\rangle}{2}}{(\kappa_2)^2} \\ \chi_{3c} &= 2\lambda_{2c}\frac{\epsilon_{33}^2 + \epsilon_{22}\epsilon_{33} + \left(\frac{1}{4}\langle\epsilon_{33} - \epsilon_{22}\rangle^2 + \frac{1}{2}(\epsilon_{23})^2\right)\left(\frac{\epsilon_{22}^{c0}}{\epsilon_{23}^{s0}}\right)^2 + \epsilon_{13}^2\left(\frac{\epsilon_{22}^{c0}}{\epsilon_{12}^{s0}}\right)^2 + \frac{\eta\langle\sigma_1\rangle}{2}}{(\kappa_2)^2} \\ \omega_{2c} &= \begin{cases} \bar{\omega}_{2c}, & \text{if } \chi_{2c} \leq \bar{\omega}_{2c} \\ \chi_{2c}, & \text{if } \chi_{2c} > \bar{\omega}_{2c} \end{cases}, \quad \omega_{3c} = \begin{cases} \bar{\omega}_{3c}, & \text{if } \chi_{3c} \leq \bar{\omega}_{3c} \\ \chi_{3c}, & \text{if } \chi_{3c} > \bar{\omega}_{3c} \end{cases} \end{aligned} \tag{5.22}$$

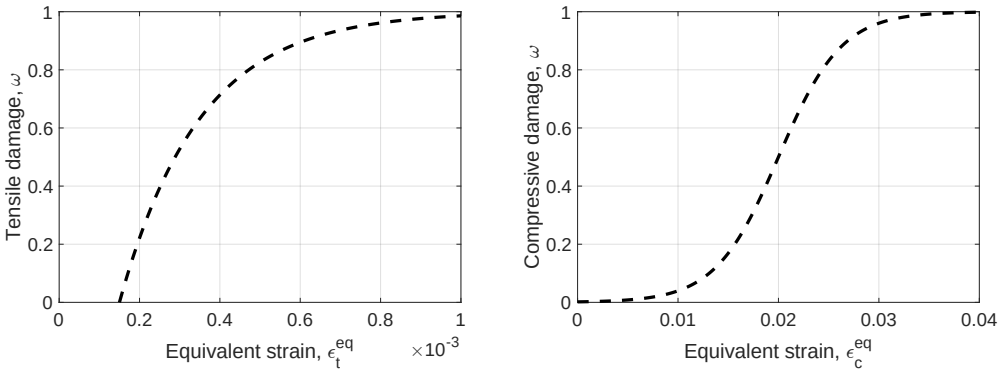

(a) Damage evolution in tension (b) Damage evolution in compression

Figure 5.3: Explicit damage evolution laws.

5.3 FEM Implementation and Validation

5.3.1 Anisotropic Nonlocal Regularization

The accumulation of damage leads to a softening behavior, which results in localized failure paths in finite element simulations. As explained in Section 4.2.4, the energy required to create a unit area of fracture, which should be a material constant, does not converge upon mesh refinement [75]. Mathematically, the partial differential equations governing quasi-static problems loose ellipticity, which makes the boundary problem ill-posed. Several regularization techniques exist to avoid mesh dependency and fracture localization, including: the introduction of integration-based variables in the constitutive model [67, 68, 284, 292], gradient-enhanced formulations [82, 70, 79, 84, 80], the micropolar (Cosserat) continuum theory [293, 89], and the local regularization of material properties based on element size and direction (crack band theory) [294, 295]. All of these regularization methods involve an internal length parameter, typically a characteristic length equal to 2 to 3 times the maximum grain size [73]. Note that the gradient theory requires additional boundary conditions, which have no physical meaning, to calculate the third order double stress tensor. The crack band theory fails to capture the process zone of macro fractures. The micropolar continuum theory is particularly suitable for modeling shear bands in granular

materials. Here, we adopt a versatile integral-based nonlocal regularization technique (the same as in Section 4.2.4), in which the damage evolution and subsequent stiffness reduction at a material point not only depend on the stress state at that point, but also on the stress of points located within a certain neighborhood, the size of which is controlled by internal length parameters. Numerically, we replace the local equivalent strains $\epsilon_{i,k}^{eq}$, used to check damage criteria, by their nonlocal counterparts $\overline{\epsilon}_{i,k}^{eq}$. The nonlocal equivalent strain $\overline{\epsilon}_{i,k}^{eq}$ is calculated as the weighted average of the local equivalent strain over an influence volume V, as follows:

$$\overline{\epsilon}_{i,k}^{eq}(\boldsymbol{x}) = \int_V \alpha(\boldsymbol{x},\boldsymbol{\xi})\epsilon_{i,k}^{eq}(\boldsymbol{\xi})\mathbf{d}V(\boldsymbol{\xi}), \quad (i = 1/2, k = t/c). \tag{5.23}$$

where $\boldsymbol{x}$ and $\boldsymbol{\xi}$ are the position vectors of the local point considered and of a point located in the influence volume, respectively. $\alpha(\boldsymbol{x},\boldsymbol{\xi})$ is a weight function, which decreases monotonically when the distance $r = \|\boldsymbol{x} - \boldsymbol{\xi}\|$ increases. In addition, it has to satisfy the normalization condition. We ensure the partition of unity by defining $\alpha(\boldsymbol{x},\boldsymbol{\xi})$ as:

$$\alpha(\boldsymbol{x},\boldsymbol{\xi}) = \frac{\alpha_0(\boldsymbol{x},\boldsymbol{\xi})}{\int_V \alpha_0(\boldsymbol{x},\boldsymbol{\xi})\mathbf{d}V(\boldsymbol{\xi})}. \tag{5.24}$$

For isotropic materials, the weight function $\alpha_0(\boldsymbol{x},\boldsymbol{\xi})$ is often defined as a Gauss function (normal distribution) or a bell-shaped function, with a single internal length. For transversely isotropic materials however, the nonlocal influence zone is direction dependent. Due to the weakening effects of the bedding plane, the development of damage at a point has more influence when cracks propagate in planes that contain the transverse directions than the axial direction (Figure 5.1). Noting l_{ci} the internal length in direction i, we have: $l_{c3} = l_{c2} > l_{c1}$. Based on these considerations, we propose the following modified bell-shaped weight function:

$$\alpha_0(\boldsymbol{x},\boldsymbol{\xi}) = \Big\langle 1 - \sum_{i=1}^{3} \frac{\|x_i - \xi_i\|^2}{l_{ci}^2} \Big\rangle^2. \tag{5.25}$$

The internal lengths l_{ci} provide the size of the volume of influence (Figure 5.4), therefore no cut-off is needed (unlike in the Gauss function).

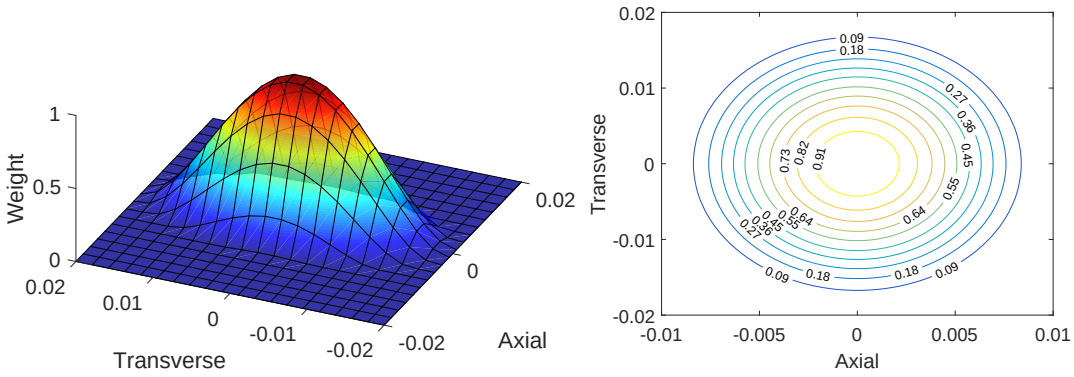

Figure 5.4: Modified bell-shaped weight function for the nonlocal formulation, with $l_{c1} = 0.01, l_{c2} = 0.02$.

In a Finite Element code, nonlocal averaging and integration are performed by summation over Gauss points located inside the influence zone [69]. For instance, the nonlocal equivalent strain is calculated as follows:

$$\bar{\epsilon}^{eq}_{i,k}(\boldsymbol{x}) = \frac{\sum_{J=1}^{N_J} \alpha(\|\boldsymbol{T}(\boldsymbol{x} - \boldsymbol{\xi}_J)^T\|)\epsilon^{eq}_{i,k}(\boldsymbol{\xi}_J)\Delta V_J}{\sum_{J=1}^{N_J} \alpha(\|\boldsymbol{T}(\boldsymbol{x} - \boldsymbol{\xi}_J)^T\|)\Delta V_J} \tag{5.26}$$

in which N_J is the total number of Gauss points located within the influence zone. ΔV_J is the integration volume associated with the j^{th} neighboring Gauss point. $\boldsymbol{T}$ is the rotation matrix that transforms global coordinates to local coordinates. In plane strain conditions (adopted in this chapter), we have:

$$\mathbf{T} = \begin{pmatrix} cos\phi & -sin\phi \\ sin\phi & cos\phi \end{pmatrix} \tag{5.27}$$

where ϕ is the counter-clockwise angle between the global and local coordinate systems. In Equation 5.26, the distance $\|x_i - \xi_i\|$ first introduced in Equation 4.21 was replaced by the components of vector $\boldsymbol{T}(\boldsymbol{x} - \boldsymbol{\xi}_J)^T$.

5.3.2 Analytical expression of the tangent stiffness matrix

Since the damage evolution laws are expressed explicitly, no iteration is needed at the Gauss point to update the state of stress, strain and damage. However, due to the nonlocal formulation adopted here, the calculation of state and internal variables at a point requires calculating the average of the values taken by those variables at the Gauss points located in the influence zone, as explained in Equation 5.26. Consequently, terms need to be added to the global stiffness matrix due to nonlocal enhancement. The global force balance equation can be expressed in Voigt notation as:

$$\boldsymbol{R} = \boldsymbol{F}^{\text{int}} - \boldsymbol{F}^{\text{ext}} = \int_{\Omega} \boldsymbol{B}^T \boldsymbol{\sigma} \mathrm{d}\Omega - \Big(\int_{\Gamma_{\mathrm{t}}} \boldsymbol{N} \bar{\boldsymbol{t}} \mathrm{d}\Gamma + \int_{\Omega} \boldsymbol{N} \boldsymbol{b} \mathrm{d}\Omega \Big) = 0 \tag{5.28}$$

where $\boldsymbol{B}$ is the strain-displacement matrix (derivative of shape functions with respect to the coordinates) and $\boldsymbol{N}$ is the shape function vector. $\bar{\boldsymbol{t}}$ and $\boldsymbol{b}$ are traction and body forces applied to the system, respectively. Linearizing the governing equation (5.28) at iteration k of the increment step $n+1$ with respect to the unknown $\boldsymbol{u}$, we have

$$\boldsymbol{R}_{n+1}^{k+1} = \boldsymbol{R}_{n+1}^{k} + \boldsymbol{J} \mathrm{d}\boldsymbol{u}_{n+1}^{k+1} = 0 \tag{5.29}$$

where $\boldsymbol{J} = \boldsymbol{R}_{,\boldsymbol{u}}$ is the Jacobian matrix (tangent stiffness matrix). Finding the analytical expression of $\mathbb{J}$ is critical to achieve a quadratic convergence rate. To this aim, we follow the procedure of Jirásek and Patzák [286]. First, we express the internal force $\boldsymbol{F}^{\text{int}}$ in terms of Gauss point contributions as

$$\boldsymbol{F}^{\text{int}} = \sum_{I=1}^{N_I} w_I \boldsymbol{B}_I^T \boldsymbol{\sigma}_I = \sum_{I=1}^{N_I} w_I \boldsymbol{B}_I^T \mathbb{C}(\omega_{1t}, \omega_{2t}) \boldsymbol{B}_I \boldsymbol{u} \tag{5.30}$$

where N_I is the total number of Gauss points, and w_I are the corresponding integration weights. We substitute Equation 5.30 into the global force balance equation (5.28), and

we use $\boldsymbol{J} = \boldsymbol{R}_{,\boldsymbol{u}}$ to obtain the Jacobian. Note that the damage components $(\omega_{it}, i = 1, 2)$ are indirect functions of displacement $\boldsymbol{u}$. According to the chain rule, the derivative, with respect to the displacement, of the stiffness tensor involved in the expression of $\boldsymbol{F}^{\text{int}}$ reads:

$$\frac{\partial \mathbb{C}(\omega_{it})}{\partial \boldsymbol{u}} = \frac{\partial \mathbb{C}}{\partial \omega_{it}} \frac{\partial \omega_{it}}{\partial \kappa_i} \frac{\partial \kappa_i}{\partial \bar{\epsilon}_{it}^{eq}} \frac{\mathrm{d}\bar{\epsilon}_{it}^{eq}}{\mathrm{d}\boldsymbol{u}} \tag{5.31}$$

For the plane strain case studied in this chapter, it is posible to obtain the explicit expression of each of the partial derivatives involved in the above equation. In particular, the derivative of stiffness with respect to damage is: Where $\partial_{\omega_{it}}\mathbb{C}$ is expressed as

$$\frac{\partial \mathbb{C}}{\partial \omega_{it}} = \frac{1}{D^2} \begin{pmatrix} \partial_{\omega_{it}} C_{11} D - \partial_{\omega_{it}} D C_{11} & \partial_{\omega_{it}} C_{12} D - \partial_{\omega_{it}} D C_{12} & 0 \\ \partial_{\omega_{it}} C_{12} D - \partial_{\omega_{it}} D C_{12} & \partial_{\omega_{it}} C_{22} D - \partial_{\omega_{it}} D C_{22} & 0 \\ 0 & 0 & \partial_{\omega_{it}} C_{33} D^2 \end{pmatrix} \tag{5.32}$$

in which

$$\begin{aligned}
\partial_{\omega_{1t}} D &= -2(1-\omega_{2t})\nu_{12}\nu_{21}\nu_{23} - (2-\omega_{2t})\nu_{12}\nu_{21} \\
\partial_{\omega_{2t}} D &= -\nu_{23}^2 - 2(1-\omega_{1t})\nu_{12}\nu_{21}\nu_{23} - (1-\omega_{1t})\nu_{12}\nu_{21} \\
\partial_{\omega_{1t}} C_{11} &= -E_1((1-\omega_{2t})\nu_{23}^2 - 1) \\
\partial_{\omega_{2t}} C_{11} &= -E_1\nu_{23}^2(1-\omega_{1t}) \\
\partial_{\omega_{1t}} C_{22} &= -E_2\nu_{12}\nu_{21}(1-\omega_{2t}) \\
\partial_{\omega_{2t}} C_{22} &= -E_2((1-\omega_{1t})\nu_{12}\nu_{21} - 1) \\
\partial_{\omega_{1t}} C_{33} &= -G_{12}(1-\omega_{2t}) \\
\partial_{\omega_{2t}} C_{33} &= -G_{12}(1-\omega_{1t}) \\
\partial_{\omega_{1t}} C_{12} &= E_1\nu_{21}(1-\omega_{2t})(1+\nu_{23}) \\
\partial_{\omega_{2t}} C_{12} &= E_1\nu_{21}(1-\omega_{1t})(1+\nu_{23})
\end{aligned} \tag{5.33}$$

According to Equations 5.16 and 5.18, the partial derivatives of the damage components

with respect to κ_i can be calculated as

$$\frac{\partial \omega_{1t}}{\partial \kappa_1} = \frac{1}{\alpha_{11}^t} \exp\left(-\frac{\kappa_1 - \epsilon_{11}^{t0}}{\alpha_{11}^t}\right), \quad \frac{\partial \omega_{2t}}{\partial \kappa_2} = \frac{1}{\alpha_{22}^t} \exp\left(-\frac{\kappa_2 - \epsilon_{22}^{t0}}{\alpha_{22}^t}\right). \tag{5.34}$$

Note that the partial derivative terms

$$\frac{\partial \kappa_1}{\partial \bar{\epsilon}_{1t}^{eq}} = \begin{cases} 0, & \text{if } \bar{\epsilon}_{1t}^{eq} < \kappa_1 \\ 1, & \text{if } \bar{\epsilon}_{1t}^{eq} = \kappa_1 \end{cases}, \quad \frac{\partial \kappa_2}{\partial \bar{\epsilon}_{2t}^{eq}} = \begin{cases} 0, & \text{if } \bar{\epsilon}_{2t}^{eq} < \kappa_2 \\ 1, & \text{if } \bar{\epsilon}_{2t}^{eq} = \kappa_2 \end{cases} \tag{5.35}$$

are actually the loading-unloading indicators.

Differentiating the nonlocal strains defined in Equation 5.23 with respect to displacement, we obtain

$$\frac{\partial \bar{\epsilon}_{it}^{eq}(\boldsymbol{x}_I)}{\partial \boldsymbol{u}} = \sum_{J=1}^{N_J} w_J \alpha_{IJ} \left(\frac{\partial \epsilon_{it}^{eq}}{\partial \boldsymbol{u}}\right)_J = \sum_{J=1}^{N_J} w_J \alpha_{IJ} \left(\frac{\mathrm{d}\epsilon_{it}^{eq}}{\mathrm{d}\boldsymbol{\epsilon}}\right)_J \frac{\partial \boldsymbol{\epsilon}_J}{\partial \boldsymbol{u}} = \sum_{J=1}^{N_J} w_J \alpha_{IJ} \left(\frac{\mathrm{d}\epsilon_{it}^{eq}}{\mathrm{d}\boldsymbol{\epsilon}}\right)_J \boldsymbol{B}_J \tag{5.36}$$

in which:

$$\alpha_{IJ} = \frac{\alpha(\boldsymbol{T}(\boldsymbol{x}_I - \boldsymbol{\xi}_J)^T)}{\sum_{J=1}^{N_J} \alpha(\boldsymbol{T}(\boldsymbol{x}_I - \boldsymbol{\xi}_J)^T) w_J} \tag{5.37}$$

and in which we changed the notation ΔV_J in Equation 5.26 to w_J in Equation 5.36. N_J is the total number of Gauss points within the nonlocal influence zone for Gauss point I. $\mathrm{d}\epsilon_{it}^{eq}/\mathrm{d}\boldsymbol{\epsilon}$ are vectors, which can be calculated from the definition of equivalent strain as

$$\frac{\mathrm{d}\epsilon_{1t}^{eq}}{\mathrm{d}\boldsymbol{\epsilon}} = \frac{1}{\epsilon_{1t}^{eq}} \begin{bmatrix} \epsilon_{11} & 0 & \epsilon_{12} \left(\frac{\epsilon_{11}^{t0}}{\epsilon_{12}^{s}}\right)^2 \end{bmatrix}, \quad \frac{\mathrm{d}\epsilon_{2t}^{eq}}{\mathrm{d}\boldsymbol{\epsilon}} = \frac{1}{\epsilon_{2t}^{eq}} \begin{bmatrix} 0 & \epsilon_{22} & \epsilon_{12} \left(\frac{\epsilon_{22}^{t0}}{\epsilon_{12}^{s0}}\right)^2 \end{bmatrix} \tag{5.38}$$

Combining all the above expressions, we can obtain the analytical expression of the Jacobian matrix by differentiating the internal force vector $\boldsymbol{F}^{\text{int}}$ with respect to the dis-

placement vector $\boldsymbol{u}$ as

$$\begin{aligned}\boldsymbol{J} &= \sum_{I=1}^{N_I} w_I \boldsymbol{B}_I^T \mathbb{C} \boldsymbol{B}_I + \sum_{I=1}^{N_I} \sum_{i=1}^{2} w_I \boldsymbol{B}_I^T \frac{\partial \mathbb{C}(\omega_{it})}{\partial \boldsymbol{u}} \boldsymbol{B}_I \boldsymbol{u}_I \\ &= \sum_{I=1}^{N_I} w_I \boldsymbol{B}_I^T \mathbb{C} \boldsymbol{B}_I + \sum_{I=1}^{N_I} \sum_{J=1}^{N_J} \sum_{i=1}^{2} w_I w_J \alpha_{IJ} \boldsymbol{B}_I^T \Big(\frac{\partial \mathbb{C}}{\partial \omega_i} \frac{\partial \omega_{it}}{\partial \kappa_i} \frac{\partial \kappa_i}{\partial \epsilon_{it}^{eq}} \Big)_I \Big(\frac{\mathrm{d} \bar{\epsilon}_{it}^{eq}}{\mathrm{d} \boldsymbol{\epsilon}} \Big)_J \boldsymbol{B}_J \boldsymbol{B}_I \boldsymbol{u}_I \end{aligned} \tag{5.39}$$

Note that we only obtain the analytical expression of the Jacobian when the material is in tension. Under compression, the yield criteria (Equation 5.19) involve stress terms, and it is impossible to find analytical expressions for the derivative of $\partial \kappa_I / \partial \bar{\boldsymbol{\epsilon}}_{ic}^{eq}$. Thus the Jacobian is calculated computationally. In the following, the sub-/super- scripts t/c are dropped and only the tensile damage cases are simulated. For compressive damage cases, please refer to the publication [162].

5.3.3 Arc Length Control

The degradation of stiffness due to damage induces strain softening, which may result in a global force-displacement curve that exhibits multiple limit points (snap through) and a descending curve (snap-back). A standard load controlled or displacement controlled algorithm based on Newton-Raphson iteration scheme is insufficient to find localized post-peak solutions. In order to overcome this limitation, we adopt an arc length control algorithm, initially proposed by Riks [296], as illustrated in Figure 5.5.

We rewrite the general equilibrium equation (5.28) of a nonlinear system as

$$\boldsymbol{F}^{\text{int}}(\boldsymbol{u}) - \boldsymbol{F}^{\text{ext}} = \boldsymbol{0} \quad \rightarrow \quad \boldsymbol{F}^{\text{int}}(\boldsymbol{u}) - \lambda \boldsymbol{q} = \boldsymbol{0} \tag{5.40}$$

where $\boldsymbol{F}^{\text{int}}$ and $\boldsymbol{F}^{\text{ext}}$ are the internal and external forces, and λ is a load scaling parameter. In the arc length control method, the non-linear system of equations has to be solved for the displacement vector $\boldsymbol{u}$ and the load scaling parameter λ. We note $(\boldsymbol{u}_0, \lambda_0)$ the converged

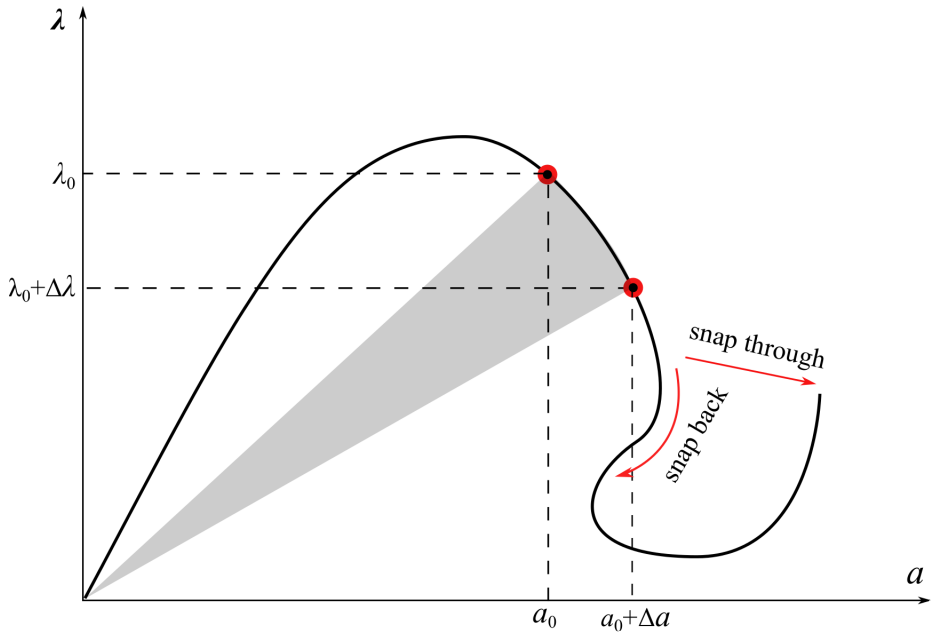

Figure 5.5: Principle of the arc-length control method. a denotes a normalized displacement, λ is the load scaling parameter. The shaded area is equal to the energy dissipation $\tau = \frac{1}{2}\boldsymbol{q}^T(\lambda_0 \Delta a - \Delta\lambda a_0)$ within an increment.

solution at the previous load increment. Noting $\Delta\boldsymbol{u}$ and $\Delta\lambda$ the variations of displacements and scaling load parameter over one increment, we have:

$$\boldsymbol{R} = \boldsymbol{F}^{\text{int}}(\boldsymbol{u}_0 + \Delta\boldsymbol{u}) - (\lambda_0 + \Delta\lambda)\boldsymbol{q} = \boldsymbol{0} \tag{5.41}$$

in which $\boldsymbol{R}$ is the residual. In general, Equation 5.41 cannot be satisfied without providing corrections $(\delta\boldsymbol{u}, \delta\lambda)$. At convergence, the residual tends to zero and we have:

$$\boldsymbol{R} = \boldsymbol{F}^{\text{int}}(\boldsymbol{u}_0 + \Delta\boldsymbol{u} + \delta\boldsymbol{u}) - (\lambda_0 + \Delta\lambda + \delta\lambda)\boldsymbol{q} = \boldsymbol{0} \tag{5.42}$$

Upon linearization at point $(\boldsymbol{u}_0 + \Delta\boldsymbol{u}, \lambda_0 + \delta\lambda)$, Equation 5.42 becomes:

$$\boldsymbol{F}^{\text{int}}(\boldsymbol{u}_0 + \Delta\boldsymbol{u}) + \left(\frac{\partial \boldsymbol{F}^{\text{int}}(\boldsymbol{u})}{\partial \boldsymbol{u}}\right)_{\boldsymbol{u}_0+\Delta\boldsymbol{u}} \cdot \delta\boldsymbol{u} - (\lambda_0 + \Delta\lambda + \delta\lambda)\boldsymbol{q} = \boldsymbol{0} \tag{5.43}$$

The derivative of the internal force vector with respect to displacement is the consistent

tangent stiffness matrix (analytical Jabobian matrix) $\boldsymbol{J}$. Thus, the system of equations can be rewritten as:

$$\boldsymbol{J}_{\boldsymbol{u}_0+\Delta\boldsymbol{u}} \cdot \delta\boldsymbol{u} - \delta\lambda\boldsymbol{q} = -\left(\boldsymbol{F}^{\text{int}}(\boldsymbol{u}_0 + \Delta\boldsymbol{u}) - (\lambda_0 + \Delta\lambda)\boldsymbol{q}\right) = -\boldsymbol{R} \tag{5.44}$$

Since the scaling load factor $\delta\lambda$ is unknown, one more equation is needed in addition to the equilibrium equation (5.42) in order to solve for both $\delta\boldsymbol{u}$ and $\delta\lambda$. The basic idea of the arc-length control method is to express a constraint that controls the iterative process to ensure that solutions obtained at convergence are indeed on the constitutive stress/strain curve. The most widely used constraint, proposed by Crisfield [297] is called spherical arc length control and involves the global norm of the displacement increment. The main challenge of the spherical arc length control method is to identify the right loading factors from the quadratic form of the constraint (complex roots). As a remedy, May and Duan [298] proposed a local version of the normal-plane arc-length control method, in which only a limited number of degrees of freedom associated with softening development are involved to form the constraint. For this method, effort is needed to identify the suitable set of degree of freedoms. In this chapter, we adopted the energy dissipation based arc length control method proposed by Verhoosel et al. [299]. As shown in Figure 5.5, the constraint is expressed as:

$$g = \frac{1}{2}\boldsymbol{q}^T(\lambda_0\Delta\boldsymbol{u} - \Delta\lambda\boldsymbol{u}_0) - \Delta l = 0 \tag{5.45}$$

where Δl is called the arc length parameter that controls the size of each increment step. Combine with Equation 5.40, the updated equilibrium function can be expressed as

$$\boldsymbol{R} = \begin{bmatrix} \boldsymbol{F}^{\text{int}}(\boldsymbol{u}) - \lambda\boldsymbol{q} \\ g \end{bmatrix} = \begin{bmatrix} \boldsymbol{0} \\ 0 \end{bmatrix} \tag{5.46}$$

We linearize the above equation with respect to displacements at the equilibrium itera-

tion k, within the incremental step $n+1$. We have

$$\boldsymbol{R}_{n+1}^{k+1} = \boldsymbol{R}_{n+1}^{k} + \begin{bmatrix} \boldsymbol{J} & -\boldsymbol{q} \\ g_{,\boldsymbol{u}} & g_{,\lambda} \end{bmatrix}_{n+1}^{k} \begin{bmatrix} \delta\boldsymbol{u} \\ \delta\lambda \end{bmatrix}_{n+1}^{k} = \boldsymbol{0} \tag{5.47}$$

where the Jacobian $\boldsymbol{J}$ is derived in Equation 5.39. The derivatives of the constraint with respect to the unknowns are:

$$\frac{\partial g}{\partial \boldsymbol{u}} = \frac{1}{2}\lambda_0 \boldsymbol{q}^T, \quad \frac{\partial g}{\partial \lambda} = -\frac{1}{2}\boldsymbol{q}^T \boldsymbol{u}_0. \tag{5.48}$$

It is clear from above equations that only the Jacobian $\boldsymbol{J}$ within the consistent tangent matrix needs to be updated for each iteration, the rest parts only need update at the start of each increment.

5.3.4 Simulation of Anisotropic Fracture Localization in Three-point Bending Test

We implemented the proposed anisotropic damage damage model with arc length solution strategy into an open source package called 'Object Oriented Finite Element Method' (OOFEM) [276, 277]. To test the ability of the model to simulate mesh-independent and direction dependent fracture propagation in mixed mode, we solve boundary value problems of three-point bending tests. The specimen geometry, notch size and boundary conditions are shown in Figure 5.6. Linear triangular elements are used in plane strain conditions. The transverse characteristic length l_{c2} is set to 20mm (internal length parallel to the bedding). We study various ratios $R = l_{c2}/l_{c1}$ to investigate the influence of nonlocal anisotropy on the global response. All the other constitutive parameters used are listed in Table 5.1. Note that the elasticity constants are calibrated against North Dakota Bakken shale [162]. The other parameters are assumed to be within the range of a typical shale.

Table 5.1: Material parameters used in the sensitivity analysis.

Direction	Elasticity			Shear	Tension	
Axial	E_1/GPa	ν_{12}	G_{12}/GPa	ϵ_{12}^{s0}	ϵ_{11}^{t}	α_{11}^{t}
	3.59	0.22	14.68	1.8×10^{-4}	1.5×10^{-4}	3.0×10^{-4}
Transverse	E_2/GPa	ν_{23}		ϵ_{23}^{s0}	ϵ_{22}^{t}	α_{22}^{t}
	3.77	0.33		2.6×10^{-4}	2.5×10^{-4}	4.0×10^{-4}

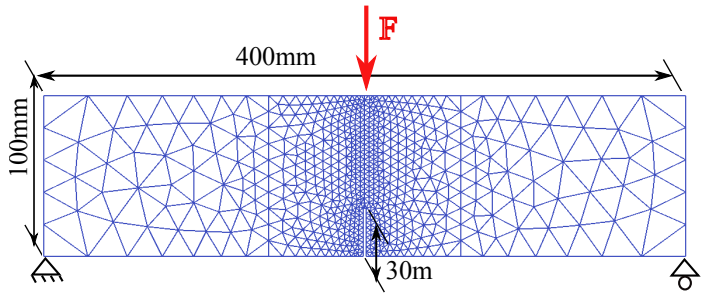

Figure 5.6: Geometry and boundary conditions adopted in the three-point bending test.

Influence of nonlocal enhancement We first test the nonlocal regularization technique by simulating the three point bending test with and without nonlocal enhancement, for three different mesh densities. In all tests, the loading direction is perpendicular to the bedding plane (orientation noted $\theta = 90°$) and the internal length ratio is set to $R = 2$. Figure 5.7 shows the post-failure distribution of the transverse damage component ω_2, which corresponds to vertical cracks perpendicular to the bedding plane that propagate by layer breaking (non-sliding mode). Comparing Figures 5.7(a) and (b), we note that simulations done with the local model exhibit a strong mesh dependency: the width of the fracture process zone is one element in size, no matter what the size of the elements is. As a result, the energy dissipated tends to zero upon mesh refinement. For very fine meshes, no convergence is reached. On the contrary, no mesh dependence is noted with the nonlocal model, as shown in Figures 5.7(c) and (d). Figure 5.10a shows the variations of the vertical force with vertical displacement at the node where the external load is applied. The peak force and subsequent softening behavior match for all simulations done with the nonlocal model, whereas they differ in the simulations done with the local model. Results

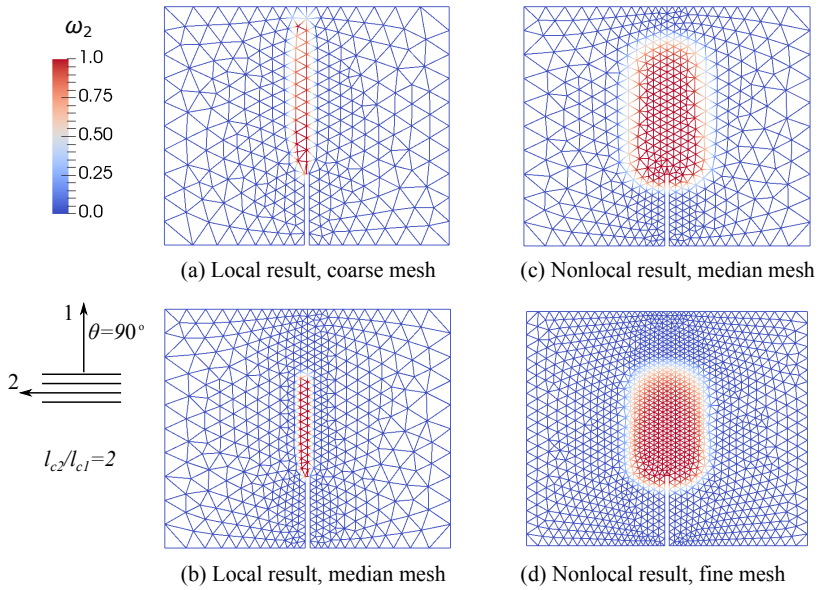

Figure 5.7: Distribution of damage along local axis-2 (i.e. vertical cracks perpendicular to the bedding plane) obtained in the three-point bending tests, without and with nonlocal enhancement, for various mesh densities. In all cases, bedding orientation angle is $\theta = 90°$, and the internal length ratio is $l_{c2}/l_{c1} = 2$.

thus confirm that the regularization technique not only alleviates mesh dependency for the failure path, but also for the global response of the domain. Note that in this particular test, nonlocal enhancement results in an increased stiffness of the domain, which turns out to be 2-3 times larger than that obtained with the local model. This points out the importance of proper calibration of the internal length parameters.

Influence of the bedding orientation (intrinsic anisotropy) Now that we showed that the nonlocal model alleviates mesh dependency, we perform all the simulations with the median-sized mesh. Figure 5.8 shows the damage process zone for different bedding orientations, and highlights the underlying failure mechanism. When the loading force is parallel to the bedding plane ($\theta = 0°$), only axial damage (ω_1) develops, wich corresponds to weak plane debonding. Damage propagates in pure mode I right above the notch. In the case of $\theta = 30°$, failure in mixed mode is observed. Damage propagates in both the axial (ω_1) and transverse (ω_2) directions of the bedding coordinate system. The failure path initially follows the bedding direction, and then turns up to be parallel to the loading force

direction. The extent of the damage zone is larger for ω_1 than ω_2. Similarly, when the bedding orientation angle is 60° with respect to the horizontal axis, damage propagates in mixed mode in both axial and transverse directions (ω_1, ω_2). The adopted resolution algorithm still has some shortcomings when the global response exhibits severe snap back behavior: convergence issues still exist and it is impossible to obtain the final expected damage zone. Here, we show the intermediate damage process zone, obtained just before the calculation stopped: at this stage, damage propagates mostly along the bedding plane; alignment with the loading force has just started. When the bedding plane is horizontal ($\theta = 90^\circ$), the damage zone aligns with the notch like in the case of a vertical bedding plane ($\theta = 0^\circ$), but failure is mostly due to layer breakage and not weak plane debonding: $\omega_2 > \omega_1$. As expected, the overall size of the damage process zone increases as the angle θ between the loading direction and the transverse bedding plane direction increases. Figure 5.10b shows the load-deflection curves obtained at the node where the external force is applied, for the four cases simulated. The maximum load force required to induce failure increases as the bedding orientation angle θ increases. This could be expected: weak plane debonding at $\theta = 0^\circ$ requires less energy than layer breakage at $\theta = 90^\circ$. Note that the arc length control method employed in the resolution algorithm makes it possible to predict the snap back behavior (decreasing load with decreasing displacement) in the case of $\theta \neq 90^\circ$.

Influence of the ratio of internal lengths (microstructure) We analyze the influence of the internal length ratio $R = l_{c2}/l_{c1}$ for $l_{c2} = 20$ mm (Figure 5.9). We use the median sized mesh and we study two bedding orientations: $\theta = 0^\circ, 90^\circ$. Damage propagates in mode I due to weak layer debonding in the case of $\theta = 0^\circ$, and due to layer breakage in the case of $\theta = 90^\circ$. Since the extent of the influence zone in the transverse direction is the same in all simulations (i.e., l_{c2} is fixed), the width of the transverse damage process zone is the same for all simulations with $\theta = 90^\circ$. By contrast, the length of the transverse damage zone increases with l_{c1}. Similarly, for $\theta = 0^\circ$, the area of the axial damage zone

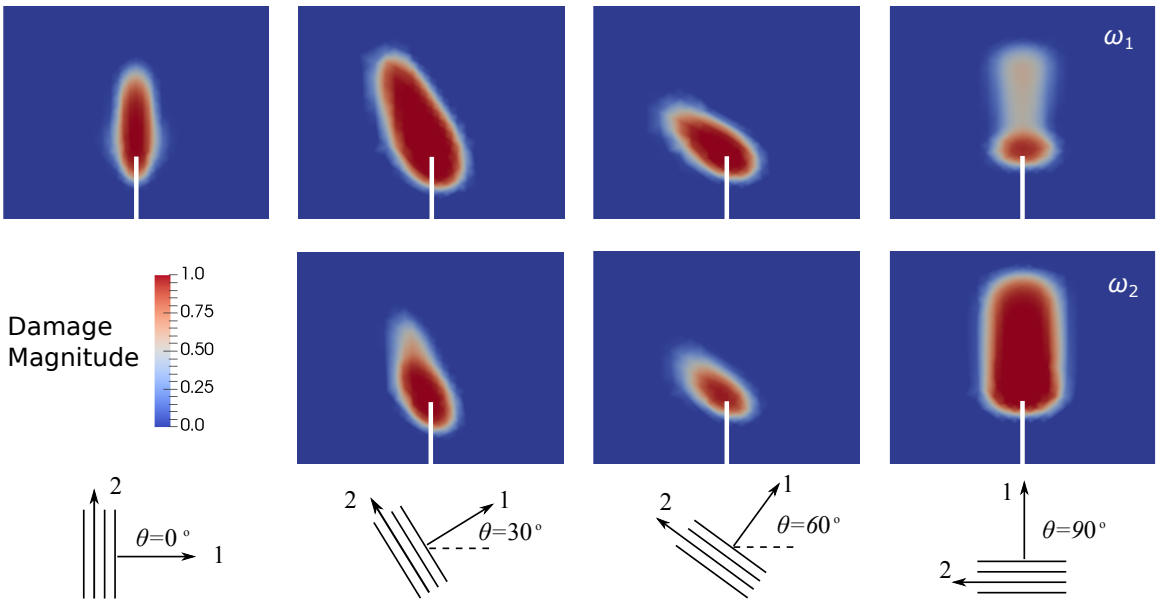

Figure 5.8: Spatial distribution of the tensile damage components expressed in the local coordinate system of the bedding plane, for loads applied at an angle $\theta = 0°, 30°, 60°, 90°$ compared to the transverse direction of the bedding plane.

increases with l_{c1} (i.e. increases when $R = l_{c2}/l_{c1}$ decreases). Microstructure anisotropy, represented by the internal length parameters, thus translates into anisotropy of the damage process zone. When comparing the load-displacement curves (Figure 5.10), we note that for both $\theta = 0°$ and $90°$, a higher peak force is reached for a lower internal length ratio R (i.e. for an increasing internal length l_{c1}). For $\theta = 0°$, we note that the post-peak portion of the load-displacement curves match. We hypothesize that the internal length l_{c2}, fixed to the same value in all the simulations, controls the post-peak softening behavior. The exceptionally high value of the peak force for $R = 1$, $\theta = 0°$ can be explained by the large size of the influence zone in that particular case, delimited by the circles in Figure 5.9.

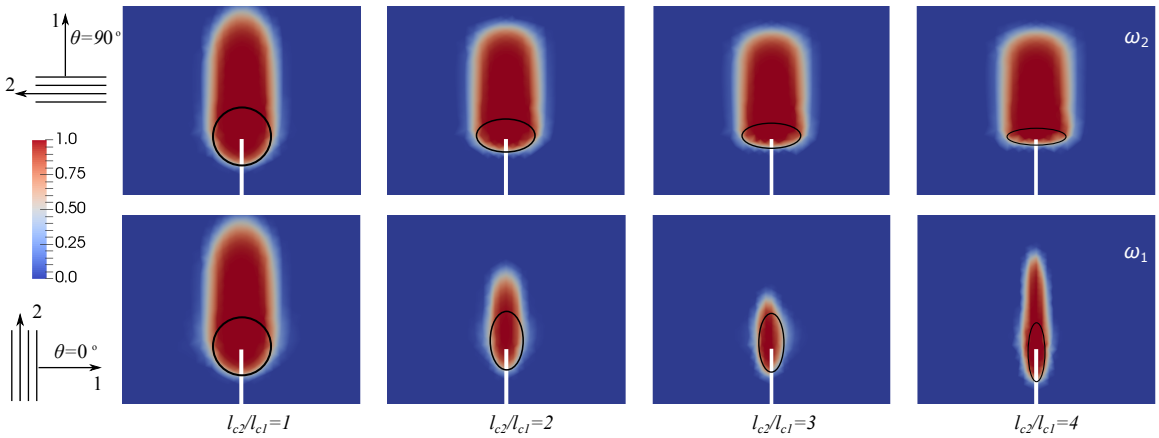

Figure 5.9: Spatial distribution of the tensile damage component in the transverse direction 2 (cracks perpendicular to the bedding plane) for orientation angle $\theta = 90°$, and in the axial direction 1 (cracks parallel to the bedding plane) for orientation angle $\theta = 0°$, for various internal length ratios defined as $R = l_{c2}/l_{c1}$.

5.4 Strong and Weak Form of the Hydro-Mechanical Coupled Governing Equations for Saturated Porous Media

5.4.1 Strong formulation

Hydraulic fracturing in porous media is a complex problem, which involves coupled physical processes that happen simultaneously, mainly: micro-crack propagation and coalescence in the solid porous matrix; fluid flow through the porous medium; fluid flow within the macro-fracture; fluid exchange between the porous matrix and the fracture. Correspondingly, the governing equations required to model these processes numerical include: momentum balance equations and constitutive laws for predicting the deformation field and micro crack development in the solid matrix (we will use the damage model proposed in Section 5.2) and the propagation of macro fractures (we will use a cohesive traction-separation law); fluid mass balance equation and fluid transport constitutive equation, both in the solid matrix and in the macro-fracture.

We start with the classical Biot theory [300] to describe the mechanical behavior of elastic porous media saturated with a single-phase fluid. Following Dormieux's approach [13], we consider that the development of micro-cracks (damage) governed by the equa-

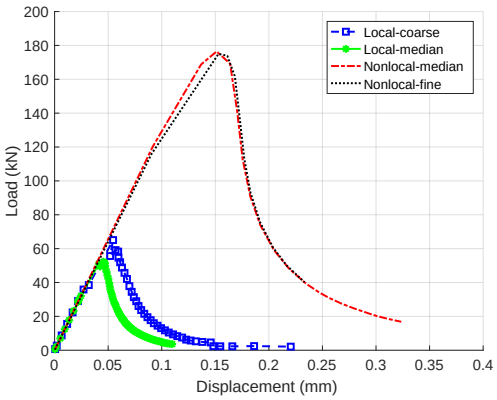

(a) Force-displacement curves with and without nonlocal enhancement.

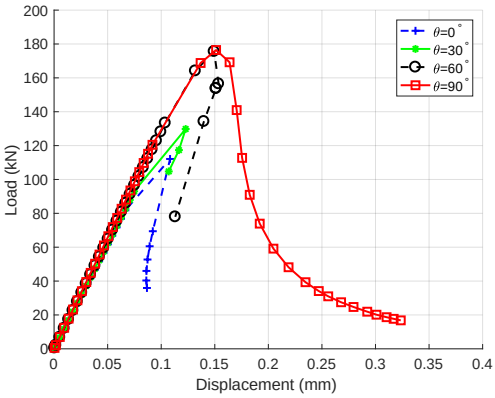

(b) Force-displacement curves for various bedding orientations.

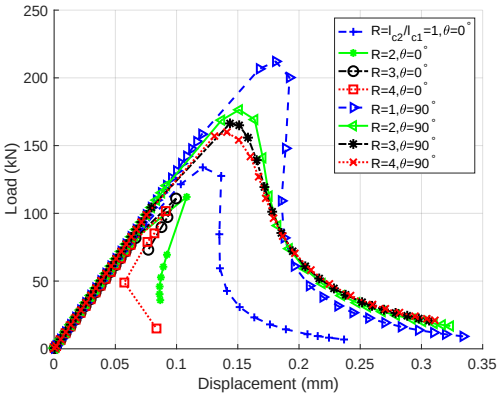

(c) Force-displacement curves for various internal length ratios.

Figure 5.10: Force-displacement curves at the node where the load is applied during the three-point bending tests.

tions explained in Section 5.2 will have a direct influence on elasticity parameters and on porosity. For the sake of simplicity, we assume that damage development (i.e., the initiation and propagation of micro cracks) does not generate inelastic deformation, i.e., damage only affects the stiffness tensor. Porosity and permeability are affected indirectly by damage, through the expression of Biot's effective stress. Consequently, the potential energy density of an REV of transversely isotropic porous material can be expressed as:

$$H_s(\boldsymbol{\epsilon}, p, \boldsymbol{\omega}) = \frac{1}{2}\boldsymbol{\epsilon} : \mathbb{C}(\boldsymbol{\omega}) : \boldsymbol{\epsilon} - \frac{p^2}{2N} - p\boldsymbol{\alpha} : \boldsymbol{\epsilon} \tag{5.49}$$

where H_s is also called Helmholtz free energy. The thermodynamic conjugation relationships provide the following state equations:

$$\begin{aligned} \boldsymbol{\sigma} &= \frac{\partial H_s}{\partial \boldsymbol{\epsilon}} = \mathbb{C}(\boldsymbol{\omega}) : \boldsymbol{\epsilon} - \boldsymbol{\alpha} p \\ \phi - \phi_0 &= -\frac{\partial H_s}{\partial p} = \boldsymbol{\alpha} : \boldsymbol{\epsilon} + \frac{p}{N} \end{aligned} \tag{5.50}$$

where $\boldsymbol{\omega}$ stands for the damage variable, which is a vector defined in Equation 5.2. $\boldsymbol{\epsilon}$ is the strain tensor, p is the unknown fluid pressure, $\boldsymbol{\sigma}$ is the Biot's effective stress tensor, ϕ represents porosity (ϕ_0 is the initial porosity), and $\alpha_{ij} = -\partial^2 G_s / \partial \epsilon_{ij} \partial p$ is Biot's coefficient tensor. $\boldsymbol{\alpha}$ linearly relates the porosity change to the strain variation when pressure is held constant ($p = 0$). Due to Maxwell's symmetry [301] , it also linearly relates the stress increment to the pressure increment when strain is held constant ($\boldsymbol{\epsilon} = 0$). $1/N = -\partial^2 G_s / \partial p^2$ is the inverse of Biot's skeleton modulus, linking pressure variation dp with the porosity variation when strain is held constant ($\boldsymbol{\epsilon} = 0$). Note that in the following, we use the following convention for noting variables: scalar A, second order tensor/vector $\boldsymbol{A}$, fourth order tensor $\mathbb{A}$.

Mixture governing equations Under quasi-static conditions, the momentum balance equation of the REV (made of the mixture solid + fluid) is:

$$\nabla \cdot \boldsymbol{\sigma} + \rho \boldsymbol{g} = 0. \tag{5.51}$$

where ρ is the average mass density of the mixture, defined as $\rho = (1-\phi)\rho_s + \phi\rho_f$, in which ρ_s (respectively ρ_f) stands for the mass density of the solid phase (respectively, density of the fluid phase). $\boldsymbol{g}$ is the body force vector. Substituting the state equation (eq. 5.50) into equation 5.51, we get the strong form of the governing equation for themixture, as follows:

$$\nabla \cdot [\mathbb{C}(\boldsymbol{\omega}) : \boldsymbol{\epsilon} - \boldsymbol{\alpha} p] + \rho \boldsymbol{g} = 0 \tag{5.52}$$

Fluid governing equations in the saturated porous matrix Fluid flow inside the porous matrix is fundamentally governed by the fluid mass balance equation, which expresses that the mass change within the considered REV should be equal to the difference between the fluid mass flowing out the REV and the fluid massflowing in the REV, as follows:

$$\nabla \cdot (\rho_f \boldsymbol{v}) + \frac{\partial m_f}{\partial t} = 0 \tag{5.53}$$

where $\boldsymbol{v}$ is the velocity vector of the fluid. ρ_f and m_f represent the mass density and the mass of the fluid, respectively. Since the porous medium is saturated with the fluid, we have: $m_f = \rho_f \phi$, where ϕ is the porosity. According to the state equation of the fluid, the mass density of the fluid is related to the pore pressure through the following equation:

$$\frac{d\rho_f}{\rho_f} = \frac{dp}{K_f} \tag{5.54}$$

where K_f is the bulk modulus of the fluid. We assume that fluid flow inside the porous matrix is laminar and that it is governed by Darcy's seepage equation as:

$$\boldsymbol{v} = -\frac{\boldsymbol{k}_m}{\mu}(\nabla p - \rho_f \boldsymbol{g}) \tag{5.55}$$

where μ is the dynamic viscosity of the fluid, $\boldsymbol{k}_m$ is the intrinsic anisotropic permeability tensor of the solid skeleton. For simplicity, we assume that permeability remains constant in this chapter. Note that future developments are necessary to account for the dependence of permeability to the geometry and connectivity of pores and cracks within the solid skeleton. By substituting the state equations (eq. 5.50 and 5.54), the Darcy's law (eq. 5.55) into equation 5.53, we get the governing equation for the fluid flow through the permeable porous medium surrounding the fracture, as follows:

$$\boldsymbol{\alpha} : \frac{\partial \boldsymbol{\epsilon}}{\partial t} + \frac{1}{M}\frac{\partial p}{\partial t} = \nabla \cdot \frac{\boldsymbol{k}_m}{\mu}(\nabla p - \rho_f \boldsymbol{g}), \tag{5.56}$$

where it is assumed that the spatial variability of the fluid mass density is negligible (i.e. $\nabla \rho_f \neq 0$). M is the so called Biot's modulus, defined by

$$\frac{1}{M} = \frac{1}{N} + \frac{\phi}{K_f}. \tag{5.57}$$

Fluid governing equations along the fracture Different from the fluid flow inside the porous matrix, the mass balance equation that governs the fluid flow inside the fracture involves a direction-dependent hydraulic conductivity. Consider an REV such that a face of the REV is a unit fracture surface, and the side perpendicular to that area has a length w, representing the local fracture width. The fluid mass change per unit of time within the REV is equal to the variation of flow rate in the direction of the fracture plane, plus the variation of flow rate in the direction perpendicular to the fracture surfaces. Mathematically,

the mass balance equation reads:

$$\nabla_s \cdot [\rho_f \boldsymbol{q}(\boldsymbol{s})] + [\![\rho_f \boldsymbol{v}(\boldsymbol{s})]\!] \cdot \boldsymbol{n}_{\Gamma_d} + \frac{\partial}{\partial t}(\rho_f w) = 0. \tag{5.58}$$

where ∇_s represents the tangent gradient in the local tangent fracture surface, in which $\boldsymbol{s}$ denotes the natural coordinate of the fracture. $\boldsymbol{q}$ is the flow rate inside the fracture. Accordingly, the first term represents the change of fluid mass due to a flow rate variation within the fracture. The velocity $\boldsymbol{v}$ is related to the flow in the matrix and can be discontinuous at the two fracture surfaces: $\boldsymbol{v}^+ \neq \boldsymbol{v}^-$. We note $[\![\boldsymbol{v}(\boldsymbol{s})]\!]$ the velocity jump across the fracture. After multiplied by the normal direction of the fracture surfaces $\boldsymbol{n}_{\Gamma_d}$ and the fluid density ρ_f, the second term represents the amount of fluid exchanged between the matrix and the fracture.

The flow rate $\boldsymbol{q}$ is normally computed by the integral of the velocity over the thickness of the fracture. It can vary with the location s of the point on the fracture surface and it is related to the pressure gradient in the fracture surface by the following law:

$$\boldsymbol{q}(\boldsymbol{s}) = -c(\boldsymbol{s})(\nabla_s p(\boldsymbol{s}) - \rho_f \boldsymbol{g}) = -\frac{w^3(\boldsymbol{s})}{12\mu}(\nabla_s p(\boldsymbol{s}) - \rho_f \boldsymbol{g}) \tag{5.59}$$

where $c(\boldsymbol{s})$ is the hydraulic conductivity of the fracture at the natural coordinate $\boldsymbol{s}$. Here, we use Poiseuille fluid flow equation and accordingly, we calcualte $c(\boldsymbol{s})$ from the cubic law.

By substituting the constitutive law (eq. 5.59) and the state equation (eq. 5.54) into equation 5.58, we get the governing equation for the fluid flow within the fracture, as follows:

$$[\![\boldsymbol{v}(\boldsymbol{s})]\!] \cdot \boldsymbol{n}_{\Gamma_d} + \frac{\partial w(\boldsymbol{s})}{\partial t} + \frac{w(\boldsymbol{s})}{K_f}\frac{\partial p(\boldsymbol{s})}{\partial t} = \nabla_s \cdot \left[\frac{w^3(\boldsymbol{s})}{12\mu}(\nabla_s p(\boldsymbol{s}) - \rho_f \boldsymbol{g})\right]. \tag{5.60}$$

Since $\boldsymbol{\epsilon}$ and w can be both expressed in terms of the displacement field in the solid

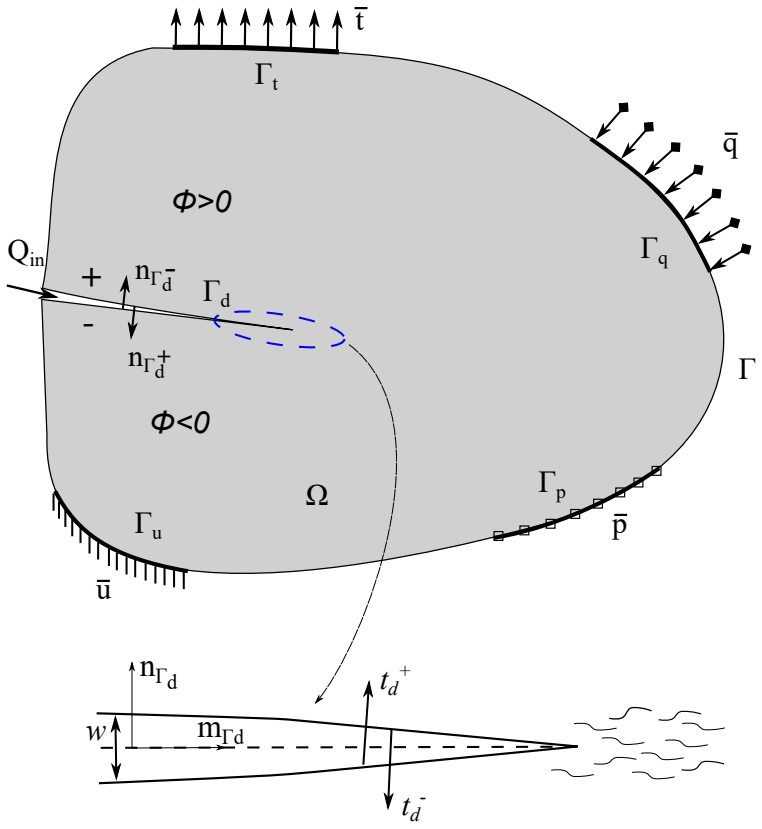

Figure 5.11: Boundary conditions on the domain Ω that contains a discontinuity Γ_d.

skeleton and of the fluid pressure, the unknowns in Equations 5.52, 5.56, and 5.60 can all be related to $\boldsymbol{u}$ and p. Thus, these governing equations are usually referred to as $\boldsymbol{u} - p$ formulation.

5.4.2 Weak Formulation

In order to obtain the weal formulation of the problem from its strong formulation, it is necessary to define the essential and natural boundary conditions at the exterior and interior boundaries of the domain. In this chapter, we focus on two-dimensional problems, as described in Figure 5.11. The domain Ω with exterior boundary Γ has a discontinuity Γ_d, which is treated as an interior boundary and may evolve due to fluid pressurization. The two surfaces of the discontinuity Γ_d are noted Γ_d^+ and Γ_d^-. We note $\boldsymbol{n}_{\Gamma_d}$ the unit normal vector on the fracture surface, pointing towards Ω^+, i.e. $(\boldsymbol{n}_{\Gamma_d} = \boldsymbol{n}_{\Gamma_d^-} = -\boldsymbol{n}_{\Gamma_d^+})$.

As shown in Figure 5.11, the essential boundary conditions (respectively, natural boundary conditions) are imposed on the external boundary of the domain by the prescribing the primary variables (respectively, the traction $\bar{\boldsymbol{t}}$ and the fluid outflow flux $\bar{q}$), as follows:

$$\begin{aligned} \boldsymbol{u} &= \bar{\boldsymbol{u}} \quad \text{on} \quad \Gamma_u \\ p &= \bar{p} \quad \text{on} \quad \Gamma_p \end{aligned} \tag{5.61}$$

and

$$\begin{aligned} \boldsymbol{\sigma} \cdot \boldsymbol{n}_\Gamma &= \bar{\boldsymbol{t}} \quad \text{on} \quad \Gamma_t \\ \boldsymbol{v} \cdot \boldsymbol{n}_\Gamma &= \bar{q} \quad \text{on} \quad \Gamma_q \end{aligned} \tag{5.62}$$

where $\boldsymbol{n}_\Gamma$ is the unit outward normal vector to the external boundary Γ. We have: $\Gamma_u \cup \Gamma_t = \Gamma$ and $\Gamma_u \cap \Gamma_t = \emptyset$ hold for solid phase, $\Gamma_p \cup \Gamma_q = \Gamma$ and $\Gamma_p \cap \Gamma_q = \emptyset$ hold for fluid phase.

From a physics perspective, the existence of the fracture Γ_d in the domain Ω leads to a hydro-mechanical coupling between the fracture and the bounding matrix. Fluid flow along the fracture exerts pressure on the two fracture surfaces and pushes them apart, while the two surfaces transmit cohesive traction. Reversely, pressure gradients drive fluid flow into/out of the bounding matrix surrounding the fracture. Thus, the essential and natural boundary conditions at the interior boundary Γ_d are expressed as

$$\begin{aligned} \boldsymbol{\sigma} \cdot \boldsymbol{n}_{\Gamma_d} &= \boldsymbol{t}_d - p\boldsymbol{n}_{\Gamma_d} \quad \text{on} \quad \Gamma_d \\ (\boldsymbol{v}^+ - \boldsymbol{v}^-) \cdot \boldsymbol{n}_{\Gamma_d} &= [\![\boldsymbol{v}]\!] \cdot \boldsymbol{n}_{\Gamma_d} = q_d \quad \text{on} \quad \Gamma_d \end{aligned} \tag{5.63}$$

where $\boldsymbol{t}_d$ is the cohesive traction which governs the mechanical behavior of the macro fracture once the fracture is initiated. In this chapter, we employ the same potential based Park-Paulino-Roesler (PPR) [255] cohesive model as in Chapter 2 (please refer to Section 4.3.2 for details about the model). Moreover, q_d represents the fluid flow into the matrix, i.e. leakage in the fracture flow model.

For the hydraulic fracturing problem, an additional boundary conditions needs to be specified at the fracture tip and at the fracture mouth (i.e., at the intersection point between the domain surface Γ and the fracture Γ_d). In typical field operations, a fluid injection rate Q_{in} is applied at the fracture mouth and a zero flux is applied at the fracture tip:

$$\boldsymbol{q}|_{\boldsymbol{s}=\boldsymbol{0}} = Q_{\text{in}}, \quad \boldsymbol{q}|_{\boldsymbol{s}=\boldsymbol{s}_{max}} = 0, \quad \text{on} \quad \partial\Gamma_d \tag{5.64}$$

We first obtain the weak form of the mixture governing equation by multiplying equation 5.52 by a virtual displacement $\delta\boldsymbol{u}$, and by integrating over the whole domain Ω. After applying the divergence theorem and the boundary conditions, we have:

$$\begin{aligned}\int_\Omega \nabla^s \delta\boldsymbol{u} : \mathbb{C}(\boldsymbol{\omega}) : \nabla^s \boldsymbol{u} d\Omega - \int_\Omega \nabla^s \delta\boldsymbol{u} : \boldsymbol{\alpha} p d\Omega + \int_{\Gamma_d} \delta[\![\boldsymbol{u}]\!] \cdot (\boldsymbol{t}_d - p\boldsymbol{n}_{\Gamma_d}) d\Gamma \\ = \int_{\Gamma_t} \delta\boldsymbol{u} \cdot \bar{\boldsymbol{t}} d\Gamma + \int_\Omega \rho \delta\boldsymbol{u} \cdot \boldsymbol{g} d\Omega\end{aligned} \tag{5.65}$$

where the kinematic strain-displacement relation $\nabla^s \boldsymbol{u} = \boldsymbol{\epsilon}$ is used. We use ∇^s to denote the symmetric part of the gradient operator. In order to make above equation hold for all admissible solutions of displacement, the virtual displacement must satisfy the essential boundary condition $\delta\boldsymbol{u}|_{\Gamma_u} = 0$. It is worth noting that the mechanical coupling term comes from the boundary condition along the fracture surfaces Γ_d, derived as follows:

$$\begin{aligned}&- \int_{\Gamma_d^+} \delta\boldsymbol{u} \cdot (\boldsymbol{\sigma} \cdot \boldsymbol{n}_{\Gamma_d^+}) d\Gamma - \int_{\Gamma_d^-} \delta\boldsymbol{u} \cdot (\boldsymbol{\sigma} \cdot \boldsymbol{n}_{\Gamma_d^-}) d\Gamma \\ &= \int_{\Gamma_d} (\delta\boldsymbol{u}^+ - \delta\boldsymbol{u}^-) \cdot (\boldsymbol{\sigma} \cdot \boldsymbol{n}_{\Gamma_d}) d\Gamma = \int_{\Gamma_d} \delta[\![\boldsymbol{u}]\!] \cdot (\boldsymbol{t}_d - p\boldsymbol{n}_{\Gamma_d}) d\Gamma\end{aligned} \tag{5.66}$$

we it is recalled that $(\boldsymbol{n}_{\Gamma_d} = \boldsymbol{n}_{\Gamma_d^-} = -\boldsymbol{n}_{\Gamma_d^+})$.

Similarly, we can obtain the weak form of the governing equation of the fluid flowing

in the matrix (eq. 5.56), as follows:

$$\begin{aligned}\int_\Omega \delta p \frac{1}{M}\frac{\partial p}{\partial t} d\Omega + \int_\Omega \delta p \boldsymbol{\alpha} : \nabla^s \frac{\partial \boldsymbol{u}}{\partial t} d\Omega + \int_\Omega \nabla \delta p \cdot (\frac{\boldsymbol{k}_m}{\mu}\nabla p) d\Omega - \int_{\Gamma_d} \delta p q_d d\Gamma \\ = -\int_{\Gamma_q} \delta p \bar{q} d\Gamma + \int_\Omega \frac{\rho_f \boldsymbol{k}_m}{\mu}\nabla \delta p \cdot \boldsymbol{g} d\Omega\end{aligned} \tag{5.67}$$

Note that δp is the virtual pressure that satisfies $\delta p|_{\Gamma_p} = 0$. The boundary condition $\frac{\boldsymbol{k}_m}{\mu}(-\nabla p + \rho_f \boldsymbol{g}) \cdot \boldsymbol{n}_\Gamma = \boldsymbol{v} \cdot \boldsymbol{n}_\Gamma = \bar{q}$ is used for the exterior boundary. Note that the hydraulic coupling term in the above formula results from the interior boundary conditions at the fracture surfaces, in virtue of the following equation:

$$\begin{aligned}\int_{\Gamma_d^+} \delta p(\boldsymbol{v} \cdot \boldsymbol{n}_{\Gamma_d^+}) d\Gamma + \int_{\Gamma_d^-} \delta p(\boldsymbol{v} \cdot \boldsymbol{n}_{\Gamma_d^-}) d\Gamma &= -\int_{\Gamma_d} \delta p(\boldsymbol{v}^+ - \boldsymbol{v}^-) \cdot \boldsymbol{n}_{\Gamma_d} d\Gamma \\ &= -\int_{\Gamma_d} \delta p q_d d\Gamma\end{aligned} \tag{5.68}$$

The above equation states that the velocity of the fluid normal to the fracture is discontinuous, which indicates, according to Darcy's law, that the gradient of fluid pressure along of the normal to the fracture surface is discontinuous. However, the fluid pressure field as well as the virtual pressure should be continuous across the fracture so that Darcy's law can be applied. Thus, we use the same virtual pressure δp as in Equation 5.67 to multiply the governing equation of the fluid flowing in the fracture (eq. 5.60), and we integrate it over the fracture domain Γ_d to obtain the following weak form:

$$\begin{aligned}\int_{\Gamma_d} \delta p [\![\boldsymbol{v}]\!] \cdot \boldsymbol{n}_{\Gamma_d} d\Gamma &= \int_{\Gamma_d} \delta p q_d d\Gamma \\ &= -\int_{\Gamma_d} \delta p \frac{\partial w}{\partial t} d\Gamma - \int_{\Gamma_d} \delta p \frac{w}{K_f}\frac{\partial p}{\partial t} d\Gamma \\ &\quad - \int_{\Gamma_d} \nabla_m \delta p \cdot \left[\frac{w^3}{12\mu}\nabla_m p\right] d\Gamma + \delta p Q_{\text{in}}|_{\boldsymbol{s}=\boldsymbol{0}}\end{aligned} \tag{5.69}$$

where ∇_m denotes the one dimensional gradient along the fracture direction ($\boldsymbol{m}_{\Gamma_d}$, as shown in Figure 5.11). The width of the fracture is computed through the following re-

lationship:

$$w = (\boldsymbol{u}^+ - \boldsymbol{u}^-) \cdot \boldsymbol{n}_{\Gamma_d} = [\![\boldsymbol{u}]\!] \cdot \boldsymbol{n}_{\Gamma_d}. \tag{5.70}$$

The weak form of governing equation for the fluid flowing in the fracture can be directly injected into the weak form of the governing equation for the fluid flowing in the matrix (eq. 5.67), since the same virtual field δp is used.

5.5 Discretization and Resolution Procedure

5.5.1 XFEM Spatial Discretization for Displacement and Pressure

To model fluid driven fracture propagation in permeable porous media, advanced numerical techniques are needed to ensure that displacement jumps are enforced with a continuous pressure pressure field and a discontinuous pressure gradient across the fracture. To model fracture propagation without remeshing, we adopt the XFEM to discretize the primary variables. The Heaviside enrichment function is employed to account for the displacement jump across the macro-fracture. Note that the bounding media is modeled by the proposed anisotropic damage model with softening, so there is no singularity at the macro fracture tip. Thus, the classical branching functions are not necessary here. As a result, the approximate function of displacement $\boldsymbol{u}^h(\boldsymbol{x}, t)$ is expressed in the following form:

$$\begin{aligned} \boldsymbol{u}^h(\boldsymbol{x}, t) &= \sum_{i \in S} N_{ui}(\boldsymbol{x}) \boldsymbol{u}_i(t) + \sum_{i \in S_H} N_{ui}(\boldsymbol{x}) \frac{1}{2} \left[H_{\Gamma_d}(\boldsymbol{x}) - H_{\Gamma_d}(\boldsymbol{x}_i) \right] \boldsymbol{a}_i(t) \\ &= \boldsymbol{N}_u(\boldsymbol{x}) \boldsymbol{U}(t) + \boldsymbol{N}_a(\boldsymbol{x}) \boldsymbol{A}(t) \end{aligned} \tag{5.71}$$

where $N_{ui}(\boldsymbol{x})$ is the standard shape function associated with node i, S is the set of all nodal points, S_H is the set of enriched nodes whose support are bisected by the fracture. $\boldsymbol{u}_i(t)$ and $\boldsymbol{a}_i(t)$ denote the nodal value of the displacement field associated with the standard and enriched degree of freedoms respectively. The Heaviside jump function $H(\boldsymbol{x})$ is defined in Equation 4.47. It is worth noting that the shifted jump function $1/2 \left[H_{\Gamma_d}(\boldsymbol{x}) - H_{\Gamma_d}(\boldsymbol{x}_i) \right]$ is

used to avoid the problem of post processing and blending elements [272]. The analytical form of the displacement jump across the fracture Γ_d is:

$$[\![\boldsymbol{u}(\boldsymbol{x},t)]\!] = \sum_{i\in S_H} N_{ui}(\boldsymbol{x})\boldsymbol{a}_i(t) = \boldsymbol{N}_a(\boldsymbol{x})\boldsymbol{A}(t) \tag{5.72}$$

For the fluid pressure field, enrichment is done with the distance function. The approximate pressure field is expressed as:

$$\begin{aligned} p^h(\boldsymbol{x},t) &= \sum_{i\in S} N_{pi}(\boldsymbol{x})p_i(t) + \sum_{i\in S_H} N_{pi}(\boldsymbol{x})\left[D_{\Gamma_d}(\boldsymbol{x}) - D_{\Gamma_d}(\boldsymbol{x}_i)\right] R(\boldsymbol{x})b_i(t) \\ &= \boldsymbol{N}_p(\boldsymbol{x})\boldsymbol{P}(t) + \boldsymbol{N}_b(\boldsymbol{x})\boldsymbol{B}(t) \end{aligned} \tag{5.73}$$

where $N_{pi}(\boldsymbol{x})$ is the standard finite element shape function associated with node i. Nodal sets S and S_H are the same as for the displacement field. $p_i(t)$ and $b_i(t)$ denote the nodal value of the fluid presure associated with the standard and enriched degree of freedoms, respectively. $D_{\Gamma_d}(\boldsymbol{x})$ is the distance function, defined as:

$$D_{\Gamma_d}(\boldsymbol{x}) = \begin{cases} +\phi(\boldsymbol{x}), & \text{if } \phi(\boldsymbol{x}) > 0 \\ -\phi(\boldsymbol{x}), & \text{if } \phi(\boldsymbol{x}) < 0 \end{cases} \tag{5.74}$$

where $\phi(\boldsymbol{x})$ is the level set function, the definition of which is illustrated in Figure 5.11. The gradient of the distance function along the direction normal to the fracture is discontinuous, with: $\nabla D_{\Gamma_d} \cdot \boldsymbol{n}_{\Gamma_d} = H_{\Gamma_d}$. As a result, the enriching the FEM with the distance function for the pressure field allows meeting the continuity requirements: continuous pressure field and discontinuous gradient of pressure across the fracture. The fluid exchange between the fracture and the matrix can be accounted for. Similar to the the displacement approximation, the shifted enrichment function $[D_{\Gamma_d}(\boldsymbol{x}) - D_{\Gamma_d}(\boldsymbol{x}_i)]$ is used and $R(\boldsymbol{x})$ is a weight function, defined as $R(\boldsymbol{x}) = \sum_{i\in S_H} N_{pi}(\boldsymbol{x})$ according to Mohammadnejad and Khoei's approach [302]. It is worth noting that the pressure field at the tip of the fracture

does not need to be enriched to satisfy the "no leakage flux" boundary condition.

From now on, we use the following (simplified) notations: $\boldsymbol{N}_u(\boldsymbol{x})$ and $\boldsymbol{N}_p(\boldsymbol{x})$ (respectively, $\boldsymbol{N}_a(\boldsymbol{x})$ and $\boldsymbol{N}_b(\boldsymbol{x})$) are the matrices of standard (respectively, enriched) shape functions for the displacement field $\boldsymbol{u}$ and for the pressure field p, respectively. $\boldsymbol{U}(t)$ and $\boldsymbol{P}(t)$ (respectively, $\boldsymbol{A}(t)$ and $\boldsymbol{B}(t)$) are the vectors of the standard (respectively, enriched) displacement and pressure degrees of freedom, respectively. By substituting the approximations (eq. 5.71, 5.73) into the governing weak form equations (eq. 5.52, 5.56, and 5.60), we can arrive at the discretized form of the governing equations, as follows:

$$
\begin{aligned}
&\boldsymbol{K}_{uu}\boldsymbol{U} + \boldsymbol{K}_{ua}\boldsymbol{A} - \boldsymbol{Q}_{up}\boldsymbol{P} - \boldsymbol{Q}_{ub}\boldsymbol{B} - \boldsymbol{F}_u^{\text{ext}} = 0 \\
&\boldsymbol{K}_{ua}^T\boldsymbol{U} + \boldsymbol{K}_{aa}\boldsymbol{A} - \boldsymbol{Q}_{ap}\boldsymbol{P} - \boldsymbol{Q}_{ab}\boldsymbol{B} - \boldsymbol{Q}_{ad}\boldsymbol{P}_d + \boldsymbol{F}_a^{\text{int}} - \boldsymbol{F}_a^{\text{ext}} = 0 \\
&\boldsymbol{Q}_{up}^T\dot{\boldsymbol{U}} + \boldsymbol{Q}_{ap}^T\dot{\boldsymbol{A}} + \boldsymbol{M}_{pp}\dot{\boldsymbol{P}} + \boldsymbol{M}_{pb}\dot{\boldsymbol{B}} + \boldsymbol{H}_{pp}\boldsymbol{P} + \boldsymbol{H}_{pb}\boldsymbol{B} - \boldsymbol{F}_p^{\text{int}} - \boldsymbol{F}_p^{\text{ext}} = 0 \\
&\boldsymbol{Q}_{ub}^T\dot{\boldsymbol{U}} + \boldsymbol{Q}_{ab}^T\dot{\boldsymbol{A}} + \boldsymbol{M}_{pb}^T\dot{\boldsymbol{P}} + \boldsymbol{M}_{bb}\dot{\boldsymbol{B}} + \boldsymbol{H}_{pb}^T\boldsymbol{P} + \boldsymbol{H}_{bb}\boldsymbol{B} - \boldsymbol{F}_b^{\text{int}} - \boldsymbol{F}_b^{\text{ext}} = 0
\end{aligned}
\tag{5.75}
$$

where the Galerkin method is used, i.e. in which the virtual displacement $\delta\boldsymbol{u}$ and the virtual pressure δp are used as weight functions. Using the anisotropic damage model proposed in Section 5.2, the consistent tangent stiffness ($\boldsymbol{K}_{\alpha\beta}, \alpha, \beta = u, a$) can be derived as:

$$
\begin{aligned}
\boldsymbol{K}_{\alpha\beta} &= \int_\Omega \Big(\boldsymbol{B}_\alpha^T \mathbb{C} \boldsymbol{B}_\beta + \boldsymbol{B}_\alpha^T \frac{\partial \mathbb{C}}{\partial \boldsymbol{u}} \boldsymbol{B}_\beta \boldsymbol{u} \Big) \mathrm{d}\Omega \\
&= \sum_{I=1}^{N_I} w_I (\boldsymbol{B}_\alpha^I)^T \mathbb{C} \boldsymbol{B}_\beta^I \\
&\quad + \sum_{I=1}^{N_I} \sum_{J=1}^{N_J} \sum_{i=1}^{2} w_I w_J \alpha_{IJ} (\boldsymbol{B}_\alpha^I)^T \Big(\frac{\partial \mathbb{C}}{\partial \omega_i} \frac{\partial \omega_{it}}{\partial \kappa_i} \frac{\partial \kappa_i}{\partial \epsilon_{it}^{eq}} \Big)_I \Big(\frac{\mathrm{d}\epsilon_{it}^{eq}}{\mathrm{d}\boldsymbol{\epsilon}} \Big)_J \boldsymbol{B}_\beta^J \boldsymbol{B}_\beta^I \boldsymbol{u}_I
\end{aligned}
\tag{5.76}
$$

Note that the the second term of the equation above represents the nonlocal contribution, derived in Section 5.3.2. $\boldsymbol{B}_u, \boldsymbol{B}_a$ are the matrices of the derivatives of enriched or standard shape functions with respect to displacement. The matrices $\boldsymbol{Q}_{\alpha\beta}(\alpha, \beta = u, p)$ are hydro-

mechanical coupling terms, which can be expressed as:

$$\begin{aligned} \boldsymbol{Q}_{up} &= \int_{\Omega} \boldsymbol{B}_u^T \boldsymbol{\alpha} \boldsymbol{N}_p \mathrm{d}\Omega, \quad \boldsymbol{Q}_{ub} = \int_{\Omega} \boldsymbol{B}_u^T \boldsymbol{\alpha} \boldsymbol{N}_b \mathrm{d}\Omega \\ \boldsymbol{Q}_{ap} &= \int_{\Omega} \boldsymbol{B}_a^T \boldsymbol{\alpha} \boldsymbol{N}_p \mathrm{d}\Omega, \quad \boldsymbol{Q}_{ab} = \int_{\Omega} \boldsymbol{B}_a^T \boldsymbol{\alpha} \boldsymbol{N}_b \mathrm{d}\Omega \end{aligned} \tag{5.77}$$

The matrices $\boldsymbol{M}_{\alpha\beta}(\alpha, \beta = p, b)$ represent the compressibility of the fluid and of the solid skeleton and it expressed as:

$$\begin{aligned} \boldsymbol{M}_{pp} &= \int_{\Omega} \boldsymbol{N}_p^T \frac{1}{\boldsymbol{M}} \boldsymbol{N}_p \mathrm{d}\Omega, \quad \boldsymbol{M}_{pb} = \int_{\Omega} \boldsymbol{N}_p^T \frac{1}{\boldsymbol{M}} \boldsymbol{N}_b \mathrm{d}\Omega \\ \boldsymbol{M}_{bb} &= \int_{\Omega} \boldsymbol{N}_b^T \frac{1}{\boldsymbol{M}} \boldsymbol{N}_b \mathrm{d}\Omega \end{aligned} \tag{5.78}$$

The matrices $\boldsymbol{H}_{\alpha\beta}(\alpha, \beta = p, b)$ represent the hydraulic conductivity and are expressed as

$$\begin{aligned} \boldsymbol{H}_{pp} &= \int_{\Omega} \nabla \boldsymbol{N}_p^T \frac{\boldsymbol{k}_m}{\mu} \nabla \boldsymbol{N}_p \mathrm{d}\Omega, \quad \boldsymbol{H}_{pb} = \int_{\Omega} \nabla \boldsymbol{N}_p^T \frac{\boldsymbol{k}_m}{\mu} \nabla \boldsymbol{N}_b \mathrm{d}\Omega \\ \boldsymbol{H}_{bb} &= \int_{\Omega} \nabla \boldsymbol{N}_b^T \frac{\boldsymbol{k}_m}{\mu} \nabla \boldsymbol{N}_b \mathrm{d}\Omega \end{aligned} \tag{5.79}$$

It is worth noting that the mass balance equation for the fluid flow in the fracture does not explicitly appear in the discrete form (equation 5.75). Instead, we introduce the internal force (flux) vector ($\boldsymbol{F}_p^{\text{int}}, \boldsymbol{F}_b^{\text{int}}$) to account for the mass exchange between the matrix and the

fracture, as follows:

$$
\begin{aligned}
\boldsymbol{F}_p^{\text{int}} &= \int_{\Gamma_{\text{q}}} \boldsymbol{N}_p^T q_d \mathrm{d}\Gamma \\
&= -\int_{\Gamma_d} \boldsymbol{N}_p^T \frac{w}{K_f} \dot{p} \mathrm{d}\Gamma - \int_{\Gamma_d} \boldsymbol{N}_p^T [\![\dot{u}]\!] \cdot \boldsymbol{n}_{\Gamma_d} \mathrm{d}\Gamma \\
&\quad - \int_{\Gamma_d} \nabla \boldsymbol{N}_p^T \cdot \boldsymbol{m}_{\Gamma_d} \frac{w^3}{12\mu} \nabla p \cdot \boldsymbol{m}_{\Gamma_d} \mathrm{d}\Gamma + \boldsymbol{N}_p Q_{\text{in}}|_{s=0} \\
\boldsymbol{F}_b^{\text{int}} &= \int_{\Gamma_{\text{q}}} \boldsymbol{N}_b^T q_d \mathrm{d}\Gamma \\
&= -\int_{\Gamma_d} \boldsymbol{N}_b^T \frac{w}{K_f} \dot{p} \mathrm{d}\Gamma - \int_{\Gamma_d} \boldsymbol{N}_b^T [\![\dot{u}]\!] \cdot \boldsymbol{n}_{\Gamma_d} \mathrm{d}\Gamma \\
&\quad - \int_{\Gamma_d} \nabla \boldsymbol{N}_b^T \cdot \boldsymbol{m}_{\Gamma_d} \frac{w^3}{12\mu} \nabla p \cdot \boldsymbol{m}_{\Gamma_d} \mathrm{d}\Gamma
\end{aligned}
\tag{5.80}
$$

The mechanical coupling term between the fracture and the matrix constitutes an other internal force vector $\boldsymbol{F}_a^{\text{int}}$ in the equilibrium equation, expressed as

$$
\boldsymbol{F}_a^{\text{int}} = \int_{\Gamma_d} \boldsymbol{N}_a^T (\boldsymbol{t}_d - p\boldsymbol{n}_{\Gamma_d}) \mathrm{d}\Gamma = \int_{\Gamma_d} \boldsymbol{N}_a^T \boldsymbol{t}_d \mathrm{d}\Gamma - \int_{\Gamma_d} \boldsymbol{N}_a^T \boldsymbol{n}_{\Gamma_d} p \mathrm{d}\Gamma. \tag{5.81}
$$

where the fluid pressure p and the cohesive traction $\boldsymbol{t}_d$ are both exerted on the fracture surfaces. The remainder of the external force (flux) vectors in Equation 5.75 are listed in the following:

$$
\begin{aligned}
\boldsymbol{F}_u^{\text{ext}} &= \int_{\Gamma_{\text{t}}} \boldsymbol{N}_u^T \bar{\boldsymbol{t}}_{n+1} \mathrm{d}\Gamma + \int_{\Omega} \rho \boldsymbol{N}_u^T \boldsymbol{g} \mathrm{d}\Omega \\
\boldsymbol{F}_a^{\text{ext}} &= \int_{\Gamma_{\text{t}}} \boldsymbol{N}_a^T \bar{\boldsymbol{t}}_{n+1} \mathrm{d}\Gamma + \int_{\Omega} \rho \boldsymbol{N}_a^T \boldsymbol{g} \mathrm{d}\Omega \\
\boldsymbol{F}_p^{\text{ext}} &= -\int_{\Gamma_{\text{q}}} \boldsymbol{N}_p^T \bar{q} \mathrm{d}\Gamma + \int_{\Omega} \frac{\rho_f \boldsymbol{k}_m}{\mu} \nabla \boldsymbol{N}_p^T \cdot \boldsymbol{g} d\Omega \\
\boldsymbol{F}_b^{\text{ext}} &= -\int_{\Gamma_{\text{q}}} \boldsymbol{N}_b^T \bar{q} \mathrm{d}\Gamma + \int_{\Omega} \frac{\rho_f \boldsymbol{k}_m}{\mu} \nabla \boldsymbol{N}_b^T \cdot \boldsymbol{g} d\Omega
\end{aligned}
\tag{5.82}
$$

5.5.2 Finite Difference Temporal Discretization and Resolution Procedure

In order to further simplify the notations in the following derivations for time discretization, we condense the enriched and standard degree of freedoms for displacement and pressure as $\mathbb{U}(\boldsymbol{U}, \boldsymbol{A})$ and $\mathbb{P}(\boldsymbol{P}, \boldsymbol{B})$. The weak form of the governing equation discretized in space (eq. 5.75) can be rewritten as

$$\begin{aligned} &\boldsymbol{K}\mathbb{U} - \boldsymbol{Q}\mathbb{P} + F_{\mathbb{U}}^{\text{int}} - F_{\mathbb{U}}^{\text{ext}} = \boldsymbol{0} \\ &\boldsymbol{Q}^T\dot{\mathbb{U}} + \boldsymbol{M}\dot{\mathbb{P}} + \boldsymbol{H}\mathbb{P} - F_{\mathbb{P}}^{\text{int}}(\dot{\mathbb{U}}, \dot{\mathbb{P}}) - F_{\mathbb{P}}^{\text{ext}} = \boldsymbol{0} \end{aligned} \tag{5.83}$$

To solve the above equations, we use a linear discretization scheme in time: first-order time derivatives $\dot{\boldsymbol{X}}$ are expressed in terms of the difference between $\boldsymbol{X}$ at time step $n+1$ and $\boldsymbol{X}$ at time step n:

$$\dot{\boldsymbol{X}}_{n+\theta} = \frac{\boldsymbol{X}_{n+1} - \boldsymbol{X}_n}{\Delta t} \tag{5.84}$$

where Δt is the time step. $\boldsymbol{X}$ at the current time is the weighted value between time step $n+1$ and time step n:

$$\boldsymbol{X}_{n+\theta} = (1-\theta)\boldsymbol{X}_n + \theta\boldsymbol{X}_{n+1} \tag{5.85}$$

in which the weight θ can be any value between 0 and 1. If $\theta = 0$, the time discretization method is the explicit forward Euler scheme; if $\theta = 1$, the time discretization method is the implicit Euler scheme. We use $\theta \geq 0.5$ to ensure unconditional stability. After injecting the time discretization equations into the spatially discretized governing equations (eq. 5.83), we obtain the residual at time step $n+1$, as follows:

$$\begin{aligned} \boldsymbol{R}_{\mathbb{U},n+1} &= \boldsymbol{K}\mathbb{U}_{n+1} - \boldsymbol{Q}\mathbb{P}_{n+1} + F_{\mathbb{U}_{n+1}}^{\text{int}} - F_{\mathbb{U}_{n+1}}^{\text{ext}} = \boldsymbol{0} \\ \boldsymbol{R}_{\mathbb{P},n+1} &= \boldsymbol{Q}^T\mathbb{U}_{n+1} + (\boldsymbol{M} + \theta\Delta t\boldsymbol{H})\mathbb{P}_{n+1} - F_{\mathbb{P}_{n+1}}^{\text{int}} - G_{\mathbb{P}_{n+1}} = \boldsymbol{0} \end{aligned} \tag{5.86}$$

where $G_{\mathbb{P}_{n+1}}$ is the vector of known values at time step n, expressed as:

$$\begin{aligned} G_{\mathbb{P}_{n+1}} =& \Delta t F^{\text{ext}}_{\mathbb{P}_{n+1}} + \boldsymbol{Q}^T \mathbb{U}_n + \Big(\boldsymbol{M} - \Delta t(1-\theta)\boldsymbol{H}\Big)\mathbb{P}_n \\ &+ \int_{\Gamma_d} \boldsymbol{N}_{\mathbb{P}}^T \frac{w}{K_f} p_n \mathrm{d}\Gamma + \int_{\Gamma_d} \boldsymbol{N}_{\mathbb{P}}^T [\![\boldsymbol{u}]\!]_n \cdot \boldsymbol{n}_{\Gamma_d} \mathrm{d}\Gamma \\ &- \Delta t(1-\theta) \int_{\Gamma_d} \nabla \boldsymbol{N}_{\mathbb{P}}^T \cdot \boldsymbol{m}_{\Gamma_d} \frac{w^3}{12\mu} \nabla p_n \cdot \boldsymbol{m}_{\Gamma_d} \mathrm{d}\Gamma \end{aligned} \tag{5.87}$$

and $F^{\text{int}}_{\mathbb{P}_{n+1}}$ is the flux vector that accounts for the mass exchange between the matrix and the fracture at time step $n+1$:

$$\begin{aligned} F^{\text{int}}_{\mathbb{P}_{n+1}} =& -\int_{\Gamma_d} \boldsymbol{N}_{\mathbb{P}}^T \frac{w}{K_f} p_{n+1} \mathrm{d}\Gamma - \int_{\Gamma_d} \boldsymbol{N}_{\mathbb{P}}^T [\![\boldsymbol{u}]\!]_{n+1} \cdot \boldsymbol{n}_{\Gamma_d} \mathrm{d}\Gamma \\ &- \Delta t\theta \int_{\Gamma_d} \nabla \boldsymbol{N}_{\mathbb{P}}^T \cdot \boldsymbol{m}_{\Gamma_d} \frac{w^3}{12\mu} \nabla p_{n+1} \cdot \boldsymbol{m}_{\Gamma_d} \mathrm{d}\Gamma + \Delta t \boldsymbol{N}_{\mathbb{P}} Q_{\text{in}}|_{s=0} \end{aligned} \tag{5.88}$$

The nonlinear system (Equation 5.86) is solved iteratively. We adopt the Newton-Raphson method to linearize the system with respect to displacement and pressure at the equilibrium iteration k within the time step $n+1$, as follows:

$$\begin{bmatrix} \boldsymbol{R}^{i+1}_{\mathbb{U},n+1} \\ \boldsymbol{R}^{i+1}_{\mathbb{P},n+1} \end{bmatrix} = \begin{bmatrix} \boldsymbol{R}^{i}_{\mathbb{U},n+1} \\ \boldsymbol{R}^{i}_{\mathbb{P},n+1} \end{bmatrix} + \begin{bmatrix} \frac{\partial \boldsymbol{R}_{\mathbb{U}}}{\partial \mathbb{U}} & \frac{\partial \boldsymbol{R}_{\mathbb{U}}}{\partial \mathbb{P}} \\ \frac{\partial \boldsymbol{R}_{\mathbb{P}}}{\partial \mathbb{U}} & \frac{\partial \boldsymbol{R}_{\mathbb{P}}}{\partial \mathbb{P}} \end{bmatrix}^{i}_{n+1} \begin{bmatrix} d\mathbb{U}^{i}_{n+1} \\ d\mathbb{P}^{i}_{n+1} \end{bmatrix} = \boldsymbol{0} \tag{5.89}$$

The derivative of the residual with respect to the unknown degrees of freedom is the Jacobian matrix $\boldsymbol{J}$. Note that the internal force and flux vectors $(F^{\text{int}}_{\mathbb{U}}, F^{\text{int}}_{\mathbb{P}})$ are functions of

the unknowns at time step $n+1$. As a result, the full consistent tangent matrix $\boldsymbol{J}$ is:

$$\begin{aligned}\boldsymbol{J} &= \begin{bmatrix} \frac{\partial \boldsymbol{R}_{\mathbb{U}}}{\partial \mathbb{U}} & \frac{\partial \boldsymbol{R}_{\mathbb{U}}}{\partial \mathbb{P}} \\ \frac{\partial \boldsymbol{R}_{\mathbb{P}}}{\partial \mathbb{U}} & \frac{\partial \boldsymbol{R}_{\mathbb{P}}}{\partial \mathbb{P}} \end{bmatrix} = \begin{bmatrix} \boldsymbol{K} + \frac{\partial F_{\mathbb{U}}^{\text{int}}}{\partial \mathbb{U}} & -\boldsymbol{Q} + \frac{\partial F_{\mathbb{U}}^{\text{int}}}{\partial \mathbb{P}} \\ \boldsymbol{Q}^T - \frac{\partial F_{\mathbb{P}}^{\text{int}}}{\partial \mathbb{U}} & \boldsymbol{M} + \theta \Delta t \boldsymbol{H} - \frac{\partial F_{\mathbb{P}}^{\text{int}}}{\partial \mathbb{P}} \end{bmatrix} \\ &= \begin{bmatrix} \boldsymbol{K}_{uu} & \boldsymbol{K}_{ua} & -\boldsymbol{Q}_{up} & -\boldsymbol{Q}_{ub} \\ \boldsymbol{K}_{ua}^T & \boldsymbol{K}_{aa} + \frac{\partial F_a^{\text{int}}}{\partial a} & -\boldsymbol{Q}_{ap} + \frac{\partial F_a^{\text{int}}}{\partial p} & -\boldsymbol{Q}_{ab} + \frac{\partial F_a^{\text{int}}}{\partial b} \\ \boldsymbol{Q}_{up}^T & \boldsymbol{Q}_{ap}^T - \frac{\partial F_p^{\text{int}}}{\partial b} & \boldsymbol{M}_{pp} + \theta \Delta t \boldsymbol{H}_{pp} - \frac{\partial F_p^{\text{int}}}{\partial p} & \boldsymbol{M}_{pb} + \theta \Delta t \boldsymbol{H}_{pb} - \frac{\partial F_p^{\text{int}}}{\partial b} \\ \boldsymbol{Q}_{ub}^T & \boldsymbol{Q}_{ab}^T - \frac{\partial F_b^{\text{int}}}{\partial b} & \boldsymbol{M}_{pb}^T + \theta \Delta t \boldsymbol{H}_{pb}^T - \frac{\partial F_b^{\text{int}}}{\partial p} & \boldsymbol{M}_{bb} + \theta \Delta t \boldsymbol{H}_{bb} - \frac{\partial F_b^{\text{int}}}{\partial b} \end{bmatrix}. \end{aligned} \tag{5.90}$$

where

$$\begin{aligned} \frac{\partial F_{\mathbb{U}}^{\text{int}}}{\partial \mathbb{U}} &= \frac{\partial F_a^{\text{int}}}{\partial a} = \int_{\Gamma_d} \boldsymbol{N}_a^T \boldsymbol{\Lambda}^T \boldsymbol{T}_{coh} \boldsymbol{\Lambda} \boldsymbol{N}_a \mathrm{d}\Gamma \\ \frac{\partial F_a^{\text{int}}}{\partial p} &= \Big(\frac{\partial F_p^{\text{int}}}{\partial a}\Big)^T = -\int_{\Gamma_d} \boldsymbol{N}_a^T \boldsymbol{n}_{\Gamma_d} \boldsymbol{N}_p \mathrm{d}\Gamma \\ \frac{\partial F_a^{\text{int}}}{\partial b} &= \Big(\frac{\partial F_b^{\text{int}}}{\partial a}\Big)^T = -\int_{\Gamma_d} \boldsymbol{N}_a^T \boldsymbol{n}_{\Gamma_d} \boldsymbol{N}_b \mathrm{d}\Gamma \\ \frac{\partial F_p^{\text{int}}}{\partial p} &= -\int_{\Gamma_d} \boldsymbol{N}_p^T \frac{w}{K_f} \boldsymbol{N}_p \mathrm{d}\Gamma - \theta \Delta t \int_{\Gamma_d} \nabla \boldsymbol{N}_p^T \cdot \boldsymbol{m}_{\Gamma_d} \frac{w^3}{12\mu} \nabla \boldsymbol{N}_p \cdot \boldsymbol{m}_{\Gamma_d} \mathrm{d}\Gamma \\ \frac{\partial F_p^{\text{int}}}{\partial b} &= \Big(\frac{\partial F_b^{\text{int}}}{\partial p}\Big)^T = -\int_{\Gamma_d} \boldsymbol{N}_p^T \frac{w}{K_f} \boldsymbol{N}_b \mathrm{d}\Gamma - \theta \Delta t \int_{\Gamma_d} \nabla \boldsymbol{N}_p^T \cdot \boldsymbol{m}_{\Gamma_d} \frac{w^3}{12\mu} \nabla \boldsymbol{N}_b \cdot \boldsymbol{m}_{\Gamma_d} \mathrm{d}\Gamma \\ \frac{\partial F_b^{\text{int}}}{\partial b} &= -\int_{\Gamma_d} \boldsymbol{N}_b^T \frac{w}{K_f} \boldsymbol{N}_b \mathrm{d}\Gamma - \theta \Delta t \int_{\Gamma_d} \nabla \boldsymbol{N}_b^T \cdot \boldsymbol{m}_{\Gamma_d} \frac{w^3}{12\mu} \nabla \boldsymbol{N}_b \cdot \boldsymbol{m}_{\Gamma_d} \mathrm{d}\Gamma \end{aligned} \tag{5.91}$$

where $\boldsymbol{\Lambda}$ is the rotation matrix, defined in Equation 4.53, used to transform the expression of the displacement jumps from the local coordinate system (Δ_n, Δ_t) to the global coordinate system $[\![\boldsymbol{u}]\!]$. $\boldsymbol{T}_{coh}$ is the derivative of the cohesive traction force $\boldsymbol{t}_d$ with respect to the local displacement jump (Δ_n, Δ_t). Since we adopt the PPR cohesive model, $\boldsymbol{T}_{coh}$ can be explicitly calculated from the expression of $\partial(T_n, T_t)/\partial(\Delta_n, \Delta_t)$, as shown by Park and Paulino [266]. Note that the above formulation does not account for fluid flow within the fracture explicitly. Instead, for those elements with enriched degrees of free-

dom, the XFEM is used to account for the influence of the fracture on the permeability matrix $\boldsymbol{H}$, on the coupling term $\boldsymbol{Q}$ and on the compressibility term $\boldsymbol{M}$, through the terms $(\partial F_{\mathbb{U}}^{\text{int}}/\partial \mathbb{U}, \partial F_{\mathbb{P}}^{\text{int}}/\partial \mathbb{P})$. This approach requires few degrees of freedom and ensures the symmetry of the Jacobian, which makes the implementation of the model easier and allows achieving faster convergence rates.

If no macro fracture is present in the considered domain, the above formulation can be simplified into a coupled system of equations that govern fluid flow in a saturated porous medium. The iterative linear system within each increment reduces to the following classical form:

$$\begin{bmatrix} \boldsymbol{K} & -\boldsymbol{Q} \\ \boldsymbol{Q}^T & \boldsymbol{M} + \theta \Delta t \boldsymbol{H} \end{bmatrix} \begin{bmatrix} d\boldsymbol{U} \\ d\boldsymbol{P} \end{bmatrix} = \begin{bmatrix} \boldsymbol{R_U} \\ \boldsymbol{R_P} \end{bmatrix}. \tag{5.92}$$

If the linear system is further constrained because the fluid is incompressible, i.e., $\boldsymbol{M} = \boldsymbol{0}$, and because the permeability is so small that the fluid diffusion rate is negligible compared to the solid deformation rate, Equation 5.92 can be further simplified as:

$$\begin{bmatrix} \boldsymbol{K} & -\boldsymbol{Q} \\ \boldsymbol{Q}^T & \boldsymbol{0} \end{bmatrix} \begin{bmatrix} d\boldsymbol{U} \\ d\boldsymbol{P} \end{bmatrix} = \begin{bmatrix} \boldsymbol{R_U} \\ \boldsymbol{R_P} \end{bmatrix}. \tag{5.93}$$

Linear systems of equations with the same matrix structure as in Equation 5.93 appears in a variety of constrained problems in solid and fluid mechanics, such as incompressible elasticity [303], fluid flow in undrained porous media [304, 305] and Stokes flow of incompressible fluid [306]. As pointed out by White and Borja [304], this linear system is numerically unstable and spurious oscillation patterns exist for the pore pressure field if approximation functions of the same order are used for both the displacement field and the pore pressure field. Mathematically, this problem arises because of the non-trivial kernel (null space) of matrix $\boldsymbol{Q}^T$. This non-trivial kernel can lead to solutions where pore pressure oscillates without influencing solid deformation [307]. In other words, Equation 5.93 is ill-posed. The necessary condition for well posedness in the problem is known as the

inf-sup condition:

$$\inf_{p^h \in V_p^h} \sup_{\boldsymbol{u}^h \in V_{\boldsymbol{u}}^h} \frac{\int_\Omega p^h \nabla \cdot \boldsymbol{u}^h d\Omega}{\|\boldsymbol{u}^h\|_1 \|p^h\|_0} \geq \gamma \tag{5.94}$$

where $V_{\boldsymbol{u}}^h$ and V_p^h are the discretized interpolation spaces for displacement and pressure. γ is a positive constant, independent of mesh size. This inf-sup condition is frequently referred to as the Ladyzhenskaya-Babuska-Breezi (LBB) condition, after the pioneering contributions of these three researchers [308, 309, 310]. The stability issue can be addressed by employing different orders of interpolation for the displacement and pressure fields. For example, the Q9P4 element satisfies the LBB condition as shown in [304]. Other stabilization procedures consist in adding a penalization term to the variational equations so that the inf-sup condition is weakly satisfied, like with the Q4P4 element for example [304, 305]. Physically, this stabilization procedure is equivalent to adding artificial permeability to diffuse the fluid pressure.

In the case of the linear system of hydraulic fracturing equations formulated in this thesis (Eq.5.89), the permeability of the elements cut by macro fracture is enhanced with the additional term $-\frac{\partial F_{\mathbb{P}}^{\text{int}}}{\partial \mathbb{P}}$, which is several orders of magnitude higher than the permeability of the rock skeleton. From a mathematical point of view, this term provides a certain degree of stabilization to the linear system. Even if the same linear shape functions are used for the interpolation of both the displacement and pressure fields, we have not experienced any instability for the pore pressure field in the following simulations. The proper stabilization for the system at a global scale will be explored in future work.

5.5.3 Damage Driven Cohesive Fracture Propagation

Following the strategy proposed in Chapter 4, the transition from continuum damage to macro-fracture is realized by inserting cohesive segments to regular finite elements when damage reaches a critical threshold. By contrast with Chapter 4, in which the critical damage is rigorously calibrated so as to consider the threshold of crack inteactions, the transition can be triggered at any level of damage since the damage model employed in

this chapter is phenomenological. Simulations done in the previous chapter show that most of the energy is dissipated to create macro fracture surfaces. So we set $\omega_{crit} = 0.1$ for the all simulation cases in this chapter. To compute the damage value at the crack tip, we adopt the method proposed in [273, 161]. As shown in Figure 5.12, we assume that the fracture propagates when the maximum component of the weighted damage vector ($\omega_i, i = 1, 2$ for 2D) over the half circle patch (shaded in blue) exceeds the threshold $\omega_{crit} = 0.1$. Mathematically, we first obtain $\bar{\omega_i}$ by using the bell-shaped weight function $\alpha_0(\|\boldsymbol{x} - \boldsymbol{\xi}\|)$, through

$$\begin{aligned} \bar{\omega_i}(\boldsymbol{x}_{tip}) &= \int_{\Omega_T} \alpha(\boldsymbol{x}_{tip}, \boldsymbol{\xi}) \omega_i(\boldsymbol{\xi}) \mathrm{d}\Omega_T(\boldsymbol{\xi}) \\ &= \frac{\sum_{j=1}^{N_{GP}} \alpha_0(\|\boldsymbol{x}_{tip} - \boldsymbol{\xi}_j\|) \omega_i(\boldsymbol{\xi}_j) \Delta V_j}{\sum_{j=1}^{N_{GP}} \alpha_0(\|\boldsymbol{x}_{tip} - \boldsymbol{\xi}_j\|) \Delta V_j}, \quad (i = 1, 2) \end{aligned} \tag{5.95}$$

where $\boldsymbol{x}_{tip}$ and $\boldsymbol{\xi}$ are the global coordinates of fracture tip and Gauss points in Ω_T. N_{GP} is the total number of Gauss points in Ω_T, and ΔV_J is the geometrical volume associated with Gauss point j. Note that the size of Ω_T is controlled by the internal length $l_c = l_{c1} = l_{c2}$ since the weight function used for non-local enhancement is the bell-shaped function (5.25). Isotropic nonlocal regularization is adopted.

The macro fracture propagates in the direction $\bar{\boldsymbol{d}}_i$, calculated as the weighted average of the damage directions in the half-circle patch, as follows:

$$\bar{\boldsymbol{d}}_i(\boldsymbol{x}_{tip}) = \int_{\Omega_T} \alpha(\boldsymbol{x}_{tip}, \boldsymbol{\xi}) \omega_i(\boldsymbol{\xi}) \frac{\boldsymbol{d}}{\|\boldsymbol{d}\|} \mathrm{d}\Omega_T(\boldsymbol{\xi}), \quad (i = 1, 2) \tag{5.96}$$

where $\boldsymbol{d} = \boldsymbol{\xi} - \boldsymbol{x}_{tip}$, as shown in Figure 5.12. To summarize, we first compare $\max(\bar{\omega_i}), i = 1, 2$ with ω_{crit}. If $\max(\bar{\omega_i}) \geq \omega_{crit}$, we propagate the fracture in the direction of $\bar{\boldsymbol{d}}_i$ with a user-defined growth length Δa. For all the simulations presented in this chapter, we choose $\Delta a = l_c$. Since only the Heaviside function is used for XFEM discretization, no cohesive segment is inserted into the tip element if the fracture tip is located inside an element.

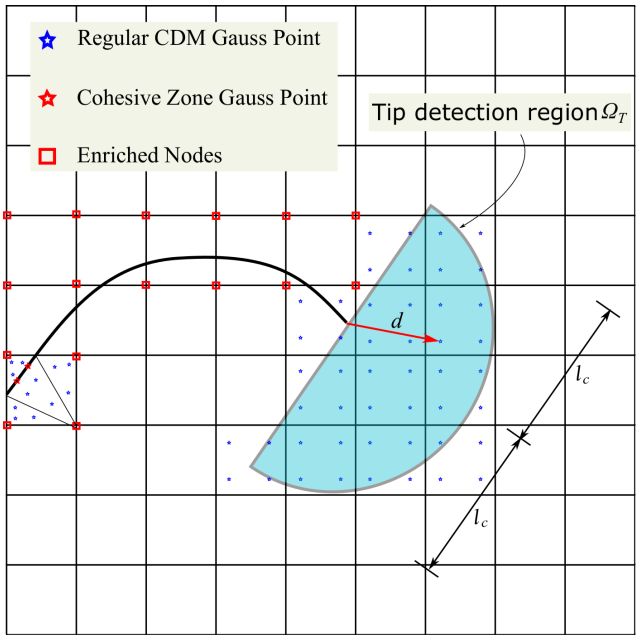

Figure 5.12: Principle of the transition between continuum damage and discrete fracture in the hydraulic fracturing problem.

5.6 Engineering Applications

We implemented the proposed numerical framework in MATLAB for modeling fluid driven multiscale fracture propagation in transversely isotropic porous media. In the following, we validate the formulation and implementation of the multi-scale hydraulic fracturing model by comparing simulation results to analytical solutions for the classical Khristianovic-Geertsma-de Klerk (KGD) problem of hydraulic fracturing. Then, we investigate the relative influence of material and stress anisotropy on the fracture path during hydraulic fracturing. Note that linear quadrilateral plane strain elements are used to discretize the domain in all cases.

5.6.1 Model verification: KGD Injection Problem

The KGD problem is that of fracture propagation due to the injection of a viscous fluid in a borehole embedded in an infinite isotropic porous medium. Figure 5.13 presents the geometry, dimensions, boundary conditions and mesh used for the simulations. Only a

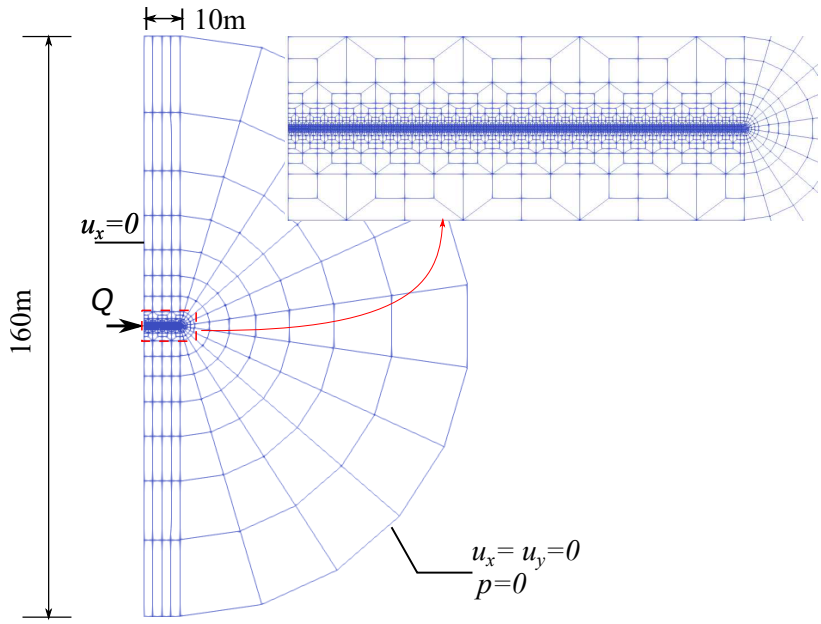

Figure 5.13: The Geometry, boundary conditions and finite element mesh of the KGD problem.

half of the plane strain domain is modeled due to symmetry, and the size of the domain is chosen to avoid boundary effects. The internal length l_c is set to 0.05m. We refine the mesh along the expected fracture propagation path with an element size 0.015m (according to the rule of thumb that the size of element should be less than 1/3 of the internal length when nonlocal regularization is used). An initial fracture with length 0.1m is placed at the borehole, and a constant injection rate of $Q = 0.0002m^2/s$ is applied at the fracture mouth. For all the simulation cases in this section, we set the initial effective stress and fluid pressure to zero, and we employ a constant time increment $\Delta t = 0.01s$ for a total simulation time of 10 s. The remainder of the material parameters for the porous medium is given in Table 5.2.

Given that the considered domain is isotropic, the elastic constants as well as the damage evolution parameters are not direction dependent (Table 5.2). In addition, we assume that the cohesive strength and the cohesive energy release rate have the same value for mode I and mode II fracture propagation ($\phi_n = \phi_t = G, \sigma_{\max} = \tau_{\max}$) in all simulation cases. It is also worth noting that the damage initiation and evolution parameters

Table 5.2: Material parameters for the KGD problem: hydraulic fracturing in an infinite isotropic porous media.

Young's modulus	$E = 15.96$ GPa
Poisson's ratio	$\nu = 0.2$
Initial tensile strain threshold	$\epsilon_{11}^{t0} = 3.5 \times 10^{-5}$
Initial shear strain threshold	$\epsilon_{12}^{t0} = 1.5 \times 10^{-4}$
Damage evolution parameter	$\alpha_{11}^{t} = 1.5 \times 10^{-4}$
Internal length	$l_c = 0.05$ m
Cohesive energy release rate	$G = 90$ N/m
Cohesive traction strength	$\sigma_{\max} = 1$ MPa
Intrinsic permeability	$\kappa = 2 \times 10^{-14}\ m^2$
Dynamic viscosity of water	$\mu = 1 \times 10^{-3}\ Pa{\cdot}s$
Bulk modulus of solid phase	$K_s = 36$ GPa
Bulk modulus of water	$K_w = 3$ GPa
Biot's constant	$\alpha = 0.79$
Initial porosity	$n = 0.19$
Critical Damage	$\omega_{crit} = 0.1$

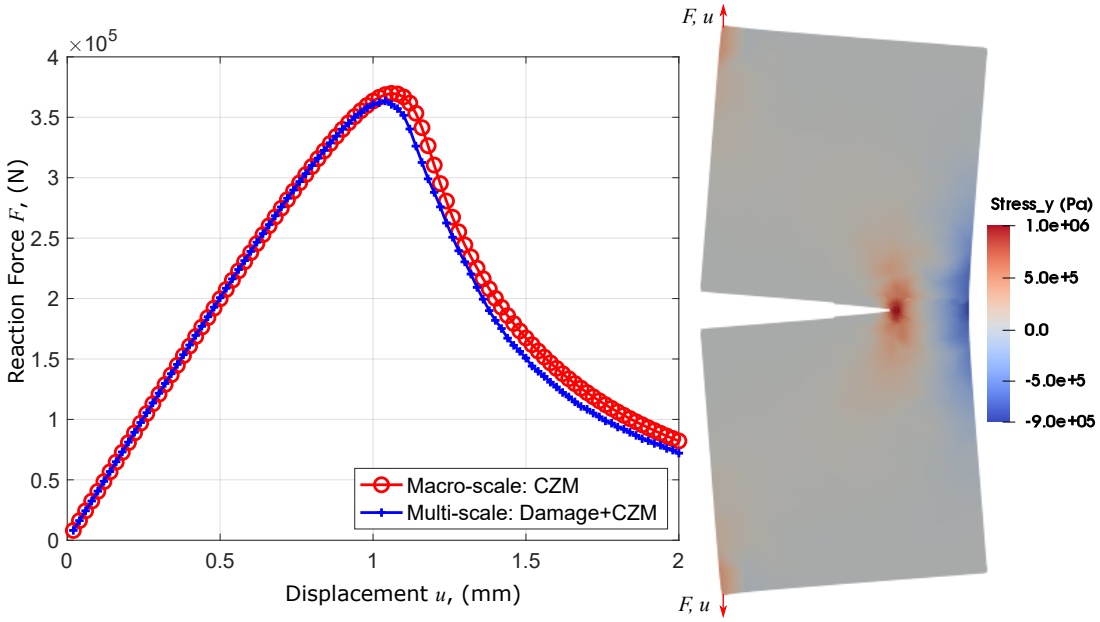

Figure 5.14: Trial and error calibration process for the multi-scale model of hydraulic fracturing: (1) Simulation of a splitting test with pre-inserted cohesive segments without damage evolution inside the matrix to obtain the global force-displacement curve; (2) Simulation of the same splitting test with the proposed multi-scale framework, in which cohesive segments are dynamically inserted, to obtain the $F - u$ curve; (3) Adjustment of the material parameters used in simulation (2) until the two $F - u$ curves match.

($\epsilon_{11}^{t0}, \epsilon_{12}^{t0}, \alpha_{11}^{t}$) as well as the cohesive fracture parameters ($G, \sigma_{\max}$) are calibrated to ensure a consistent transition from damage to fracture. In Chapter 4, in which we dynamically track the amount of energy dissipated by damage evolution and we calculate the cohesive energy release rate as the difference between the total energy release rate and the damage energy release rate. Here, by contrast, we assign constant cohesive strength and energy release rate for all the inserted cohesive segments during fracture propagation. As explained in Figure 5.14, we first simulate a mode I splitting test using cohesive segments without damage development within the matrix. All the cohesive segments are inserted along the predefined fracture path (assumed to be known a priori in this particular case) and we use $G = 100N/m, \sigma_{\max} = 1MPa$. Like in Chapter 4, we choose the rest of the parameters of the PPR cohesive model ($m = n = 4, \lambda_n = \lambda_t = 0.01$) so as to represent brittle fracture propagation and to ensure fast convergence. We track the global response of the opening displacement (u) and the reaction force (F) at the point where the displacement boundary is applied and we obtain the displacement-force curve marked with red circles in Figure 5.14. We carry out another simulation with the same boundary conditions, with the proposed multi-scale hydraulic fracturing model this time, in which nonlocal damage is modeled in the matrix in the first place, and cohesive segments are dynamically inserted once the maximum weighted damage component exceeds the threshold (ω_{crit}). We adjust the damage initiation and evolution parameters ($\epsilon_{11}^{t0}, \epsilon_{12}^{t0}, \alpha_{11}^{t}$) and the cohesive fracture parameters ($G, \sigma_{\max}$) by trial and error, until the global response ($u - F$ curve marked with blue plus signs in Figure 5.14) matches the response obtained when only cohesive segments are considered. For the two simulation cases, the same Young's modulus and Poisson ratio are used (Table 5.2), and the nonlocal internal length is fixed as $l_c = 0.05m$. After calibration, we obtain the same cohesive strength $\sigma_{\max} = 1MPa$ for the multi-scale framework as for the cohesive segment model, but a lower cohesive energy release rate $G_I = 90N/m$. In summary, simulating cross-scale fracture propagation with the calibrated parameters represents fracture propagation in a porous material that has a 1 MPa strength and a 100 N/m

energy release rate according to laboratory measurements.

Figure 5.15 shows the distribution of damage, nonlocal equivalent strain, pore pressure and stress on the deformed mesh (displacements multiplied by 1,000) at $t = 10$ s. As expected, diffused damage ω_2 (horizontal micro-cracks) is obtained within the process zone surrounding the macro fracture. Note that damaged elements are replaced by cohesive segments when the weighted damage exceeds the threshold $\omega_{crit} = 0.1$, and not when a particular component of daamge exceeds that threshold. That explains why the fracture tip does not advance when $\max(\bar{\omega_i}) < \omega_{crit}$, even when the value of damage components at a few gauss points within the tip detection region Ω_T exceed the threshold $(\max(\omega_i) \geq \omega_{crit})$ (Figure 5.12). The distribution of the nonlocal equivalent strain $\bar{\epsilon}^{eq}$ shown in Figure 5.15 indicates that tensile strains only exist in the area near the fracture tip. The fracture surface behind the tip is under compressive strain even when the pore pressure in this area is positive. Note that we assume that the entire simulation domain including the macro fracture is saturated, i.e. the fluid lag is not considered. However, a suction zone with negative pore pressure is obtained at the fracture tip, which is an indirect account of the fluid lag. The distribution of σ_2 further confirms that only a limited zone close to the fracture tip is under tension during hydraulic fracturing; the rest of the domain is under compression.

An analytical solution to the KGD problem was obtained for an elastic and impermeable medium in which a fracture propagates due to the injection of an incompressible fluid [178], as follows:

$$\begin{aligned} \text{CMOD} &= 1.87\Big(\frac{\mu(1-\nu)Q^3}{G_s}\Big)^{1/6} t^{1/3} \\ L &= 0.68\Big(\frac{G_s Q^3}{\mu(1-\nu)}\Big)^{1/6} t^{2/3} \\ \text{CMP} &= 1.38\Big(\frac{G_s^3 Q\mu}{(1-\nu)^3 L^2}\Big)^{1/4} \end{aligned} \tag{5.97}$$

where G_s is the shear modulus, L is the fracture length at time t, CMOP stands for crack

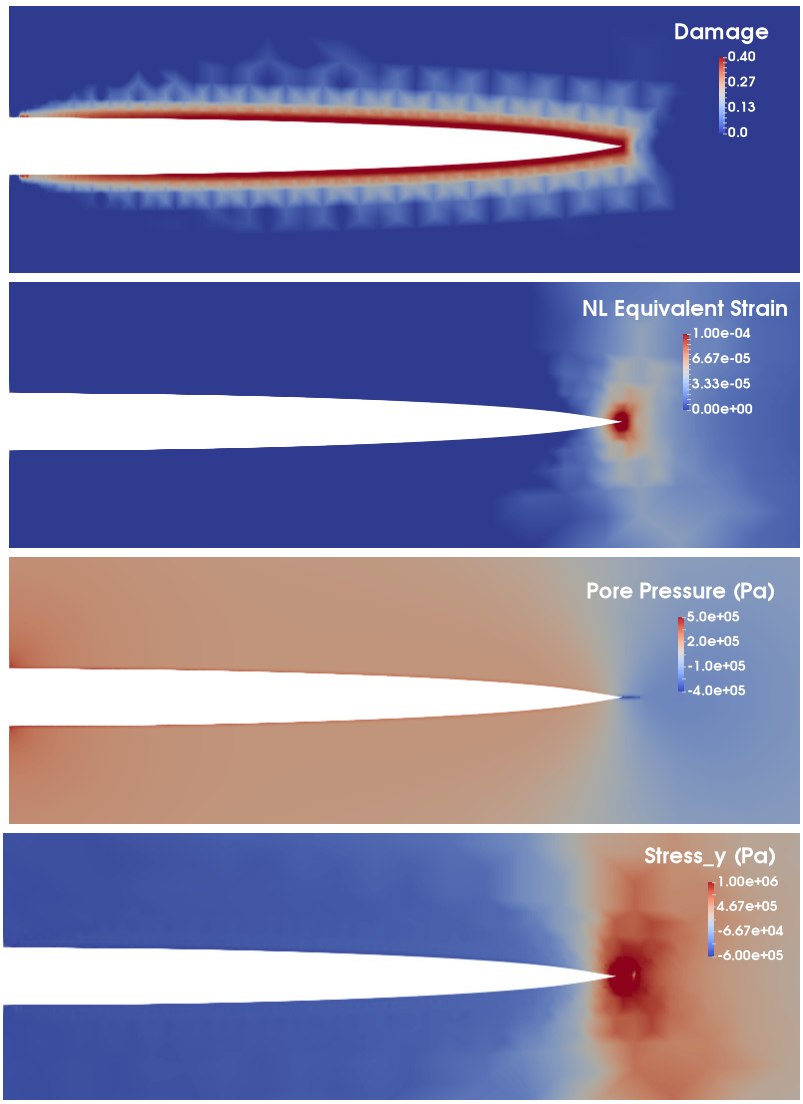

Figure 5.15: Distribution of damage component ω_2, nonlocal equivalent strain $\bar{\epsilon}^{eq}$, pore pressure, and stress component σ_2 on the deformed mesh (displacements multipled 10^3 times) at the end of simulation ($t = 10$ s). Note that the fracture propagates in direction 1 (x-axis).

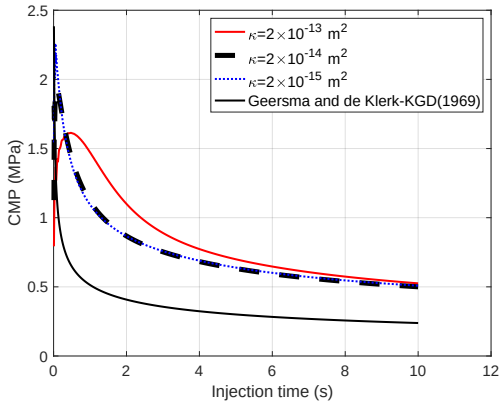

(a) Evolution of fracture mouth pressure against injection time

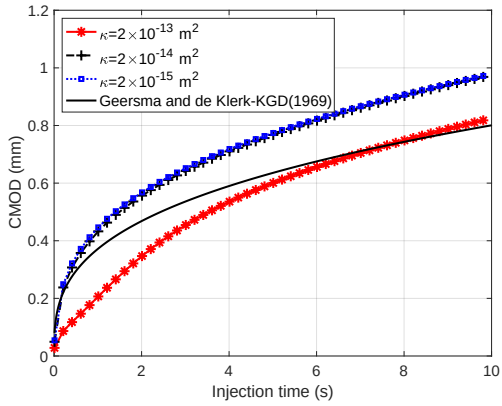

(b) Evolution of fracture mouth opening displacement against injection time

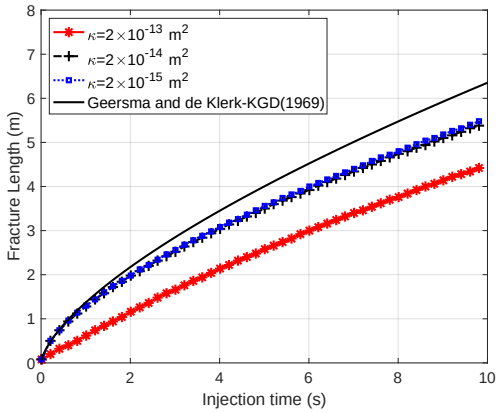

(c) Evolution of fracture length over time

Figure 5.16: Comparison of injection simulation results for various bounding medium permeabilities against the KGD analytical solution, in which the medium is assumed to be impermeable.

mouth opening displacement, and CMP stands for crack mouth pressure. The other notations are the same as in Table 5.2.

Figure 5.16 shows our simulation results of CMP, CMOP and L, plotted them against injection time. We also simulated the KGD test with different permeabilities ($\kappa = 2 \times 10^{-13}m^2$, and $\kappa = 2 \times 10^{-15}m^2$), with the rest of the parameters as listed Table 5.2. Results are compared with the predictions of analytical solution [178]. As expected, results highlight the significant influence of the intrinsic permeability on the evolution of the fracture geometry ($\kappa = 2 \times 10^{-13}m^2$ vs $\kappa = 2 \times 10^{-14}m^2$). The CMP builds up and lasts

longer for porous media with high permeability (Figure 5.16a). Because the fluid leak off decreases the fluid pressure in the facture, the final fracture length is smaller in porous media with higher permeability. On the contrary, the CMP quickly decreases for porous media with low permeability, because the macro fracture propagates quickly, thus creating space for the fluid to flow into. This phenomenon does not hold for all permeabilities. Below a certain permeability value, the CMP does not change any longer ($\kappa = 2 \times 10^{-14} m^2$ vs $\kappa = 2 \times 10^{-15} m^2$). For $t \leq 1$s, with a very low intrinsic permeability, the evolutions of L and of the CMOD found numerically match the analytical solution, in which the bounding medium is assumed to be impermeable. After 1s, the analytical solution overestimates the fracture length L and underestimates the CMOD. This discrepancy is because: (1) even for media with very low permeability, the assumption of impermeability does not hold because the fluid flow into the matrix decreases the effective stress that applies to the fracture faces; (2) the proposed multi-scale hydraulic fracture propagation model depends on the material's strength and energy release rate, while the analytical solution is for a purely brittle fracture propagation problem, independent of strength or energy release rate.

We further investigate the influence of the fluid injection rate on hydraulic fracturing for the KGD problem. All the material parameters are kept the same as in Table 5.2, and we vary the injection rate from $Q = 0.0001 m^2/s$ to $Q = 0.0003 m^2/s$. Figure 5.17 shows the results of CMOD and fracture length against the injection time, as well as the crack opening displacement profile at the end of simulation (at $t = 10$ s). The evolution of the CMOD and of the fracture length show that a higher injection rate results in faster fracture propagation and a wider fracture mouth opening. The profile of fracture opening at the end of the simulation further confirms that both the length and the width of the fracture increase with increasing injection rate. In addition, the increase rate is not linear, since the difference of fracture length between $Q = 0.0001 m^2/s$ and $Q = 0.0002 m^2/s$ is not equal to that between $Q = 0.0002 m^2/s$ and $Q = 0.0003 m^2/s$.

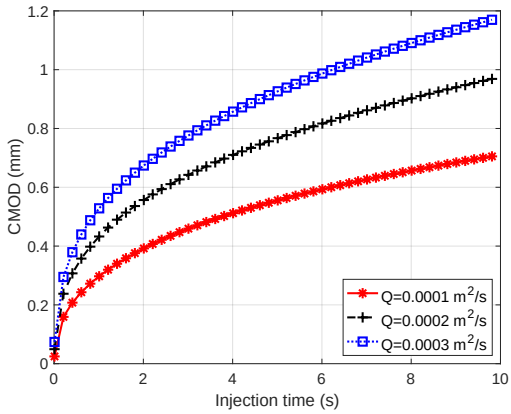

(a) The evolution of fracture month opening displacement against injection time

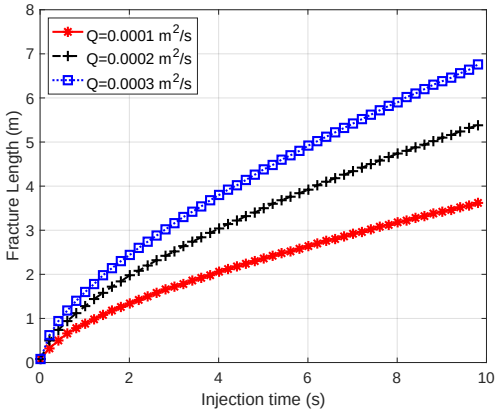

(b) Propagated fracture length history

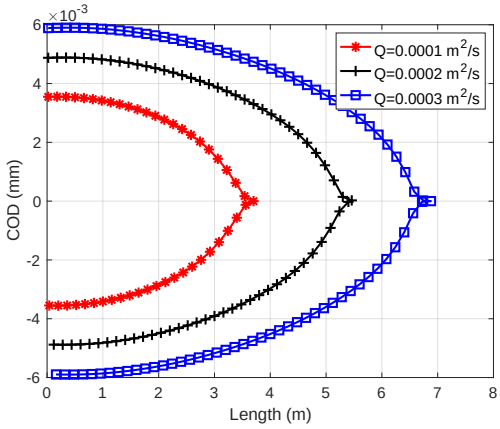

(c) Fracture opening profile at t=10 s

Figure 5.17: Simulation results for a fluid driven fracture in a porous medium with different injection rates.

5.6.2 Influence of Material and Stress Anisotropy on Hydraulic Fracturing

The second engineering problem is chosen to demonstrate the performance of the proposed computational framework in modeling the hydro-mechanical behavior of saturated media subjected to both material and stress anisotropy. A square domain 500 mm by 500 mm is considered. The solid skeleton is transversely isotropic with horizontal layers. We carry out three series of simulations (Figure 5.18). In test 1, all normal displacements at the boundary are fixed. An initial fracture 40 mm length, oriented at an angle θ with respect to horizontal axis is placed at the center of the domain (Figure 5.18a). We investigate the

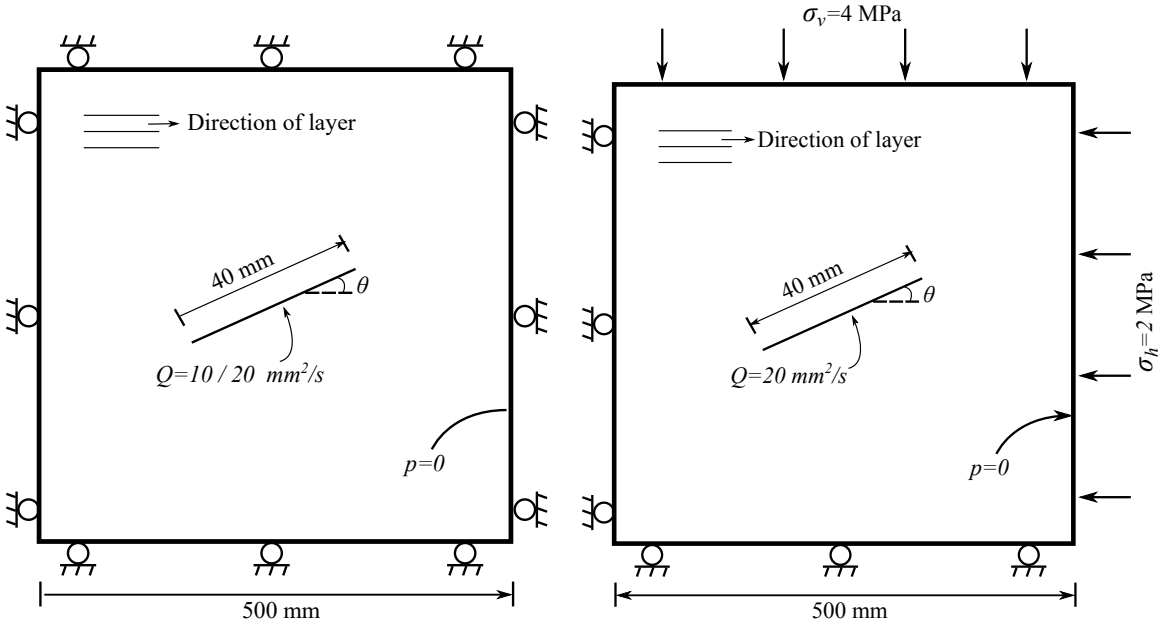

(a) Without in situ stress (tests 1 and 2) (b) With anisotropic in situ stress (test 3)

Figure 5.18: Geometry and boundary conditions used to investigate the influence of material and stress anisotropy on hydraulic fracturing in transversely isotropic materials.

effect of material anisotropy on hydraulic fracturing by varying the angle θ with constant fluid injection rate $Q = 10mm^2/s$. About 6,500 linear plane strain elements were used to discretize the domain. We set the initial pore pressure at zero, and we run the simulation in 0.2 s with the time increment $\Delta t = 0.005$ s. In test 2, we use the same initial and boundary conditions, but we change the fluid injection rate from $Q = 10mm^2/s$ to $Q = 20mm^2/s$. Comparing the results of tests 1 and 2 informs on the influence of injection rate on hydraulic fracturing in an anisotropic material. In test 3, anisotropic in situ stress is applied at the boundary in addition and the angle θ is non-zero, as shown in Figure 5.18b. The other initial and boundary conditions are the same as in the previous two cases. The parameters used for the three simulations are listed in Table 5.3.

Like in the KGD case, we calibrate by trial and error the material parameters that control damage evolution ($\epsilon_{11}^{t0}, \epsilon_{22}^{t0}, \epsilon_{12}^{t0}, \alpha_{11}^{t}, \alpha_{22}^{t}$) and those that govern the cohesive fracture behavior ($G_{,1}, G_{,2}, \sigma_{\text{max},1}, \sigma_{\text{max},2}$) in the directions perpendicular and parallel to the layer. We use the same local coordinate system as shown Figure 5.1, in which axis-1

Table 5.3: Material parameters used in the simulations that investigate the influence material and stress anisotropy on hydraulic fracturing.

Parameters	Perpendicular to the layer	Paralllel to the layer
Young's modulus	$E_{11} = 10$ GPa	$E_{22} = 20$ GPa
Poisson's ratio	$\nu_{11} = 0.2$	$\nu_{22} = 0.2$
In plane shear modulus	$G_{12} = 6.25$ GPa	
Initial tensile strain threshold	$\epsilon_{11}^{t0} = 8 \times 10^{-5}$	$\epsilon_{22}^{t0} = 9 \times 10^{-5}$
Initial shear strain threshold	$\epsilon_{12}^{t0} = 6.8 \times 10^{-4}$	
Damage evolution parameter	$\alpha_{11}^{t} = 3.5 \times 10^{-4}$	$\alpha_{22}^{t} = 4 \times 10^{-4}$
Internal length	10 mm	
Cohesive energy release rate	$G_{,1} = 0.095$ N/mm	$G_{,2} = 0.19$ N/mm
Cohesive traction strength	$\sigma_{\text{max},1}$ =1 MPa	$\sigma_{\text{max},2}$ =2 MPa
Intrinsic permeability	$\kappa = 2 \times 10^{-14}\ m^2$	$\kappa = 4 \times 10^{-14}\ m^2$
Dynamic viscosity of water	$\mu = 1 \times 10^{-3}\ Pa{\cdot}s$	
Bulk modulus of solid phase	$K_s = 36$ GPa	
Bulk modulus of water	$K_w = 3$ GPa	
Biot's constant	$\alpha_{11} = 0.75$	$\alpha_{22} = 0.65$
Initial porosity	$n = 0.19$	
Critical Damage	$\Omega_{cr} = 0.1$	

is perpendicular to the layer, and axis-2 is parallel to the layer. Note that in the following simulations, we fix the local coordinate system in such a way that axis-1 is always vertical. As explained in Figure 5.19, we first simulate two splitting tests with pre-inserted cohesive segments parallel and perpendicular the layer, for which the cohesive energy values are $G_{,1} = 0.1N/mm, G_{,2} = 0.2N/mm$ and the cohesive strengths are $\sigma_{\text{max},1} = 1$ MPa, $\sigma_{\text{max},2} = 2$ MPa. Let us recall that in the PPR cohesive model, we employ $\phi_n = \phi_t = G, \sigma_{\text{max}} = \tau_{\text{max}}, m = n = 4, \lambda_n = \lambda_t = 0.01$ to account for mixed mode fracture propagation and brittle fracture propagation [255, 266, 311]. We extract the global force-displacement curves (red circles for fractures parallel to the layer and marked in green square for fracture perpendicular to the layer). Next we run the same two simulations using the multi-scale hydraulic fracturing model, in which, and cohesive segments are dynamically inserted when the weighted damage at the fracture tip exceeds the critical value $\omega_{crit} = 0.1$. After a number of simulations with different input parameters, which control meso-scale damage evolution and macro-scale cohesive fracture propagation, we

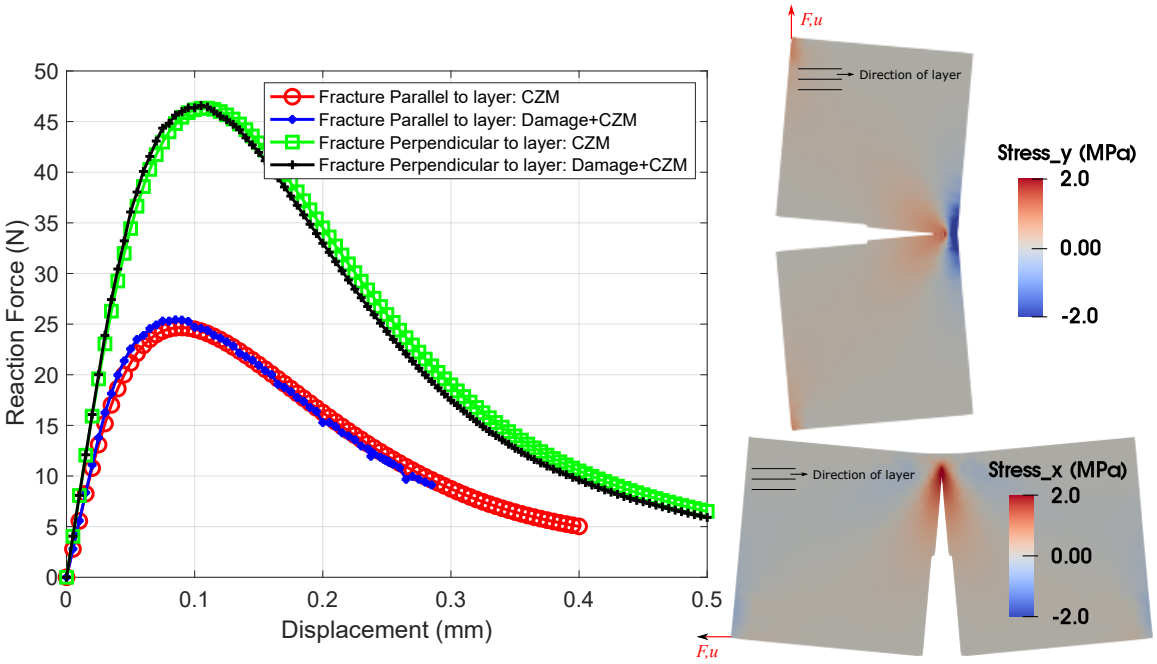

Figure 5.19: Trial and error calibration process for coupling nonlocal damage with cohesive fracture for transversely isotropic materials: (1) Simulation of two splitting test with pre-inserted cohesive segments parallel (respectively perpendicular) to the layer to obtain the global force-displacement curve in the case of horizontal (respectively vertical) bedding; (2) Simulation of the same splitting tests with the multi-scale hydraulic fracturing model, in which the cohesive segments are dynamically inserted, to obtain the $F-u$ curves; (3) Adjustment of the multi-scale hydraulic fracturing model parametrs until the $F-u$ curves match for both fracture propagation directions.

find the best match for the $F-u$ curve, as shown in Figure 5.19. The calibrated parameters are listed in Table 5.3. It is worth noting that we use isotropic nonlocal regularization with $l_{c1} = l_{c2} = 10$ mm for simplicity. In summary, the calibrated multi-scale fracture propagation model is globally equivalent to a model of fracture propagation in a transversely isotropic material with $G_{,1} = 0.1N/mm, \sigma_{\max,1} = 1$ MPa in direction parallel to the layer, and $G_{,2} = 0.2N/mm, \sigma_{\max,2} = 2$ MPa in direction perpendicular to the layer.

The calibration process only provides the cohesive parameters when the fracture propagates in the direction parallel or perpendicular to the bedding. To determine the cohesive parameters when the fracture propagation direction is neither parallel or perpendicular to the bedding, a whole series of laboratory experiments would need to be carried out. In this thesis, we propose to obtain the cohesive parameters by projection on an elliptical failure

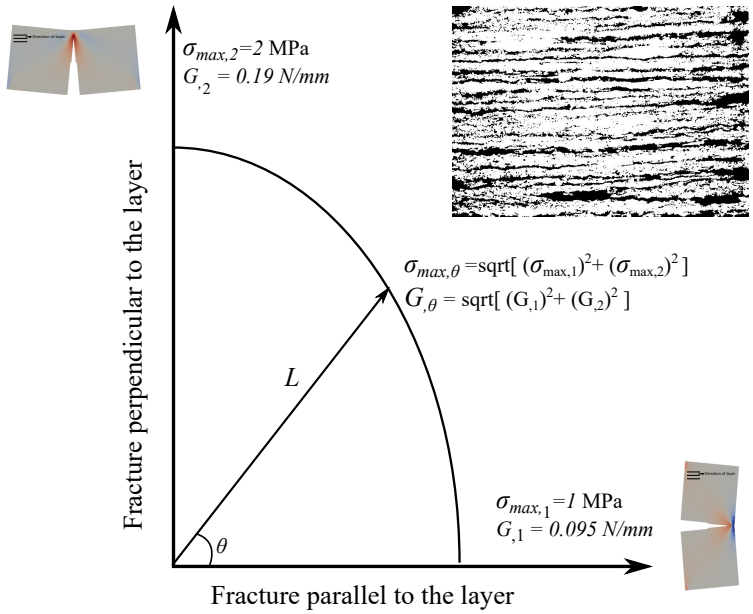

Figure 5.20: Elliptical failure curve used to determine cohesive parameters when the fracture propagates at an angle θ relative to the layer.

curve, as shown in Figure 5.20. The cohesive strength and the energy release rate of a fracture that propagate at an angle θ to the layer are expressed as:

$$\begin{aligned} \sigma_{\max,\theta} &= \sqrt{(\sigma_{\max,1})^2 + (\sigma_{\max,2})^2} \\ G_{,\theta} &= \sqrt{(G_{,1})^2 + (G_{,2})^2} \end{aligned}, \tag{5.98}$$

Fundamentally, we assume that the strength and the energy release rate at different propagation angles form an ellipse in plane strain.

Figure 5.21 shows the pore pressure p, the effective stress component σ_x and the fracture paths at the end of the simulation (at $t = 0.02$ s) for test 3 with the boundary conditions $\sigma_v = 4$ MPa, $\sigma_h = 2$ MPa, and $Q = 20\ mm^2/s$. The increased pore pressure near the fracture in Figures 5.21a and 5.21b demonstrates that the proposed numerical tool can predict the fluid leak off from the macro fracture to the porous matrix. Compared to the case $\theta = 90°$, the higher pore pressure observed for $\theta = 0°$ is due to the lower permeability in the direction perpendicular to the layer (Table 5.3): more fluid pressure builds up and less fracture space is created (less fracture length and less width). In agreement with physical

expectations, for $\theta = 30°, 60°$, compressive effective stress is observed in the area behind the fracture tip, and tensile effective stress only concentrates in the areas ahead of fracture tip. For $\theta = 30°, 60°, 90°$, the fracture propagates in the direction of maximum compressive in situ stress, which is exactly what is reported in literature. For $\theta = 0°$, we expect to see two branches emerging from the tips of the initial horizontal fracture, that finally form vertical fractures. Instead, we obtain the horizontal fracture shown in Figure 5.21a, because of the continuum dmage to fracture transition criterion, based on a weighted damage threshold (Section 5.5.3). Even is the continuum damage model predicts damage development in the two vertical branch directions, the weighted damage direction is horizontal.

Figure 5.22 shows the pore pressure distribution and the fracture paths at the end of the simulations (at $t = 0.02s$) for the three tests, when $\theta = 30°$ and when $\theta = 60°$. In test 1 (no in situ stress, $Q = 10\ mm^2/s$), the fracture propagates in the horizontal direction parallel to the layer, for both $\theta = 30°$ (Figure 5.22a) and $\theta = 60°$ (Figure 5.22b). However, when the injection rate increases to $Q = 20\ mm^2/s$ (tests 2 and 3), the fracture path is horizontal only for $\theta = 30°$ under zero in situ stress (Figure 5.22c). A vertical fracture path is predicted for $\theta = 60°$ under the same boundary conditions (Figure 5.22c). This questionable result can be attributed to: (1) The weighted damage driven fracture propagation criterion, which cannot predict accurately the fracture branch orientation; (2) The rapid injection of the fluid, which can change the fracture propagation direction if it does not align with the weak layer. Further laboratory experiments are needed to understand which of these two phenomena dominates. In tests 3, the fracture path is parallel to maximum compressive stress, irrespective of the initial fracture direction (the figure shows the case of $\sigma_v = 4MPa, \sigma_h = 2MPa$).

We further extracted the propagated fracture paths for all the tests simulated, as illustrated in Figure 5.23. When only material anisotropy is considered, results show that a horizontal fracture path parallel to the layer forms (Figure 5.23a). Typically, teh fracture length and width increase with the injection rate. Questionable results are obtained in some

of the cases with $\theta \geq 60^{\circ}$, due to the weighted damage driven fracture propation criterion. Figure 5.23b presents a comparison between the cases with material anisotropy only (tests 1 and 2) and the cases with both maerial and stress anisotropy (test 3). For all orientations θ considered, the predicted fracture length is shorter when situ stress is applied. This is because a part of the energy is dissipated to overcome the compressive in situ stress. Some cases need further examined by laboratory experiments and more advanced fracture propagation criteria, especially when a horizontal fracture path is predicted under non-zero in situ stress, or when a vertical fracture is predicted under zero in situ stress.

5.7 Conclusions

In this chapter, we formulated and implemented a numerical tool to model multi-scale mixed mode fluid driven fracture propagation in transversely isotropic porous media. We first proposed a phenomenology based nonlocal damage model to predict the complex nonlinear behavior of materials with intrinsic anisotropy upon fracture propagation. The principle of equivalent elastic deformation is used to calculate the stiffness tensor of the damaged material. Following the choice of stress invariants made in Hill's quadratic yield criteria (for orthotropic materials) and Hashin's failure criteria (for unidirectional fiber composites), four equivalent strain measures are constructed to distinguish the mechanical response of the material in tension and compression, along the direction perpendicular to the bedding plane and within the bedding plane. Damage evolution laws are formulated explicitly in terms of the maximum equivalent strain ever encountered in the loading history. For Finite Element implementation, the equivalent strains are replaced by nonlocal counterparts, defined as weighted averages over a certain neighborhood, the size of which is controlled by two internal length parameters that represent microstructure anisotropy. The consistent tangent stiffness is derived analytically, with an account to the non-local terms, for a plain strain case. We solve the Finite Element equations with an energy dissipation based arc length control algorithm, which allows passing limit points in case of snap back or snap

through. Results of three-point bending simulations reveal that mixed mode fracture propagation dominates when the loading force is not aligned with the bedding plane, demonstrating the proposed damage model is capable of modeling direction dependent fracture propagation.

We then coupled the proposed nonlocal anisotropic damage model with the PPR cohesive macro-fracture model to simulate the transition between microscopic crack propagation and macroscopic fracture localization. The transition from continuum damage to cohesive fracture is done by dynamically inserting cohesive segments once the weighted damage exceeds a certain threshold. Diffusion equations are used to model fluid flow inside the porous matrix and within the macro fracture, in which conductivity is obtained by Darcy's law and the cubic law, respectively. We presented the strong and weak forms of the hydraulic fracturing problem. The XFEM is employed to approximate the solution for the fully coupled $\boldsymbol{u} - p$ formulation, in which the macro fracture is modeled by Heaviside jump functions for displacement and by modified level set functions for the fluid flow. After discretizing the system of equations in time, the entire nonlinear system is linearized and solved by using the Newton-Raphson iteration scheme. We simulate the KGD mode I fracture propagation in an infinite porous medium. We check that for low volumes of fluid injected in a porous medium of low permeability, the model provides predictions that are in agreement with the analytical solution proposed for impermeable media. We then examine the effect of material and stress anisotropy on hydraulic fracturing by simulating an injection test in an inclined fracture embedded in a transversely anisotropic porous medium. As expected, the fracture propagates along the bedding direction in the absence of in situ stress and along the direction of maximum compressive stress when anisotropic stress boundary conditions are applied. The length and width of the fracture increase with the injection rate. Some discrepancies are noted, especially when both material and stress anisotropy are accounted for, because of the choice of the damage-to-fracture transition criterion, which is based on a weighted average of damage ahead of the fracture tip.

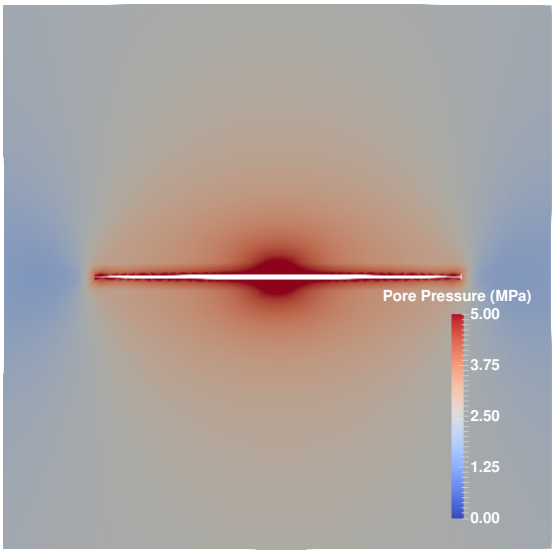

(a) Pore pressure, $\theta = 0°$

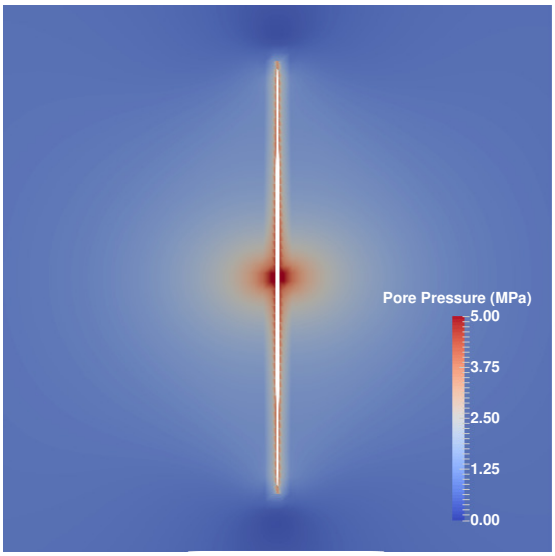

(b) Pore pressure, $\theta = 90°$

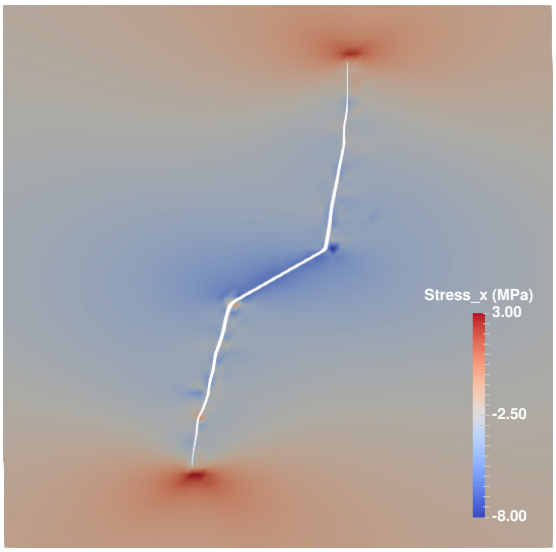

(c) Horizontal effective stress, $\theta = 30°$

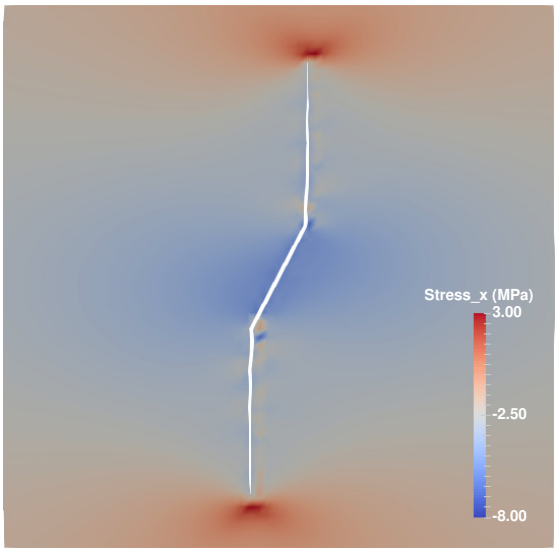

(d) Horizontal effective stress, $\theta = 60°$

Figure 5.21: Pore pressure and effective stress distributions shown on the deformed mesh (fracture opening magnified 50 times) at the end of the test 3 with $\sigma_v = 4$ MPa, $\sigma_h = 2$ MPa, and $Q = 20\ mm^2/s$.

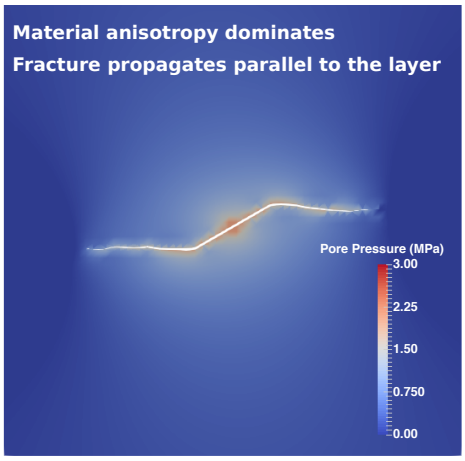

(a) $\sigma_v = \sigma_h = 0, Q = 10mm^2/s, \theta = 30°$

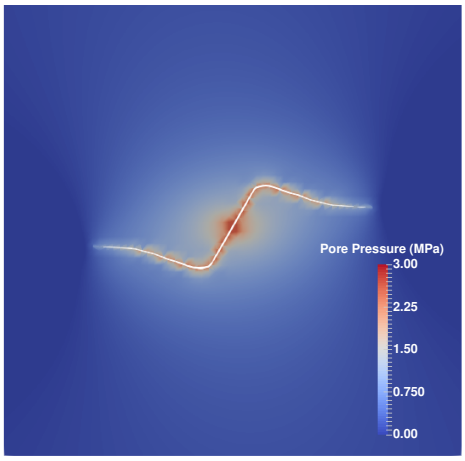

(b) $\sigma_v = \sigma_h = 0, Q = 10mm^2/s, \theta = 60°$

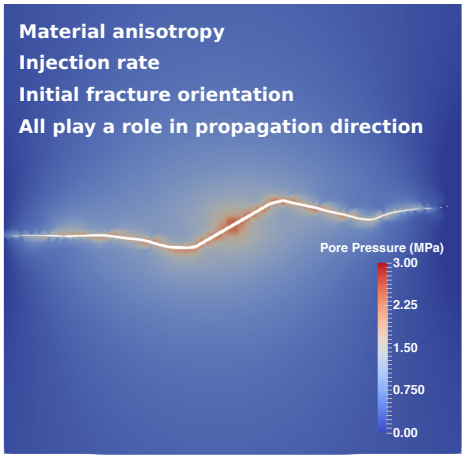

(c) $\sigma_v = \sigma_h = 0, Q = 20mm^2/s, \theta = 30°$

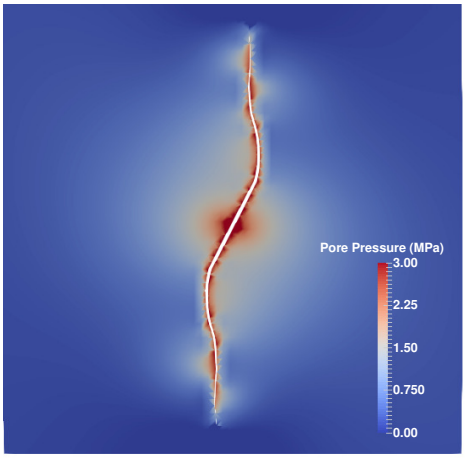

(d) $\sigma_v = \sigma_h = 0, Q = 20mm^2/s, \theta = 60°$

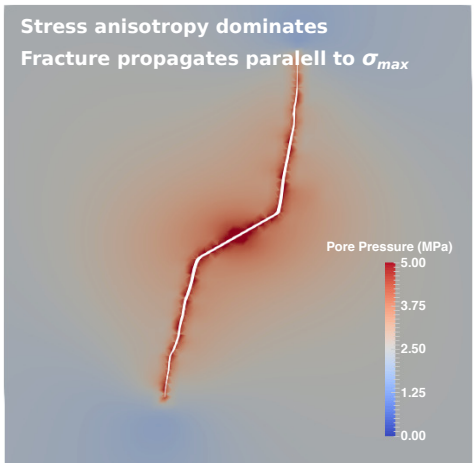

(e) $\sigma_v = 4MPa, \sigma_h = 2MPa, Q = 20mm^2/s, \theta = 30°$

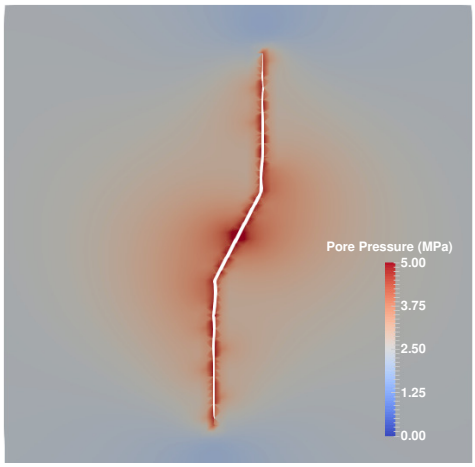

(f) $\sigma_v = 4MPa, \sigma_h = 2MPa, Q = 20mm^2/s, \theta = 60°$

Figure 5.22: Pore pressure distribution shown on the deformed mesh (crack opening magnified 50 times) at the end of the tests simulated.

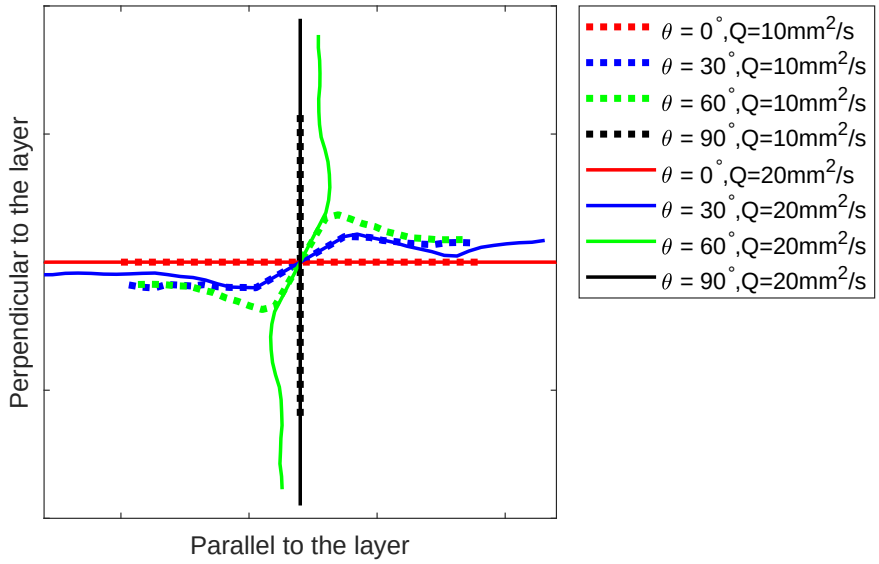

(a) Influence of the injection rate in transversely isotropic materials without in situ stress.

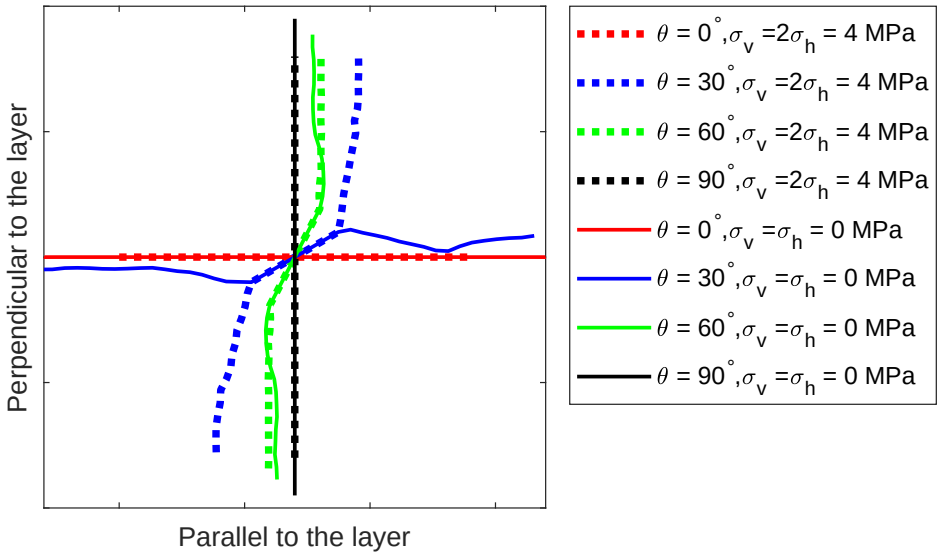

(b) Influence of stress and material anisotropy on the hydraulic fracturing path with $Q = 20\,mm^2/s$.

Figure 5.23: Simulated fracture paths.

CHAPTER 6
CONCLUSIONS AND FUTURE WORK

6.1 Main Contributions

In this work, we aimed to explain and predict the meso-scale mechanical behavior of brittle materials, by modeling the inception and growth of micro-cracks, the continuous propagation and coalescence of micro-cracks and the resulting localized macro-fracture. We explored state-of-art computational tools to capture the multiscale behavior of brittle materials subjected to hydro-mechanical loads. We first established the connection between the REV-scale behavior and micro-scale crack evolution by employing principles of micromechanics and thermodynamics. Then, we modeled the diffused damage inception and extensive damage localization leading to macro-fracture propagation, by coupling a nonlocal micromechanical damage model with a cohesive zone model. Finally, we extended the framework of transition from continuum damage to discrete fracture to transversely isotropic materials (e.g. shale) subjected to hydraulic loads. Five main contributions to the field of theoretical and computational geomechanics were made:

1. *Micromechanical damage model based on the wing crack theory*: Observing that wing cracks develop during compression in brittle materials, a novel discrete-equivalent-wing-crack-damage (DEWCD) model was proposed, in which (i) the free energy is obtained by adding the elastic energy stored in the matrix and the energy stored in the displacement jumps of a discrete set of crack families; (ii) stress driven fracture mechanics criteria are used at the microscopic scale to control crack growth,; in particular, wing cracks initiate and propagate in the direction of maximum compressive stress; (iii) flow rules are expressed by means of a hyperbolic hardening law and a linear damage potential. Gauss point simulations demonstrate that the model can

capture the following REV-scale phenomena:

- Non-linear stress/strain relationship with anisotropic stiffness reduction
- Volumetric expansion and unilateral effects
- Confinement-dependent transition from brittle behavior to ductile behavior
- Different mechanical responses in tension and compression

2. *Micromechanical damage model with thermodynamically consistent and non-smooth yield surfaces*: In order to implement a constitutive law that connects the REV-scale mechanical behavior with micro-processes into a FEM package, such as UMAT in Abaqus, a micromechanics-based discrete damage model with multiple non-smooth yield surfaces was formulated, in which (i) the expression of the REV Gibbs energy is the same as in the DEWCD model; (ii) damage driven forces, which are thermodynamically conjugated to the tensile and compressive crack densities for each crack family, are used to construct damage criteria; (iii) all cracks are assumed to grow radially without wing crack development, with open cracks (respectively, closed cracks) propagating in pure mode II (respectively, in mixed mode). We derived the tangent matrix analytically and we employed the closest projection algorithm (a type of return mapping method) for solving the FEM equations. FE simulations demonstrate that the model captures all the REV-scale phenomena captured by the DEWCD model, with the advantage of being fully implemented in UMAT.

3. *Cross-scale fracture propagation*: A novel numerical framework that couples a non-local anisotropic damage model with a cohesive zone model was proposed to simulate the whole fracture propagation process, from the nucleation of micro-cracks to the formation of a macro-fracture. The framework includes:

   - A micromechanics-based continuum damage model based on the assumption that all cracks are open;

- A non-local integration-based enrichment with the equivalent strain to predict damage evolution;
- A rigorous calibration procedure to find the critical damage level that marks the transition from continuum damage to discrete fracture (here, $\Omega_{crit} = 0.2$);
- A damage-fracture equivalence scheme that ensures that the balance of energy at the scale of the whole system;
- An XFEM-based space discretization, with enriched degrees of freedom that allow predicting fracture propagation without pre-assigned path

4. *Anisotropic nonlocal damage model for materials with intrinsic transverse isotropy*: An original phenomenological anisotropic damage model enhanced with nonlocal regularization was formulated for transversely isotropic materials. In this model: (i) three independent damage scalars are used to account for anisotropic stiffness reduction; (iii) four equivalent strain measures are constructed to distinguish the mechanical response of the material in tension and compression, along the direction perpendicular to the bedding plane and within the bedding plane; (iii) damage evolution laws are formulated explicitly in terms of the maximum nonlocal equivalent strain ever encountered in the loading history. After implementation into an open source finite element package, results of three-point bending simulations demonstrate that the model can capture direction dependent fracture propagation in mixed mode.

5. *Hydraulic fracturing in transversely isotropic materials*: A computational tool was developed to model fluid driven multiscale fracture propagation in transversely isotropic materials. In this numerical scheme: (i) the nonlinear deformation of the porous matrix is taken into account by the proposed anisotropic nonlocal damage model; (ii) multiscale fracture propagation is modeled by the transition from diffused continuum damage to localized cohesive fracture; (iii) fluid flow inside the matrix (respectively, inside the fracture) is governed by Darcy's law (respectively, the cubic law); (iv) the

coupled problem is discretized with the XFEM, and solved with Newton-Raphson's iteration scheme. The numerical model was validated against the KGD analytical solution, and parametric studies were carried out to investigate the influence of material and stress anisotropy on hydraulic fracturing paths.

6.2 Plans for Future Research

The work presented in this thesis can be improved to address some limitations of the proposed numerical methods. Several topics for future study are listed below.

1. The main advantage of the wing crack growth model is to explain the REV-scale behavior with only a few material parameters that all have a sound physical meaning. However, the proposed DEWCD model is formulated with stress-driven micro-crack propagation laws, which are difficult to implement in the FEM, in which load increments are controlled in strain. Future research will focus on transforming the wing crack growth model in terms of strain components and to simulate engineering scale problems with the FEM.

2. The continuum damage model used to capture the transition from diffused damage to localized fracture is based on dilute homogenization, which does not permit simulating continuum behavior after damages reaches the critical threshold Ω_{crit}. The choice of this CDM model further limits the CDM-CZM framework for mixed model micro-macro fracture propagation. This challenge can be addressed in the future studies by employing the Mori-Tanaka homogenization scheme, which accounts for crack interaction.

3. In this dissertation, multiscale fracture propagation is represented as the transition from continuum damage to discrete fracture. Micro-structure evolution is indirectly reflected through the evolution of internal state variables (damage/crack density) within the constitutive law. It would be intersting to model micro-structure explic-

itly during multiscale fracture propagation by using the hierarchical FE^2 scheme, and to compare the results from the FE^2 scheme with our damage-fracture transition scheme. Further benchmarking against stress-strain behavior with Computed Tomography would provide guidelines to choose adapted computational tools to solve engineering problems.

4. Another future research goal is to improve the macro-fracture propagation criteria. The weighted damage value works perfectly for fractures that propagate in one direction. However, it is challenging to account for fracture branching. On the one hand, a more detailed algorithm is needed to process the evolution of damage at the tip and predict branching paths; On the other hand, the level set method used to identify fracture paths in XFEM has inherent limitations to account for multiple fracture branchings and intersections, especially in 3D. To overcome these limitations, we will explore other numerical methods, such as techniques based on the dynamic insertion of cohesive interface elements, peridynamics and phase field methods.

5. In the hydraulic fracturing model, the permeability change within the macro-fracture is accounted for by the cubic law. The permeability of the porous matrix is constant. However, the micro-structure evolution within the process zone surrounding the macro fracture clearly influences the permeability. The permeability change in this area affects the fluid exchange between the matrix and the fracture, which, in turn, influences the propagation of the macro fracture. Research is still needed to establish a relationship between micro-structure (damage) and permeability evolutions, and to implement that relation in the FEM to simulate hydraulic fracturing more accurately.

6. Hydraulic fracturing is typically used in rock formations that contain fractures prior to fluid injection. In addition, injections are performed at multiple perforated notches at the same time. Thus, multiple fluid-driven fractures may propagate simultane-

ously. A major future research goal is to extend the current formulation and implementation to account for multiple fluid driven fracture that intersect with a pre-existing fracture network.

7. The formulation and implementation for hydro-mechanical coupling is based on the assumption that the porous medium is fully saturated, the fluid lag is indirectly reflected through negative fluid pressure. Thus, another future research direction is to extend the current formulation to unsaturated media, and to consider fluid lag explicitly.

8. The proposed multi-scale damage-to-fracture transition computational tool can be used in many problems other than hydraulic fracturing in tight rock formations, e.g., fault reactivation and stick-slip, concrete structure performance and integrity.

REFERENCES

[1] C. F. Tsang, F. Bernier, and C. Davies, "Geohydromechanical processes in the excavation damaged zone in crystalline rock, rock salt, and indurated and plastic claysin the context of radioactive waste disposal," *International Journal of Rock Mechanics and Mining Sciences*, vol. 42, no. 1, pp. 109–125, 2005.

[2] C. Arson and B. Gatmiri, "Thermo-hydro-mechanical modeling of damage in unsaturated porous media: Theoretical framework and numerical study of the edz," *International Journal for Numerical and Analytical Methods in Geomechanics*, vol. 36, no. 3, pp. 272–306, 2012.

[3] R. Puri, G. King, I. Palmer, *et al.*, "Damage to coal permeability during hydraulic fracturing," in *Low Permeability Reservoirs Symposium*, Society of Petroleum Engineers, 1991.

[4] X. Weng, O. Kresse, C. E. Cohen, R. Wu, H. Gu, *et al.*, "Modeling of hydraulic fracture network propagation in a naturally fractured formation," in *SPE Hydraulic Fracturing Technology Conference*, Society of Petroleum Engineers, 2011.

[5] K. Katagiri, W. Ott, and B. Nutley, "Hydraulic fracturing aids geothermal field development," *World Oil*, vol. 191, no. 7, 1980.

[6] B. Legarth, E. Huenges, and G. Zimmermann, "Hydraulic fracturing in a sedimentary geothermal reservoir: Results and implications," *International Journal of Rock Mechanics and Mining Sciences*, vol. 42, no. 7-8, pp. 1028–1041, 2005.

[7] C. Zhu, "Microstructure-based modeling of damage and healing in salt rock with application to geological storage," PhD thesis, Georgia Institute of Technology, 2016.

[8] W. D. Gunter, S. Bachu, and S. Benson, "The role of hydrogeological and geochemical trapping in sedimentary basins for secure geological storage of carbon dioxide," *Geological Society, London, Special Publications*, vol. 233, no. 1, pp. 129–145, 2004.

[9] S. M. Benson and F. M. Orr, "Carbon dioxide capture and storage," *MRS bulletin*, vol. 33, no. 4, pp. 303–305, 2008.

[10] S.-N. Roth, P. Léger, and A. Soulaïmani, "A combined xfem–damage mechanics approach for concrete crack propagation," *Computer Methods in Applied Mechanics and Engineering*, vol. 283, pp. 923–955, 2015.

[11] V. Lyakhovsky and Y. Ben-Zion, "Evolving geometrical and material properties of fault zones in a damage rheology model," *Geochemistry, Geophysics, Geosystems*, vol. 10, no. 11, 2009.

[12] T. Suzuki, "Understanding of dynamic earthquake slip behavior using damage as a tensor variable: Microcrack distribution, orientation, and mode and secondary faulting," *Journal of Geophysical Research: Solid Earth*, vol. 117, no. B5, 2012.

[13] L. Dormieux, D. Kondo, and F.-J. Ulm, *Microporomechanics*. John Wiley & Sons, 2006.

[14] J. D. Eshelby, "The determination of the elastic field of an ellipsoidal inclusion, and related problems," in *Proceedings of the Royal Society of London A: Mathematical, Physical and Engineering Sciences*, The Royal Society, vol. 241, 1957, pp. 376–396.

[15] J. F. Shao and J. Rudnicki, "A microcrack-based continuous damage model for brittle geomaterials," *Mechanics of Materials*, vol. 32, no. 10, pp. 607–619, 2000.

[16] B. Paliwal and K. Ramesh, "An interacting micro-crack damage model for failure of brittle materials under compression," *Journal of the Mechanics and Physics of Solids*, vol. 56, no. 3, pp. 896–923, 2008.

[17] R. Bargellini, D. Halm, and A. Dragon, "Modelling of anisotropic damage by microcracks: Towards a discrete approach," *Archives of Mechanics*, vol. 58, no. 2, pp. 93–123, 2006.

[18] D. Krajcinovic, M. Basista, and D. Sumarac, "Micromechanically inspired phenomenological damage model," *Journal of Applied Mechanics*, vol. 58, no. 2, pp. 305–310, 1991.

[19] A.-S. Chiarelli, J.-F. Shao, and N Hoteit, "Modeling of elastoplastic damage behavior of a claystone," *International Journal of Plasticity*, vol. 19, no. 1, pp. 23–45, 2003.

[20] S. Yuan and J. Harrison, "A review of the state of the art in modelling progressive mechanical breakdown and associated fluid flow in intact heterogeneous rocks," *International Journal of Rock Mechanics and Mining Sciences*, vol. 43, no. 7, pp. 1001–1022, 2006.

[21] S. Murakami, *Continuum damage mechanics: a continuum mechanics approach to the analysis of damage and fracture*. Springer Science & Business Media, 2012, vol. 185.

[22] R. O. Davis and A. P. Selvadurai, *Plasticity and geomechanics*. Cambridge University Press, 2005.

[23] J. Mazars, "A description of micro- and macroscale damage of concrete structures," *Engineering Fracture Mechanics*, vol. 25, no. 5, pp. 729–737, 1986.

[24] J. Mazars and G. Pijaudier-Cabot, "Continuum damage theory-application to concrete," *Journal of Engineering Mechanics*, vol. 115, no. 2, pp. 345–365, 1989.

[25] C. Comi and U. Perego, "Fracture energy based bi-dissipative damage model for concrete," *International Journal of Solids and Structures*, vol. 38, no. 36, pp. 6427–6454, 2001.

[26] S. Murakami and K. Kamiya, "Constitutive and damage evolution equations of elastic-brittle materials based on irreversible thermodynamics," *International Journal of Mechanical Sciences*, vol. 39, no. 4, pp. 473–486, 1997.

[27] K. Hayakawa and S. Murakami, "Thermodynamical modeling of elastic-plastic damage and experimental validation of damage potential," *International Journal of damage mechanics*, vol. 6, no. 4, pp. 333–363, 1997.

[28] D. Halm and A. Dragon, "A model of anisotropic damage by mesocrack growth; unilateral effect," *International Journal of Damage Mechanics*, vol. 5, no. 4, pp. 384–402, 1996.

[29] ——, "An anisotropic model of damage and frictional sliding for brittle materials," *European Journal of Mechanics-A/Solids*, vol. 17, no. 3, pp. 439–460, 1998.

[30] A. Dragon, D. Halm, and T. Désoyer, "Anisotropic damage in quasi-brittle solids: Modelling, computational issues and applications," *Computer methods in applied mechanics and engineering*, vol. 183, no. 3, pp. 331–352, 2000.

[31] R. K. A. Al-Rub, G. Z. Voyiadjis, and D. J. Bammann, "A thermodynamic based higher-order gradient theory for size dependent plasticity," *International Journal of Solids and Structures*, vol. 44, no. 9, pp. 2888–2923, 2007.

[32] G. Z. Voyiadjis, Z. N. Taqieddin, and P. I. Kattan, "Anisotropic damage–plasticity model for concrete," *International Journal of Plasticity*, vol. 24, no. 10, pp. 1946–1965, 2008.

[33] J.-L. Chaboche, "Continuous damage mechanics—a tool to describe phenomena before crack initiation," *Nuclear Engineering and Design*, vol. 64, no. 2, pp. 233–247, 1981.

[34] J. Simo and J. Ju, "Strain-and stress-based continuum damage models—i. formulation," *International journal of solids and structures*, vol. 23, no. 7, pp. 821–840, 1987.

[35] J.-L. Chaboche, "Continuum damage mechanics: Part ii—damage growth, crack initiation, and crack growth," *Journal of applied mechanics*, vol. 55, no. 1, pp. 65–72, 1988.

[36] D. Krajcinovic, "Damage mechanics," *Mechanics of materials*, vol. 8, no. 2, pp. 117–197, 1989.

[37] I. Collins and G. Houlsby, "Application of thermomechanical principles to the modelling of geotechnical materials," in *Proceedings of the Royal Society of London A: Mathematical, Physical and Engineering Sciences*, The Royal Society, vol. 453, 1997, pp. 1975–2001.

[38] V. Lubarda, D. Krajcinovic, and S. Mastilovic, "Damage model for brittle elastic solids with unequal tensile and compressive strengths," *Engineering Fracture Mechanics*, vol. 49, no. 5, pp. 681–697, 1994.

[39] M. Frémond and B. Nedjar, "Damage, gradient of damage and principle of virtual power," *International Journal of Solids and Structures*, vol. 33, no. 8, pp. 1083–1103, 1996.

[40] G. Swoboda and Q. Yang, "An energy-based damage model of geomaterials—i. formulation and numerical results," *International journal of solids and structures*, vol. 36, no. 12, pp. 1719–1734, 1999.

[41] B. Budiansky and R. J. O'connell, "Elastic moduli of a cracked solid," *International Journal of Solids and Structures*, vol. 12, no. 2, pp. 81–97, 1976.

[42] M. L. Kachanov, "Effective elastic properties of cracked solids: Critical review of some basic concepts," *Applied Mechanics Reviews*, vol. 45, no. 8, pp. 304–335, 1992.

[43] ——, "Elastic solids with many cracks and related problems," 1993.

[44] ——, "A microcrack model of rock inelasticity part i: Frictional sliding on microcracks," *Mechanics of Materials*, vol. 1, no. 1, pp. 19–27, 1982.

[45] ——, "A microcrack model of rock inelasticity part ii: Propagation of microcracks," *Mechanics of Materials*, vol. 1, no. 1, pp. 29–41, 1982.

[46] V. Pensée, D. Kondo, and L. Dormieux, "Micromechanical analysis of anisotropic damage in brittle materials," *Journal of Engineering Mechanics*, vol. 128, no. 8, pp. 889–897, 2002.

[47] V. Pensee and D. Kondo, "Micromechanics of anisotropic brittle damage: Comparative analysis between a stress based and a strain based formulation," *Mechanics of materials*, vol. 35, no. 8, pp. 747–761, 2003.

[48] L. Gambarotta and S. Lagomarsino, "A microcrack damage model for brittle materials," *International Journal of Solids and Structures*, vol. 30, no. 2, pp. 177–198, 1993.

[49] S. Nemat-Nasser and M. Obata, "A microcrack model of dilatancy in brittle materials," *Journal of applied mechanics*, vol. 55, no. 1, pp. 24–35, 1988.

[50] X. Lee and J. Ju, "Micromechanical damage models for brittle solids. part ii: Compressive loadings," *Journal of Engineering Mechanics*, vol. 117, no. 7, pp. 1515–1536, 1991.

[51] J. Ju and X. Lee, "Micromechanical damage models for brittle solids. part i: Tensile loadings," *Journal of Engineering Mechanics*, vol. 117, no. 7, pp. 1495–1514, 1991.

[52] T. Mori and K. Tanaka, "Average stress in matrix and average elastic energy of materials with misfitting inclusions," *Acta metallurgica*, vol. 21, no. 5, pp. 571–574, 1973.

[53] Q. Zhu, D. Kondo, and J. Shao, "Micromechanical analysis of coupling between anisotropic damage and friction in quasi brittle materials: Role of the homogenization scheme," *International Journal of Solids and Structures*, vol. 45, no. 5, pp. 1385–1405, 2008.

[54] Q. Zhu, D. Kondo, and J.-F. Shao, "Homogenization-based analysis of anisotropic damage in brittle materials with unilateral effect and interactions between microcracks," *International Journal for Numerical and Analytical Methods in Geomechanics*, vol. 33, no. 6, pp. 749–772, 2009.

[55] Q. Zhu and J.-F. Shao, "A refined micromechanical damage–friction model with strength prediction for rock-like materials under compression," *International Journal of Solids and Structures*, vol. 60, pp. 75–83, 2015.

[56] M. Qi, J. Shao, A. Giraud, Q. Zhu, and J. Colliat, "Damage and plastic friction in initially anisotropic quasi brittle materials," *International Journal of Plasticity*, vol. 82, pp. 260–282, 2016.

[57] M. Qi, J. Shao, A. Giraud, Q. Zhu, and J. Colliat, "A numerical damage model for initially anisotropic materials," *International Journal of Solids and Structures*, vol. 100–101, no. 245–256, 2016.

[58] G. Swoboda and Q. Yang, "An energy-based damage model of geomaterials—ii. deductionof damage evolution laws," *International journal of solids and structures*, vol. 36, no. 12, pp. 1735–1755, 1999.

[59] D. Krajcinovic and D. Sumarac, "A mesomechanical model for brittle deformation processes: Part i," *Journal of Applied Mechanics*, vol. 56, no. 1, pp. 51–56, 1989.

[60] J. Ju, "On two-dimensinal self-consistent micromechanical damage models for brittle solids," *International Journal of Solids and Structures*, vol. 27, no. 2, pp. 227–258, 1991.

[61] Z. P. Bažant and P. C. Prat, "Microplane model for brittle-plastic material: I. theory," *Journal of Engineering Mechanics*, vol. 114, no. 10, pp. 1672–1688, 1988.

[62] Z. P. Bažant and J. Ozbolt, "Nonlocal microplane model for fracture, damage, and size effect in structures," *Journal of Engineering Mechanics*, vol. 116, no. 11, pp. 2485–2505, 1990.

[63] Z. P. Bažant, Y. Xiang, and P. C. Prat, "Microplane model for concrete. i: Stress-strain boundaries and finite strain," *Journal of Engineering Mechanics*, vol. 122, no. 3, pp. 245–254, 1996.

[64] Z. P. Bažant, F. C. Caner, I. Carol, M. D. Adley, and S. A. Akers, "Microplane model m4 for concrete. i: Formulation with work-conjugate deviatoric stress," *Journal of Engineering Mechanics*, vol. 126, no. 9, pp. 944–953, 2000.

[65] Z. P. Bažant and F. C. Caner, "Microplane model m5 with kinematic and static constraints for concrete fracture and anelasticity. i: Theory," *Journal of engineering mechanics*, vol. 131, no. 1, pp. 31–40, 2005.

[66] F. C. Caner and Z. P. Bažant, "Microplane model m7 for plain concrete. i: Formulation," *Journal of Engineering Mechanics*, vol. 139, no. 12, pp. 1714–1723, 2012.

[67] G. Pijaudier-Cabot and Z. P. Bažant, "Nonlocal damage theory," *Journal of Engineering Mechanics*, vol. 113, no. 10, pp. 1512–1533, 1987.

[68] Z. P. Bažant and G. Pijaudier-Cabot, "Nonlocal continuum damage, localization instability and convergence," *Journal of Applied Mechanics*, vol. 55, no. 2, pp. 287–293, 1988.

[69] J. De Vree, W. Brekelmans, and M. Van Gils, "Comparison of nonlocal approaches in continuum damage mechanics," *Computers & Structures*, vol. 55, no. 4, pp. 581–588, 1995.

[70] R. Peerlings, R. De Borst, W. Brekelmans, J. De Vree, and I. Spee, "Some observations on localisation in non-local and gradient damage models," *European Journal of Mechanics - A/Solids*, vol. 15, pp. 937–954, 1996.

[71] D. Lasry and T. Belytschko, "Localization limiters in transient problems," *International Journal of Solids and Structures*, vol. 24, no. 6, pp. 581–597, 1988.

[72] Z. P. Bažant and M. Jirasek, "Nonlocal integral formulations of plasticity and damage: Survey of progress," *Journal of Engineering Mechanics*, vol. 128, no. 11, pp. 1119–1149, 2002.

[73] Z. P. Bažant and G. Pijaudier-Cabot, "Measurement of characteristic length of nonlocal continuum," *Journal of Engineering Mechanics*, vol. 115, no. 4, pp. 755–767, 1989.

[74] M. Geers, R. De Borst, W. Brekelmans, and R. Peerlings, "Validation and internal length scale determination for a gradient damage model: Application to short glass-fibre-reinforced polypropylene," *International Journal of Solids and Structures*, vol. 36, no. 17, pp. 2557–2583, 1999.

[75] M. Jirasek, "Nonlocal models for damage and fracture: Comparison of approaches," *International Journal of Solids and Structures*, vol. 35, no. 31, pp. 4133–4145, 1998.

[76] Z. P. Bažant and F.-B. Lin, "Nonlocal smeared cracking model for concrete fracture," *Journal of structural engineering*, vol. 114, no. 11, pp. 2493–2510, 1988.

[77] H. Askes and L. Sluys, "Explicit and implicit gradient series in damage mechanics," *European Journal of Mechanics-A/Solids*, vol. 21, no. 3, pp. 379–390, 2002.

[78] H. Askes, J. Pamin, and R. de Borst, "Dispersion analysis and element-free galerkin solutions of second-and fourth-order gradient-enhanced damage models," *International Journal for Numerical Methods in Engineering*, vol. 49, no. 6, pp. 811–832, 2000.

[79] R. Peerlings, R De Borst, and J. De Vree, "Gradient enhanced damage for quasi-brittle materials," *International Journal for numerical methods in engineering*, vol. 39, no. De Vree, JHP, pp. 3391–3403, 1996.

[80] R. Peerlings, R. De Borst, W. Brekelmans, and M. Geers, "Gradient-enhanced damage modelling of concrete fracture," *Mechanics of Cohesive-frictional Materials*, vol. 3, no. 4, pp. 323–342, 1998.

[81] R. Peerlings, M. Geers, R De Borst, and W. Brekelmans, "A critical comparison of nonlocal and gradient-enhanced softening continua," *International Journal of solids and Structures*, vol. 38, no. 44, pp. 7723–7746, 2001.

[82] R. De Borst, J. Pamin, R. Peerlings, and L. Sluys, "On gradient-enhanced damage and plasticity models for failure in quasi-brittle and frictional materials," *Computational Mechanics*, vol. 17, no. 1-2, pp. 130–141, 1995.

[83] R. de Borst, J. Pamin, and M. G. Geers, "On coupled gradient-dependent plasticity and damage theories with a view to localization analysis," *European Journal of Mechanics-A/Solids*, vol. 18, no. 6, pp. 939–962, 1999.

[84] M. Geers, R De Borst, W. Brekelmans, and R. Peerlings, "Strain-based transient-gradient damage model for failure analyses," *Computer Methods in Applied Mechanics and Engineering*, vol. 160, no. 1, pp. 133–153, 1998.

[85] R. A. Toupin, "Theories of elasticity with couple-stress," *Archive for Rational Mechanics and Analysis*, vol. 17, no. 2, pp. 85–112, 1964.

[86] R. Mindlin, "Micro-structure in linear elasticity," *Archive for Rational Mechanics and Analysis*, vol. 16, no. 1, pp. 51–78, 1964.

[87] R. Mindlin and N. Eshel, "On first strain-gradient theories in linear elasticity," *International Journal of Solids and Structures*, vol. 4, no. 1, pp. 109–124, 1968.

[88] P. Germain, "The method of virtual power in continuum mechanics. part 2: Microstructure," *SIAM Journal on Applied Mathematics*, vol. 25, no. 3, pp. 556–575, 1973.

[89] F. Vernerey, W. K. Liu, and B. Moran, "Multi-scale micromorphic theory for hierarchical materials," *Journal of the Mechanics and Physics of Solids*, vol. 55, no. 12, pp. 2603–2651, 2007.

[90] T. Matsushima, R. Chambon, and D. Caillerie, "Second gradient models as a particular case of microstructured models: A large strain finite elements analysis," *CRAS-Série II b*, vol. 328, no. 2, pp. 179–186, 2000.

[91] R. Chambon, D. Caillerie, and T. Matsuchima, "Plastic continuum with microstructure, local second gradient theories for geomaterials: Localization studies," *International Journal of Solids and Structures*, vol. 38, no. 46, pp. 8503–8527, 2001.

[92] E. Cosserat, F. Cosserat, *et al.*, "Théorie des corps déformables," 1909.

[93] A. C. Eringen, "Theory of micropolar fluids," *Journal of Mathematics and Mechanics*, pp. 1–18, 1966.

[94] H. Kadowaki and W. K. Liu, "Bridging multi-scale method for localization problems," *Computer methods in applied mechanics and engineering*, vol. 193, no. 30, pp. 3267–3302, 2004.

[95] J. Sulem and I. G. Vardoulakis, *Bifurcation analysis in geomechanics*. CRC Press, 2004.

[96] C. Tamagnini, R. Chambon, and D. Caillerie, "A second gradient elastoplastic cohesive-frictional model for geomaterials," *Comptes Rendus de l'Académie des Sciences-Series IIB-Mechanics*, vol. 329, no. 10, pp. 735–739, 2001.

[97] R. Chambon, D. Caillerie, and C. Tamagnini, "A strain space gradient plasticity theory for finite strain," *Computer Methods in Applied Mechanics and Engineering*, vol. 193, no. 27, pp. 2797–2826, 2004.

[98] W. Zhou, J. Zhao, Y. Liu, and Q. Yang, "Simulation of localization failure with strain-gradient-enhanced damage mechanics," *International journal for numerical and analytical methods in geomechanics*, vol. 26, no. 8, pp. 793–813, 2002.

[99] J. Zhao, D. Sheng, and W. Zhou, "Shear banding analysis of geomaterials by strain gradient enhanced damage model," *International journal of solids and structures*, vol. 42, no. 20, pp. 5335–5355, 2005.

[100] H. Niandou, J. Shao, J. Henry, and D. Fourmaintraux, "Laboratory investigation of the mechanical behaviour of tournemire shale," *International Journal of Rock Mechanics and Mining Sciences*, vol. 34, no. 1, pp. 3–16, 1997.

[101] R. Gautam and R. C. Wong, "Transversely isotropic stiffness parameters and their measurement in colorado shale," *Canadian Geotechnical Journal*, vol. 43, no. 12, pp. 1290–1305, 2006.

[102] H. Sone and M. D. Zoback, "Mechanical properties of shale-gas reservoir rocks—part 1: Static and dynamic elastic properties and anisotropy," *Geophysics*, vol. 78, no. 5, pp. D381–D392, 2013.

[103] F. Oka, S. Kimoto, H. Kobayashi, and T. Adachi, "Anisotropic behavior of soft sedimentary rock and a constitutive model," *Soils and foundations*, vol. 42, no. 5, pp. 59–70, 2002.

[104] M. Nasseri, K. Rao, and T. Ramamurthy, "Anisotropic strength and deformational behavior of himalayan schists," *International Journal of Rock Mechanics and Mining Sciences*, vol. 40, no. 1, pp. 3–23, 2003.

[105] Y. F. Dafalias, A. G. Papadimitriou, and X. S. Li, "Sand plasticity model accounting for inherent fabric anisotropy," *Journal of Engineering Mechanics*, vol. 130, no. 11, pp. 1319–1333, 2004.

[106] Y. Fu, M. Iwata, W. Ding, F. Zhang, and A. Yashima, "An elastoplastic model for soft sedimentary rock considering inherent anisotropy and confining-stress dependency," *Soils and Foundations*, vol. 52, no. 4, pp. 575–589, 2012.

[107] J.-W. Cho, H. Kim, S. Jeon, and K.-B. Min, "Deformation and strength anisotropy of asan gneiss, boryeong shale, and yeoncheon schist," *International Journal of Rock Mechanics and Mining Sciences*, vol. 50, pp. 158–169, 2012.

[108] A. Vervoort, K.-B. Min, H. Konietzky, J.-W. Cho, B. Debecker, Q.-D. Dinh, T. Frühwirt, and A. Tavallali, "Failure of transversely isotropic rock under brazilian test conditions," *International Journal of Rock Mechanics and Mining Sciences*, vol. 70, pp. 343–352, 2014.

[109] S. Heng, Y. Guo, C. Yang, J. J. Daemen, and Z. Li, "Experimental and theoretical study of the anisotropic properties of shale," *International Journal of Rock Mechanics and Mining Sciences*, vol. 74, pp. 58–68, 2015.

[110] F. A. Donath, "Experimental study of shear failure in anisotropic rocks," *Geological Society of America Bulletin*, vol. 72, no. 6, pp. 985–989, 1961.

[111] R. Hill, "A theory of the yielding and plastic flow of anisotropic metals," in *Proceedings of the Royal Society of London A: Mathematical, Physical and Engineering Sciences*, The Royal Society, vol. 193, 1948, pp. 281–297.

[112] O. Hoffman, "The brittle strength of orthotropic materials," *Journal of Composite Materials*, vol. 1, no. 2, pp. 200–206, 1967.

[113] S. W. Tsai and E. M. Wu, "A general theory of strength for anisotropic materials," *Journal of composite materials*, vol. 5, no. 1, pp. 58–80, 1971.

[114] J. Schellekens and R. De Borst, "The use of the hoffman yield criterion in finite element analysis of anisotropic composites," *Computers & Structures*, vol. 37, no. 6, pp. 1087–1096, 1990.

[115] F. Hashagen and R. De Borst, "Enhancement of the hoffman yield criterion with an anisotropic hardening model," *Computers & Structures*, vol. 79, no. 6, pp. 637–651, 2001.

[116] K. Reinicke and T. Ralston, "Plastic limit analysis with an anisotropic, parabolic yield function," *International Journal of Rock Mechanics and Mining Sciences & Geomechanics Abstracts*, vol. 14, no. 3, pp. 147–162, 1977.

[117] S. J. Semnani, J. A. White, and R. I. Borja, "Thermoplasticity and strain localization in transversely isotropic materials based on anisotropic critical state plasticity," *International Journal for Numerical and Analytical Methods in Geomechanics*, vol. 40, no. 18, pp. 2423–2449, 2016.

[118] J. P. Boehler and A. Sawczuk, "On yielding of oriented solids," *Acta Mechanica*, vol. 27, no. 1-4, pp. 185–204, 1977.

[119] O. Cazacu, N. Cristescu, J. Shao, and J. Henry, "A new anisotropic failure criterion for transversely isotropic solids," *Mechanics of Cohesive-frictional Materials*, vol. 3, no. 1, pp. 89–103, 1998.

[120] O. Cazacu and N. D. Cristescu, "A paraboloid failure surface for transversely isotropic materials," *Mechanics of materials*, vol. 31, no. 6, pp. 381–393, 1999.

[121] A. Rouabhi, M. Tijani, and A. Rejeb, "Triaxial behaviour of transversely isotropic materials: Application to sedimentary rocks," *International Journal for Numerical and Analytical Methods in Geomechanics*, vol. 31, no. 13, pp. 1517–1535, 2007.

[122] S. Pietruszczak and Z. Mroz, "Formulation of anisotropic failure criteria incorporating a microstructure tensor," *Computers and Geotechnics*, vol. 26, no. 2, pp. 105–112, 2000.

[123] ——, "On failure criteria for anisotropic cohesive-frictional materials," *International Journal for Numerical and Analytical Methods in Geomechanics*, vol. 25, no. 5, pp. 509–524, 2001.

[124] S. Pietruszczak, D. Lydzba, and J.-F. Shao, "Modelling of inherent anisotropy in sedimentary rocks," *International Journal of Solids and Structures*, vol. 39, no. 3, pp. 637–648, 2002.

[125] L. Chen, J.-F. Shao, and H. Huang, "Coupled elastoplastic damage modeling of anisotropic rocks," *Computers and Geotechnics*, vol. 37, no. 1, pp. 187–194, 2010.

[126] M. Oda and H. Nakayama, "Yield function for soil with anisotropic fabric," *Journal of Engineering Mechanics*, vol. 115, no. 1, pp. 89–104, 1989.

[127] D. Halm, A. Dragon, and Y. Charles, "A modular damage model for quasi-brittle solids–interaction between initial and induced anisotropy," *Archive of Applied Mechanics*, vol. 72, no. 6-7, pp. 498–510, 2002.

[128] B. Nedjar, "On a concept of directional damage gradient in transversely isotropic materials," *International Journal of Solids and Structures*, vol. 88, pp. 56–67, 2016.

[129] L. Chen, J. F. Shao, Q. Z. Zhu, and G. Duveau, "Induced anisotropic damage and plasticity in initially anisotropic sedimentary rocks," *International Journal of Rock Mechanics and Mining Sciences*, vol. 51, pp. 13–23, 2012.

[130] D. Hu, H. Zhou, F. Zhang, J. Shao, and J. Zhang, "Modeling of inherent anisotropic behavior of partially saturated clayey rocks," *Computers and Geotechnics*, vol. 48, pp. 29–40, 2013.

[131] C. Li, F. C. Caner, V. T. Chau, and Z. P. Bažant, "Spherocylindrical microplane constitutive model for shale and other anisotropic rocks," *Journal of the Mechanics and Physics of Solids*, vol. 103, pp. 155–178, 2017.

[132] Y. Ma and H. Huang, "Dem analysis of failure mechanisms in the intact brazilian test," *International Journal of Rock Mechanics and Mining Sciences*, vol. 102, pp. 109–119, 2018.

[133] A. Yin, X. Yang, S. Yang, and W. Jiang, "Multiscale fracture simulation of three-point bending asphalt mixture beam considering material heterogeneity," *Engineering Fracture Mechanics*, vol. 78, no. 12, pp. 2414–2428, 2011.

[134] J. Oliver, M. Caicedo, E. Roubin, A. E. Huespe, and J. A. Hernández, "Continuum approach to computational multiscale modeling of propagating fracture," *Computer Methods in Applied Mechanics and Engineering*, vol. 294, pp. 384–427, 2015.

[135] M. G. Geers, V. G. Kouznetsova, and W. Brekelmans, "Multi-scale computational homogenization: Trends and challenges," *Journal of computational and applied mathematics*, vol. 234, no. 7, pp. 2175–2182, 2010.

[136] J.-C. Michel, H. Moulinec, and P. Suquet, "Effective properties of composite materials with periodic microstructure: A computational approach," *Computer methods in applied mechanics and engineering*, vol. 172, no. 1-4, pp. 109–143, 1999.

[137] F. Feyel, "A multilevel finite element method (fe2) to describe the response of highly non-linear structures using generalized continua," *Computer Methods in applied Mechanics and engineering*, vol. 192, no. 28-30, pp. 3233–3244, 2003.

[138] C. R. Searcy, "A multiscale model for predicting damage evolution in heterogeneous viscoelastic media," PhD thesis, Texas A&M University, 2004.

[139] J. Fish and Z. Yuan, "Multiscale enrichment based on partition of unity," *International Journal for Numerical Methods in Engineering*, vol. 62, no. 10, pp. 1341–1359, 2005.

[140] Z. Yuan and J. Fish, "Toward realization of computational homogenization in practice," *International Journal for Numerical Methods in Engineering*, vol. 73, no. 3, pp. 361–380, 2008.

[141] A. Abdulle and A. Nonnenmacher, "A short and versatile finite element multiscale code for homogenization problems," *Computer Methods in Applied Mechanics and Engineering*, vol. 198, no. 37-40, pp. 2839–2859, 2009.

[142] V. Kouznetsova, M. G. Geers, and W. M. Brekelmans, "Multi-scale constitutive modelling of heterogeneous materials with a gradient-enhanced computational homogenization scheme," *International Journal for Numerical Methods in Engineering*, vol. 54, no. 8, pp. 1235–1260, 2002.

[143] V. Kouznetsova, M. Geers, and W. Brekelmans, "Multi-scale second-order computational homogenization of multi-phase materials: A nested finite element solution strategy," *Computer Methods in Applied Mechanics and Engineering*, vol. 193, no. 48-51, pp. 5525–5550, 2004.

[144] T. Massart, R. Peerlings, and M. Geers, "An enhanced multi-scale approach for masonry wall computations with localization of damage," *International journal for numerical methods in engineering*, vol. 69, no. 5, pp. 1022–1059, 2007.

[145] T. Belytschko, S. Loehnert, and J. H. Song, "Multiscale aggregating discontinuities: A method for circumventing loss of material stability," *International Journal for Numerical Methods in Engineering*, vol. 73, no. 6, pp. 869–894, 2008.

[146] T. Belytschko and J. H. Song, "Coarse-graining of multiscale crack propagation," *International journal for numerical methods in engineering*, vol. 81, no. 5, pp. 537–563, 2010.

[147] M. Kulkarni, K Matouš, and P. Geubelle, "Coupled multi-scale cohesive modeling of failure in heterogeneous adhesives," *International Journal for Numerical Methods in Engineering*, vol. 84, no. 8, pp. 916–946, 2010.

[148] C. V. Verhoosel, J. J. Remmers, M. A. Gutiérrez, and R. De Borst, "Computational homogenization for adhesive and cohesive failure in quasi-brittle solids," *International Journal for Numerical Methods in Engineering*, vol. 83, no. 8-9, pp. 1155–1179, 2010.

[149] V. P. Nguyen, M. Stroeven, and L. J. Sluys, "An enhanced continuous–discontinuous multiscale method for modeling mode-i cohesive failure in random heterogeneous quasi-brittle materials," *Engineering Fracture Mechanics*, vol. 79, pp. 78–102, 2012.

[150] O. Lloberas-Valls, D. J. Rixen, A. Simone, and L. J. Sluys, "Multiscale domain decomposition analysis of quasi-brittle heterogeneous materials," *International Journal for Numerical Methods in Engineering*, vol. 89, no. 11, pp. 1337–1366, 2012.

[151] P.-A. Guidault, O. Allix, L. Champaney, and J.-P. Navarro, "A two-scale approach with homogenization for the computation of cracked structures," *Computers & structures*, vol. 85, no. 17-18, pp. 1360–1371, 2007.

[152] T. Hettich, A. Hund, and E. Ramm, "Modeling of failure in composites by x-fem and level sets within a multiscale framework," *Computer Methods in Applied Mechanics and Engineering*, vol. 197, no. 5, pp. 414–424, 2008.

[153] S. Eckardt and C. Könke, "Adaptive damage simulation of concrete using heterogeneous multiscale models," *Journal of Algorithms & Computational Technology*, vol. 2, no. 2, pp. 275–298, 2008.

[154] M. Xu, R. Gracie, and T. Belytschko, *Multiscale modeling with extended bridging domain method*, Oxford University Press, 2002.

[155] P. R. Budarapu, R. Gracie, S.-W. Yang, X. Zhuang, and T. Rabczuk, "Efficient coarse graining in multiscale modeling of fracture," *Theoretical and Applied Fracture Mechanics*, vol. 69, pp. 126–143, 2014.

[156] N. Guo and J. Zhao, "A coupled fem/dem approach for hierarchical multiscale modelling of granular media," *International Journal for Numerical Methods in Engineering*, vol. 99, no. 11, pp. 789–818, 2014.

[157] M. Jirasek and T. Zimmermann, "Embedded crack model. part ii: Combination with smeared cracks," *International Journal for Numerical Methods in Engineering*, vol. 50, no. 6, pp. 1291–1305, 2001.

[158] A. Simone, G. N. Wells, and L. J. Sluys, "From continuous to discontinuous failure in a gradient-enhanced continuum damage model," *Computer Methods in Applied Mechanics and Engineering*, vol. 192, no. 41, pp. 4581–4607, 2003.

[159] C. Comi, S. Mariani, and U. Perego, "An extended fe strategy for transition from continuum damage to mode i cohesive crack propagation," *International Journal for Numerical and Analytical Methods in Geomechanics*, vol. 31, no. 2, p. 213, 2007.

[160] S. Cuvilliez, F. Feyel, E. Lorentz, and S. Michel-Ponnelle, "A finite element approach coupling a continuous gradient damage model and a cohesive zone model within the framework of quasi-brittle failure," *Computer methods in applied mechanics and engineering*, vol. 237, pp. 244–259, 2012.

[161] Y. Wang and H. Waisman, "From diffuse damage to sharp cohesive cracks: A coupled xfem framework for failure analysis of quasi-brittle materials," *Computer Methods in Applied Mechanics and Engineering*, vol. 299, pp. 57–89, 2016.

[162] W. Jin and C. Arson, "Anisotropic nonlocal damage model for materials with intrinsic transverse isotropy," *International Journal of Solids and Structures*, vol. 139, pp. 29–42, 2018.

[163] A. Simone, H. Askes, and L. J. Sluys, "Incorrect initiation and propagation of failure in non-local and gradient-enhanced media," *International journal of solids and structures*, vol. 41, no. 2, pp. 351–363, 2004.

[164] S. Leon, D. Spring, and G. Paulino, "Reduction in mesh bias for dynamic fracture using adaptive splitting of polygonal finite elements," *International Journal for Numerical Methods in Engineering*, vol. 100, no. 8, pp. 555–576, 2014.

[165] J. Planas, M. Elices, and G. V. Guinea, "Cohesive cracks versus nonlocal models: Closing the gap," *International Journal of Fracture*, vol. 63, no. 2, pp. 173–187, 1993.

[166] J. Mazars and G. Pijaudier-Cabot, "From damage to fracture mechanics and conversely: A combined approach," *International Journal of Solids and Structures*, vol. 33, no. 20, pp. 3327–3342, 1996.

[167] F. Cazes, M. Coret, A. Combescure, and A. Gravouil, "A thermodynamic method for the construction of a cohesive law from a nonlocal damage model," *International Journal of Solids and Structures*, vol. 46, no. 6, pp. 1476–1490, 2009.

[168] F. Cazes, A. Simatos, M. Coret, and A. Combescure, "A cohesive zone model which is energetically equivalent to a gradient-enhanced coupled damage-plasticity model," *European Journal of Mechanics-A/Solids*, vol. 29, no. 6, pp. 976–989, 2010.

[169] M. Jirasek and T. Zimmermann, "Embedded crack model: I. basic formulation," *International journal for numerical methods in engineering*, vol. 50, no. 6, pp. 1269–1290, 2001.

[170] C. Comi, S. Mariani, and U. Perego, "From localized damage to discrete cohesive crack propagation in nonlocal continua," in *Proceedings of the Fifth World Congress on Computational Mechanics (WCCM V)*, Vienna University of Technology, 2002.

[171] Y. Wang and H. Waisman, "Progressive delamination analysis of composite materials using xfem and a discrete damage zone model," *Computational Mechanics*, vol. 55, no. 1, pp. 1–26, 2015.

[172] J. Leclerc, L. Wu, V. D. Nguyen, and L. Noels, "A damage to crack transition model accounting for stress triaxiality formulated in a hybrid nonlocal implicit discontinuous galerkin-cohesive band model framework," *International Journal for Numerical Methods in Engineering*, vol. 113, no. 3, pp. 374–410, 2018.

[173] I. N. Sneddon, "The distribution of stress in the neighbourhood of a crack in an elastic solid," *Proc. R. Soc. Lond. A*, vol. 187, no. 1009, pp. 229–260, 1946.

[174] A. Green and I. Sneddon, "The distribution of stress in the neighbourhood of a flat elliptical crack in an elastic solid," in *Mathematical Proceedings of the Cambridge Philosophical Society*, Cambridge University Press, vol. 46, 1950, pp. 159–163.

[175] S. Khristianovic and Y. Zheltov, "Formation of vertical fractures by means of highly viscous fluids," in *Proc. 4th world petroleum congress, Rome*, vol. 2, 1955, pp. 579–586.

[176] T. Perkins, L. Kern, *et al.*, "Widths of hydraulic fractures," *Journal of Petroleum Technology*, vol. 13, no. 09, pp. 937–949, 1961.

[177] R. Nordgren *et al.*, "Propagation of a vertical hydraulic fracture," *Society of Petroleum Engineers Journal*, vol. 12, no. 04, pp. 306–314, 1972.

[178] J. Geertsma, F. De Klerk, *et al.*, "A rapid method of predicting width and extent of hydraulically induced fractures," *Journal of Petroleum Technology*, vol. 21, no. 12, pp. 1–571, 1969.

[179] D. A. Spence and P. Sharp, "Self-similar solutions for elastohydrodynamic cavity flow," *Proc. R. Soc. Lond. A*, vol. 400, no. 1819, pp. 289–313, 1985.

[180] H. Abe, L. M. Keer, and T. Mura, "Growth rate of a penny-shaped crack in hydraulic fracturing of rocks, 2," *Journal of Geophysical Research*, vol. 81, no. 35, pp. 6292–6298, 1976.

[181] H Abe, L. Keer, and T Mura, "Theoretical study of hydraulically fractured penny-shaped cracks in hot, dry rocks," *International Journal for Numerical and Analytical Methods in Geomechanics*, vol. 3, no. 1, pp. 79–96, 1979.

[182] E. Detournay, "Propagation regimes of fluid-driven fractures in impermeable rocks," *International Journal of Geomechanics*, vol. 4, no. 1, pp. 35–45, 2004.

[183] J. I. Adachi and E. Detournay, "Self-similar solution of a plane-strain fracture driven by a power-law fluid," *International Journal for Numerical and Analytical Methods in Geomechanics*, vol. 26, no. 6, pp. 579–604, 2002.

[184] J. I. Adachi and E. Detournay, "Plane strain propagation of a hydraulic fracture in a permeable rock," *Engineering Fracture Mechanics*, vol. 75, no. 16, pp. 4666–4694, 2008.

[185] D. I. Garagash and E. Detournay, "Plane-strain propagation of a fluid-driven fracture: Small toughness solution," *Journal of Applied Mechanics*, vol. 72, no. 6, pp. 916–928, 2005.

[186] D. Garagash, "Transient solution for a plane-strain fracture driven by a shear-thinning, power-law fluid," *International journal for numerical and analytical methods in geomechanics*, vol. 30, no. 14, pp. 1439–1475, 2006.

[187] D. I. Garagash, "Plane-strain propagation of a fluid-driven fracture during injection and shut-in: Asymptotics of large toughness," *Engineering fracture mechanics*, vol. 73, no. 4, pp. 456–481, 2006.

[188] J. Hu and D. I. Garagash, "Plane-strain propagation of a fluid-driven crack in a permeable rock with fracture toughness," *Journal of Engineering Mechanics*, vol. 136, no. 9, pp. 1152–1166, 2010.

[189] A. Savitski and E. Detournay, "Propagation of a penny-shaped fluid-driven fracture in an impermeable rock: Asymptotic solutions," *International Journal of Solids and Structures*, vol. 39, no. 26, pp. 6311–6337, 2002.

[190] A. P. Bunger and E. Detournay, "Asymptotic solution for a penny-shaped near-surface hydraulic fracture," *Engineering fracture mechanics*, vol. 72, no. 16, pp. 2468–2486, 2005.

[191] ——, "Early-time solution for a radial hydraulic fracture," *Journal of engineering mechanics*, vol. 133, no. 5, pp. 534–540, 2007.

[192] J. Adachi, E. Siebrits, A. Peirce, and J. Desroches, "Computer simulation of hydraulic fractures," *International Journal of Rock Mechanics and Mining Sciences*, vol. 44, no. 5, pp. 739–757, 2007.

[193] E. Detournay and A. Peirce, "On the moving boundary conditions for a hydraulic fracture," *International Journal of Engineering Science*, vol. 84, pp. 147–155, 2014.

[194] J. Desroches, E. Detournay, B. Lenoach, P. Papanastasiou, J. R. A. Pearson, M. Thiercelin, and A. Cheng, "The crack tip region in hydraulic fracturing," *Proc. R. Soc. Lond. A*, vol. 447, no. 1929, pp. 39–48, 1994.

[195] B. Lenoach, "The crack tip solution for hydraulic fracturing in a permeable solid," *Journal of the Mechanics and Physics of Solids*, vol. 43, no. 7, pp. 1025 –1043, 1995.

[196] D. I. Garagash, E. Detournay, and J. Adachi, "Multiscale tip asymptotics in hydraulic fracture with leak-off," *Journal of Fluid Mechanics*, vol. 669, pp. 260–297, 2011.

[197] E. Dontsov and A. Peirce, "A non-singular integral equation formulation to analyse multiscale behaviour in semi-infinite hydraulic fractures," *Journal of Fluid Mechanics*, vol. 781, 2015.

[198] J. D. McLennan, J. C. Picardy, *et al.*, "Pseudo-three-dimensional fracture growth modeling," in *The 26th US Symposium on Rock Mechanics (USRMS)*, American Rock Mechanics Association, 1985.

[199] A. Settari, M. P. Cleary, *et al.*, "Development and testing of a pseudo-three-dimensional model of hydraulic fracture geometry," *SPE Production Engineering*, vol. 1, no. 06, pp. 449–466, 1986.

[200] I. Palmer, H. Carroll Jr, *et al.*, "Numerical solution for height and elongated hydraulic fractures," in *SPE/DOE Low Permeability Gas Reservoirs Symposium*, Society of Petroleum Engineers, 1983.

[201] C. E. Cohen, O. Kresse, X. Weng, *et al.*, "A new stacked height growth model for hydraulic fracturing simulation," in *49th US Rock Mechanics/Geomechanics Symposium*, American Rock Mechanics Association, 2015.

[202] E. Dontsov and A. Peirce, "An enhanced pseudo-3d model for hydraulic fracturing accounting for viscous height growth, non-local elasticity, and lateral toughness," *Engineering Fracture Mechanics*, vol. 142, pp. 116–139, 2015.

[203] L. Vandamme and J. H. Curran, "A three-dimensional hydraulic fracturing simulator," *International Journal for Numerical Methods in Engineering*, vol. 28, no. 4, pp. 909–927, 1989.

[204] A. Peirce and E. Detournay, "An implicit level set method for modeling hydraulically driven fractures," *Computer Methods in Applied Mechanics and Engineering*, vol. 197, no. 33-40, pp. 2858–2885, 2008.

[205] E. Siebrits and A. P. Peirce, "An efficient multi-layer planar 3d fracture growth algorithm using a fixed mesh approach," *International journal for numerical methods in engineering*, vol. 53, no. 3, pp. 691–717, 2002.

[206] S. Advani, T. Lee, and J. Lee, "Three-dimensional modeling of hydraulic fractures in layered media: Part i—finite element formulations," *Journal of Energy Resources Technology*, vol. 112, no. 1, pp. 1–9, 1990.

[207] E. Dontsov and A. Peirce, "Implementing a universal tip asymptotic solution into an implicit level set algorithm (ilsa) for multiple parallel hydraulic fractures," in *50th US Rock Mechanics/Geomechanics Symposium*, American Rock Mechanics Association, 2016.

[208] A. Peirce, "Modeling multi-scale processes in hydraulic fracture propagation using the implicit level set algorithm," *Computer Methods in Applied Mechanics and Engineering*, vol. 283, pp. 881–908, 2015.

[209] E. Dontsov and A. Peirce, "A multiscale implicit level set algorithm (ilsa) to model hydraulic fracture propagation incorporating combined viscous, toughness, and leak-off asymptotics," *Computer Methods in Applied Mechanics and Engineering*, vol. 313, pp. 53–84, 2017.

[210] P. Gupta and C. A. Duarte, "Simulation of non-planar three-dimensional hydraulic fracture propagation," *International Journal for Numerical and Analytical Methods in Geomechanics*, vol. 38, no. 13, pp. 1397–1430, 2014.

[211] B. Carter, J Desroches, A. Ingraffea, and P. Wawrzynek, "Simulating fully 3d hydraulic fracturing," *Modeling in geomechanics*, vol. 200, pp. 525–557, 2000.

[212] M. Vahab and N. Khalili, "X-fem modeling of multizone hydraulic fracturing treatments within saturated porous media," *Rock Mechanics and Rock Engineering*, pp. 1–21, 2018.

[213] M. Haddad and K. Sepehrnoori, "Integration of xfem and czm to model 3d multiple-stage hydraulic fracturing in quasi-brittle shale formations: Solution-dependent propagation direction," in *Proceedings of the AADE National Technical Conference and Exhibition, AADE2015, San Antonio, Texas, 8-9 April 2015*, 2015.

[214] A. R. Khoei, M. Hirmand, M. Vahab, and M. Bazargan, "An enriched fem technique for modeling hydraulically driven cohesive fracture propagation in impermeable media with frictional natural faults: Numerical and experimental investigations," *International Journal for Numerical Methods in Engineering*, vol. 104, no. 6, pp. 439–468, 2015.

[215] A. Khoei, M Vahab, and M. Hirmand, "Modeling the interaction between fluid-driven fracture and natural fault using an enriched-fem technique," *International Journal of Fracture*, vol. 197, no. 1, pp. 1–24, 2016.

[216] O. Kresse, X. Weng, H. Gu, and R. Wu, "Numerical modeling of hydraulic fractures interaction in complex naturally fractured formations," *Rock mechanics and rock engineering*, vol. 46, no. 3, pp. 555–568, 2013.

[217] Z. Chen, "Finite element modelling of viscosity-dominated hydraulic fractures," *Journal of Petroleum Science and Engineering*, vol. 88, pp. 136–144, 2012.

[218] M. Faivre, B. Paul, F. Golfier, R. Giot, P. Massin, and D. Colombo, "2d coupled hm-xfem modeling with cohesive zone model and applications to fluid-driven fracture network," *Engineering Fracture Mechanics*, vol. 159, pp. 115–143, 2016.

[219] C. Miehe, S. Mauthe, and S. Teichtmeister, "Minimization principles for the coupled problem of darcy–biot-type fluid transport in porous media linked to phase field modeling of fracture," *Journal of the Mechanics and Physics of Solids*, vol. 82, pp. 186–217, 2015.

[220] H. Wang, "Numerical modeling of non-planar hydraulic fracture propagation in brittle and ductile rocks using xfem with cohesive zone method," *Journal of Petroleum Science and Engineering*, vol. 135, pp. 127–140, 2015.

[221] M. Haddad and K. Sepehrnoori, "Simulation of hydraulic fracturing in quasi-brittle shale formations using characterized cohesive layer: Stimulation controlling factors," *Journal of Unconventional Oil and Gas Resources*, vol. 9, pp. 65–83, 2015.

[222] X. Wang, C. Liu, H. Wang, H. Liu, and H. Wu, "Comparison of consecutive and alternate hydraulic fracturing in horizontal wells using xfem-based cohesive zone method," *Journal of Petroleum Science and Engineering*, vol. 143, pp. 14–25, 2016.

[223] Z. Chen, A. Bunger, X. Zhang, and R. G. Jeffrey, "Cohesive zone finite element-based modeling of hydraulic fractures," *Acta Mechanica Solida Sinica*, vol. 22, no. 5, pp. 443–452, 2009.

[224] Z. Chen, "An abaqus implementation of the xfem for hydraulic fracture problems," in *Effective and sustainable hydraulic fracturing*, InTech, 2013.

[225] A. R. Khoei, M. Vahab, E. Haghighat, and S. Moallemi, "A mesh-independent finite element formulation for modeling crack growth in saturated porous media based on an enriched-fem technique," *International Journal of Fracture*, vol. 188, no. 1, pp. 79–108, 2014.

[226] E. Remij, J. Remmers, J. Huyghe, and D. Smeulders, "The enhanced local pressure model for the accurate analysis of fluid pressure driven fracture in porous materials," *Computer Methods in Applied Mechanics and Engineering*, vol. 286, pp. 293–312, 2015.

[227] A. R. Lamb, G. J. Gorman, and D. Elsworth, "A fracture mapping and extended finite element scheme for coupled deformation and fluid flow in fractured porous media," *International journal for numerical and analytical methods in geomechanics*, vol. 37, no. 17, pp. 2916–2936, 2013.

[228] S. Salimzadeh and N. Khalili, "A three-phase xfem model for hydraulic fracturing with cohesive crack propagation," *Computers and Geotechnics*, vol. 69, pp. 82–92, 2015.

[229] E. Gordeliy and A. Peirce, "Coupling schemes for modeling hydraulic fracture propagation using the xfem," *Computer Methods in Applied Mechanics and Engineering*, vol. 253, pp. 305–322, 2013.

[230] H. Horii and S. Nemat-Nasser, "Overall moduli of solids with microcracks: Load-induced anisotropy," *Journal of the Mechanics and Physics of Solids*, vol. 31, no. 2, pp. 155–171, 1983.

[231] M. L. Kachanov, B. Shafiro, and I. Tsukrov, *Handbook of elasticity solutions*. Springer Science & Business Media, 2013.

[232] P. Bažant and B. H. Oh, "Efficient numerical integration on the surface of a sphere," *ZAMM-Journal of Applied Mathematics and Mechanics/Zeitschrift für Angewandte Mathematik und Mechanik*, vol. 66, no. 1, pp. 37–49, 1986.

[233] A. E. Ehret, M. Itskov, and H. Schmid, "Numerical integration on the sphere and its effect on the material symmetry of constitutive equations—a comparative study," *International journal for numerical methods in engineering*, vol. 81, no. 2, pp. 189–206, 2010.

[234] S. Levasseur, F. Collin, R. Charlier, and D. Kondo, "On micromechanical damage modeling in geomechanics: Influence of numerical integration scheme," *Journal of Computational and Applied Mathematics*, vol. 246, pp. 215–224, 2013.

[235] S. Nemat-Nasser and H. Horii, "Compression-induced nonplanar crack extension with application to splitting, exfoliation, and rockburst," *Journal of Geophysical Research: Solid Earth*, vol. 87, no. B8, pp. 6805–6821, 1982.

[236] M. F. Ashby and S. Hallam, "The failure of brittle solids containing small cracks under compressive stress states," *Acta Metallurgica*, vol. 34, no. 3, pp. 497–510, 1986.

[237] H. Horii and S. Nemat-Nasser, "Brittle failure in compression: Splitting, faulting and brittle-ductile transition," *Philosophical Transactions of the Royal Society of London A: Mathematical, Physical and Engineering Sciences*, vol. 319, no. 1549, pp. 337–374, 1986.

[238] E. Bombolakis and W. Brace, "A note on brittle crack growth in compression," *Journal of Geophysical Research*, vol. 68, no. 12, pp. 3709–3713, 1963.

[239] A. Dyskin and R. Salganik, "Model of dilatancy of brittle materials with cracks under compression," *Mechanics of solids*, vol. 22, no. 6, pp. 165–173, 1987.

[240] F. Lehner and M. L. Kachanov, "On modelling of 'winged" cracks forming under compression," *International Journal of Fracture*, vol. 77, no. 4, R69–R75, 1996.

[241] L. Germanovich, R. Salganik, A. Dyskin, and K. Lee, "Mechanisms of brittle fracture of rock with pre-existing cracks in compression," *Pure and Applied Geophysics*, vol. 143, no. 1-3, pp. 117–149, 1994.

[242] E. Sahouryeh, A. Dyskin, and L. Germanovich, "Crack growth under biaxial compression," *Engineering Fracture Mechanics*, vol. 69, no. 18, pp. 2187–2198, 2002.

[243] L. Scholtès and F. V. Donzé, "Modelling progressive failure in fractured rock masses using a 3d discrete element method," *International Journal of Rock Mechanics and Mining Sciences*, vol. 52, pp. 18–30, 2012.

[244] L. Savalli and T. Engelder, "Mechanisms controlling rupture shape during subcritical growth of joints in layered rocks," *Geological Society of America Bulletin*, vol. 117, no. 3-4, pp. 436–449, 2005.

[245] D. Amendt, S. Busetti, Q. Wenning, *et al.*, "Mechanical characterization in unconventional reservoirs: A facies-based methodology," *Petrophysics*, vol. 54, no. 05, pp. 457–464, 2013.

[246] R. H. Byrd, J. C. Gilbert, and J. Nocedal, "A trust region method based on interior point techniques for nonlinear programming," *Mathematical Programming*, vol. 89, no. 1, pp. 149–185, 2000.

[247] R. A. Waltz, J. L. Morales, J. Nocedal, and D. Orban, "An interior algorithm for nonlinear optimization that combines line search and trust region steps," *Mathematical Programming*, vol. 107, no. 3, pp. 391–408, 2006.

[248] H. Sone and M. D. Zoback, "Mechanical properties of shale-gas reservoir rocks—part 2: Ductile creep, brittle strength, and their relation to the elastic modulus," *Geophysics*, vol. 78, no. 5, pp. D393–D402, 2013.

[249] J. Mazars, Y. Berthaud, and S. Ramtani, "The unilateral behaviour of damaged concrete," *Engineering Fracture Mechanics*, vol. 35, no. 4, pp. 629–635, 1990.

[250] J. Simo and T. J. Hughes, *Computational inelasticity, volume 7 of interdisciplinary applied mathematics*, 1998.

[251] V. K. Papanikolaou and A. J. Kappos, "Confinement-sensitive plasticity constitutive model for concrete in triaxial compression," *International Journal of Solids and Structures*, vol. 44, no. 21, pp. 7021–7048, 2007.

[252] H. Xu and C. Arson, "Mechanistic analysis of rock damage anisotropy and rotation around circular cavities," *Rock Mechanics and Rock Engineering*, vol. 48, no. 6, pp. 2283–2299, 2015.

[253] W. Jin, H. Xu, C. Arson, and S. Busetti, "Computational model coupling mode ii discrete fracture propagation with continuum damage zone evolution," *International Journal for Numerical and Analytical Methods in Geomechanics*, vol. 41, pp. 223–250, 2017.

[254] M. Hassanzadeh, "Behaviour of fracture process zones in concrete influenced by simultaneously applied normal and shear displacements," PhD thesis, Lund University, 1992.

[255] K. Park, G. H. Paulino, and J. R. Roesler, "A unified potential-based cohesive model of mixed-mode fracture," *Journal of the Mechanics and Physics of Solids*, vol. 57, no. 6, pp. 891–908, 2009.

[256] J. Shao, D. Hoxha, M. Bart, F. Homand, G. Duveau, M. Souley, and N. Hoteit, "Modelling of induced anisotropic damage in granites," *International Journal of Rock Mechanics and Mining Sciences*, vol. 36, no. 8, pp. 1001–1012, 1999.

[257] V. Lubarda and D. Krajcinovic, "Damage tensors and the crack density distribution," *International Journal of Solids and Structures*, vol. 30, no. 20, pp. 2859–2877, 1993.

[258] Q. Yang, W. Zhou, and G. Swoboda, "Micromechanical identification of anisotropic damage evolution laws," *International journal of fracture*, vol. 98, no. 1, pp. 55–76, 1999.

[259] M. L. Kachanov, "Continuum model of medium with cracks," *Journal of the engineering mechanics division*, vol. 106, no. 5, pp. 1039–1051, 1980.

[260] W. Jin and C. Arson, "Nonlocal enrichment of a micromechanical damage model with tensile softening: Advantages and limitations," *Computers and Geotechnics*, vol. 94, pp. 196–206, 2018.

[261] M. L. Kachanov, "Elastic solids with many cracks: A simple method of analysis," *International Journal of Solids and Structures*, vol. 23, no. 1, pp. 23–43, 1987.

[262] L. Shen and S. Yi, "New solutions for effective elastic moduli of microcracked solids," *International journal of solids and structures*, vol. 37, no. 26, pp. 3525–3534, 2000.

[263] L. Shen and J. Li, "A numerical simulation for effective elastic moduli of plates with various distributions and sizes of cracks," *International journal of solids and structures*, vol. 41, no. 26, pp. 7471–7492, 2004.

[264] S. H. Song, G. H. Paulino, and W. G. Buttlar, "A bilinear cohesive zone model tailored for fracture of asphalt concrete considering viscoelastic bulk material," *Engineering Fracture Mechanics*, vol. 73, no. 18, pp. 2829–2848, 2006.

[265] K. Park and G. H. Paulino, "Cohesive zone models: A critical review of traction-separation relationships across fracture surfaces," *Applied Mechanics Reviews*, vol. 64, no. 6, p. 060 802, 2011.

[266] ——, "Computational implementation of the ppr potential-based cohesive model in abaqus: Educational perspective," *Engineering Fracture Mechanics*, vol. 93, pp. 239–262, 2012.

[267] X. Xu and A. Needleman, "Numerical simulations of fast crack growth in brittle solids," *Journal of the Mechanics and Physics of Solids*, vol. 42, no. 9, pp. 1397–1434, 1994.

[268] V. P. Nguyen, "Discontinuous galerkin/extrinsic cohesive zone modeling: Implementation caveats and applications in computational fracture mechanics," *Engineering Fracture Mechanics*, vol. 128, pp. 37–68, 2014.

[269] W. Celes, G. H. Paulino, and R. Espinha, "A compact adjacency-based topological data structure for finite element mesh representation," *International journal for numerical methods in engineering*, vol. 64, no. 11, pp. 1529–1556, 2005.

[270] N. Moës and T. Belytschko, "Extended finite element method for cohesive crack growth," *Engineering fracture mechanics*, vol. 69, no. 7, pp. 813–833, 2002.

[271] J. M. Melenk and I. Babuška, "The partition of unity finite element method: Basic theory and applications," *Computer methods in applied mechanics and engineering*, vol. 139, no. 1-4, pp. 289–314, 1996.

[272] T.-P. Fries, "A corrected xfem approximation without problems in blending elements," *International Journal for Numerical Methods in Engineering*, vol. 75, no. 5, pp. 503–532, 2008.

[273] G. Wells, L. Sluys, and R De Borst, "Simulating the propagation of displacement discontinuities in a regularized strain-softening medium," *International Journal for Numerical Methods in Engineering*, vol. 53, no. 5, pp. 1235–1256, 2002.

[274] T. P. Fries and T. Belytschko, "The extended/generalized finite element method: An overview of the method and its applications," *International Journal for Numerical Methods in Engineering*, vol. 84, no. 3, pp. 253–304, 2010.

[275] O. C. Zienkiewicz and J. Z. Zhu, "The superconvergent patch recovery and a posteriori error estimates. part 1: The recovery technique," *International Journal for Numerical Methods in Engineering*, vol. 33, no. 7, pp. 1331–1364, 1992.

[276] B. Patzák and Z. Bittnar, "Oofem–an object oriented framework for finite element analysis," *Acta Polytechnica*, vol. 44, no. 5-6, 2004.

[277] B. Patzák, "Oofem—an object-oriented simulation tool for advanced modeling of materials and structures," *Acta Polytechnica*, vol. 52, no. 6, 2012.

[278] E. Denarie, V. Saouma, A. Iocco, and D. Varelas, "Concrete fracture process zone characterization with fiber optics," *Journal of engineering mechanics*, vol. 127, no. 5, pp. 494–502, 2001.

[279] D. Zhang and K. Wu, "Fracture process zone of notched three-point-bending concrete beams," *Cement and Concrete Research*, vol. 29, no. 12, pp. 1887–1892, 1999.

[280] G. A. Waters, R. E. Lewis, D. Bentley, *et al.*, "The effect of mechanical properties anisotropy in the generation of hydraulic fractures in organic shales," in *SPE Annual Technical Conference and Exhibition*, Society of Petroleum Engineers, 2011.

[281] Y. Zhi, G. Ahmad, *et al.*, "Deformation properties of saw-cut fractures in barnett, mancos and pierre shales," in *50th US Rock Mechanics/Geomechanics Symposium*, American Rock Mechanics Association, 2016.

[282] M. N. Bramlette, *US Geological Survey Professional Paper. No. 212.* US Government Printing Office, 1943.

[283] A. Huerta and G. Pijaudier-Cabot, "Discretization influence on regularization by two localization limiters," *Journal of engineering mechanics*, vol. 120, no. 6, pp. 1198–1218, 1994.

[284] R. Desmorat, F. Gatuingt, and F. Ragueneau, "Nonlocal anisotropic damage model and related computational aspects for quasi-brittle materials," *Engineering Fracture Mechanics*, vol. 74, no. 10, pp. 1539–1560, 2007.

[285] C. Comi and U. Perego, "Criteria for mesh refinement in nonlocal damage finite element analyses," *European Journal of Mechanics-A/Solids*, vol. 23, no. 4, pp. 615–632, 2004.

[286] M. Jirásek and B. Patzák, "Consistent tangent stiffness for nonlocal damage models," *Computers & structures*, vol. 80, no. 14, pp. 1279–1293, 2002.

[287] Z. Hashin, "Failure criteria for unidirectional fiber composites," *Journal of applied mechanics*, vol. 47, no. 2, pp. 329–334, 1980.

[288] Y. M. Tien and M. C. Kuo, "A failure criterion for transversely isotropic rocks," *International Journal of Rock Mechanics and Mining Sciences*, vol. 38, no. 3, pp. 399–412, 2001.

[289] C. Gallant, J. Zhang, C. A. Wolfe, J. Freeman, T. M. Al-Bazali, M. Reese, *et al.*, "Wellbore stability considerations for drilling high-angle wells through finely laminated shale: A case study from terra nova," in *SPE Annual Technical Conference and Exhibition*, Society of Petroleum Engineers, 2007.

[290] W. Jin and C. Arson, "Discrete equivalent wing crack based damage model for brittle solids," *International Journal of Solids and Structures*, vol. 110-111, pp. 279–293, 2017.

[291] ——, "Micromechanics based discrete damage model with multiple non-smooth yield surfaces: Theoretical formulation, numerical implementation and engineering applications," *International Journal of Damage Mechanics*, vol. 27, no. 5, pp. 611–639, 2018.

[292] P. Grassl, D. Xenos, M. Jirásek, and M. Horák, "Evaluation of nonlocal approaches for modelling fracture near nonconvex boundaries," *International Journal of Solids and Structures*, vol. 51, no. 18, pp. 3239–3251, 2014.

[293] J. Lin, W. Wu, and R. I. Borja, "Micropolar hypoplasticity for persistent shear band in heterogeneous granular materials," *Computer Methods in Applied Mechanics and Engineering*, vol. 289, pp. 24–43, 2015.

[294] C. G. Hoover and Z. P. Bažant, "Cohesive crack, size effect, crack band and work-of-fracture models compared to comprehensive concrete fracture tests," *International Journal of Fracture*, vol. 187, no. 1, pp. 133–143, 2014.

[295] Z. P. Bažant and B. H. Oh, "Crack band theory for fracture of concrete," *Materials and structures*, vol. 16, no. 3, pp. 155–177, 1983.

[296] E. Riks, "An incremental approach to the solution of snapping and buckling problems," *International Journal of Solids and Structures*, vol. 15, no. 7, pp. 529–551, 1979.

[297] M. A. Crisfield, "A fast incremental/iterative solution procedure that handles "snap-through"," *Computers & Structures*, vol. 13, no. 1, pp. 55–62, 1981.

[298] I. May and Y. Duan, "A local arc-length procedure for strain softening," *Computers & structures*, vol. 64, no. 1, pp. 297–303, 1997.

[299] C. V. Verhoosel, J. J. Remmers, and M. A. Gutiérrez, "A dissipation-based arc-length method for robust simulation of brittle and ductile failure," *International Journal for Numerical Methods in Engineering*, vol. 77, no. 9, pp. 1290–1321, 2009.

[300] M. A. Biot, "General theory of three-dimensional consolidation," *Journal of applied physics*, vol. 12, no. 2, pp. 155–164, 1941.

[301] O. Coussy, *Poromechanics*. John Wiley & Sons, 2004.

[302] T. Mohammadnejad and A. Khoei, "An extended finite element method for fluid flow in partially saturated porous media with weak discontinuities; the convergence analysis of local enrichment strategies," *Computational Mechanics*, vol. 51, no. 3, pp. 327–345, 2013.

[303] H. Chi, C. Talischi, O. Lopez-Pamies, and G. H. Paulino, "A paradigm for higher-order polygonal elements in finite elasticity using a gradient correction scheme," *Computer Methods in Applied Mechanics and Engineering*, vol. 306, pp. 216–251, 2016.

[304] J. A. White and R. I. Borja, "Stabilized low-order finite elements for coupled solid-deformation/fluid-diffusion and their application to fault zone transients," *Computer Methods in Applied Mechanics and Engineering*, vol. 197, no. 49-50, pp. 4353–4366, 2008.

[305] W. Sun, J. T. Ostien, and A. G. Salinger, "A stabilized assumed deformation gradient finite element formulation for strongly coupled poromechanical simulations at finite strain," *International Journal for Numerical and Analytical Methods in Geomechanics*, vol. 37, no. 16, pp. 2755–2788, 2013.

[306] K.-J. Bathe, "The inf–sup condition and its evaluation for mixed finite element methods," *Computers & structures*, vol. 79, no. 2, pp. 243–252, 2001.

[307] F. Brezzi and M. Fortin, *Mixed and hybrid finite element methods*. Springer Science & Business Media, 2012, vol. 15.

[308] I. Babuška, "The finite element method with lagrangian multipliers," *Numerische Mathematik*, vol. 20, no. 3, pp. 179–192, 1973.

[309] O. Ladyzhenskaya, *The mathematical theory of viscous incompressible flow*. Gordon and Breach, New York, 1969, vol. 76.

[310] F. Brezzi, "On the existence, uniqueness and approximation of saddle-point problems arising from lagrangian multipliers," *Revue française d'automatique, informatique, recherche opérationnelle. Analyse numérique*, vol. 8, no. R2, pp. 129–151, 1974.

[311] K. Park, H. Choi, and G. H. Paulino, "Assessment of cohesive traction-separation relationships in abaqus: A comparative study," *Mechanics Research Communications*, vol. 78, pp. 71–78, 2016.

VITA

Wencheng Jin was born on June 2, 1989, in a small village called Zongjiaba, Sichuan Province, China. He obtained his Bachelor of Engineering Degree (2011) and Master of Engineering Degree (2014) from Sichuan University in China. From August 2014, he started his Ph.D. study under the supervision of Dr. Chloé Arson at the Georgia Institute of Technology. He obtained his Master of Science Degree in 2016 and will receive his Ph.D. degree in August 2018 from Georgia Institute of Technology.